Title
Physical Properties of Mesoporous Silica Nanoparticles for Stimuli-Responsive Drug Delivery

Author
Dong, Juyao

Publication Date
2014

Peer reviewed|Thesis/dissertation

University of California

Los Angeles

Physical Properties of Mesoporous Silica Nanoparticles for Stimuli-Responsive Drug Delivery

A dissertation submitted in partial satisfaction

of the requirements for the degree

Doctor of Philosophy in Chemistry

by

Juyao Dong

2014

Abstract of the Dissertation

Physical Properties of Mesoporous Silica Nanoparticles for Stimuli-Responsive Drug Delivery

by

Juyao Dong

Doctor of Philosophy in Chemistry

University of California, Los Angeles, 2014

Professor Jeffrey I. Zink, Chair

The on-demand drug release of mesoporous silica nanoparticles is investigated by chemical modifications of nanomachines and by spectroscopic examination of their physical properties. To improve and diversify their biological performances, acid responsive nanovalve release systems are integrated with gadolinium MRI contrast agents and polyethylene imine-polyethylene glycol surface coatings. Nanoparticles, and bulk media for comparison, are heated superparamagnetically and their temperatures are monitored using the luminescence spectra of lanthanide upconversion nanocrystals. This thermometry technique is applied again in azobenzene nanoimpeller particles to analyze the photothermal and photochemical contributions of IR radiation in initiating cargo release. The emission spectra prove capable of revealing the nanoscale temperature change and the macroscopic dye release simultaneously. Mesoporous silica nanoparticles demonstrate versatile nanomedical delivery capabilities *in vitro* and *in vivo*.

The dissertation of Juyao Dong is approved.

Miguel A. Garcia-Garibay

Michael A. Jura

Jeffrey I. Zink, Committee Chair

University of California, Los Angeles

2014

To my parents

Table of Contents

List of Figures

List of Tables

Acknowledgments

The research work of this dissertation would not be possible without the support of many people: mentors, colleagues, friends, and my beloved family. I wish to express my gratitude to all of them, but would like to acknowledge a few in particular.

Dr. Jeffrey I. Zink, my advisor, has been inspiring, guiding, and supporting me and my research throughout my time at UCLA. Without his vision and encouragement, the work would have gone south a long time ago. But just as remarkable is his dedication to the fundamentals of science, especially in a field focusing on all practical uses. From him, I have learned to think critically and thoroughly, as well as to perform spectroscopic experiments. I will always remember our most inspirational discussions on quiet Saturday afternoons. One could not ask for a more intellectual and dedicated mentor.

I take a great pride in being part of the Zink group and want to thank my dearest lab members. Dr. Min Xue helped me start one of my early projects, not including the countless other times when I sought for advice, a knowledgeable teacher and colleague in the lab, and a reliable friend out of the lab. Dr. Zongxi Li has oftentimes felt like an elder sister to me, who trained me when I first joined the lab. We have great memories of spending the holidays together in this country. Angela Hwang and I started in the same year, and from taking care of classes to taking care of safety issues, she has always been there by my side. I am grateful, not only because she shares lab duties, like presenting to visiting professors, but also because she is the one I would turn to for a hug when time was really tough. I am thankful that we have Janie Chen with us, the most organized and patient one. The three of us went

through five years of ups and downs together. I learned a lot of spectroscopy skills and ideas from Janie and Dr. Matt Kiesz. Thanks to Matt, for constantly trying to be cheerful by being "annoying". For many years, Dr. Yuen Lau had a desk next to mine. Ever since she left, I have been missing our discussions of numerous topics, from chemistry to politics to cultural differences to tasty food. Dr. Derrick Tarn, a talented chemist and musician, brought enjoyable music to the lab, even with the sad cello pieces. Dr. Daniel Ferris was full of creative ideas, and helped me with all sorts of things from explaining biological concepts to fixing a hissing gas regulator. Dr. Courtney Thomas had conducted the previous study of one of my projects and had volunteered to organize the lab chores. Dr. Sanaz Gardner had been the most warm-hearted person I have ever met and warmed my early days in this new environment. Thanks to Zilu Li and Chia-jung Yu for bringing joy to lab and for carrying on research to the next phase.

I am very grateful to work with a group of brilliant collaborators. Dr. Zhaoxia Ji, Dr. Ruibin Li, Dr. Bingbing Sun, Dr. Yang Zhao, Dr. Huan Meng and Dr. Tian Xia from Dr. Andre E. Nel's group, and Dr. Carlotta A. Glackin and her group, all deserve special mentions. Without their insight and hard work, I would never be able to learn so much about nanomedicine and apply my work into a biological context.

I would like to thank my friends for their support. To Yan Jin, for being so energetic and organizing our group activities. To Yuxi Zhao, for sharing so many first times with me in this new country and being my best friend. To Yuewei Sheng, for wearilessly looking after me. To Xing Wei, for patiently listening to my stories from another continent and exploring the southern France with me. To Yu Shi, for being you and never giving up your dream.

To Jonathan Friedman, for being there for me whenever I need. To the girls in Chinese folk dance group, for the lovely memories on and off the stage, and our precious friendships. To my peers who came here with me, you guys made the early bitter days not so lonely at all. To Chris, a friend and a confidant, who has helped me that no one else could have. For that, I will always be grateful.

Finally, I am deeply indebted to my family, especially to my parents. Their unconditional love has been upholding me in the most difficult times, and continuously motivates me to be a better person. I am grateful to have their understanding and support to pursue my dreams on such a different path. I could never thank them enough for always believing in me. Special thanks to my aunts, uncles, and cousins, for taking care of my grandmas while I am thousands of miles away.

I would like to acknowledge Dr. Michael A. Jura, Dr. Richard B. Kaner and Dr. Miguel A. Garcia-Garibay, for their time to serve on my committee, and for all the valuable suggestions.

Vita

2009	HSBC Scholarship
2009	Bachelor of Science in Chemistry, Nanjing University
2009 - 2013	Teaching Assistant Department of Chemistry & Biochemistry, UCLA
2009 - 2014	Graduate Student Researcher Zink Research Group Department of Chemistry & Biochemistry, UCLA
2011	Master of Science in Chemistry, University of California, Los Angeles
2014	ACS Division of Inorganic Chemistry Travel Award
2014	UCLA Research Showcase Fellowship
2014	UCLA Department of Chemistry & Biochemistry Inorganic Chemistry Dissertation Award

Publications and Presentations

J. Dong and J. I. Zink. "Light or Heat? - Thermal Contribution of Continuous Near-IR Irradiation in Activating Nanomachines on Mesoporous Silica Nanoparticles Embedded with Upconversion Nanocrystals ." *Manuscript in preparation.*

J. Dong and J. I. Zink. "Taking the Temperature of the Interiors of Magnetically Heated Nanoparticles." *ACS Nano* **8**, 5199-5207 (2014). **Highlighted in *Nature Physics* 10**, 408 (2014).

R. Li, Z. Ji, C. H. Chang, D. R. Dunphy, X. Cai, H. Meng, H. Zhang, B. Sun, X. Wang, **J. Dong**, S. Lin, M. Wang, Y. Liao, C. J. Brinker, A. Nel and T. Xia. "Surface Interactions with Compartmentalized Cellular Phosphates Explain Rare Earth Oxide Nanoparticle Hazard and Provide Opportunities for Safer Design." *ACS Nano* **8**, 1771-1783 (2014). **Featured as ACS Editors' Choice**.

J. Dong, M. Xue and J. I. Zink. "Functioning of Nanovalves on Polymer Coated Mesoporous Silica Nanoparticles." *Nanoscale* **5**, 10300-10306 (2013).

H. Meng, Y. Zhao, **J. Dong**, M. Xue, Y. Lin, Z. Ji, W. X. Mai, H. Zhang, C. H. Chang, C. J. Brinker, J. I. Zink and A. E. Nel. "Two-wave Nanotherapy To Target the Stroma and

Optimize Gemcitabine Delivery To a Human Pancreatic Cancer Model in Mice." *ACS Nano* **7**, 10048-10065 (2013).

B. Sun, Z. Ji, Y. Liao, M. Wang, X. Wang, **J. Dong**, C. H. Chang, R. Li, H. Zhang, A. E. Nel and T. Xia. "Engineering an Effective Immune Adjuvant by Designed Control of Shape and Crystallinity of Aluminum Oxyhydroxide Nanoparticles." *ACS Nano* **7**, 10834-10849 (2013).

J. Friedman, H. Herman, N. Truong, M. B. Srivastava, **J. Dong** and D. Torres. "Considerations for the Design of an Epipelagic Biomimetic Electrostatic Imaging Element." *Proceedings of the Sixth ACM International Workshop on Underwater Networks* **11** (2011).

J. Friedman, D. Torres, T. Schmid, **J. Dong** and M. B. Srivastava. "A Biomimetic Quasi-static Electric Field Physical Channel for Underwater Ocean Networks." *Proceedings of the Fifth ACM International Workshop on UnderWater Networks* **7** (2010).

"Taking the Temperature of the Interiors of Mesoporous Silica Nanoparticles." *International Conference on Nanostructured Materials*, Flic-en-Flac, Mauritius, September 2014 (oral).

"Internal Temperature Measurement of Functional Mesoporous Silica Nanoparticles for Drug Delivery." *248th American Chemical Society National Meeting*, San Francisco, California, August 2014 (oral).

"The Physical Properties of Functional Mesoporous Silica Nanoparticles for Drug Delivery." *248th American Chemical Society National Meeting*, San Francisco, California, August 2014 (poster).

"Optical Temperature Detection inside Mesoporous Silica Nanoparticles with Superparamagnetic Nano-heaters." *247th American Chemical Society National Meeting*, Dallas, Texas, March 2014 (oral).

"Polymer Coated Mesoporous Silica Nanoparticles Controlled by Nanovalves for Drug Delivery." *245th American Chemical Society National Meeting*, New Orleans, Louisiana, April 2013 (poster).

"pH-Stimulated Mesoporous Silica Nanoparticle System for the Delivery of MRI Contrast Agent." *Southern California Inorganic Photochemistry Conference*, Catalina Island, California, September 2010 (oral).

"Mesoporous Silica Based Nanoimpeller and the Modification." *UCLA Cross-disciplinary Scholars in Science and Technology Final Presentation*, Los Angeles, California, May 2009 (oral).

Part I

Introduction

CHAPTER 1

Mesoporous Silica Nanoparticles for Controlled Drug Delivery

1.1 Mesoporous Silica Nanoparticles

Mesoporous silica nanoparticles (MSNs) are a family of nanomateirals composed primarily of silica containing nanoscale pores for applications such as drug delivery, imaging, catalysis, absorption and optical devices. The original silica porous structure discovered in the 90s [1, 2] has evolved into a group of materials that is tunable in almost every structural aspect. The particle dimension ranges from nanometers to centimeters [3]. The porous structure can be hexagonal (MCM-41), three-dimensional cubic (MCM-49), worm-like, radial, helical and lamellar [3, 4, 5, 6, 7]. By changing the templating agents and the synthetic procedures, the pore size can be adjusted from 2 to 27 nm [5]. The material morphology includes spheres, rods, hollow spheres, sheets, core-shell spheres and more complicated hierarchical structures [8]. Regarding to the composition, pure silica is the most popular form, with organic silicate incorporated sometimes to enhance the catalytic properties [9]. Porous nanostructures composed of other oxide compounds have also been synthesized such as porous Al_2O_3, TiO_2 and ZrO_2 [10], but these compositions are out of the scope of our discussion here. The great

structural flexibility of MSN is beneficial for the various applications. For our controlled drug delivery platform, this dissertation focuses on the hexagonal porous MCM-41 particles with an average diameter ranging from 50 to 120 nm.

1.1.1 Synthesis Mechanism

We are using a modified Stöber's method to synthesize the MSNs [11, 12], which involves two simultaneous processes: the sol-gel chemical process to make the silica precursors and the micelle self-assembly templating process. The former produces the silica composition, and the later provides the porous organization. The two parts are strongly cooperative in generating the designed nanostructure morphology.

The sol-gel chemistry used by Stöber in 1968 started with tetraalkyl silicates in a solution of alcohol and water with ammonia as the catalyst [11], where the tetraalkyl silicates undergoes hydrolysis and condensation reactions:

Hydrolysis:

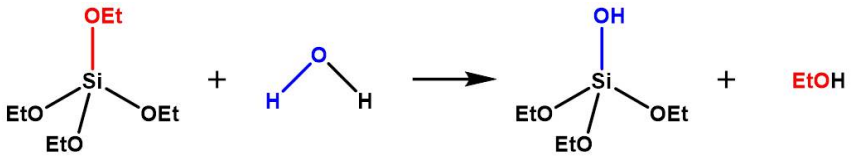

Condensation:

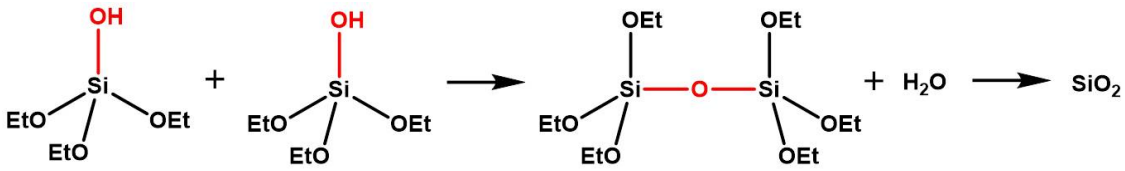

In the hydrolysis step, the alkoxy group reacts with water and is replaced by a hydroxyl group. The silanol products generated in this process react with each other and undergo

intermolecular condensation to produce the Si−O−Si bond. The reaction continues with the unsubstituted alkoxy groups. Eventually, the silicates are transformed into the SiO_2 scaffold, where the silicon atoms are interconnected by Si-O-Si bonds. The formula above illustrates this process with tetraethyl orthosilicate (TEOS), the most widely applied silica precursor for MSNs.

The second component in the synthesis of MSNs is the micelle self-assembly silica templating process. A cationic surfactant is introduced based on the Stöber's method, first by Grun *et al.* in 1997 [12], to construct the mesoporous structure. In our procedure, this templating surfactant is cetyltrimethylammonium bromide (CTAB, molecule length ∼2.2 nm), with a sixteen carbon chain on the hydrophobic side and a trimethyl ammonium on the hydrophilic side. When the surfactant concentration is above the critical micelle concentration (CMC), the CTAB molecules pack into micelles, self-assemble and organize into hexagonal arrays (Figure 1.1 on page 15). Whether the silica precursors contribute to the formation of this hexagonal structure have been debated [5, 13, 14]. The liquid-crystal templating theory states that the surfactant micelles arrange themselves into the hexagons in water and form the liquid-crystal phase. The silica precursors deposit into the space between the micelles and condense around them to generate the long-range ordered structures [14]. The cooperative self-assembly hypothesis, on the other hand, argues that the inorganic silicates interact with the isotropic organic micelles due to the opposite charge. The assembly process is thus initiated and is driven by the charge density difference at the inorganic/organic interface to reduce the energy [5, 13]. Hence the silica precursor is necessary for the hexagonal assembly of templating agents. The contributions of the two pathways are considered to vary among

different surfactant-silicate combinations as well as the different synthetic procedures. For our system, tetraethyl orthosilicate is believed to contribute to the self-assembly process of cetyltrimethylammonium bromide [1, 13].

As illustrated in Figure 1.1, the templating surfactant molecules are removed after synthesis in order to expose the space within the pores. Either calcination or solvent extraction are applied for this purpose. During the air calcination, the nanomaterial is heated to several hundred degrees and the organic surfactants are burnt out [1, 2]. As for the solvent extraction procedure, the as-prepared nanoparticles are dispersed in an acidic alcohol solution and refluxed. Because the negatively charged silanol surface are protonated and the surfactants have high solubilities in hot alcohols, the electrostatic interaction between silica frames and templating agents are reduced and the later are readily dissolved in the solution. Since the calcination methods would result in particle aggregation, we use the solvent extraction method to remove CTAB molecules for our biological applications.

As we have mentioned at the beginning of the chapter, mesoporous silica nanoparticles compose of a variety of nanostructures, and MCM-41 particle synthesized by CTAB and TEOS in an aqueous method is only a small part. For example, by changing the alkyl group in the cationic surfactant, the mesopore size could be adjusted accordingly [1]. Different silica precursors have different hydrolysis and condensation rates, and thus influence the morphology of MSNs. For example, TEOS reacts faster than tetrabutoxysilane, but slower than tetramethoxysilane [5]. In addition to the commonly used cationic surfactants, anionic and nonionic surfactants such as the poly(ethylene oxide) contained block copolymer have also been introduced to reduce the cost and to expand the material variation [15]. Moreover,

in order to generate uniformly sized particles or to modify the structural properties, a second templating agent can be added. The nonionic surfactant Pluronic F127 has been widely used to reduce the particle size by stopping the particle growth [16]. Both ethyl acetate and perfluorooctanoic acid have been shown to yield helical MCM-41 in the presence of CTAB [17, 18]. Additionally, both acidic and base catalysis has been employed, such as the hydrochloride acid used for the synthesis of SBA-15 [15].

1.1.2 Synthesis Procedures and Characterization Methods

The synthesis of our 100 nm MCM-41 particles starts with suspending the templating agent CTAB into a water solution. By adding sodium hydroxide solution into it, the reaction medium is tuned to pH 11. The mixture is stablized at 80 °C before the silica precursor TEOS is slowly added under vigorous stirring. The hydrolysis and condensation reaction of TEOS are thus carried out at the same time as that of the surfactant self-assembly process. After reacting and aging at 80 °C for two hours, the generated particles are collected via centrifugation. They are washed with water and methanol several times to remove the reactant residue. To extract the templating agents, the particles are suspended in methanol with HCl and refluxed at 60 °C for overnight.

The typical characterization methods include: X-ray powder diffraction (XRD) - to verify the silica crystal structure and the ordered porous structure; transmission electron microscopy (TEM) and scanning transmission electron microscopy (STEM) - to characterize the particle morphology and the porous structure; dynamic light scattering (DLS) - to characterize the hydrodynamic radius of particles in different solvents; N_2 absorption-desorption

analysis - to evaluate the macro- and mesoporous structures together with the information about particle surface areas and pore sizes; zeta-potential analysis - to determine the surface charge of particles; Fourier transform infrared spectroscopy (FTIR) - to confirm the chemical modification of silica particles, such as the removal of organic surfactants after solvent extractions, by monitoring the C−H vibration bands.

1.1.3 MSNs for Biomedical Applications

Mesoporous silica materials serve as a versatile platform for biomedical applications, especially for drug delivery.

(i) The porous materials have large surface areas and storing volumes. The average surface area for MSNs is about several hundred to a thousand square meters per gram, rendering them a great absorption medium. Thus, small drug molecules would have a high absorption affinity towards the porous structures. Moreover, variable pore diameters can be achieved by tuning the templating agents or the synthetic methods, providing the necessary storage space for cargo molecules of different sizes. The pore volume has been reported to be around 0.7 - 1.4 cm^3/g for mesoporous silica materials [4, 15].

(ii) In the context of drug delivery, the capacity of storing cargoes inside the pores is beneficial not only for controlling the release, but also for reducing the undesired interference between cargo molecules and biological molecules. As we will explain more detail later, the stored cargoes can be sterically separated from the external environment by a "gate" molecule attached to the pore openings. The gate can open and close the pores on demand, and thus prevent the premature leak of cargoes. The pores also protect the cargoes from degradation

by enzymes in biological systems [19].

(iii) Mesoporous silica nanomaterials are subject to versatile surface modification and functionalization by silane chemistry, which can be realized either during or after the particle synthesis. During the sol-gel reaction, the process is accomplished by introducing a functional silane reactant, such as the 3-aminopropyltrimethoxysilane (APTES). The amino silane molecule condenses into the silica scaffold, shifting the particle surface charge towards more positive and leaving an amino group for further reactions. On the other hand, the post-synthesis modification can be carried out with the unreacted silanol groups. An ortho silane molecule that has three alkoxy substitutes (like methoxy and ethoxy), can condense with the silanol groups and graft the particle surface with designed functional groups, such as chlorides, iodides, amines, hydroxyls, isocyanates and phosphonates [4, 20, 21]. Lots of organic synthetic methods can then be used to decorate the particles with active organic groups, polymers, antibodies and proteins [22, 23].

(iv) Silica nanoparticles are biocompatible. The biocompatibility of silica nanoparticles have been intensively studies at the *in vitro* and *in vivo* levels [20, 24, 25, 26, 27]. Studies carried out by our group and others have observed that the silica nanoparticles did not introduce toxicity within the concentration limit of 100 μg/mL,[20, 24, 25, 26, 28, 29]. This value is much higher than the usual dosage of MSNs for cellular and animal model experiments, which is about 1 to 30 μg/mL. More detailed research has revealed that the silica particles injected intravenously in mice can be excreted within 4 days through the urine and feces [29].

1.1.4 Other Biomedical Nanocarriers

Mesoporous silica is merely one member among the various drug delivery platforms. Nanostructures composed of polymers, dendrimers, liposomes, gold, iron oxide and semiconductors such as quantum dots are all adaptable drug carriers with their own advantages and disadvantages. Polymer nanoparticles have flexible backbone structures and high loading capacities, and usually accomplish controlled cargo release by their chemical property change, such as solubility variation or structural deformation [30]. Dendrimers are highly branched molecules and can incorporate cargoes via the guest-host interactions [31]. Liposomes have similar chemical compositions as that of the cell membranes, and thus can be internalized easily during the circulation [32]. In an effort to take advantage of the plasmonic effect, gold nanoparticles have been introduced to carry out photothermal therapies [33], and also benefit from their near-infrared emissions [34]. Iron oxides are paramagnetic or superparamagnetic materials, which enhance the contrast in the T_2-weighted magnetic resonance imaging (MRI) and can be physically manipulated by magnets [25]. Quantum dots are benefited from their intrinsic fluorescence and the broad absorption bands and can serve as a multifunctional carrier performing the imaging and drug delivery simultaneously [35, 36].

1.2 Nanomachines for Controlled Drug Delivery by MSNs

1.2.1 Strategies for Controlled Drug Delivery by MSNs

The idea of controlled drug delivery benefits the medical field from different perspectives. For diabetes treatment, the slow and regulated insulin release stabilizes the glucose concen-

tration in circulation systems and reduces the risk of combinations [19]. For the delivery of antibiotics, protecting the drugs from direct exposures will effectively decrease the consumption of drugs before reaching the designated tissues, extend the circulation time and increase the delivery rate [37]. For chemotherapy medicines, minimizing the premature release will not only enhance delivery efficacies but also reduce damages to health tissues. A higher local concentration of therapeutics could be achieved near the leisions, with less side effects. This dissertation will primarily focus on the controlled drug delivery for cancer treatment.

The on-command drug delivery based on mesoporous silica nanoparticles have been achieved by various methods. The initial research involved using nanocrystals to cap the nanopore openings and release the payloads upon breaking the connection bond. The nanocrystals, such as CdS and Fe_3O_4, were covalently attached to silica particles via a disulfide bond, which could be reduced by cellular antioxidants or reducing agents like dithiothreitol [38, 39], and thus open the pores and free the payloads. Another strategy is macromolecule capping. Polymers, dendrimers and lipids have been coated on the surface of silica particles, preventing the free diffusion of cargoes. The on-demand release usually takes advantage of the macromolecule property change [40, 41, 42]. For example, the poly(N-isopropylacrylamide) has higher hydrophobicity at the temperatures above its lower critical solution temperature (LCST). By coating poly(N-isopropylacrylamide) on silica surfaces, the cargo can be trapped inside the pores at temperatures below the LCST. Once the temperature raises above the LCST (about 32 °C), the polymer network collapses and the cargoes can be released [41]. Similarly, poly(acrylic acid), poly(4-vinyl pyridine) and a few coordination polymers are pH sensitive and have been applied on MSNs for nanocarriers that respond to

acidic or basic environments [43, 44, 45]. Another method for on-command cargo release, as we will discuss in more detail in the next part, involves the nanomachine constructions.

1.2.2 Nanomachines

This dissertation focuses on the controlled cargo release realized by nanomachines on mesoporous silica particles. Similarly to the conventional concept of a machine, a nanomachine composes of a moving part and a solid support to accomplish a particular objective, with appropriate power supplies. More specifically, the solid support is the mesoporous silica nanoparticles, either their exterior porous surfaces or their interior surfaces along the pores. The moving part is a functional organic modification that is covalently bonded onto the silica scaffold, and undergoes large amplitude motions upon stimulations. The stimulations refer to the environmental condition variations, such as the pH change, the temperature fluctuation, the light irradiation, the redox potential change and the enzyme introduction. These variations trigger the chemical or physical property change of the organic modifications and release the stored chemical energy to power the machine operation. The objective is to manipulate the movement of cargoes by the motions of organic functional part, achieving the stimulus-responsive drug release to designated tumor tissues without premature release.

The concept of nanomachine was proposed by our group about ten years ago, and since that time, we have designed and synthesized a family of nanomachines constructed of different operative groups suitable for specific biological targets and achieving the controlled drug delivery by various mechanisms [4, 20, 21, 28, 46, 47, 48, 49, 50, 51, 52, 53]. Several examples are shown in Figure 1.2 on page 16. The snap-top has a "stalk" attached to the silica surface

and a cyclic molecule threaded onto it to close the pore openings. A bulky group is modified to the free end of stalks, serving as a "stopper" to prevent the dethreading of cyclic molecules. The stopper is cleavable from the stalk upon light irradiation or redox reaction, thus releasing the payloads [48, 51]. In nanopistons, the cyclic molecule is bonded onto the silica surface, while the stopper is held close to pores via the guest-host interaction with the cyclic groups. Upon decreasing the pH, the stopper leaves the cyclic molecule and frees the cargo molecules inside the pores [53]. The operation of nanovalves and nanoimpellers are explained in detail in the following paragraphs.

A nanovavle construction is similar to that of a snap-top, but different in the sense that the machine operation does not involve chemical bond breaking. The cyclic molecule threads onto the stalk via guest-host interactions or hydrophobic forces, functioning as a cap. If the stalk has two binding sites for the cap, the shifting of the cap between the two sites would "close" and "open" the nano pores, which leads to the reversible release of cargoes. On the other hand, if the stalk only possesses one binding site, the dethreading of caps would let out the trapped cargoes. The transition between the close and the open states, could be introduced by pH change, redox reactions, light activation and temperature change [4, 20, 26, 47, 52, 54].

In one example of the pH-sensitive nanovalves, a phenlyamine group that has an inclusion interaction with α-cyclodextrin is attached to the particle surface. Thus, the cyclodextrin is kept close to the pore openings to trap the cargo. Upon lowering the solution pH, the amine group is protonated and the binding affinity between the phenyl group and the cyclodextrin reduces. The cyclodextrin detaches from the stalk and drug molecules are free to diffuse out

of the pores [4].

Besides cyclodextrins, cucurbituril is another type of cyclic molecule that has been used for nanovalves. At neutral pH, cucurbit[6]uril forms inclusion complexes with diaminoalkanes. The complex is not stable in basic environment and is thus suitable for a nanovalve that opens at higher pH [54]. The inclusion also weakens as the temperature rises. Because magnetic nanocrystals generate heat when exposed to a high-frequency oscillating magnetic field, iron oxide nanocrystals are embeded into the silica matrix with the particle surfaces modified with the cucurbit[6]uril valve. Therefore, upon placing the system in an oscillating magnetic field, the silica particle interior is heated by the iron oxide, destabilizing the cucurbit[6]uril-diaminoalkane interaction and releasing the loaded cargoes [26].

The nanoimpeller is a light-activated nanomachine. Azobenzene molecules are co-condensed into the silica scaffold via a linker molecule and stretch out into the pore interiors, physically blocking the movement of cargoes. The azobenzene moiety has two conformational isomers: the *trans* and the *cis* isomers. Under irradiation with a wavelength of 403 nm - the isosbestic point in the absorption spectra - the azobenzene molecules undergo photoisomerization. The constant conformational change produces a wagging motion that effectively forces the cargo molecules out of the pores, thus accomplishing light stimulated cargo release [28].

1.2.3 Multifunctional Drug Delivery Platform

Mesoporous silica nanoparticles serve as a versatile and multifunctional platform for nano biomedicines. Besides drug delivery, they also have the capacity to perform gene therapy,

targeting, imaging and hyperthermia in biological systems. The gene therapy is realized by coating the particle surface with positively charge polymers, such as polyethylene imine, which incorporates negatively charged nucleic acids by electrostatic attraction. The siRNA and DNA molecules are transported into cells by the MSNs. Because the polymers are protonated at lower pH, the nucleic acids are released under the acidic condition in lysosomes [23, 55]. Targeting to cancer cells by MSNs has also been investigated by using folic acid, transferrin and RGD proteins [22, 25]. These targeting agents are bonded to the particle surface by various linker molecules and enhance the specific delivery rate of drugs to tumor tissues. Moreover, different imaging methods based on MSNs can be achieved. Both T_1-weighted and T_2-weighted MRI imaging is realized by introducing Gd or Fe compounds or nanocrystals into the MSNs (Chapter 2 and 4). Similarly, heavy metal elements were introduced for positron emission tomography (PET) and computed tomography (CT). Fluorescence imaging is commonly used in current research to locate the MSNs. They are decorated with fluorescein isothiocyanate (FITC), rhodamine isothiocyanate (RITC) and other fluorescent molecules. Upconversion imaging has also been studied by embedding the lanthanide nanocrystals into the silica particles (Chapter 7). In addition, magnetic materials embedded MSNs could function as heating centers for hyperthermia therapies.

1.3 Motivation

The research of this dissertation focuses on two aspects of mesoporous silica materials for the purpose of improving their biological performances in drug delivery. One aspect is the direct investigation of the nanomachine systems to advance their functionality, such

as introducing the T_1-weighted MRI imaging model (Chapter 2), simultaneously delivering nucleic acids with therapeutics (Chapter 3), and examining their biological performances (Chapter 7). Another aspect is the investigation of their physical properties in order to deepen our understanding of the physical property dependent cargo release performance and to facilitate nanomachine design. Chapter 4 is purely a thermal property study of the material. Chapters 5 and 6 consider a combination of the two aspects, where the direct influence of the physical property on machine performances is carefully examined, and a novel detection method is used to monitor both the physical property change and the cargo release simultaneously.

1.4 Figures

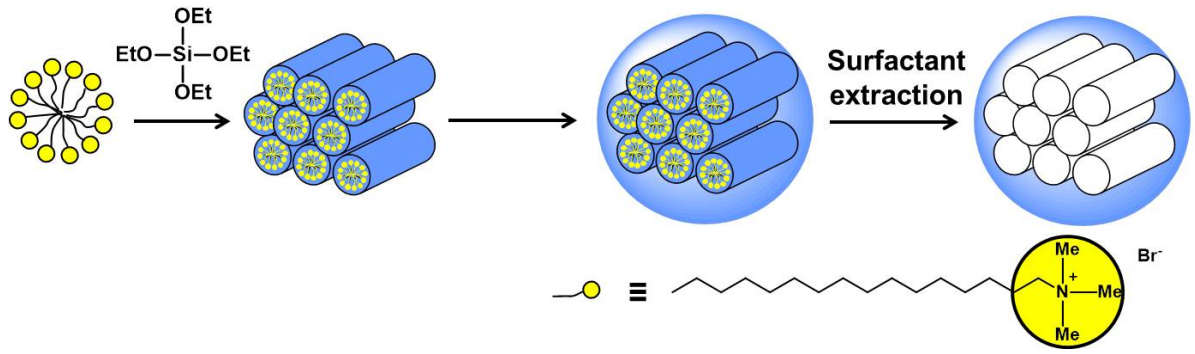

Figure 1.1 Illustration of the templated sol-gel process in the synthesis of MSNs using TEOS as the silica precursor and CTAB as the templating agent.

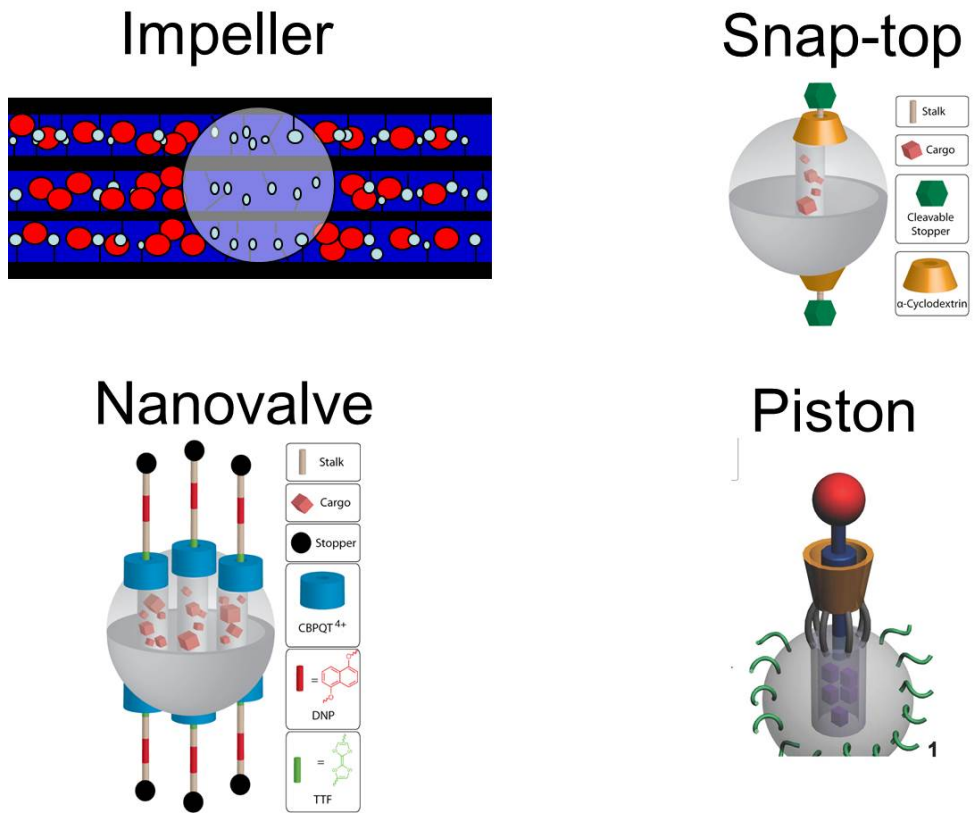

Figure 1.2 Types of Nanomachines

1.5 References

[1] C. Kresge, M. Leonowicz, W. Roth, J. Vartuli, and J. Beck. "Ordered Mesoporous Molecular-Sieves Synthesized by a Liquid-Crystal Template Mechanism." *Nature*, **359** (6397):710–712, 1992.

[2] T. Yanagisawa, T. Shimizu, K. Kuroda, and C. Kato. "The Preparation of Alkyltrimethylammonium–Kaneinite Complexes and Their Conversion to Microporous Materials." *Bull. Chem. Soc. Jpn.*, **63**(4):988–992, 1990.

[3] S.-H. Wu, C.-Y. Mou, and H.-P. Lin. "Synthesis of mesoporous silica nanoparticles." *Chem. Soc. Rev.*, **42**(9):3862–3875, 2013.

[4] L. Du, S. Liao, H. A. Khatib, J. F. Stoddart, and J. I. Zink. "Controlled-Access Hollow Mechanized Silica Nanocontainers." *J. Am. Chem. Soc.*, **131**(42):15136–15142, 2009.

[5] Y. Wan and Zhao. "On the Controllable Soft-Templating Approach to Mesoporous Silicates." *Chem. Rev.*, **107**(7):2821–2860, 2007.

[6] Z. Li, J. C. Barnes, A. Bosoy, J. F. Stoddart, and J. I. Zink. "Mesoporous silica nanoparticles in biomedical applications." *Chem. Soc. Rev.*, **41**(7):2590–2605, 2012.

[7] K. Schumacher, C. d. F. v. Hohenesche, K. K. Unger, R. Ulrich, A. D. Chesne, U. Wiesner, and H. W. Spiess. "The Synthesis of Spherical Mesoporous Molecular Sieves MCM-48with Heteroatoms Incorporated into the Silica Framework." *Adv. Mater.*, **11**(14): 1194–1198, 1999.

[8] Z. Li, J. L. Nyalosaso, A. A. Hwang, D. P. Ferris, S. Yang, G. Derrien, C. Charnay, J.-O. Durand, and J. I. Zink. "Measurement of Uptake and Release Capacities of Mesoporous Silica Nanoparticles Enabled by Nanovalve Gates." *J. Phys. Chem. C*, **115**(40):19496–19506, 2011.

[9] S. Inagaki, S. Guan, Y. Fukushima, T. Ohsuna, and O. Terasaki. "Novel Mesoporous Materials with a Uniform Distribution of Organic Groups and Inorganic Oxide in Their Frameworks." *J. Am. Chem. Soc.*, **121**(41):9611–9614, 1999.

[10] P. Yang, D. Zhao, D. I. Margolese, B. F. Chmelka, and G. D. Stucky. "Generalized syntheses of large-pore mesoporous metal oxides with semicrystalline frameworks." *Nature*, **396**(6707):152–155, 1998.

[11] W. Stber, A. Fink, and E. Bohn. "Controlled growth of monodisperse silica spheres in the micron size range." *J. Colloid Interface Sci.*, **26**(1):62–69, 1968.

[12] M. Grun, I. Lauer, and K. K. Unger. "The synthesis of micrometer- and submicrometer-size spheres of ordered mesoporous oxide MCM-41." *Adv. Mater.*, **9**(3):254–257, 1997.

[13] C.-Y. Chen, S. L. Burkett, H.-X. Li, and M. E. Davis. "Studies on mesoporous materials II. Synthesis mechanism of MCM-41." *Microporous Mater.*, **2**(1):27–34, 1993.

[14] S. Bhattacharyya, G. Lelong, and M.-L. Saboungi. "Recent progress in the synthesis and selected applications of MCM-41: a short review." *J. Exp. Nanosci.*, **1**(3):375–395, 2006.

[15] D. Zhao, J. Feng, Q. Huo, N. Melosh, G. H. Fredrickson, B. F. Chmelka, and G. D. Stucky. "Triblock Copolymer Syntheses of Mesoporous Silica with Periodic 50 to 300 Angstrom Pores." *Science*, **279**(5350):548–552, 1998.

[16] P. Feng, X. Bu, and D. J. Pine. "Control of Pore Sizes in Mesoporous Silica Templated by Liquid Crystals in Block CopolymerCosurfactantWater Systems." *Langmuir*, **16** (12):5304–5310, 2000.

[17] S. Yang, L. Zhao, C. Yu, X. Zhou, J. Tang, P. Yuan, D. Chen, and D. Zhao. "On the Origin of Helical Mesostructures." *J. Am. Chem. Soc.*, **128**(32):10460–10466, 2006.

[18] B. Wang, C. Chi, W. Shan, Y. Zhang, N. Ren, W. Yang, and Y. Tang. "Chiral Mesostructured Silica Nanofibers of MCM-41." *Angew. Chem. Int. Ed.*, **45**(13):2088–2090, 2006.

[19] Y. Tozuka, E. Sugiyama, and H. Takeuchi. "Release profile of insulin entrapped on mesoporous materials by freezethaw method." *Int. J. Pharm.*, **386**(12):172–177, 2010.

[20] H. Meng, M. Xue, T. Xia, Y.-L. Zhao, F. Tamanoi, J. F. Stoddart, J. I. Zink, and A. E. Nel. "Autonomous *in Vitro* Anticancer Drug Release from Mesoporous Silica Nanoparticles by pH-Sensitive Nanovalves." *J. Am. Chem. Soc.*, **132**(36):12690–12697, 2010.

[21] D. Tarn, M. Xue, and J. I. Zink. "pH-Responsive Dual Cargo Delivery from Mesoporous Silica Nanoparticles with a Metal-Latched Nanogate." *Inorg. Chem.*, **52**(4):2044–2049, 2013.

[22] D. P. Ferris, J. Lu, C. Gothard, R. Yanes, C. R. Thomas, J.-C. Olsen, J. F. Stoddart, F. Tamanoi, and J. I. Zink. "Synthesis of Biomolecule-Modified Mesoporous Silica Nanoparticles for Targeted Hydrophobic Drug Delivery to Cancer Cells." *Small*, **7**(13): 1816–1826, 2011.

[23] J. Dong, M. Xue, and J. I. Zink. "Functioning of nanovalves on polymer coated mesoporous silica Nanoparticles." *Nanoscale*, **5**(21):10300–10306, 2013.

[24] S. P. Hudson, R. F. Padera, R. Langer, and D. S. Kohane. "The biocompatibility of mesoporous silicates." *Biomaterials*, **29**(30):4045–4055, 2008.

[25] M. Liong, J. Lu, M. Kovochich, T. Xia, S. G. Ruehm, A. E. Nel, F. Tamanoi, and J. I. Zink. "Multifunctional Inorganic Nanoparticles for Imaging, Targeting, and Drug Delivery." *ACS Nano*, **2**(5):889–896, 2008.

[26] C. R. Thomas, D. P. Ferris, J.-H. Lee, E. Choi, M. H. Cho, E. S. Kim, J. F. Stoddart, J.-S. Shin, J. Cheon, and J. I. Zink. "Noninvasive Remote-Controlled Release of Drug Molecules *in Vitro* Using Magnetic Actuation of Mechanized Nanoparticles." *J. Am. Chem. Soc.*, **132**(31):10623–10625, 2010.

[27] H. Meng, M. Xue, T. Xia, Z. Ji, D. Y. Tarn, J. I. Zink, and A. E. Nel. "Use of Size and a Copolymer Design Feature To Improve the Biodistribution and the Enhanced Permeability and Retention Effect of Doxorubicin-Loaded Mesoporous Silica Nanoparticles in

a Murine Xenograft Tumor Model." *ACS Nano*, **5**(5):4131–4144, 2011.

[28] J. Lu, E. Choi, F. Tamanoi, and J. I. Zink. "Light-Activated Nanoimpeller-Controlled Drug Release in Cancer Cells." *Small*, **4**(4):421–426, 2008.

[29] J. Lu, M. Liong, Z. Li, J. I. Zink, and F. Tamanoi. "Biocompatibility, Biodistribution, and Drug-Delivery Efficiency of Mesoporous Silica Nanoparticles for Cancer Therapy in Animals." *Small*, **6**(16):1794–1805, 2010.

[30] P. Kallinteri, S. Higgins, G. A. Hutcheon, C. B. St. Pourain, and M. C. Garnett. "Novel Functionalized Biodegradable Polymers for Nanoparticle Drug Delivery Systems." *Biomacromolecules*, **6**(4):1885–1894, 2005.

[31] D. Bhadra, S. Bhadra, S. Jain, and N. K. Jain. "A PEGylated dendritic nanoparticulate carrier of fluorouracil." *Int. J. Pharm.*, **257**(12):111–124, 2003.

[32] D. B. Kirpotin, D. C. Drummond, Y. Shao, M. R. Shalaby, K. Hong, U. B. Nielsen, J. D. Marks, C. C. Benz, and J. W. Park. "Antibody Targeting of Long-Circulating Lipidic Nanoparticles Does Not Increase Tumor Localization but Does Increase Internalization in Animal Models." *Cancer Res*, **66**(13):6732–6740, 2006.

[33] P. Ghosh, G. Han, M. De, C. K. Kim, and V. M. Rotello. "Gold nanoparticles in delivery applications." *Adv. Drug Deliv. Rev.*, **60**(11):1307–1315, 2008.

[34] X. Qian, X.-H. Peng, D. O. Ansari, Q. Yin-Goen, G. Z. Chen, D. M. Shin, L. Yang, A. N. Young, M. D. Wang, and S. Nie. "*In vivo* tumor targeting and spectroscopic detection with surface-enhanced Raman nanoparticle tags." *Nat. Biotech.*, **26**(1):83–90, 2008.

[35] P. Zrazhevskiy, M. Sena, and X. Gao. "Designing multifunctional quantum dots for bioimaging, detection, and drug delivery." *Chem. Soc. Rev.*, **39**(11):4326–4354, 2010.

[36] X. Gao, Y. Cui, R. M. Levenson, L. W. K. Chung, and S. Nie. "*In vivo* cancer targeting and imaging with semiconductor quantum dots." *Nat. Biotech.*, **22**(8):969–976, 2004.

[37] D. L. Clemens, B.-Y. Lee, M. Xue, C. R. Thomas, H. Meng, D. Ferris, A. E. Nel, J. I. Zink, and M. A. Horwitz. "Targeted Intracellular Delivery of Antituberculosis Drugs to Mycobacterium tuberculosis-Infected Macrophages via Functionalized Mesoporous Silica Nanoparticles." *Antimicrob. Agents Chemother.*, **56**(5):2535–2545, 2012.

[38] C.-Y. Lai, B. G. Trewyn, D. M. Jeftinija, K. Jeftinija, S. Xu, S. Jeftinija, and V. S.-Y. Lin. "A Mesoporous Silica Nanosphere-Based Carrier System with Chemically Removable CdS Nanoparticle Caps for Stimuli-Responsive Controlled Release of Neurotrans-

mitters and Drug Molecules." *J. Am. Chem. Soc.*, **125**(15):4451–4459, 2003.

[39] S. Giri, B. G. Trewyn, M. P. Stellmaker, and V. S.-Y. Lin. "Stimuli-Responsive Controlled-Release Delivery System Based on Mesoporous Silica Nanorods Capped with Magnetic Nanoparticles." *Angew. Chem. Int. Ed.*, **44**(32):5038–5044, 2005.

[40] D. R. Radu, C. Y. Lai, K. Jeftinija, E. W. Rowe, S. Jeftinija, and V. S. Y. Lin. "A polyamidoamine dendrimer-capped mesoporous silica nanosphere-based gene transfection reagent." *J. Am. Chem. Soc.*, **126**(41):13216–13217, 2004.

[41] P.-W. Chung, R. Kumar, M. Pruski, and V. S.-Y. Lin. "Temperature responsive solution partition of organic-inorganic hybrid poly(N-isopropylacrylamide)-coated mesoporous silica nanospheres." *Adv. Funct. Mater.*, **18**(9):1390–1398, 2008.

[42] C. E. Ashley, E. C. Carnes, G. K. Phillips, D. Padilla, P. N. Durfee, P. A. Brown, T. N. Hanna, J. Liu, B. Phillips, M. B. Carter, et al. "The targeted delivery of multicomponent cargos to cancer cells by nanoporous particle-supported lipid bilayers." *Nat. Mater.*, **10**(6):476–476, 2011.

[43] L. Yuan, Q. Tang, D. Yang, J. Z. Zhang, F. Zhang, and J. Hu. "Preparation of pH-Responsive Mesoporous Silica Nanoparticles and Their Application in Controlled Drug Delivery." *J. Phys. Chem. C*, **115**(20):9926–9932, 2011.

[44] R. Liu, P. Liao, J. Liu, and P. Feng. "Responsive Polymer-Coated Mesoporous Silica as a pH-Sensitive Nanocarrier for Controlled Release." *Langmuir*, **27**(6):3095–3099, 2011.

[45] L. Xing, H. Zheng, Y. Cao, and S. Che. "Coordination Polymer Coated Mesoporous Silica Nanoparticles for pH-Responsive Drug Release." *Adv. Mater.*, **24**(48):6433–6437, 2012.

[46] T. Nguyen, K.-F. Leung, M. Liong, Y. Liu, J. Stoddart, and J. Zink. "Versatile Supramolecular Nanovalves Reconfigured for Light Activation." *Adv. Funct. Mater.*, **17**(13):2101–2110, 2007.

[47] T. D. Nguyen, H.-R. Tseng, P. C. Celestre, A. H. Flood, Y. Liu, J. F. Stoddart, and J. I. Zink. "A reversible molecular valve." *Proc. Natl. Acad. Sci.*, **102**(29):10029–10034, 2005.

[48] K. Patel, S. Angelos, W. R. Dichtel, A. Coskun, Y.-W. Yang, J. I. Zink, and J. F. Stoddart. "Enzyme-Responsive Snap-Top Covered Silica Nanocontainers." *J. Am. Chem. Soc.*, **130**(8):2382–2383, 2008.

[49] R. Hernandez, H.-R. Tseng, J. W. Wong, J. F. Stoddart, and J. I. Zink. "An Operational Supramolecular Nanovalve." *J. Am. Chem. Soc.*, **126**(11):3370–3371, 2004.

[50] K. C.-F. Leung, T. D. Nguyen, J. F. Stoddart, and J. I. Zink. "Supramolecular Nanovalves Controlled by Proton Abstraction and Competitive Binding." *Chem. Mater.*, **18**(25):5919–5928, 2006.

[51] M. W. Ambrogio, T. A. Pecorelli, K. Patel, N. M. Khashab, A. Trabolsi, H. A. Khatib, Y. Y. Botros, J. I. Zink, and J. F. Stoddart. "Snap-Top Nanocarriers." *Org. Lett.*, **12** (15):3304–3307, 2010.

[52] D. P. Ferris, Y.-L. Zhao, N. M. Khashab, H. A. Khatib, J. F. Stoddart, and J. I. Zink. "Light-Operated Mechanized Nanoparticles." *J. Am. Chem. Soc.*, **131**(5):1686–1688, 2009.

[53] Y.-L. Zhao, Z. Li, S. Kabehie, Y. Y. Botros, J. F. Stoddart, and J. I. Zink. "pH-Operated Nanopistons on the Surfaces of Mesoporous Silica Nanoparticles." *J. Am. Chem. Soc.*, **132**(37):13016–13025, 2010.

[54] S. Angelos, Y.-W. Yang, K. Patel, J. Stoddart, and J. Zink. "pH-Responsive Supramolecular Nanovalves Based on Cucurbit[6]uril Pseudorotaxanes." *Angew. Chem. Int. Ed.*, **47**(12):2222–2226, 2008.

[55] T. Xia, M. Kovochich, M. Liong, H. Meng, S. Kabehie, S. George, J. I. Zink, and A. E. Nel. "Polyethyleneimine Coating Enhances the Cellular Uptake of Mesoporous Silica Nanoparticles and Allows Safe Delivery of siRNA and DNA Constructs." *ACS Nano*, **3**(10):3273–3286, 2009.

Part II

Chemical Modification of Nanomachines on Mesoporous Silica Nanoparticles

CHAPTER 2

Mesoporous Silica Nanoparticles for Controlled Release of MRI Contrast Agent

2.1 Introduction

The work of this chapter focuses on exploring the mesoporous silica nanoparticle as a delivery vehicle for contrast agents for magnetic resonance imaging (MRI) in addition to its on-demand cargo release property. The goal is to achieve a multifunctional platform based on MSNs that serves as both a drug carrier and an imaging probe. The research conducted here endeavors to incorporate gadolinium compounds into the nanovalve systems by several approaches, for the purpose of enhancing the contrast in T_1-weighted MRI. The structural designs, synthetic methods and experimental results are analyzed and presented.

Magnetic resonance imaging is one of the major radiology diagnosis methods in modern medicine. Employing the same mechanism as the nuclear magnetic resonance (NMR) spectroscopy, MR imaging relies on the changing of relaxation times (T_1 and T_2) to enhance the signal from tissues and organs in living organisms. Yet, often times, the image contrast is too poor to clearly show the anatomy. Hence, magnetic materials are introduced to enhance the image contrast. Gadolinium(III) has seven unpaired electrons and is thus strong param-

agnetic. By using the gadolinium compounds as the contrast agents, they can reduce the T_1 relaxation time and brighten the T_1-weighted images [1, 2]. Superparamagnetic iron oxide could, on the other hand, darken the T_2-weight images and enhance the contrast too [3].

A group of gadolinium compounds have been approved for clinical uses. All are based on Gd chelating complexes with ligand DOTA (1,4,7,10-tetraazacyclododecane-1,4,7,10-tetra-acetic acid) or DTPA (diethylenetriaminepentacetate) [4, 5, 6]. DOTA and DTPA form strong metal-ligand bonds with Gd via tertiary amine groups and unprotonated carboxyl groups. The coordination number is usually eight for Gd, with another binding site left available for interactions with water molecules in tissues to shorten the proton T_1 relaxation time [7, 8, 9]. The structure of one of the Gd contrast agents, gadolinium diethylenetri-aminepentacetate (Gd-DTPA), is shown in the upper left corner in Figure 2.1 on page 32.

2.2 Design and Synthesis of Gd Incorporated Nanomachine System

The effort of incorporating the Gd complexes into the MSNs nanomachine systems has been pursued by three approaches. The first involves loading the contrast agent as a cargo into the porous structure; the second is to chemically modify nanomachines with Gd compounds; in the later stage of our investigation, we have also tried to bond the contrast agent onto the particle surfaces to fulfill the task.

The nanomachine we have employed here is the pH-responsive cyclodextrin nanovalve [10]. As we have described in the last chapter, the nanovalves have two components: a phenylamine stalk that bonds to the silica surface via silanol chemistry and a α-cyclodextrin

molecule that threads onto the stalk as the cap. The two form guest-host inclusion complexes at neutral pH and upon acidification, the binding affinity decreases and the cap leaves the stalk molecule. The free movement of the cargo is thus limited by the bulky cyclodextrins, and cargo can only leave the pore interiors when the caps are dethreaded (Figure 2.2 on page 32).

Our first approach is designed to trap the Gd-DTPA complex inside the nanopores and release them in acidic environment. The second approach tries to covalently bind Gd-DTPA with α-cyclodextrins via a peptide bond with the amine modified cyclodextrins, so that the contrast agent could be delivered similarly as a cargo (Figure 2.1). The last approach is to coat the silica particle surface with polyethylene imine to integrate the Gd-DOTA molecule into the particles.

2.3 Delivery of the Contrast Agent as the Cargo Molecule

The MCM-41 particles were first synthesized by the sol-gel procedure that we have discussed in Chapter 1. The as-synthesized particle morphology and porous structure were characterized by TEM images and XRD patterns. Shown in Figure 2.3a on page 33 is the X-ray diffraction spectrum as a function of the reflection angle 2θ. By converting the angle to distance d using the Bragg's Law, the lattice distance is calculated as 4.1 nm (Figure 2.3b). TEM images show that the spherical particle size is about 95 - 125 nm (Figure 2.4 on page 33). The hexagonally organized pores in the particles are presented too.

Nanovalve stalk modification on the particle surfaces were carried out by the silanol chemistry via a linker molecule, following a previous publication [10] (see Chapter 3). A flu-

orescence dye molecule, propidium iodide, was first loaded into the functionalized nanoparticles. Next α-cyclodextrin was added into the loading solution to cap the nanovalves. The particles were then thoroughly washed by water to remove the surface absorbed dyes. A time resolved fluorescence spectroscopic method was employed to examine the machine function. Particles after drying were placed in the corner of a cuvette and water was slowly added into the cuvette without disturbing the particles. A small stir bar was immersed in water. A probe laser beam (448 nm) shone onto the supernatant solution, and the solution fluorescence intensity was monitored continuously by a CCD detector. The detection wavelength range was set as the emission range of the cargo molecules, so that the cargo concentration variation in the supernatant was represented by the emission intensity change. In Figure 2.5 on page 34, the left graph in the first row illustrates such a release profile. The fluorescence intensity was plotted as a function of time. Initially, the fluorescence signal was quite weak and constant, but upon the acidification of the solution (indicated by the red arrow), the intensity dramatically increased, suggesting that the nanovalves were opened by the pH change and that the loaded dye molecules were released into the solution.

Similar experiments were performed using the Gd contrast agent as the cargo. Because the Gd compound does not have a strong fluorescence emission in the visible range, a Eu complex with the same ligand was used instead [11, 12, 13, 14]. The two complexes have similar electronic configurations and atomic radii, thus the release behavior of Eu-DTPA is representative of Gd-DTPA. The result is shown in Figure 2.5 on the right side of the first row. After adding the acid solution, there was no obvious cargo concentration increase in the supernatant. The slope of the curve gradually increased at a later stage of the experiment,

yet it is not conclusive whether the nanomachines have successfully released the lanthanide chelating compound.

We modified the acid responsive nanovalve systems to improve the performance. Considering that the Gd atoms are chelated by negatively charged carboxyl groups and the molecule size is relatively small compared to organic dyes such as propidium iodide, two parameters were fine tuned: the nanoparticle surfaces were decorated with more positively charged amine groups or the stalk amount was doubled to provide a better trap. Controll studies using propidium iodide as the cargo had validated the machine functioning. The release of Eu-DTPA was improved when the nanomachine amount was increased, because an obvious slope change was presented, yet the release amount was still quite small (Figure 2.5).

Nevertheless, the result indicated that the size of lanthanide complexes might be the obstacle in preventing the proper on-demand release, which motivated us to use a nanoparticle with smaller pores to enhance the efficiency. Instead of the sixteen carbon chain surfactant CTAB, we introduced the twelve carbon chain dodecyltrimethylammonium bromide (DTAB) as the templating agent. The particle TEM images showed great homogenity and dispersibility, and their sizes are about 220 nm (Figure 2.6 on page 34). Since the concern is that the cargo molecule might be too small, we synthesized another pH nanovalve that uses a similar functioning mechanism and has a shorter stalk, where the cap would be placed closer to the pore openings to prevent the cargo escape. The machine structures and their performances using fluorescent dyes are illustrated in Figure 2.7 on page 35. Even though both of the nanovalves operated well with dye molecule payloads, we could still not detect a substantial release when using Eu-DTPA as the cargo.

Continuing the idea of chemical modifications on particles and nanovalves, we tested the short stalk nanovalve with positive surface charges. Moreover, because the Eu-DTPA complex has stronger ionic character than the organic dyes, a base activated nanovalve was used to examine whether the acidic release environment was causing the problem. Functioning of both systems were tested and confirmed with dye molecules (Figure 2.8a and b, on page 35). However, upon replacing the dyes with Eu-DTPA, the on-command release behavior was not detectable any more (Figure 2.8c).

2.4 Contrast Agent Covalently Bonded with α-cyclodextrins

Our first approach of loading the contrast agent into the nanopores for on-demand release did not give promising results. All the nanomachines were operating with organic dyes, but not the lanthanide complexes. We hypothesized that their strong ionic character prevents them from being efficiently loaded into the nanopores and resulted in the faint release that was observed for most of the experimental conditions. To address this issue, the contrast agents were covalently bonded onto the cap molecule α-cyclodextrins to ensure sufficient incorporating [15, 16]. The α-cyclodextrin modification scheme is shown in Figure 2.1 on page 32. The product structure was analyzed by NMR and matrix-assisted laser desorption/ionization mass spectroscopy (MALDI). Both the α-cyclodextrin amine modification and the corresponding DTPA attachment via the peptide bond were verified by the NMR and mass spectra (Figure 2.9 on page 36 and Figure 2.10 on page 36) [15, 16].

2.5 Attachment of Gd-DOTA on Particle Surfaces and New Characterization Methods

Our third approach was to attach the contrast agent to particle surfaces via covalent bonds. For the purpose of improving the biodistribution of nanoparticles, we used a polyethylene imine-polyethylene glycol (PEI-PEG) co-polymer coated MCM-41 system [17]. On the particle surface, the abundant amine groups from PEI were reacted with a N-Hydroxysuccinimide (NHS) functionalized DOTA ligand (DOTA-NHS).The chelating ligand has been changed, part of an effort to examine whether the DTPA ligand was causing the problem. Figure 2.11 on page 38 illustrated the synthesis scheme as well as the DLS characterization result of the co-polymer coated nanoparticles. The particles presented a narrow size distribution with an average diameter of 121.8 nm.

Besides the new approach of integrating the Gd component, we decided that the fluorescence intensity spectra might not be an ideal detection method because the lanthanide elements all have narrow absorption and emission peaks and we did not have an available laser line that overlaps well with the Eu or Gd absorption peaks. Since the aim was to detect a heavy metal element, we employed inductively coupled plasma atomic emission spectroscopy (ICP-AES) to measure the amount of Gd^{3+} ions in nanoparticles. As shown in Table 2.1 on page 41, the ratio between particles and DOTA-NHS linker molecules and the ratio between linker molecule with Gd were carefully tuned. The results were characterized by the weight of Gd^{3+} ions in the particles in comparison with the particle total weight. The highest loading efficiency was generated by using more DOTA-NHS linkers to bind to the surfaces and the 1:1 molar ratio between the Gd and the linker molecule. Similarly, we have

examined how much Gd^{3+} ion could be absorbed into the particles due to the electrostatic interaction by soaking polymer coated particles into Gd solutions without binding the ligand DOTA first. About 14 % of Gd loading was detected in compare to the ligand modified particles (0.065 versus 0.47 wt.%), thus the chelating binding was the primary driving force for Gd incorporation.

The chelating reaction between the free Gd^{3+} ions and the DOTA attached particles were further analyzed by collecting the residue of loading solutions and comparing that with the particle Gd content. More specifically, the Gd^{3+} ion solution used in loading was collected after centrifugation, and during the particle washing process, all the supernatant solutions were collected by the same method. For each sample, the supernatant Gd concentrations were analyzed by ICP together with the Gd content in particles. The five samples that have different Gd - linker molecule ratios were examined, and the results are in Figure 2.12a on page 39. The total amount of Gd detected for each group were calculated by summing up all the supernatant and the particles. The relative Gd amount in each supernatant was compared to the total amount of the group. The results indicate that the amount of Gd that could be integrated into the particles was limited by the amount of DOTA ligand, thus proving that the Gd incorporation was due to the chelating bonds with DOTA ligands.

Moreover, the Gd contrast agent was introduced for the purpose of changing the magnetic properties of particles, thus we studied their electron paramagnetic resonance (EPR) spectra and their proton T_1 relaxation times. Two polymer coated MSN particles were used as the control group and were compared with their derivatives that have reacted with Gd. In the first derivative of EPR spectrum, a broad band was observed in the Gd reacted derivatives,

indicating the presence of unpaired electrons and thus confirming the incorporation of Gd^{3+} ions . In another experiment, a NMR spectrometer was used to measure the proton T_1 relaxation times in the presence of particles. One sample is the PEI-PEG coated MSNs with the DOTA-Gd modification, while the other one is the polymer MSNs with DOTA only. The calculated T_1 relaxation time for the former is 10.68 ms, much shorter than the relaxation time of the latter, which is 381.10ms (Figure 2.13a on page 40).

2.6 Summary

In summary, we have investigated three approaches to incorporate gadolinium MRI contrast agent into the nanomachine functionalized MSNs to explore the imaging properties of the drug delivery platform. Contrast agents were directly loaded into the particles, and chemically bonded onto the nanovalve caps and the particle surface coatings. With little success in using fluorescence emissions of the lanthanide complexes to detect their release, the elemental analysis method of ICP-OES was more promising in quantifying the Gd integration. The highest Gd content was detected when a large amount of chelating ligands was attached to particles and when the same molar amount of the ligand and the free ion were used. The magnetic properties of Gd integrated nanoparticles were confirmed by the EPR spectra and by the shortened proton T_1 relaxation times in NMR detections.

2.7 Figures and Tables

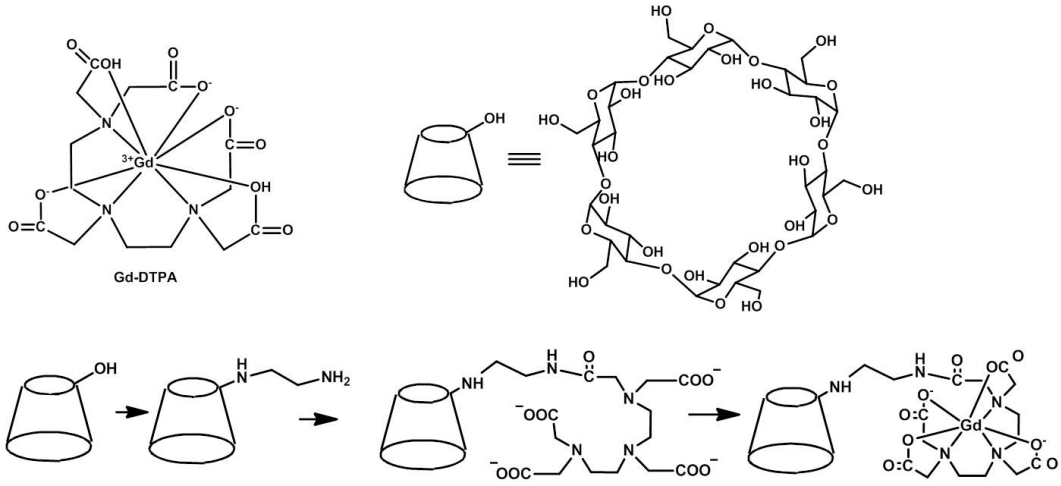

Figure 2.1 Gd-DTPA structure and the synthesis scheme to bind Gd-DTPA on to the cyclodextrins. One of the hydroxyl group of cyclodextrin is converted into an amine group and further reacted with the carboxyl group on Gd-DTPA to form the peptide bond.

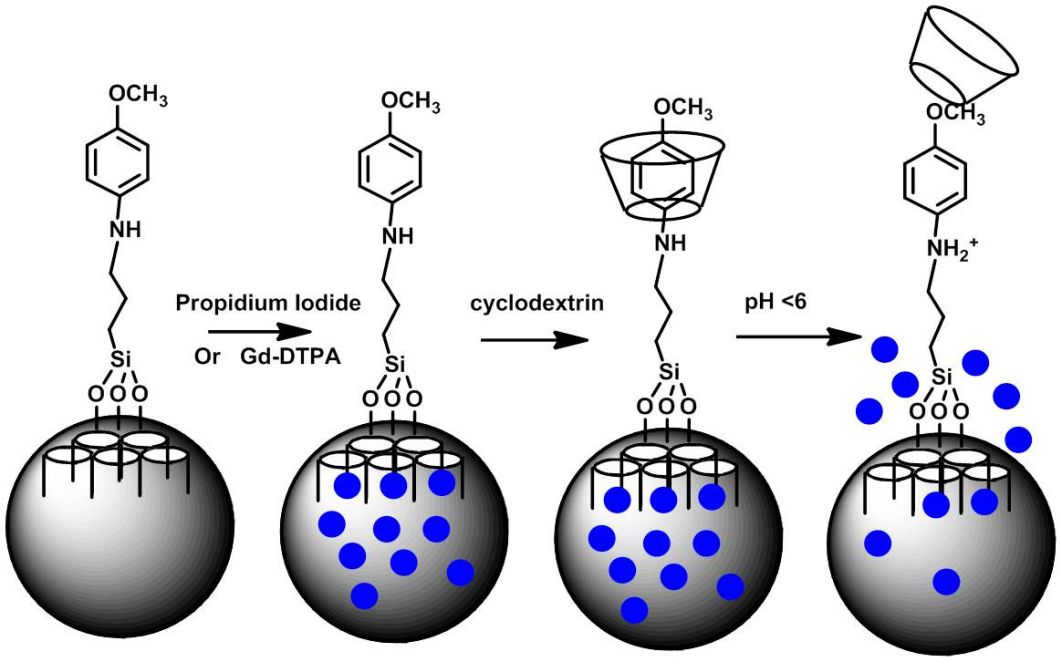

Figure 2.2 pH responsive nanovalve structure and release scheme. Blue circles represent the cargo molecule, such as propidium iodide and Gd-DTPA.

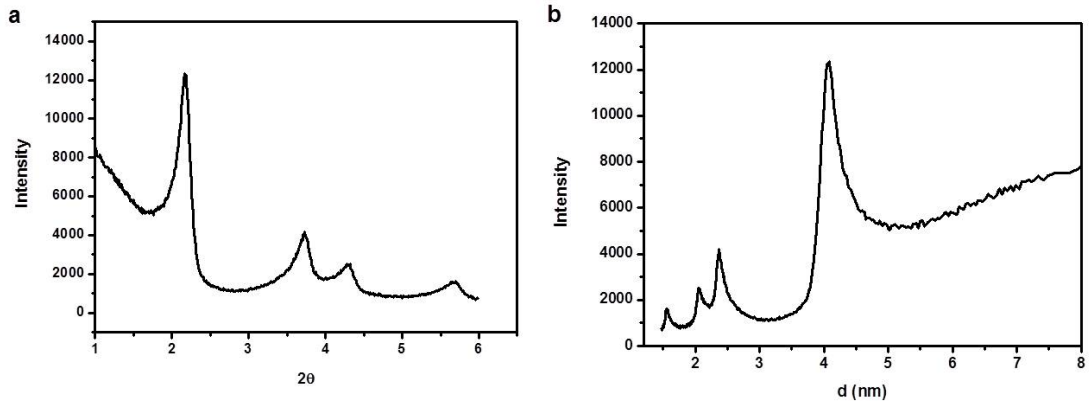

Figure 2.3 XRD patterns of MCM-41 particles. (a) XRD pattern plotted as a function of the reflection angle 2θ. (b) XRD spectrum plotted as a function of lattice distance d.

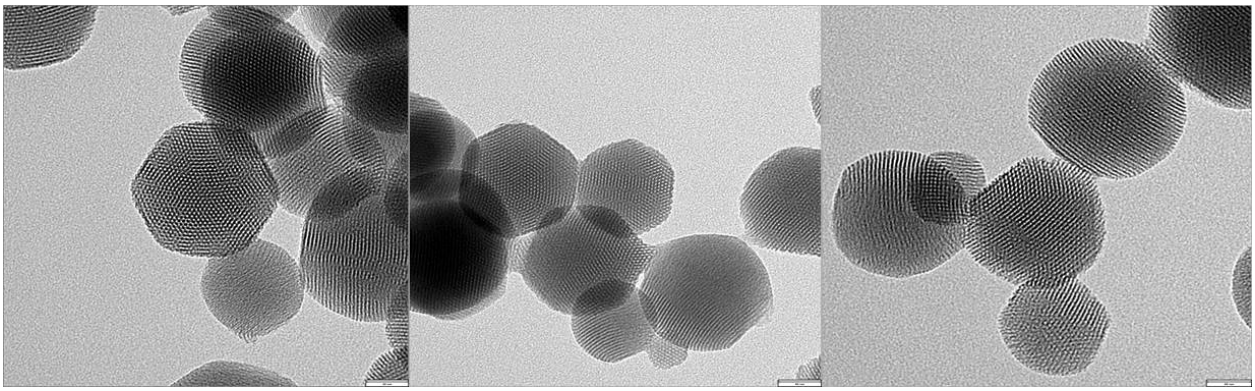

Figure 2.4 TEM images of MCM-41 particles. Scale bar: 40 nm

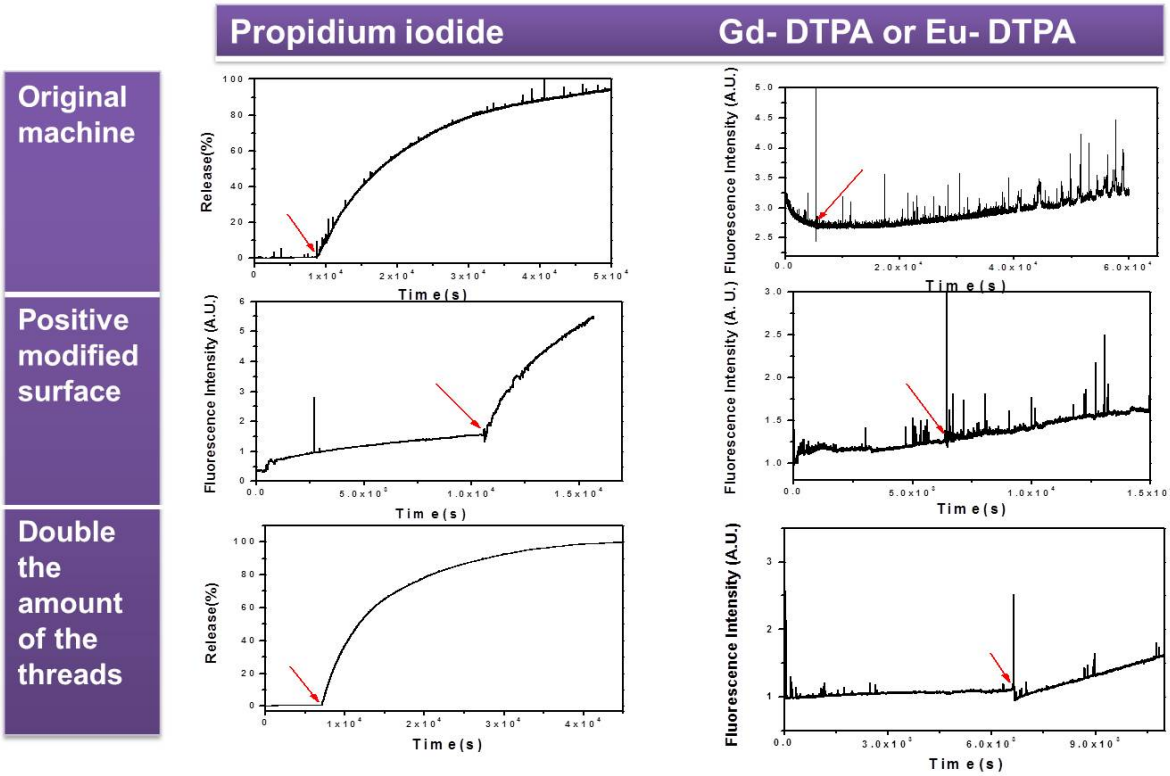

Figure 2.5 Release profiles of lanthanide complexes by nanovalves in comparison with those of the propidium iodide. Both molecules serve as the cargo molecules. Besides the original nanomachine construction, two variations were performed : nanoparticle surfaces were modified by positively charged amine groups in the second row and the nanomachine amount was doubled in the third row.

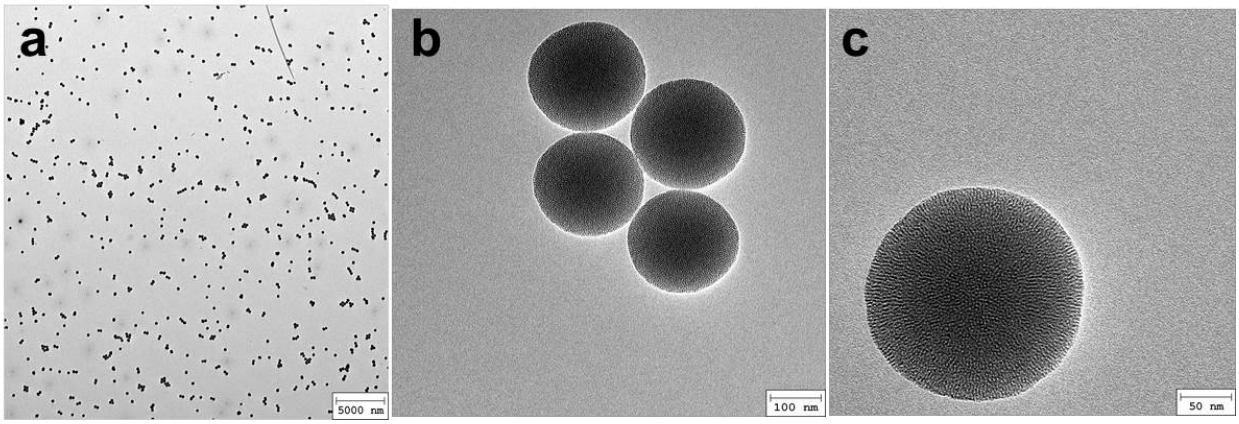

Figure 2.6 TEM images of different magnifications showing MSNs synthesized by using DTAB as the templating agent. Scale bar: 5 μm, 100 nm, 50 nm

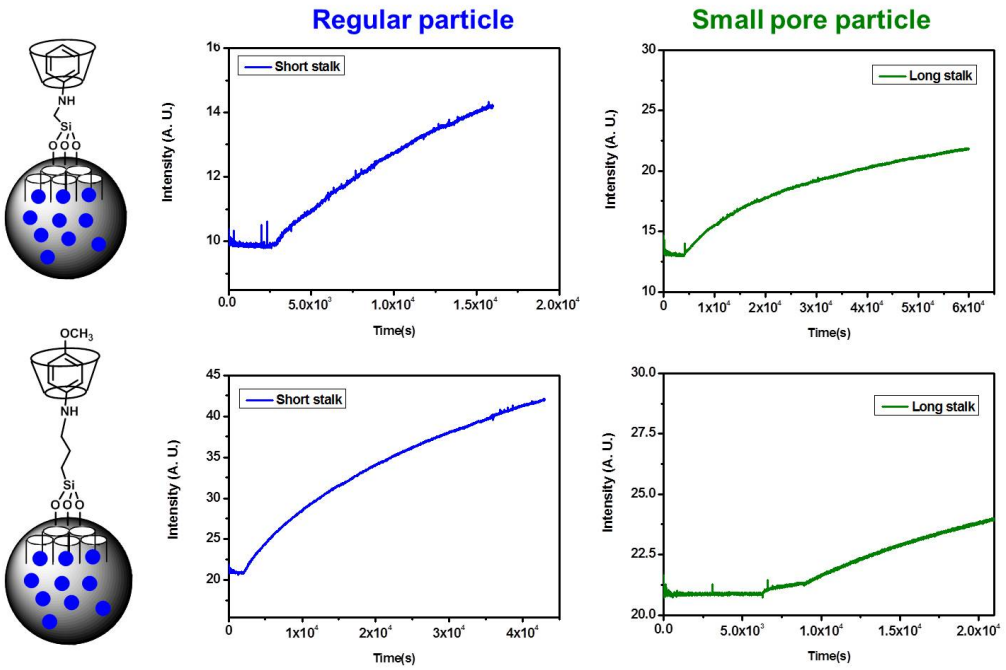

Figure 2.7 Release profiles of DTAB particles using Hoechst dye as the cargo. Acid responsive nanovalves of two different stalk lengths were examined. The release of DTAB particles was compared with that of the CTAB templated particles.

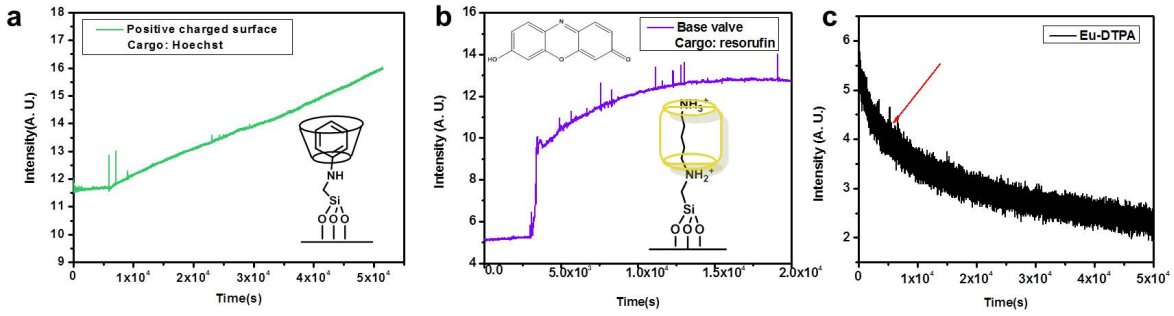

Figure 2.8 More chemical modification of nanovalve systems and their release performances using either dye molecules or lanthanide complexes. (a) Hoechst release of CTAB particles with short stalk acid valves and positive surface charge modification. (b) Resorufin release using a base stimulated nanovalve. The structures of nanovalves and the dye resorufin are shown inset. (c) Typical release profile of Eu-DTPA using similar nanovalve systems.

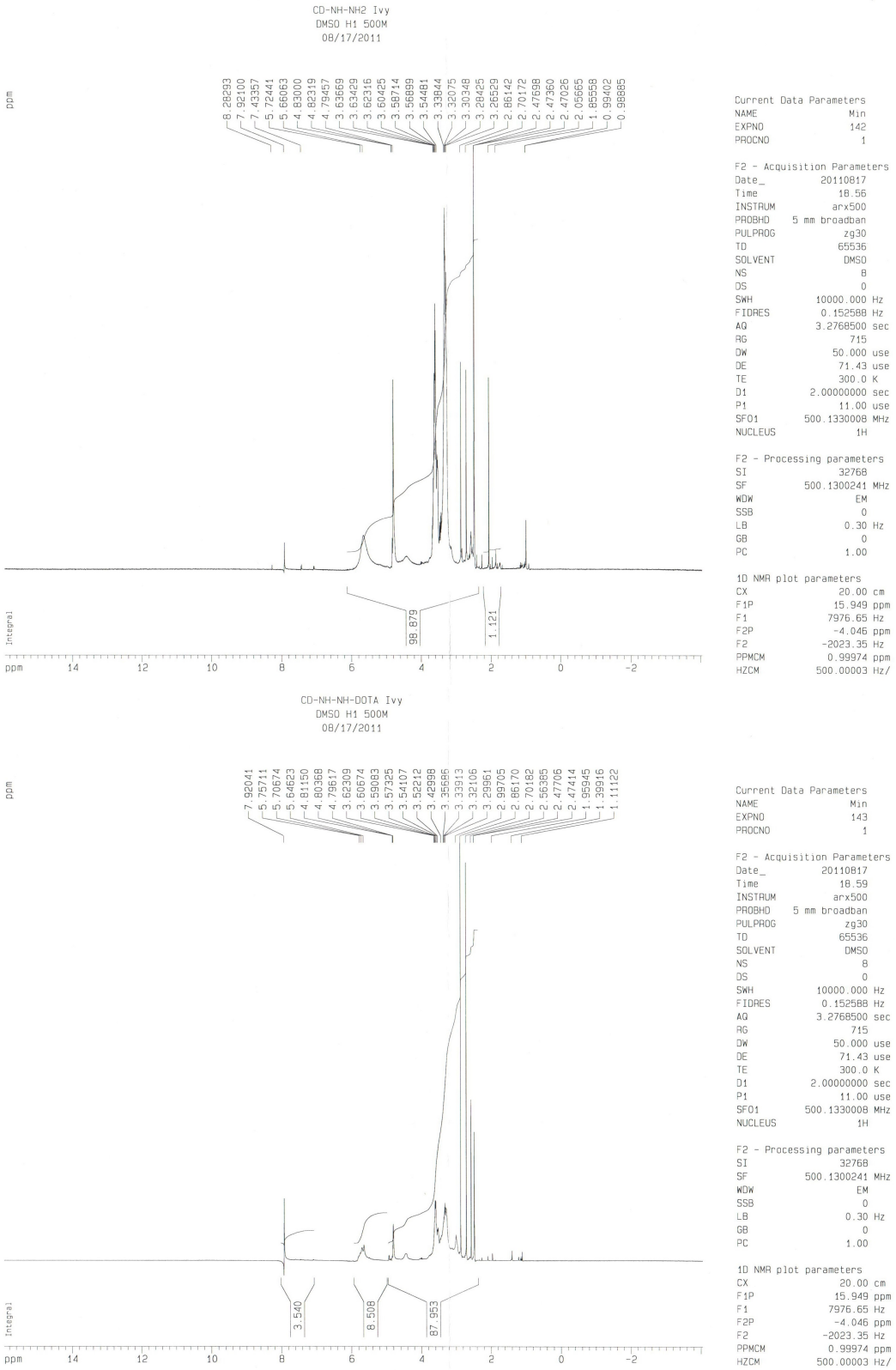

Figure 2.9 NMR analysis of the product of α-cyclodextrin modifications. Top: NMR spectra of cyclodextrin amine modification. The peaks between 2.4 - 2.9 ppm confirms the ethylamine modification. Bottom: the NMR spectra of cyclodextrin-DOTA derivative.

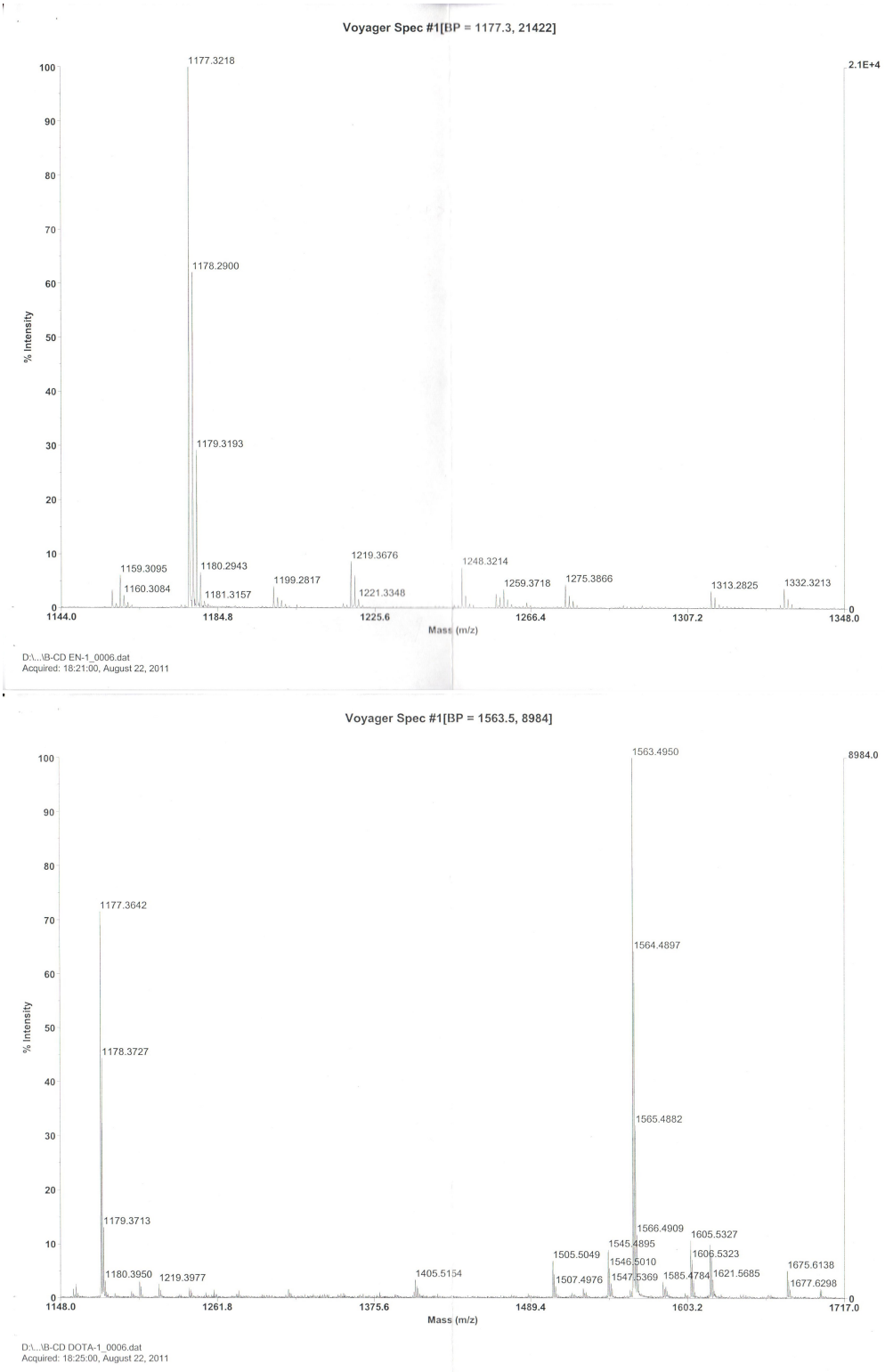

Figure 2.10 MALDI analysis of the product of α-cyclodextrin modifications. MALDI analysis of the product of α-cyclodextrin modifications. Top: MALDI spectra of cyclodextrin amine modification, whose molecular ion peak is shown at m/z 1177. Bottom: the MALDI spectra of cyclodextrin-DOTA derivative. Its molecular ion peak is at m/z 1563.

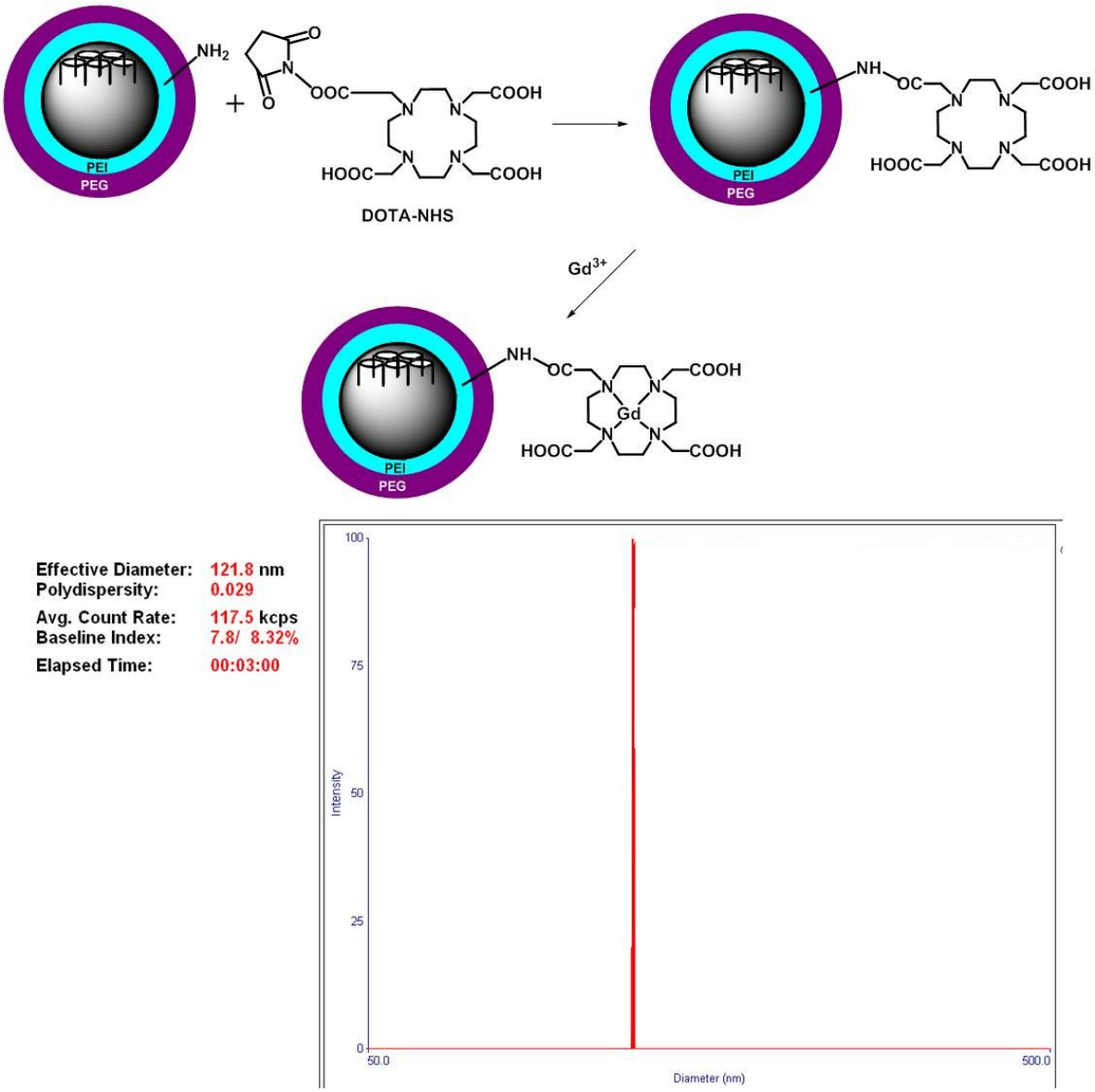

Figure 2.11 Chemical modifications of PEI-PEG coated silica nanoparticles to integrate Gd complex and the DLS analysis of the particles. The average particle size is shown as 121.8 nm

.

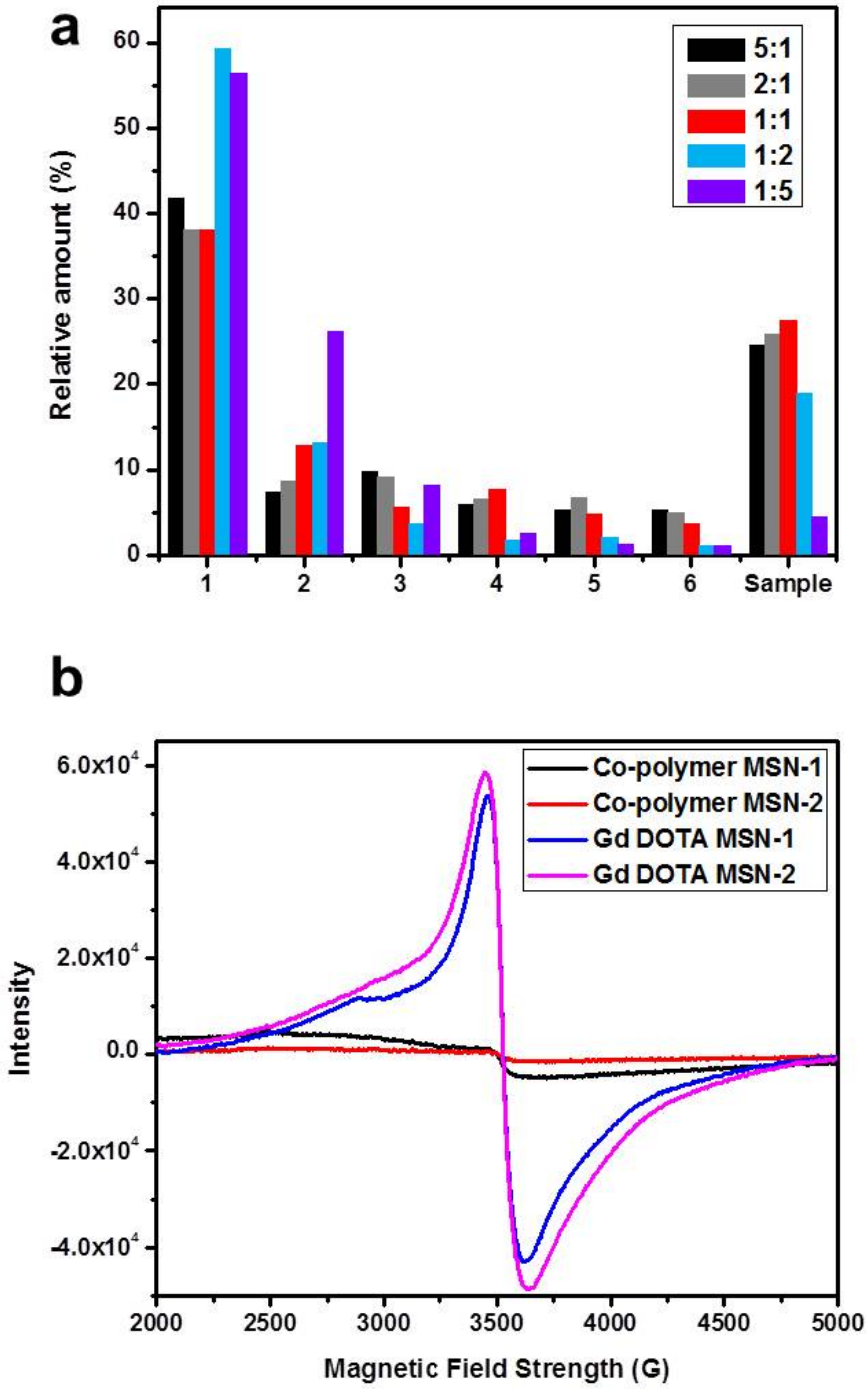

Figure 2.12 ICP analysis result and EPR first derivative spectra of Gd particles. (a) The ICP analysis results of five samples and the Gd loss during the loading and washing process. Five samples of different ligand to Gd molar ratios were examined. Their loading solution and the washing supernatant were collected and analyzed. Relative amounts of each supernatant (1 - 6) in compare to the total Gd amount for this sample were plotted. (b) EPR first derivative spectra of Gd reacted particles showed a broad band compared to the flat curves of controls.

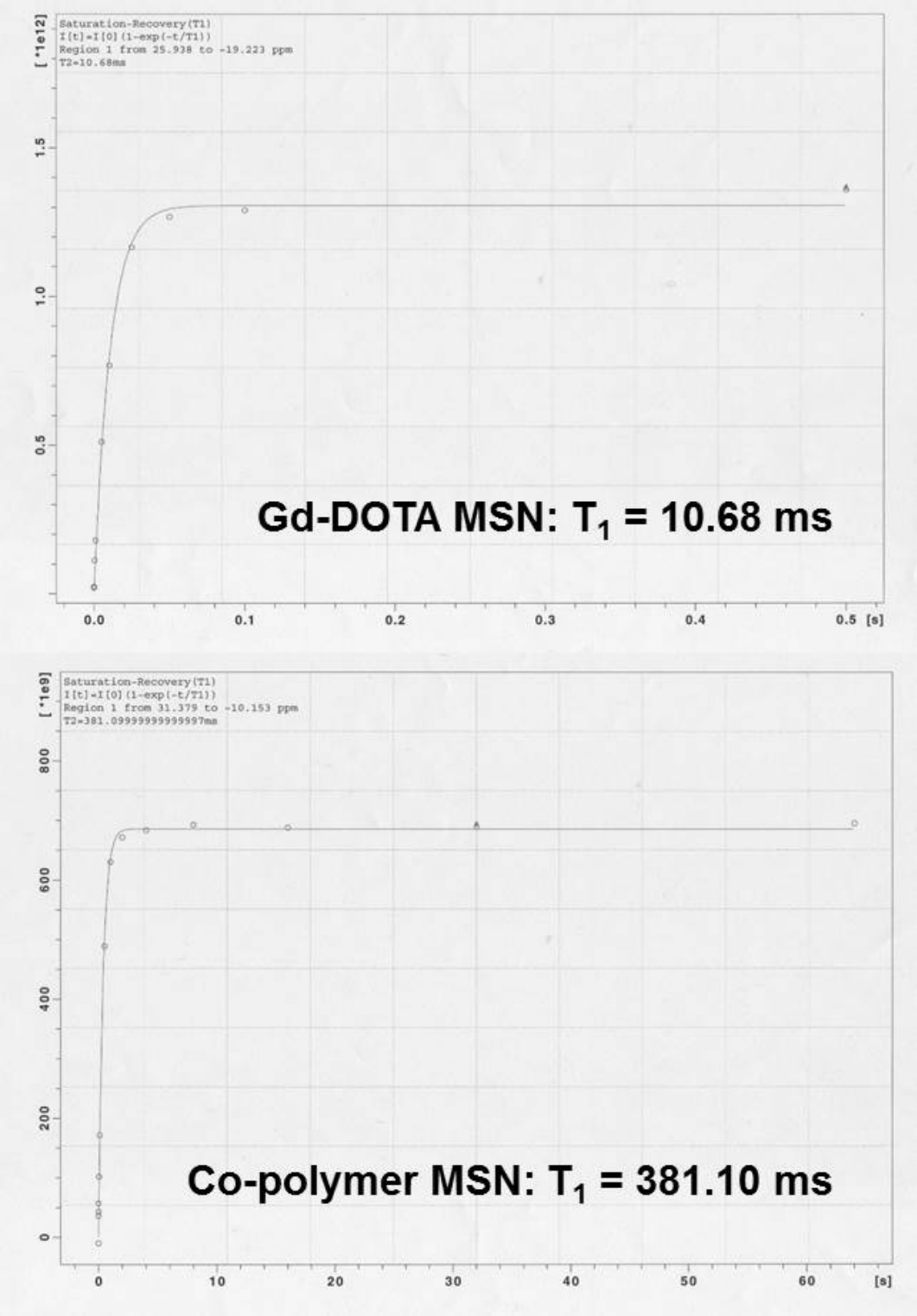

Figure 2.13 Proton T_1 relaxation times in the presence of Gd incorporated particles (top) in compare with control particles (bottom). Signal decay as a function of time was measured by NMR spectrometer and fitted to generate the T_1 relaxation time. This value is shortened by the Gd modifications (10.68 ms) compared to the polymer coated particles without Gd incorporation (381.10 ms).

Table 2.1 ICP analysis in optimizing the Gd loading efficiency into the DOTA modified copolymer coated MSNs.

Particle - DOTA relative amount optimization					
Sample No.	1	2	3	4	5
m(particle):m(linker)	500	200	100	50	20
m(Gd):m(particle) (10^{-3})	0.263	0.535	1.06	1.87	**3.36**

DOTA - Gd relative amount optimization					
Sample No.	6	7	8	9	10
m(linker):m(Gd-DOTA)	5:1	2:1	1:1	1:2	1:5
m(Gd):m(particle) (10^{-3})	1.35	4.76	**7.33**	6.37	4.01

2.8 References

[1] P. Caravan, J. J. Ellison, T. J. McMurry, and R. B. Lauffer. "Gadolinium(III) Chelates as MRI Contrast Agents: Structure, Dynamics, and Applications." *Chem. Rev.*, **99** (9):2293–2352, 1999.

[2] P. Caravan. "Strategies for increasing the sensitivity of gadolinium based MRI contrast agents." *Chem. Soc. Rev.*, **35**(6):512–523, 2006.

[3] J. W. M. Bulte and D. L. Kraitchman. "Iron oxide MR contrast agents for molecular and cellular imaging." *NMR Biomed.*, **17**(7):484–499, 2004.

[4] H. Weinmann, R. Brasch, W. Press, and G. Wesbey. "Characteristics of gadolinium-DTPA complex: a potential NMR contrast agent." *Am. J. Roentgenol.*, **142**(3):619–624, 1984.

[5] X. Wang, T. Jin, V. Comblin, A. Lopez-Mut, E. Merciny, and J. F. Desreux. "A kinetic investigation of the lanthanide DOTA chelates. Stability and rates of formation and of dissociation of a macrocyclic gadolinium(III) polyaza polycarboxylic MRI contrast agent." *Inorg. Chem.*, **31**(6):1095–1099, 1992.

[6] A. Borel, J. Bean, R. Clarkson, L. Helm, L. Moriggi, A. Sherry, and M. Woods. "Towards the Rational Design of MRI Contrast Agents: Electron Spin Relaxation Is Largely Unaffected by the Coordination Geometry of Gadolinium(III)–DOTA-Type Complexes." *Chem. Eur. J.*, **14**(9):2658–2667, 2008.

[7] M. Botta. "Second Coordination Sphere Water Molecules and Relaxivity of Gadolinium(III) Complexes: Implications for MRI Contrast Agents." *Eur. J. Inorg. Chem.*, **2000**(3):399–407, 2000.

[8] V. C. Pierre, M. Botta, S. Aime, and K. N. Raymond. "Substituent Effects on Gd(III)-Based MRI Contrast Agents: Optimizing the Stability and Selectivity of the Complex and the Number of Coordinated Water Molecules1." *Inorg. Chem.*, **45**(20):8355–8364, 2006.

[9] N. Viola-Villegas and R. P. Doyle. "The coordination chemistry of 1,4,7,10-tetraazacyclododecane-N,N′,N″,N‴-tetraacetic acid (H_4DOTA): Structural overview and analyses on structure–stability relationships." *Coordin. Chem. Rev.*, **253**(13–14): 1906–1925, 2009.

[10] L. Du, S. Liao, H. A. Khatib, J. F. Stoddart, and J. I. Zink. "Controlled-Access Hollow Mechanized Silica Nanocontainers." *J. Am. Chem. Soc.*, **131**(42):15136–15142, 2009.

[11] E. M. Goldys, K. Drozdowicz-Tomsia, S. Jinjun, D. Dosev, I. M. Kennedy, S. Yatsunenko, and M. Godlewski. "Optical Characterization of Eu-Doped and Undoped Gd_2O_3 Nanoparticles Synthesized by the Hydrogen Flame Pyrolysis Method." *J. Am. Chem. Soc.*, **128**(45):14498–14505, 2006.

[12] W. T. Carnall, P. R. Fields, and K. Rajnak. "Electronic Energy Levels of the Trivalent Lanthanide Aquo Ions. IV. Eu^{3+}." *J. Chem. Phys.*, **49**(10):4450–4455, 1968.

[13] W. T. Carnall, P. R. Fields, and K. Rajnak. "Electronic Energy Levels of the Trivalent Lanthanide Aquo Ions. II. Gd^{3+}." *J. Chem. Phys.*, **49**(10):4443–4446, 1968.

[14] A. P. Bassett, S. W. Magennis, P. B. Glover, D. J. Lewis, N. Spencer, S. Parsons, R. M. Williams, L. De Cola, and Z. Pikramenou. "Highly Luminescent, Triple- and Quadruple-Stranded, Dinuclear Eu, Nd, and Sm(III) Lanthanide Complexes Based on Bis-Diketonate Ligands." *J. Am. Chem. Soc.*, **126**(30):9413–9424, 2004.

[15] T. J. Wenzel, M. S. Bogyo, and E. L. Lebeau. "Lanthanide-Cyclodextrin Complexes as Probes for Elucidating Optical Purity by NMR Spectroscopy." *J. Am. Chem. Soc.*, **116**(11):4858–4865, 1994.

[16] B. L. May, S. D. Kean, C. J. Easton, and S. F. Lincoln. "Preparation and characterization of 6A-polyamine-mono-substituted β-cyclodextrins." *J. Chem. Soc. [Perkin 1]*, **11**(21):3157–3160, 1997.

[17] H. Meng, M. Xue, T. Xia, Y.-L. Zhao, F. Tamanoi, J. F. Stoddart, J. I. Zink, and

A. E. Nel. "Autonomous in Vitro Anticancer Drug Release from Mesoporous Silica Nanoparticles by pH-Sensitive Nanovalves." *J Am Chem Soc*, **132**(36):12690–12697, 2010.

CHAPTER 3

Functioning of Nanovalves on Polymer Coated Mesoporous Silica Nanoparticles

3.1 Abstract

Nanomachines activated by a pH change can be combined with polymer coatings on mesoporous silica nanoparticles to produce a new generation of nanoparticles for drug delivery that exhibits properties of both components. The nanovalves can trap cargos inside the mesoporous silica nanoparticles without premature release and only respond to specific stimuli, resulting in a high local concentration of drugs at the site of release. The polymer surface coatings can increase the cellular uptake, avoid the reticuloendothelial uptake, provide protected space for storing siRNA, and enhance the biodistribution of nanoparticles. Two nanovalve-polymer systems are designed and their successful assembly is confirmed by solid state NMR and thermogravimetric analysis. The fluorescence spectroscopy results demonstrate that the controlled release functions of the nanomachines in both of the systems are not hindered by the polymer surface coatings. These new multifunctional nanoparticles combining stimulated molecule release together with the functionality provided by the polymers produce enhanced biological properties and multi-task drug delivery applications.

3.2 Introduction

Over the past decade, mesoporous silica nanoparticles (MSNs) have become a promising platform for therapeutic applications [1, 2, 3, 4, 5, 6, 7]. Benefiting from the high surface area, large pore volume, nontoxicity and well-developed silanol chemistry derivatization, a variety of surface and interior modifications have been applied to MSN to perform on-demand drug delivery, fluorescence imaging and active targeting [8, 9]. Among the various functionalization of MSN [10, 11, 12, 13], multiple methods have been developed to fulfill the on-demand release of payloads, including nanomachine constructions [12, 14, 15], nanocrystal cappings [16, 17] and macromolecule cappings [18, 19, 20, 21, 22, 23]. For nanomachine constructions, the pore openings of mesoporous structure are blocked by functional groups that have variable binding under different conditions. Upon applying external or internal biological stimuli such as light, magnetic field, pH change or redox change, the pore openings can be readily closed or opened and therefore provide a smart drug delivery system that operates in a controlled fashion [10, 11, 24, 25].

In addition to molecular capping agents, various surface coating agents such as polymers and lipid bilayers [26, 27] have been applied to mesoporous silica nanoparticles to introduce unique functions or to optimize their biological behavior. One example involves grafting polyethylene glycol on MSN surface in order to avoid uptake by the reticuloendothelial system, increase its blood circulation time and improve its biodistribution properties [27, 28, 29]. Moreover, the surface coating agents can provide useful storage space for carrying large molecules such as small interfering RNA (siRNA) and DNA molecules to conduct gene therapies [26, 30, 31]. It would be ideal if the surface coatings could be incorporated with

the controlled-release capping systems to deliver both nucleic acids and small therapeutic molecules simultaneously, presenting a multi-functional delivery platform with enhanced biological properties.

In this study, we investigate for the first time whether the surface coating strategy is compatible with the controlled-release systems. Two polymer coated MSN models were incorporated with pH responsive nanovalves to examine the functionality of the nanomachines in the combined system. The first model is based on 120 nm MSNs with an acid-responsive nanovalve and a small molecular weight polyethylene imine (PEI) coating (Figure 3.1a on page 62). The nanovalves are bonded on the silica surface, and keep the nanopores closed under neutral pH but open them when pH is decreased [24]. A 1.8 kDa PEI is utilized in this model due to its efficiency in delivering siRNA with minimal cytotoxicity and enhanced cellular uptake [26, 30, 31]. As for the second model, 50 nm MSNs with polyethylene imine-polyethylene glycol (PEI-PEG) co-polymer coatings were combined with a nanovalve that opens at pH 5 (Figure 3.1b). The 50 nm sized MSN with PEI-PEG co-polymer coating has demonstrated excellent properties in delivering drugs at *in vivo* levels with a high passive accumulation rate at the tumor site, thanks to the enhanced permeability and retention effect (EPR effect) [27]. To optimize the delivery capacity of anticancer drugs, it would be ideal to incorporate a controlled release nanomachine. Therefore, a nanovalve that opens at pH 5 is employed, and together with the co-polymer coated MSN, is chosen as the second model for examining the operations of nanomachines with the polymer coating. We demonstrate for the first time that through proper design, the nanomachines can be integrated into the polymer coated MSN system, and are capable of releasing the cargos in an on-demand

fashion.

3.3 Design and Nanomachine Operation of LPEI group

3.3.1 System Construction

For the purpose of comparison, three samples were synthesized in the LPEI group. As shown in Figure 3.2a on page 63, LPEI-1 has only the nanomachine construction on MSN, LPEI-2 is PEI coated MSN without any nanomachine attachment, and LPEI-3 is the fully-assembled system which has both the nanomachine modification and the PEI polymer coating. LPEI-1 is used in order to estimate the nanomachine performance, and LPEI-2 is used as a control. The synthesis procedures for the derivatized nanoparticles are also illustrated in Figure 3.2.

In the LPEI group, the nanomachines are composed of two parts: a bulky cyclodextrin moiety and an aromatic amine stalk. The stalk is covalently bonded to the silica surface via silanol reaction and the cyclodextrin cap is threaded onto the stalk. The host-guest binding constant between the stalk and the cyclodextrin molecule varies under different pH and renders a functional nanomachine next to the mesopore opening [32, 33]. At neutral pH, the cyclodextrin encircles the stalk via a supramolecular interaction, blocks the pore entrances and retains the cargo. When the environment is acidified, the binding constant significantly decreases, resulting in the dissociation of cyclodextrin from the stalk and the release of payloads from pore openings [24].

The PEI polymer coating is achieved by electrostatic interactions and hydrogen bond-

ing between the polymer and the phosphonate-modified silica surface [34]. The negatively charged phosphonate groups are attached to the MSN surface by the silanol condensation of 3-(trihydroxysilyl)propyl methylphosphonate. The PEI chosen for this study has a molecular weight of about 1.8 kDa, because it maintains the effective nucleic acid delivery capacity and no toxicity was observed due to the low molecular weight.16 The abundant amine groups on PEI provide positive charges that are utilized to electrostatically attract and hold the polymer on the negatively charged MSN surface.

3.3.2 Characterization

The successful attachment of nanovalve stalks in LPEI-1 and LPEI-3, and the polymer coatings on silica particles in LPEI-2 and LPEI-3 are verified by ^{13}C CPMAS NMR (Figure 3.5a on page 66). The characteristic peaks from the substituted alkane groups on the PEI and the aromatic carbons on the nanovalve stalks are both observed in LPEI-3. Moreover, the thermogravimetric analysis was performed and the PEI polymer part is 16.4 wt.% of the LPEI-3 sample (TGA, Table 3.1). We calculated that the total polymer surface area is much larger than that of the silica nanoparticles, which suggests that the PEI polymers have a full coverage on the MSN surface (see Methods on page 58).

Transmission electron microscopy (TEM) images of these MSNs were collected and no major morphology difference was observed after surface modifications. Figure 3.3a on page 64 shows the TEM picture of typical 120 nm MSNs without any surface decoration. Figure 3.3b is the TEM picture of LPEI-3 that has both the PEI coating and the nanomachine modifications. In LPEI-3, the particles have maintained the porous structure and the overall

morphology is not changed. The particles exhibit slightly mottled surfaces compared to those of the bare particles, which is attributed to the PEI polymer coating. The N_2 adsorption desorption isotherms and X-ray powder diffraction spectra were collected to confirm the porosity of the nanoparticles (Figure 3.6 on page 67 and Figure 4.2 on page 99).

3.3.3 Nanomachine Operation Test

A time-resolved fluorescence spectroscopy method was employed to test the operation of nanovalves in the presence of the PEI coating [10, 11, 12, 24]. In brief, the particles were suspended in 1mM Hoechst 33342 solution for two days to load the mesopores with fluorescent dyes. The α-cyclodextrin cap was then added into the solution to cap the nanovalves, close the pore openings and trap the loaded cargos. The particles were then thoroughly washed to remove the dye molecules absorbed on the particle surfaces or in the polymer coatings. Dried particles were then placed in a corner of a cuvette and phosphate-buffered saline (PBS) was gently added. This solution was stirred slowly to avoid disturbing the MSNs. The fluorescence intensity of the aqueous solution was recorded continuously to monitor the amount of dye molecules diffused into the solution as the pH varies. Upon finishing the release experiment, the UV-Vis absorption spectrum of the supernatant solution was collected (Figure 3.9 on page 70) and the absolute amount of released cargo was calculated by Beers law. The recorded fluorescence intensity was converted to the corresponding concentration of dye molecules in the solution, generating the release profile in Figure 3.3.

As shown in Figure 3.3c, the release profile of nanovalve-modified MSN with PEI coating (red curve LPEI-3) is similar to that of the sample with the nanovalve alone (blue curve

LPEI-1). Under neutral pH, the concentration of fluorescent dye molecules in the solution was negligible because the nanomachine was closed. Upon tuning the pH to 3.5 by adding dilute HCl, both samples showed an obvious increase of fluorescent dyes in the supernatant solutions as a result of nanomachine opening. The increasing trend continued for several hours until the diffusion out of the pores was complete. This pH-stimulated release character of LPEI-3 shows that the existence of the PEI polymer does not hinder the nanomachines from opening and releasing the cargo.

A control experiment was carried out in order to further prove that the cargo release in LPEI-3 is induced by the nanomachine operation. A PEI polymer coated sample without nanomachine modification was tested under the same conditions (Figure 3.3c, black curve LPEI-2). In this release profile, only a very weak fluorescence intensity change was detected upon acidifying the solution. It was caused by the small amount of dye that was not washed out of the polymer coating. This implies that the large quantity of released cargo observed in the combined system (LPEI-3 red curve) was a result of nanovalve operation and proves that the nanomachine functioning was not interfered with the PEI surface coating.

3.4 Design and Nanomachine Operation of SPEIPEG group

3.4.1 System Construction

The SPEIPEG group employs the PEI-PEG co-polymer coated 50 nm MSN with a nanovalve that opens at pH 5. The PEI-PEG coated small MSNs have demonstrated enhanced biodistribution and biodispersibility properties at an *in vivo* level [27]. The acid

nanovalve with an operational pH close to the lysosomal pH is added in this system [24]. The nanovalve stalk has a methoxy group on the end and has a higher pKa value, that leads to the higher operational pH.

Similarly to the LPEI group, three samples were synthesized in the SPEIPEG group. SPEIPEG-1 has only the nanomachine modification, SPEIPEG-2 has only the PEI-PEG coating, and SPEIPEG-3 has both the nanomachines and the co-polymer coating. For the co-polymer decoration, the PEI component was absorbed onto the particles and the PEG part was grafted onto PEI via an N-hydroxysulfosuccinimide (NHS) ester coupling reaction (Figure 3.2b on page 63) [27]. The PEI part offers electrostatic repulsion between nanoparticles, and the PEG part serves to sterically separate them. Both effects contribute to the excellent dispersal in biological environments [29, 35]. As for the nanovalve attachment, the stalk was synthesized separately before bonding to the silica surface via silanol chemistry (Figure 3.2c).

3.4.2 Characterization

The successful modification of MSNs with the nanomachines and the co-polymer was confirmed by ^{13}C CPMAS NMR (Figure 3.5) and TGA (Table 3.1). Both the substituted alkanes of the co-polymer and the aromatic carbons on the nanovalve stalks were presented in the solid state NMR spectrum of SPEIPEG-3. The TGA results indicate that about 8.3 wt.% of the SPEIPEG-3 is composed of the co-polymers. With a similar method as that of the LPEI-3, the surface area of the polymers in SPEIPEG-3 is calculated (see Methods section on page 58). Since it is much larger than that of the silica nanoparticles, the PEI-PEG

co-polymer has a good coverage on the nanoparticle surfaces.

Figure 4.9a on page 105 shows the TEM images of bare 50 nm silica particles, and Figure 4.9b is the fully-assembled nanoparticles that have both the PEI-PEG co-polymer coating and nanomachine construction. The TEM images show that the particle morphology was not changed by surface modifications. Particle porosity was verified by N_2 adsorption-desorption and powder XRD (Figure 3.7 on page 68 and Figure 4.2).

3.4.3 Nanomachine Operation Test

The same method of time-resolved fluorescence spectroscopy described previously is applied to investigate the functionality of nanovalves in this integrated system. As illustrated in Figure 4.9c, the fully-assembled system with both the PEI-PEG co-polymer and nanomachine construction (red curve SPEIPEG-3) shows a release profile similar to that of the sample that has only the nanovalve modification (blue curve SPEIPEG-1). The nanomachines were able to keep the pore openings closed under neutral pH and open them under acidic conditions, even in the presence of the polymer coating. The sample with only co-polymer coating is used as a control (black curve SPEIPEG-2) and a much smaller dye amount change was observed after solution acidification. These results are consistent with those of the LPEI group. The pH-stimulated dissociation of cyclodextrin can occur even in the presence of surface polymer coatings, and the nanovalves remain fully operative in the combined system.

The investigation of two polymer-nanomachine systems shows that the bulky polymer coating does not sterically hinder the operation of nanovalves, nor does it stop the release

of payload molecules. The polymer moiety is loosely collapsed on the silica surface and does not prevent the movement of cyclodextrins or small molecule dyes. Apart from the steric effect, because the pKa of amine groups on PEI is higher than that of the aromatic amine groups on nanovalve stalk [36, 37, 38], the protonated amine groups on PEI will not interact with α-cyclodextrin (α-CD) during the capping process and thus render no direct influence on the nanomachine operations.

The polymer coating does have an effect on the diffusion rate of the cargo, as well as on the total amount of the cargo that is released from the particles. As shown in Figure 3.3c and Figure 4.9c, the combined systems (the red curves) showed slightly reduced release capacities and faster initial release rates when compared to the nanomachine samples without polymer coatings (the blue curves). The reduced release capacity is due to the fact that both the PEI polymer and the cargo molecule Hoechst 33342 carry positive charge [11, 39]. In the loading process, the PEI polymer produces an electrostatic repulsion force to the positively-charged Hoechst molecules. The dye molecules were able to diffuse into the pore structures due to the concentration gradient, but the total amount of dyes stored in the particles was reduced. We have observed similar effects on the loading capacity when the silica surface was derivatized with functional groups [11, 39]. On the other hand, the faster initial release rate in the combined system is surprising. We observed a similar increase in facilitated payload release when ammonium modified MSNs were used to deliver positively-charged doxorubicin. It was attributed to the electrostatic interaction between the charged cargos and the silica surfaces [11]. Whether or not the same mechanism applies to the phenomena in the polymer-nanomachine systems is still under investigation.

3.5 Summary

In summary, we have combined two nanovalves with two types of coating polymers to demonstrate that the polymer coated on the MSN surface will not interfere with the on-demand release function of nanovalve-modified silica particles. The nanomachines are pH-sensitive nanovalves that operate under acidic conditions, and the two polymer coatings both have showed advanced biological applications either in siRNA delivery or in improving biodistribution of silica particles. Even with the polymer absorbed on the silica surface, the pore openings were kept closed by the nanomachines under neutral pH and opened upon acidification, as in the case of nanomachine alone. This finding offers a new strategy in introducing featured polymers into functionalized-nanomachine systems for enhanced biological properties and multi-task drug delivery applications.

3.6 Methods

3.6.1 Material

Cetyltrimethylammonium bromide (CTAB) (95%, Aldrich), Pluronic F127 (Aldrich), tetraethyl orthosilicate (TEOS) (98%, Aldrich), polyethyleneimine (PEI) (1.8 kD, Aldrich), 4-(dimethylamino) pyridine (99% Aldrich), N,N-disuccinimidyl carbonate (95%, Aldrich), poly(ethylene glycol) methyl ether(m-PEG) (MW 5kD, Aldrich), toluene (99.5%, Aldrich), methanol (99.9%, Firsher), N,N-Dimethyl formamide (DMF) (anhydrous, 99.8%, Aldrich), triethylamine (99.5%, EMD), ethanol (200 proof, Pharmaco-AAPER), N-phenylaminopropyl trimethoxysilane (PhAPTMS) (95%, Gelest), 3-iodopropyltrimethoxysiliane (IPTMS) (95%,

Gelest), p-anisidine (99%, Aldrich), bisBenzimide H 33342 trihydrochloride (Hoechst 33342) (97%, Aldrich), α-cyclodextrin (α-CD) (98%, Aldrich), 3-(trihydroxysilyl)propyl methylphosphonate monosodium aqueous solution (42%, Aldrich), and phosphate-buffered saline (PBS) (pH 7.4, Invitrogen) are used. All chemicals were reagent grade and used without further purification or modification.

3.6.2 Characterization

Transmission electron microscopy (TEM) was carried out on a JEM1200-EX (JEOL) instrument. UV-vis spectra were collected by a Cary 500 UV-vis-NIR spectrophotometer. The release profiles were recorded by an Acton Spectra Pro 2300i CCD. ^{13}C CPMAS NMR spectra were obtained by a Bruker DSX-300 MHz Spectrometer with a 4 mm double resonance Bruker probe head. Ziconium oxide 4 mm rotors were used with Kel-F caps. Thermogravimetric analysis (TGA) was performed by a Pyris Diamond TG/DTA (Perkin-Elmer Instruments). N_2 adsorption-desorption isotherms were collected on a Quadrasorb SI surface area analyser and the BET model was used to calculate the surface areas. The X-ray powder diffraction (XRD) was performed on a Panalytical XPert Pro Powder X-ray Diffractometer (Cu K-alpha radiation).

3.6.3 Synthesis of MSN

The first system based on the large 120 nm MSN with PEI coating is denoted as the LPEI group. The second model using the smaller 50 nm MSN with the PEI-PEG co-polymer is called the SPEIPEG group.

The mesoporous silica nanoparticle for the LPEI group was synthesized according to a well-established procedure [6, 7, 9]. CTAB (250 mg) was added into H_2O (120 mL) with NaOH solution (875 L 2M). The solution was then heated to 80 °C and maintained at the temperature for half an hour before TEOS (1.2 mL) was added slowly into the solution with vigorous stirring. After 20 min, 3-(trihydroxysilyl)propyl methylphosphonate (300 μL) was added and the reaction was kept at 80 °C for another two hours. The synthesized particles were collected and washed with water and methanol. To extract the templating agents, the particles were suspended in methanol (60 mL) with concentrated HCl (2.3 mL) and refluxed at 60 °C overnight. The as-synthesized particles have a lattice distance of about 4.1 nm and the pore size of the mesoporous structure is ∼2.2 nm.

The synthesis of smaller-sized mesoporous silica nanoparticles was slightly different [27]. Pluronic F127 (200 mg) was dissolved in the H_2O solution together with CTAB and NaOH. It was then heated to 80 °C for 30 min before TEOS (1.2 mL) was added. After 20 min, 3-(trihydroxysilyl)propyl methylphosphonate (300 μL) was added and the reaction was kept at 80 °C for two hours before centrifugation and washing.

3.6.4 LPEI Surface Modification

For the attachment of nanomachine stalks in LPEI-1 and LPEI-3, the thread molecule PhAPTMS was directly bonded to the silica surface by reacting with the particles in toluene. PhAPTMS (30 μL) was added into 100 mg particles in toluene (10 mL). It was then heated to 75 °C and refluxed under nitrogen gas at for 24 h. The aniline-modified particles were then washed and dried for later use. The polymer coating was applied for both LPEI-2 and

LPEI-3. As-prepared particles (50 mg) with (LPEI-3) or without the nanomachine stalk (LPEI-2) were dissolved in methanol (5 mL) and mixed with PEI ethanol solution (1.8 kD, 5 mL, 2.5 mg/mL) for half an hour. The coating procedure was repeated before washing with ethanol and water.

3.6.5 SPEIPEG Surface Modification

The nanomachine stalk molecule for SPEIPEG-1 and SPEIPEG was synthesized by reacting p-anisidine (0.123g), IPTMS (40 μL) and triethylamine (420 μL) in toluene (15 mL) at 75 °C under N_2 gas for 24 h. As-synthesized small particles (100 mg) in toluene (15 mL) were added into the stalk solution and reacted at 75 °C under N_2 gas for 24 h. The thoroughly washed particles were then suspended in H_2O (120 mL) and methanol (120 mL) with NH_4NO_3 (0.8 g) to remove the surfactants Pluronic F127 and CTAB, prior to washing and drying. Since SPEIPEG-2 is not decorated by nanomachines, only the surfactant extraction part was performed.

The PEI-PEG co-polymer coating for SPEIPEG-2 and SPEIPEG-3 was performed by electrostatically absorbing PEI onto the silica surface and reacting with the activated m-PEG [9]. Particles (50 mg) after surfactant extraction were mixed with PEI ethanol solution (1.8 kD, 5 mL, 2.5 mg/mL) for half an hour. This step was repeated again and the particles were reacted with activated m-PEG (250 mg) in DMF (5 mL) for 24 h before centrifugation (15000 rpm, 30 min) and washing.

3.6.6 Cargo Loading and Capping

Cargo loading was carried out by suspending as-prepared particles (20 mg) in Hoechst 33342 solution (2 mL, 1mM buffered water solution) for 24 h. Nanomachine stalk-modified samples were added with α-CD (40 mg) and stirred for another 24 h to cap the nanovalves. All samples were washed repeatedly with PBS buffer to remove dye molecules on the silica surface and polymers.

3.6.7 Time-resolved Fluorescence Spectroscopy Release Profile Measurements

Dye loaded sample (4 mg) was weighed and carefully placed in a corner of a cuvette before PBS (6 mL) buffer was added. A 376 nm excitation laser beam was used to excite the emission of Hoechst 33342, and the solution fluorescence spectra were recorded continuously by a spectrophotometer. After collecting a baseline, the solution pH was tuned to 3.5 in the case for LPEI and 5 in the SPEIPEG group to activate the acid nanovalves. Upon the completion of cargo release, the UV-vis absorption spectrum of the supernatant was measured and the dye concentration was calculated using Beers law. The mass of cargo molecules being released was obtained and the corresponding weight percent of cargo to the particle was calculated.

3.6.8 Estimation of the Polymer Coverage on the MSNs

In this part, we calculated the total surface area of silica nanoparticles and that of the polymer molecules coated on the particles. In comparing the two areas, we try to estimate the polymer coverage on the surface of MSNs.

The surface areas of polymer molecules were calculated using software ChemBio3D. Assuming all the molecules are flat, the surface area of an 1800 Da PEI molecule is about 9.97 nm^2 and that of a 5000 Da PEG molecule is about 10.19 nm^2.

3.6.8.1 LPEI-3

For LPEI-3, polymer weight percentage: 31.2 - 14.8 = 16.4

For 100 mg of MSN, there is about 16.4 mg of PEI polymer on the silica surface. The weight for the silica nanoparticles is: 100 - 31.2 = 68.8 mg

Assume the silica density is 2.65 g/cm^3, the particle radius is 60 nm. Number of silica particles in 68.8 mg MSN:

$$N_{MSN} = \frac{68.8\,mg}{2.65\,g/cm^3} \times \frac{1}{(4/3\pi(60\,nm)^3} = 2.87 \times 10^{13}$$

Total surface area of 68.8 mg MSN:

$$S_{MSN-total} = S_0 \times N_{MSN} = 4\pi \times (60\,nm)^2 \times 2.87 \times 10^{13} = 1.30 \times 10^{18}\,nm^2$$

For a PEI molecule of weight 1800 Da, if we assume it is a flat molecule, the length is roughly 6.168 nm and the width is 1.617 nm. Then the area of every molecule would be $6.168 \times 1.617 \approx 9.97 nm^2$

Total area of 16.4 mg PEI polymer molecules:

$$S_{polymer-total} = \frac{9.97\,nm^2 \times 16.4\,mg \times 6.02 \times 10^{23}}{1800\,g} = 5.47 \times 10^{19} nm^2$$

Since $S_{polymer-total} \gg S_{MSN-total}$, this indicates that the PEI polymer has a full coverage on the particle surface.

3.6.8.2 The SPEIPEG-3

Due to the lack of information about the exact weights of PEI and PEG components, an exact calculation similar to that of the LPEI group cannot be conducted. Nevertheless, we can estimate the polymer coverage if it is all composed of PEI or if it is all made of PEG, and the actual coverage should fall between the these two extremes.

In 100mg of SPEIPEG-3, the polymer part weight is: 31.3 - 23.1 = 8.2 mg

The silica nanoparticle weight is: 100 - 31.3 = 68.7 mg

Number of silica particles in 68.7 mg of small particle (30 nm radius):

$$N_{MSN} = \frac{68.7\,mg}{2.65\,g/cm^3} \times \frac{1}{4/3\pi(30nm)^3} = 2.29 \times 10^{14}$$

Total surface area of silica nanoparticles:

$$S_{MSN-total} = S_0 \times N_{MSN} = 4\pi \times (30\,nm)^2 \times 2.29 \times 10^{14} = 2.59 \times 10^{18}\,nm^2$$

If the polymer is mainly composed of PEI, then the total area of 8.2 mg PEI polymer molecules:

$$S_{PEI-total} = \frac{9.97\,nm^2 \times 8.2\,mg \times 6.02 \times 10^{23}}{1800\,g} = 2.73 \times 10^{19} nm^2$$

Since $S_{PEI-total} \gg S_{MSN-total}$, the MSNs are fully covered by the polymer, if it is mainly PEI.

If the polymer is mainly composed of PEG, then the total area of 8.2 mg PEG polymer molecules:

Assuming that PEG is a flat molecule, then the surface area of one molecule would be :

$$40.55\,nm \times 0.2513\,nm \approx 10.19 nm^2$$

$$S_{PEG-total} = \frac{10.19\,nm^2 \times 8.2\,mg \times 6.02 \times 10^{23}}{5000\,g} = 1.01 \times 10^{19} nm^2$$

Since $S_{PEG-total} \gg S_{MSN-total}$, the small MSNs are fully covered by the polymer, if it is mainly PEG.

The calculation results suggested that the PEI-PEG co-polymer has a good coverage on the surface of SPEIPEG-3, regardless of the actually composition between the PEI part and the PEG part.

3.7 Figures and Tables

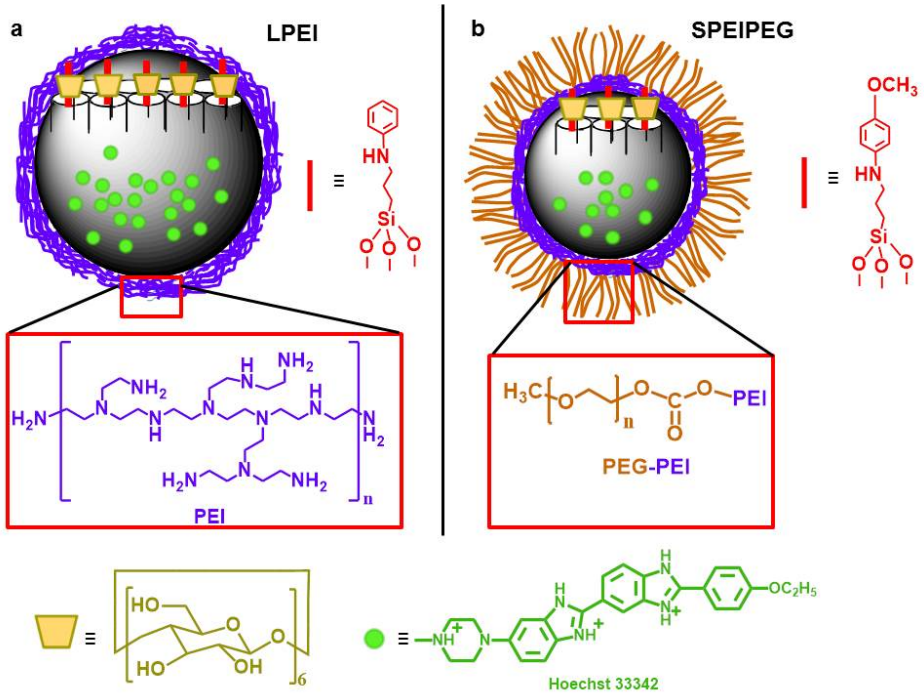

Figure 3.1 Depictions of the two fully-assembled polymer-nanomachine systems based on mesoporous silica nanoparticles. In the LPEI group (a), the particles are about 120 nm in diameter and the polymer coating is PEI. The nanomachine stalk structure is shown on the right side of the particle. In the SPEIPEG group(b), the particle size is about 50 nm and a PEI-PEG co-polymer is coated on the particle surface. For both of the groups, Hoechst 33342 is the cargo for the release study and the α-cyclodextrin is used as the cap on the two types of stalks.

Table 3.1 TGA results of the LPEI group (top) and the SPEIPEG group (bottom) confirm the nanomachine stalk modifications and the full coverage of polymer coatings.

	LPEI-1	LPEI-2	LPEI-3
Organic Part (wt.%)	14.8	22.5	31.2
	SPEIPEG-1	SPEIPEG-2	SPEIPEG-3
Organic Part (wt.%)	23.1	25.5	31.3

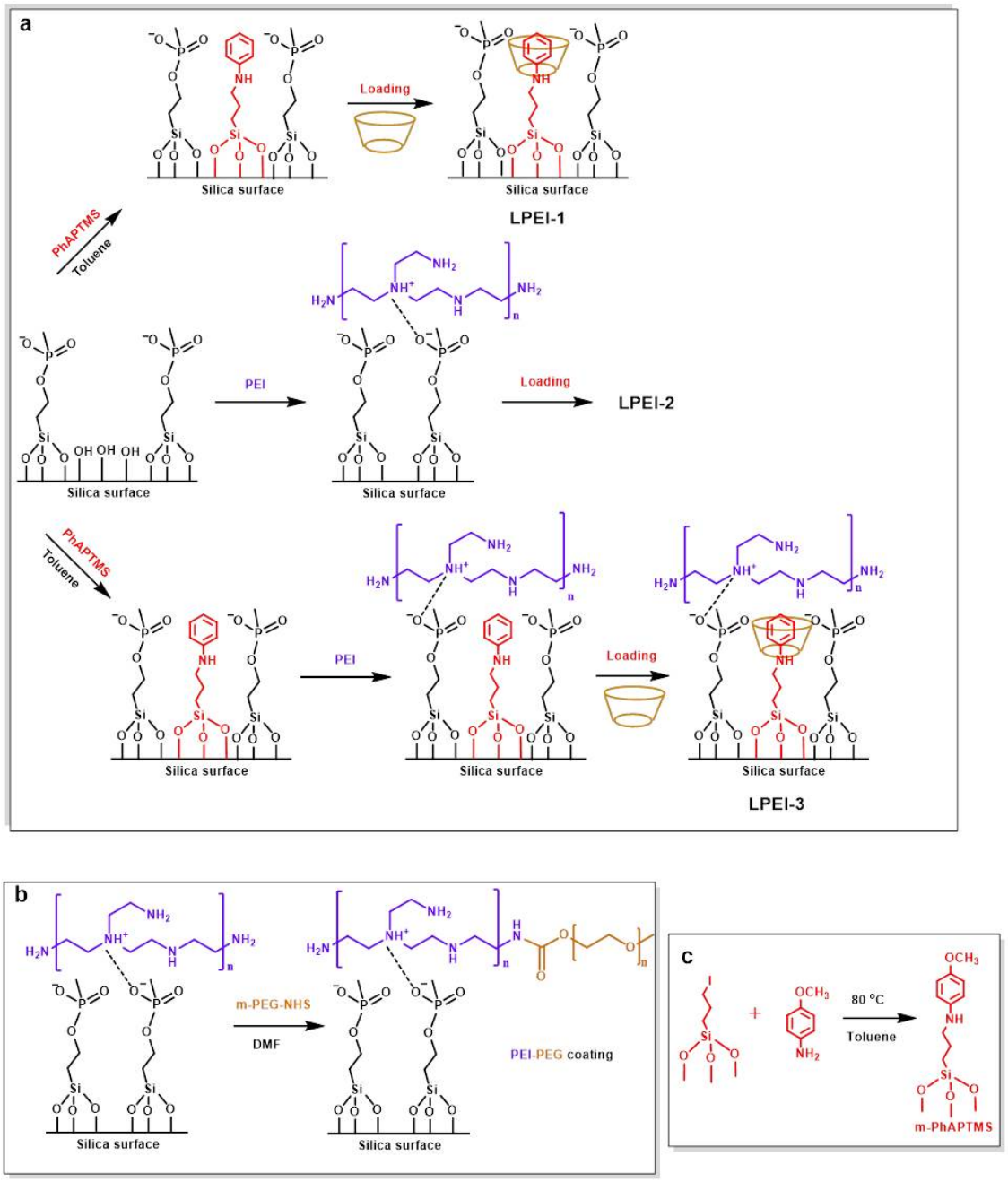

Figure 3.2 Synthesis procedures and sample names for the LPEI group (a). LPEI-1 has only the nanomachine modification, LPEI-2 has only the PEI surface coating, and LPEI-3 has both. Similar naming is used for the SPEIPEG group: SPEIPEG-1 has only the acid nanovalve, SPEIPEG-2 has only the PEI-PEG coating, and SPEIPEG-3 has both the nanovalves as well as the PEI-PEG co-polymer coating. In the SPEIPEG group, the overall synthesis steps are similar to that of the LPEI group, only that the polymer and nanovalves used are different. The detailed synthesis steps for the PEI-PEG co-polymer and the nanovalve stalk are shown in (b) and (c) respectively.

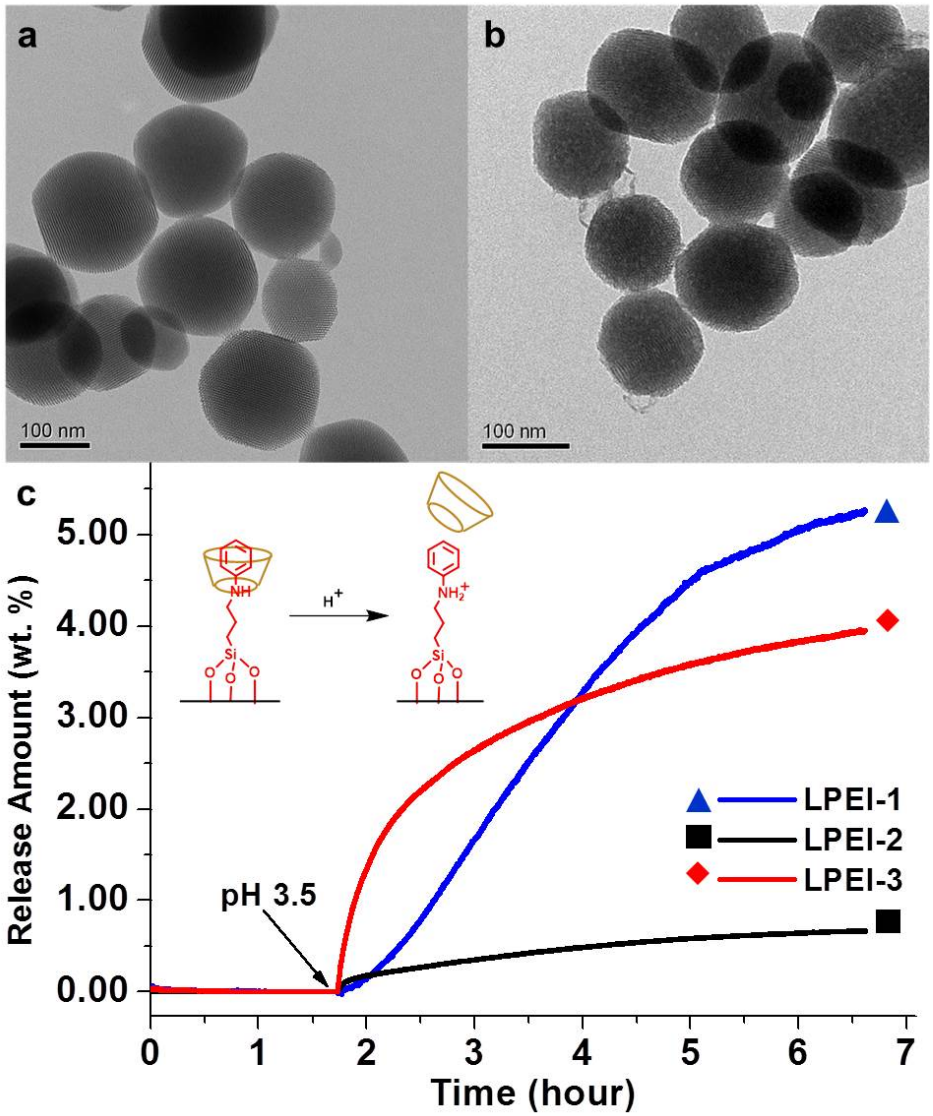

Figure 3.3 TEM images of particles without surface modifications (a) and with both nanomachine and polymer modifications (b). No major morphology or structural difference is observed after the surface modifications were applied. (c) shows the release profiles of the LPEI samples. Particles were kept in a neutral solution before acidification. No cargo leakage was observed under neutral pH and a large amount of cargo was released upon pH change in LPEI-1 and LPEI-3. The release amount is the weight percentage of the released cargos over the nanoparticles.

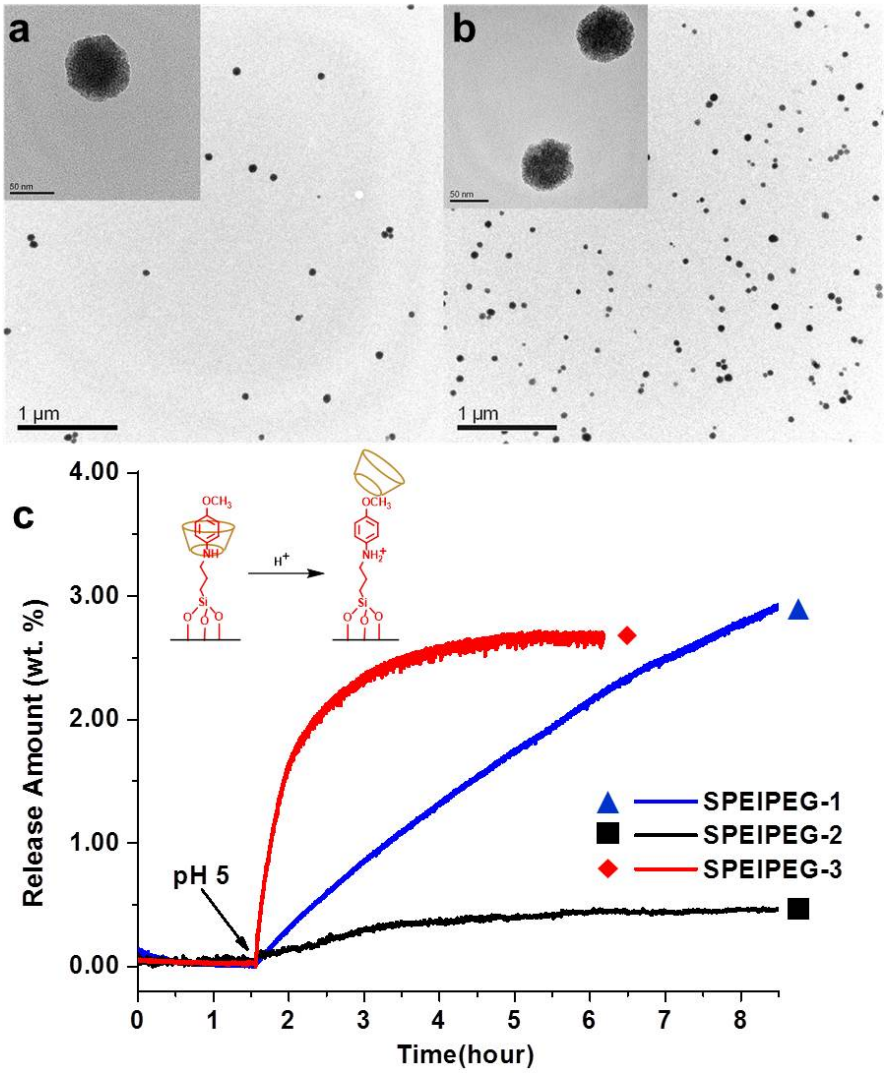

Figure 3.4 TEM images of particles without surface modifications (a) and with both nanomachine and PEI-PEG co-polymer modifications (b). The scale bar is 50 nm for the inset TEM images. The images show similar particle morphology and dispersibility. (c) shows the release profiles of the SPEIPEG group. The nanomachines in SPEIPEG-1 and SPEIPEG-3 were maintained closed under neutral pH and were opened upon pH change, releasing the cargos. For SPEIPEG-3, the release was complete at 6 hours. The release amount is the weight percentage of the released cargos over the nanoparticles.

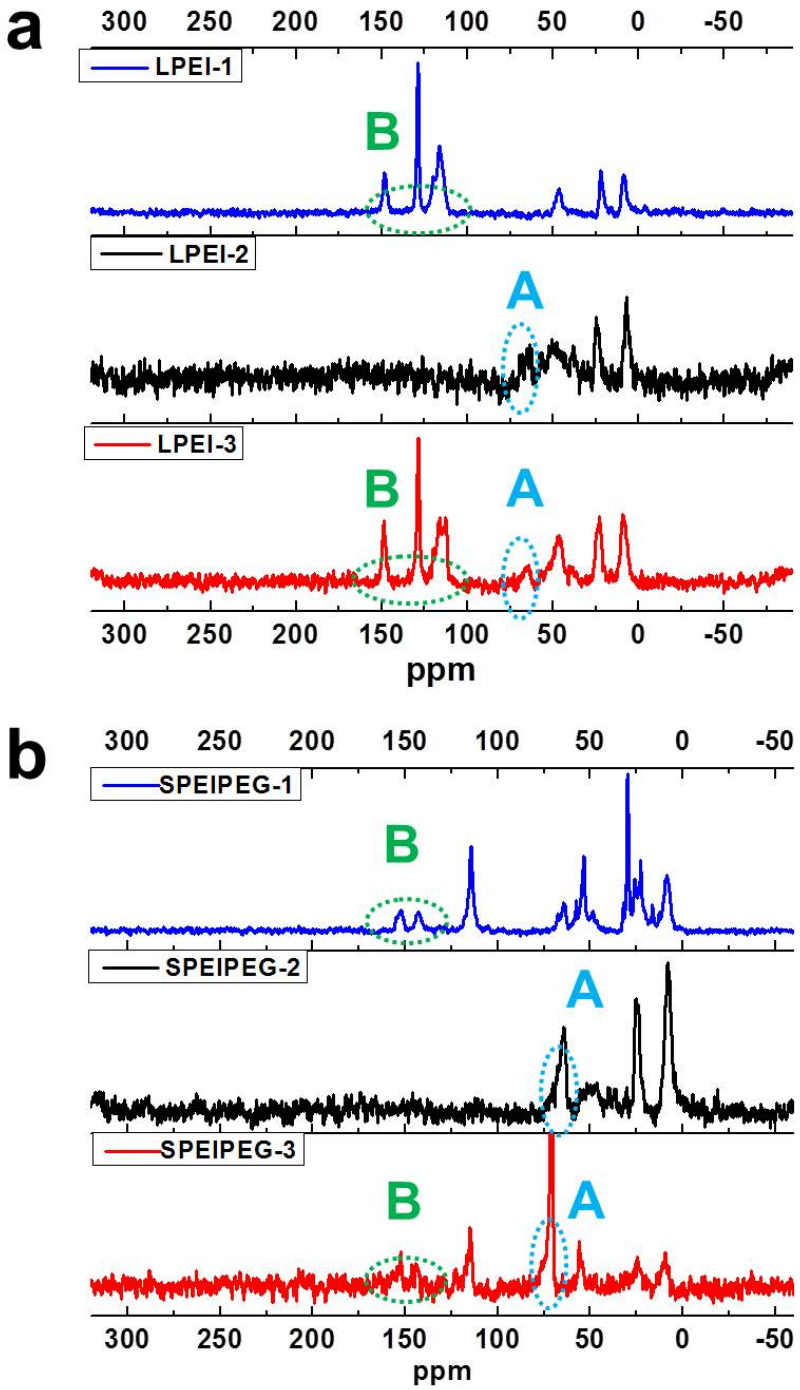

Figure 3.5 ^{13}C CPMAS solid state NMR spectra for LPEI group (a) and SPEIPEG group (b). Range **A** marks the characteristic peaks for substituted alkanes on the polymer coatings and range **B** represents the major aromatic carbons on the nanovalve stalks. The spectra confirm that both the nanovalve modifications and polymer coatings are successfully performed for LPEI-3 and SPEIPEG-3.

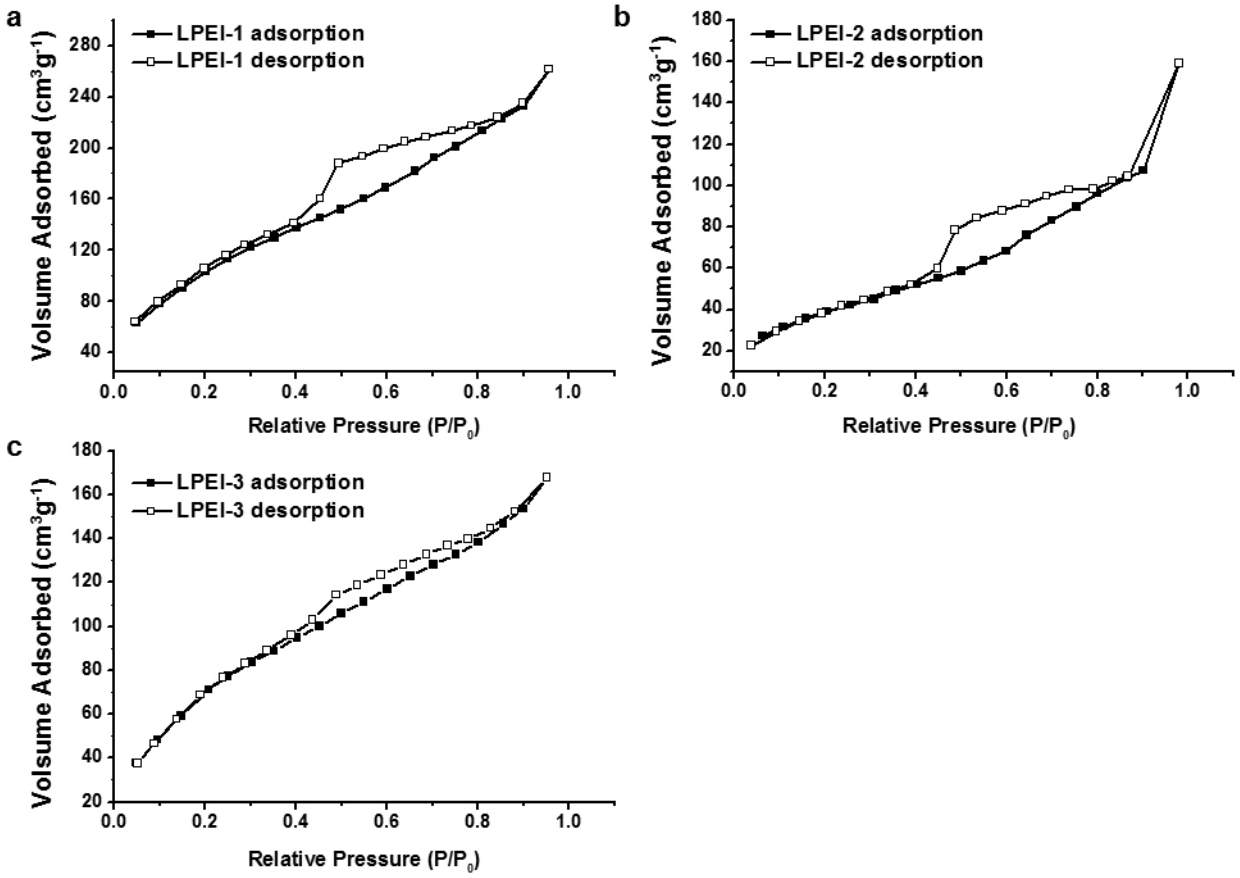

Figure 3.6 N_2 adsorption-desorption isotherms of LPEI samples exhibiting the type IV isotherms for ordered mesoporous structures. The surface areas calculated by BET model are 418 m^2/g for LPEI-1, 149 m^2/g for LPEI-2 and 305 m^2/g for LPEI-3.

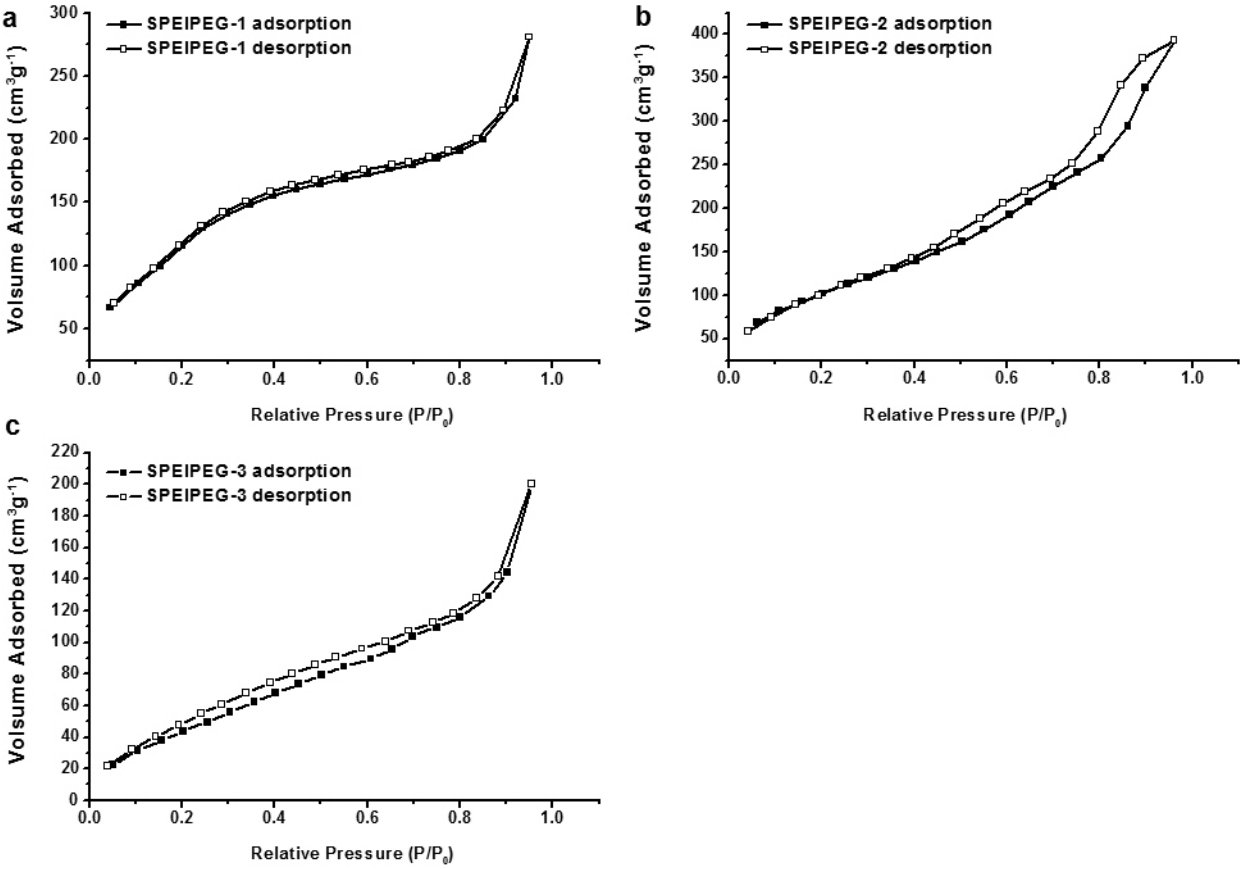

Figure 3.7 N_2 adsorption-desorption isotherms of SPEIPEG groups exhibiting the type IV isotherms for ordered mesoporous structures. The surface areas based on BET model are: 492 m^2/g for SPEIPEG-1, 397 m^2/g for SPEIPEG-2 and 189 m^2/g for SPEIPEG-3.

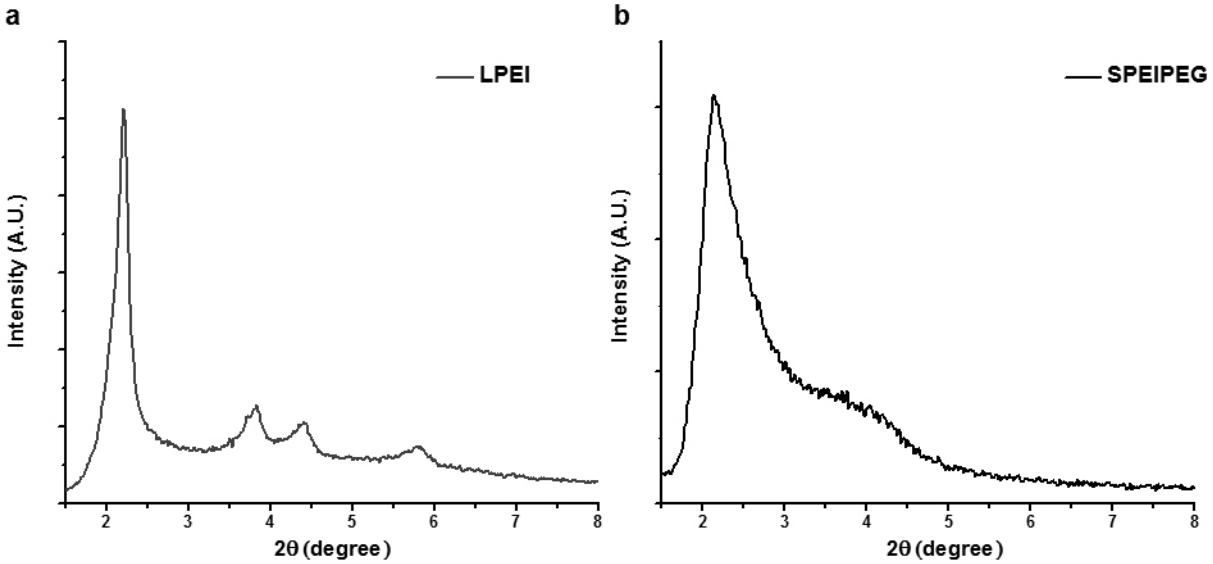

Figure 3.8 The XRD spectra of LPEI (left) and SPEIPEG (right) particles. The interplanar spacing $d(100)$ is 4.0 nm for LPEI and 4.1 nm for SPEIPEG. The SPEIPEG particles have used two templating agents that broaden the d-space distributions.

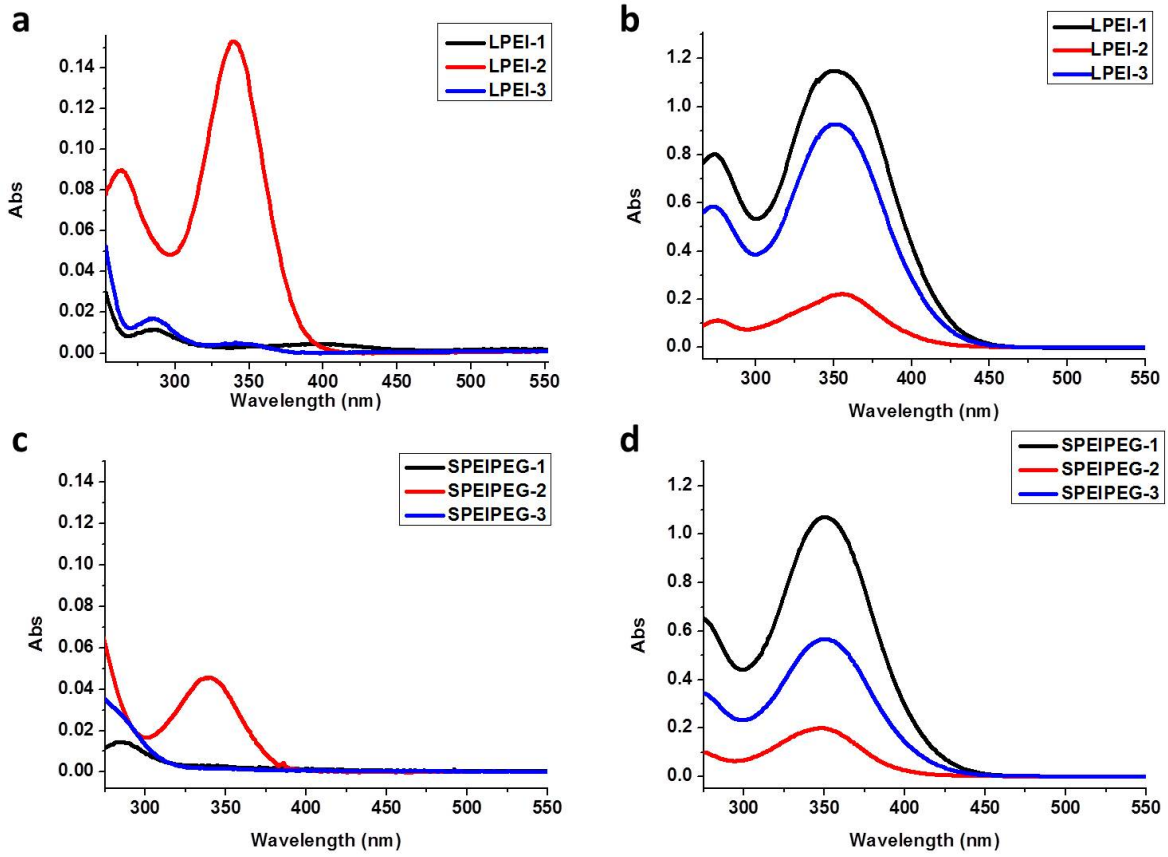

Figure 3.9 Supernatant absorption spectra of LPEI group before (a) and after cargo release(b). (c,d) are the spectra for SPEIPEG group, where (c) is before the release and (d) is after the release. The nanovalves on LPEI-1 and LPEI-3 were able to trap the cargo in the mesopores under neutral pH and release them after acidification. Similar results were also observed in SPEIPEG-1 and SPEIPEG-3.

3.8 References

[1] C. Kresge, M. Leonowicz, W. Roth, J. Vartuli, and J. Beck. "Ordered Mesoporous Molecular-Sieves Synthesized by a Liquid-Crystal Template Mechanism." *Nature*, **359** (6397):710–712, 1992.

[2] Q. Cai, Z. S. Luo, W. Q. Pang, Y. W. Fan, X. H. Chen, and F. Z. Cui. "Dilute solution routes to various controllable morphologies of MCM-41 silica with a basic medium." *Chem. Mat.*, **13**(2):258–263, 2001.

[3] B. G. Trewyn, I. I. Slowing, S. Giri, H.-T. Chen, and V. S.-Y. Lin. "Synthesis and functionalization of a mesoporous silica nanoparticle based on the sol-gel process and

applications in controlled release." *Accounts Chem. Res.*, **40**(9):846–853, 2007.

[4] J. Liu, Q. Yang, L. Zhang, H. Yang, J. Gao, and C. Li. "OrganicInorganic Hybrid Hollow Nanospheres with Microwindows on the Shell." *Chem. Mater.*, **20**(13):4268–4275, 2008.

[5] M. Mandal and M. Kruk. "Family of Single-Micelle-Templated Organosilica Hollow Nanospheres and Nanotubes Synthesized through Adjustment of Organosilica/Surfactant Ratio." *Chem. Mater.*, **24**(1):123–132, 2012.

[6] M. W. Ambrogio, C. R. Thomas, Y.-L. Zhao, J. I. Zink, and J. F. Stoddartt. "Mechanized Silica Nanoparticles: A New Frontier in Theranostic Nanomedicine." *Accounts Chem. Res.*, **44**(10):903–913, 2011.

[7] Z. Li, J. C. Barnes, A. Bosoy, J. F. Stoddart, and J. I. Zink. "Mesoporous silica nanoparticles in biomedical applications." *Chem. Soc. Rev.*, **41**(7):2590–2605, 2012.

[8] M. Vallet-Regi, F. Balas, and D. Arcos. "Mesoporous materials for drug delivery." *Angew. Chem.-Int. Edit.*, **46**(40):7548–7558, 2007.

[9] M. Liong, J. Lu, M. Kovochich, T. Xia, S. G. Ruehm, A. E. Nel, F. Tamanoi, and J. I. Zink. "Multifunctional inorganic nanoparticles for imaging, targeting, and drug delivery." *ACS Nano*, **2**(5):889–896, 2008.

[10] D. P. Ferris, Y.-L. Zhao, N. M. Khashab, H. A. Khatib, J. F. Stoddart, and J. I. Zink. "Light-Operated Mechanized Nanoparticles." *J. Am. Chem. Soc.*, **131**(5):1686–1688, 2009.

[11] H. Meng, M. Xue, T. Xia, Y.-L. Zhao, F. Tamanoi, J. F. Stoddart, J. I. Zink, and A. E. Nel. "Autonomous in Vitro Anticancer Drug Release from Mesoporous Silica Nanoparticles by pH-Sensitive Nanovalves." *J. Am. Chem. Soc.*, **132**(36):12690–12697, 2010.

[12] J. Lu, E. Choi, F. Tamanoi, and J. I. Zink. "Light-activated nanoimpeller-controlled drug release in cancer cells." *Small*, **4**(4):421–426, 2008.

[13] I. I. Slowing, B. G. Trewyn, and V. S.-Y. Lin. "Mesoporous silica nanoparticles for intracellular delivery of membrane-impermeable proteins." *J. Am. Chem. Soc.*, **129** (28):8845–8849, 2007.

[14] T. D. Nguyen, K. C.-F. Leung, M. Liong, C. D. Pentecost, J. F. Stoddart, and J. I. Zink. "Construction of a pH-driven supramolecular nanovalve." *Org. Lett.*, **8**(15):3363–3366, 2006.

[15] T. D. Nguyen, Y. Liu, S. Saha, K. C.-F. Leung, J. F. Stoddart, and J. I. Zink. "Design and optimization of molecular nanovalves based on redox-switchable bistable rotaxanes." *J. Am. Chem. Soc.*, **129**(3):626–634, 2007.

[16] S. Giri, B. G. Trewyn, M. P. Stellmaker, and V. S. Y. Lin. "Stimuli-responsive controlled-release delivery system based on mesoporous silica nanorods capped with magnetic nanoparticles." *Angew. Chem. Int. Edit.*, **44**(32):5038–5044, 2005.

[17] R. Liu, Y. Zhang, X. Zhao, A. Agarwal, L. J. Mueller, and P. Feng. "pH-Responsive Nanogated Ensemble Based on Gold-Capped Mesoporous Silica through an Acid-Labile Acetal Linker." *J. Am. Chem. Soc.*, **132**(5):1500–1501, 2010.

[18] D. R. Radu, C. Y. Lai, K. Jeftinija, E. W. Rowe, S. Jeftinija, and V. S. Y. Lin. "A polyamidoamine dendrimer-capped mesoporous silica nanosphere-based gene transfection reagent." *J. Am. Chem. Soc.*, **126**(41):13216–13217, 2004.

[19] P.-W. Chung, R. Kumar, M. Pruski, and V. S.-Y. Lin. "Temperature responsive solution partition of organic-inorganic hybrid poly(N-isopropylacrylamide)-coated mesoporous silica nanospheres." *Adv. Funct. Mater.*, **18**(9):1390–1398, 2008.

[20] Y. Yang, X. Yan, Y. Cui, Q. He, D. Li, A. Wang, J. Fei, and J. Li. "Preparation of polymer-coated mesoporous silica nanoparticles used for cellular imaging by a "graft-from" method." *J. Mater. Chem.*, **18**(47):5731–5737, 2008.

[21] C.-Y. Hong, X. Li, and C.-Y. Pan. "Fabrication of smart nanocontainers with a mesoporous core and a pH-responsive shell for controlled uptake and release." *J. Mater. Chem.*, **19**(29):5155–5160, 2009.

[22] R. Liu, P. Liao, J. Liu, and P. Feng. "Responsive Polymer-Coated Mesoporous Silica as a pH-Sensitive Nanocarrier for Controlled Release." *Langmuir*, **27**(6):3095–3099, 2011.

[23] B. Chang, X. Sha, J. Guo, Y. Jiao, C. Wang, and W. Yang. "Thermo and pH dual responsive, polymer shell coated, magnetic mesoporous silica nanoparticles for controlled drug release." *J. Mater. Chem.*, **21**(25):9239–9247, 2011.

[24] L. Du, S. Liao, H. A. Khatib, J. F. Stoddart, and J. I. Zink. "Controlled-Access Hollow Mechanized Silica Nanocontainers." *J. Am. Chem. Soc.*, **131**(42):15136–15142, 2009.

[25] C. R. Thomas, D. P. Ferris, J.-H. Lee, E. Choi, M. H. Cho, E. S. Kim, J. F. Stoddart, J.-S. Shin, J. Cheon, and J. I. Zink. "Noninvasive Remote-Controlled Release of Drug Molecules in Vitro Using Magnetic Actuation of Mechanized Nanoparticles." *J. Am. Chem. Soc.*, **132**(31):10623–10625, 2010.

[26] H. Meng, M. Liong, T. Xia, Z. Li, Z. Ji, J. I. Zink, and A. E. Nel. "Engineered Design of Mesoporous Silica Nanoparticles to Deliver Doxorubicin and P-Glycoprotein siRNA to Overcome Drug Resistance in a Cancer Cell Line." *ACS Nano*, **4**(8):4539–4550, 2010.

[27] H. Meng, M. Xue, T. Xia, Z. Ji, D. Y. Tarn, J. I. Zink, and A. E. Nel. "Use of Size and a Copolymer Design Feature To Improve the Biodistribution and the Enhanced Permeability and Retention Effect of Doxorubicin-Loaded Mesoporous Silica Nanoparticles in a Murine Xenograft Tumor Model." *ACS Nano*, **5**(5):4131–4144, 2011.

[28] V. Cauda, C. Argyo, and T. Bein. "Impact of different PEGylation patterns on the long-term bio-stability of colloidal mesoporous silica nanoparticles." *J. Mater. Chem.*, **20**(39):8693–8699, 2010.

[29] Q. He, Z. Zhang, F. Gao, Y. Li, and J. Shi. "In vivo Biodistribution and Urinary Excretion of Mesoporous Silica Nanoparticles: Effects of Particle Size and PEGylation." *Small*, **7**(2):271–280, 2011.

[30] T. Xia, M. Kovochich, M. Liong, H. Meng, S. Kabehie, S. George, J. I. Zink, and A. E. Nel. "Polyethyleneimine Coating Enhances the Cellular Uptake of Mesoporous Silica Nanoparticles and Allows Safe Delivery of siRNA and DNA Constructs." *ACS Nano*, **3**(10):3273–3286, 2009.

[31] C. Hom, J. Lu, M. Liong, H. Luo, Z. Li, J. I. Zink, and F. Tamanoi. "Mesoporous Silica Nanoparticles Facilitate Delivery of siRNA to Shutdown Signaling Pathways in Mammalian Cells." *Small*, **6**(11):1185–1190, 2010.

[32] W. Chen, C. E. Chang, and M. K. Gilson. "Calculation of cyclodextrin binding affinities: Energy, entropy, and implications for drug design." *Biophys. J.*, **87**(5):3035–3049, 2004.

[33] Q. X. Guo, L. Liu, W. S. Cai, Y. Jiang, and Y. C. Liu. "Driving force prediction for inclusion complexation of alpha-cyclodextrin with benzene derivatives by a wavelet neural network." *Chem. Phys. Lett.*, **290**(4-6):514–518, 1998.

[34] B. Thierry, L. Zimmer, S. McNiven, K. Finnie, C. Barbe, and H. J. Griesser. "Electrostatic self-assembly of PEG copolymers onto porous silica nanoparticles." *Langmuir*, **24**(15):8143–8150, 2008.

[35] V. Cauda, A. Schlossbauer, and T. Bein. "Bio-degradation study of colloidal mesoporous silica nanoparticles: Effect of surface functionalization with organo-silanes and poly(ethylene glycol)." *Micropor. Mesopor. Mat.*, **132**(1-2):60–71, 2010.

[36] J. Suh, H. Paik, and B. Hwang. "Ionization of Poly(ethylenimine) and Poly(allylamine)

at Various pHs." *Bioorganic Chem.*, **22**(3):318–327, 1994.

[37] J. King, R. Rathore, J. Lam, Z. Guo, and D. Klassen. "pH Optimization of Nucleophilic Reactions in Water." *J. Am. Chem. Soc.*, **114**(8):3028–3033, 1992.

[38] J. King, Z. Guo, and D. Klassen. "Nucleophilic-Attack Vs General Base Assisted Hydrolysis in the Reactions." *J. Org. Chem.*, **59**(5):1095–1101, 1994.

[39] Z. Li, J. L. Nyalosaso, A. A. Hwang, D. P. Ferris, S. Yang, G. Derrien, C. Charnay, J.-O. Durand, and J. I. Zink. "Measurement of Uptake and Release Capacities of Mesoporous Silica Nanoparticles Enabled by Nanovalve Gates." *J. Phys. Chem. C*, **115**(40):19496–19506, 2011.

Part III

Upconversion Lanthanide Nanocrystal Embedded Mesoporous Silica Nanoparticles for Temperature Sensing and Drug Delivery

CHAPTER 4

Taking the Temperature of the Interiors of Magnetically Heated Nanoparticles

4.1 Abstract

The temperature increase inside mesoporous silica nanoparticles induced by encapsulated smaller superparamagnetic nanocrystals in an oscillating magnetic field is measured using a crystalline optical nanothermometer. The detection mechanism is based on the temperature-dependent intensity ratio of two luminescence bands in the upconversion emission spectrum of $NaYF_4$:Yb^{3+}, Er^{3+}. A facile stepwise phase transfer method is developed to construct a dual-core mesoporous silica nanoparticle that contains both a nanoheater and a nanothermometer in its interior. The magnetically induced heating inside the nanoparticles varies with different experimental conditions, including the magnetic field induction power, the exposure time to the magnetic field, and the magnetic nanocrystal size. The temperature increase of the immediate nanoenvironment around the magnetic nanocrystals is monitored continuously during the magnetic oscillating field exposure. The interior of the nanoparticles becomes much hotter than the macroscopic solution and cools to the temperature of the ambient fluid on a time scale of seconds after the magnetic field is turned off. This continuous

absolute temperature detection method offers new insight into the nanoenvironment around magnetic materials and opens a path for optimizing local temperature controls for physical and biomedical applications.

4.2 Introduction

Ferromagnetic compositions generate heat under a high frequency oscillating magnetic field (OMF) as a result of hysteresis energy loss and Neel or Brown relaxation[1, 2, 3]. Numerous magnetic materials have been designed to conduct hyperthermia therapy for cancer treatment, benefiting from the higher sensitivity of lesions to raised temperatures compared to normal tissues [4, 5, 6, 7]. With the advance of nanomedicines, hypotheses have suggested single cell heating, termed intracellular hyperthermia, based on the idea that magnetic nanoparticles are able to raise the temperature of their immediate surroundings more efficiently than that of the overall volume [8]. It was proposed to provide a more selective heating to targeted cells, which is thus superior to the intercellular hyperthermia method. However, several theoretical thermal studies analyzed the heat generation and heat flow by nanoparticles, and argued that the temperature rise localized in the magnetic particle surroundings is negligible and that the entire occupied volume should have a homogeneous temperature distribution [9, 10].

In an effort to solve the puzzle by experimental methods, researchers have examined chemical and biological evidence of local heating in the vicinity of magnetic nanoparticles [11, 12, 13]. Either thermal-sensitive chemical bond breaking or temperature-regulated protein activity has been monitored after applying the OMF, and the results indicated that

higher local temperature was achieved compared to the macroscopic temperature. However, indirect temperature characterizations do not carry quantitative information with high sensitivity and could not distinguish between events that happened during the exposure or afterward. Given the fast heat processing on the nanoscale, a continuous direct measurement method is required for accurate understanding. To date, the nanoenvironment temperature change induced by magnetic materials during the oscillating magnetic field exposure has not been quantified and remains crucial in the efficiency evaluation and development of nano-hyperthermia therapy.

A facile, direct, and sensitive detection method is needed for the nanoscale experimental measurement. Instead of the temperature-dependent properties that are used in bulk analyses, such as density and resistance change, a temperature-sensitive optical signal is more accessible and offers enhanced spatial and temporal resolution. Previously, Polo-Corrales *et al.* observed a larger fluorescence intensity increase of a copolymer when placed in the oscillating magnetic field compared to that when the field was off, even though the monitored solution temperature was the same, suggesting a different local temperature environment in the vicinity of magnetic nanoparticles [14]. Later on, Freddi *et al.* used the excited-state lifetime of rhodamine B electrostatically absorbed in a polymer matrix to monitor the surface temperature of gold nanoparticles with different shapes [15]. Compared to other spectral changes such as fluorescence intensity quenching [16], a thermal responsive intensity ratio variation in the spectra has the advantages of absolute measurement, high sensitivity, and simpler equipment requirements and is less subject to environmental perturbations. The ratiometric method of temperature detection has been achieved either by incorporating two

fluorophores with one of them showing a strong thermal response, such as a semiconducting polymer particle with organic dye molecules [17]; or, for some fluorophores, by intrinsic thermally coupled excited states, as demonstrated by Vetrone *et al.* in their work of cell temperature mapping [18]. The upconversion fluorescence spectra of Yb^{3+}- and Er^{3+}- doped $NaYF_4$ nanocrystals have two green emission bands, from which the intensity ratio is a function of temperature, independent of the total luminescence intensity changes caused by experimental variations [18, 19, 20, 21, 22, 23].

To measure the local nanoenvironment temperature change around magnetic nanocrystals, a hybrid dual-core mesoporous silica nanoparticle (MSN) is synthesized. MSNs were chosen as the container because they are studied extensively as a biocompatible platform for drug delivery [24, 25, 26], catalysis [27, 28] and hyperthermia [29, 30]. A detailed interior temperature examination of MSNs would provide quantitative guidelines for optimizing designs for magnetically induced on-demand drug delivery and hyperthermia. The controlled synthesis of an organized mesoporous silica scaffold embedded with two types of nanocrystals is much more difficult than that of a solid silica shell structure [31, 32], due to the sensitivity of the self-assembling of the templating surfactants to perturbations. In this study, by using a stepwise phase transfer method, the $NaYF_4$:Yb^{3+}, Er^{3+} optical thermometer nanocrystal (UCNC) and the superparamagnetic Fe_3O_4 nanocrystal (MNC) are encapsulated in the same mesoporous silica nanoparticle that provides the rigid structure support. The construction is designed to immobilize the thermometer next to the nanoheater in a nanoenvironment that is distinct from the bulk surroundings. Upon the exposure to a high-frequency oscillating magnetic field, the superparamagnetic iron oxide nanocrystals generate heat inside the

MSNs. The upconversion nanocrystal encapsulated in the same MSN senses the temperature change and gives a direct luminescence read-out of this nanoenvironment temperature.

In this project, we describe the synthesis of the dual-core mesoporous silica nanoparticles, quantify the nanoparticle interior temperature changes initiated by nanoheaters during an oscillating magnetic field exposure, and measure the temperature gradient between the nano- and macroenvironment as it evolves.

4.3 Synthesis of the Nanocrystals and the Dual-core Mesoporous Silica Nanoparticles

The UCNCs were synthesized by a modified thermolysis approach using lanthanide chlorides as the precursors and oleic acid as the stabilizing surfactant [33, 34]. These single crystalline nanorods have a narrow size distribution (49 ± 2 nm long and 23 ± 1 nm wide, Figure 4.1a on page 98). The hexagonal lattice structure of -$NaYF_4$ is confirmed by high-resolution transmission electron microscopy images (HRTEM, Figure 4.1b) and X-ray power diffraction (XRD, Figure 4.2 on page 99). The MNCs of two different sizes were obtained from a commercial source, and the average size is 6.4 ± 1.0 nm for MNC5 and 17 ± 2 nm for MNC20 (Figure 4.3 on page 99).

We developed a synthetic method to assemble a mesoporous silica nanoparticle system that encapsulates simultaneously both the superparamagnetic nanocrystals and the temperature-sensitive upconversion nanocrystals. This approach starts with the stepwise phase transfers of the hydrophobic nanocrystals into the aqueous solutions, featuring a thorough mix of two types of nanocrystals and a facile preparation for the construction of MSNs

later on. The as-synthesized UCNCs were first transferred from chloroform to water by coating them with the surfactant hexadecyltrimethylammonium bromide (CTAB) and then evaporating the organic solvent. The aqueous solution dispersed with UCNCs was then mixed with the MNCs in chloroform. The CTAB-stabilized UCNCs help the MNCs to transfer from the hydrophobic phase to the hydrophilic phase and promote the mixing of the MNCs into their coating matrix. Compared to the direct blending of two types of nanocrystals in the same phase, this stepwise phase transfer method uses the surface-coated surfactants on one nanocrystal to extract a different nanocrystal over the phase boundary, reduces the surface tension, offers more control of a homogeneous distribution, and prevents the aggregation of nanocrystals. The aqueous solution containing both nanocrystals was introduced into the sol-gel reaction solution, followed by adding the silica precursor to construct the dual-core mesoporous silica nanoparticles. The nanocrystal ratio and the surfactant amount were carefully tuned to facilitate the formation of a one-to-one composition in MSNs. To further enhance the homogeneity, a magnet was used to separate particles that contain the MNCs, so that the temperature of only the silica nanoparticles that encapsulate both the MNCs and the UCNCs is studied. The measurement is the sum of all mesoporous silica nanoparticles under detection. A control sample of MSNs with only the UCNCs (UCNC@MS) was also synthesized (Figure 4.1c,d). Both 5 and 20 nm spherical Fe_3O_4 MNCs are used in this study for size comparison (Figure 4.3 on page 99). UCNC:MNC5@MS contains both the UCNCs and the 5nm MNCs (Figure 4.1e), and UCNC:MNC20@MS has both the UCNCs and the 20 nm MNCs (Figure 4.1f, Figure 4.4a on page 100).

The energy-dispersive X-ray (EDX) spectra and element mappings confirm that both

MNC and UCNC are embedded in the same UCNC:MNC20@MS nanoparticles (Figure 4.4a on page 100). The average distance between the UCNC and the MNC is about 8 and 9 nm (Table 4.1). After the magnet separation, the population of nanoparticles with a 1:1 ratio between UCNC and MNC is about 70 percent by statistical analyses (Table 4.1). Another 10 percent of nanoparticles contain two heating nanocrystals. A portion of particles have only MNCs embedded, but they do not give an optical signal. The mesoporosity of the two samples was analyzed by N_2 adsorption-desorption, and the calculated pore volume is 0.792 cm^3/g for UCNC:MNC5@MS and 0.631 cm^3/g for UCNC:MNC20@MS (Figure 4.5 on page 101).

4.4 Temperature Detection Mechanism

The upconversion luminescence spectra of UCNCs were collected at different bulk temperatures and the emission peak intensity ratios were plotted as a function of the temperature to generate a working curve (Figure 4.6 on page 102 and Figure 4.7 on page 103). After two sequential energy transfers from Yb^{3+} ions to Er^{3+} ions, the excited Er^{3+} ions undergo nonradiative relaxations to the thermally coupled $^2H_{11/2}$ and $^4S_{3/2}$ states and radiatively transfer back to the ground state, giving rise to two green emission bands (Figure 4.6a) [23]. The fine peak structures in the bands are due to the energy level splittings in the crystal field [35]. The relative populations respond to the temperature: as the temperature increases, the higher level gains more population, while that of the lower level decreases. The natural log of this intensity ratio is linearly related to the inverse of the temperature according to the Boltzmann distribution (Equation 4.1), where I_{520} and I_{540} are the peak intensities, ΔE

is the energy gap between the two excited states, k is the Boltzmann constant, and T is the absolute temperature. The thermal sensitivity of intensity ratio is about 28.8 $\times 10^{-4}$ /K for the nanocrystals (see Methods section on page 93). After collecting the emission spectra, they were fitted by a multipeak fitting program with fixed peak positions (Figure 4.6b). The reason for the peak fitting calculation instead of direct integration of peak areas is that the 520 nm and the 540 nm peak overlap around 535 nm. To distinguish the contribution from the two peaks in this area, the peak fitting procedure is necessary. The spectra collected at different temperatures and the corresponding working curve are shown in Figure 4.6c and d.

$$Ln\frac{I_{520}}{I_{540}} = \frac{A - \Delta E}{kT} \tag{4.1}$$

4.5 Measurement of Nanoparticle Interior Temperature Change Induced by Magnetic Nanocrystals

The magnetically induced heating is examined by comparing the spectra of UCNCs before and after the OMF exposure (Figure 4.8 on page 104). The oscillating magnetic field was generated using a five-turn induction coil and an oscillation frequency of 375 kHz (See Methods section). The following paragraphs discuss the impact of the magnetic nanoparticle size, the magnetic field induction power, and the OMF exposure length.

The heating rate is faster for the 20 nm MNCs than for the 5 nm MNCs at a constant magnetic field induction power. The temperature increase in the UCNC:MNC20@MS is almost double that of the UCNC:MNC5@MS (Figure 4.9a on page 105) and the same trend is observed for different exposure times. UCNC:MNC20@MS (Figure 4.6a inset black square)

shows a higher rate increase in the exposure time dependency plot as a result of higher specific loss power expected for larger single domain superparamagnetic particles [2]. Similar trends are observed when the magnetic field induction power is reduced by half (Figure 4.6b).

The possible heating from the Yb^{3+} and the Er^{3+} ions in an OMF, both of which are paramagnetic in their ground and excited states, was also examined. UCNC@MS were studied as the control group. As shown in Figure 4.6a (left columns), with a 30, 60, and 90 s OMF exposure, their temperature increases are much smaller than those of the MNC-embedded samples.

The heating is directly proportional to the induction power of the oscillating magnetic field. For UCNC:MNC20@MS, a linear dependency of temperature increase on the magnetic field induction power is observed for various exposure times (Figure 4.6c). The linear relation can be explained by the correlation between the induction power and the MNC heat dissipation power. The magnetic field induction power (P_i) is proportional to the square of electrical current, and thus proportional to the square of the magnetic amplitude (H), $P_i \propto H^2$. The dissipation power (P_d) from a MNC under an OMF is also proportional to the square of the magnetic amplitude, $P_d = \mu_0 \pi \chi f H^2$ [1]. Thus the MNC dissipation power is linearly related to the field induction power, ($P_i \propto P_d$). Assuming that the thermal conductivity and heat capacity of the nanoenvironment are not strongly temperature dependent, the temperature increase inside the nanoparticle depends only on the dissipation power of the MNCs and thus the induction power of the magnetic field. A similar linear dependency of the temperature increase on the input energy has been observed previously in polymer capsules with gold nanoparticles in optical heating systems [36].

The temperature increase is proportional to the OMF exposure time. Proportional correlations are preserved for both the UCNC:MNC20@MS and UCNC:MNC5@MS under full magnetic field induction power (Figure 4.9a inset) and reduced power (Figure 4.9b inset). However, we observed an eventual saturation as the exposure time approaches 5 min (Figure 4.9d and Figure 4.10 on page 106). The UCNC:MNC20@MS temperature increase grows with the longer exposure time, but the rate decreases at times longer than 90 s. The longer exposure time leads to a higher temperature gradient and thus more efficient heat dissipation. The balance between the heating and the dissipation results in the leveling off of the temperature change rate as the exposure time increases.

4.6 Comparison of Nanoparticle Interior Temperature with that of the Bulk Media during the Exposure to the Oscillating Magnetic Field

The magnitude of the temperature difference (if any) between the interiors of the silica particles and the surrounding liquid is monitored using a field on experiment where the temperatures were recorded during the OMF exposure. (A control study was carried out to confirm that the OMF did not affect the intensity ratio in the emission spectrum of the UCNCs, Figure 4.11 on page 107.) The *in situ* nanoparticle interior temperature change was recorded at different time intervals during the exposure period. In a parallel experiment, the UCNCs were suspended directly in the solution but the MNCs were embedded in the MSNs, forming the single-core nanoparticles (MNC20@MS, Figure 4.12 on page 108), such that the nanoheaters are separated from the nanothermometers and the nanothermometers

measure the bulk solution temperature. The mesoporous nanoparticles in the two cases have similar particle sizes and the same silica surfaces are exposed to the solution. Thus, they do not have any differences between the heating center distances [37]. Figure 4.13a shows the field on temperature evolution for both the nanoparticles and the bulk solution for a 90 s exposure (on page 108), and Figure 4.13b is that for a 5 min exposure. In both cases, the nanoparticle interior temperature (red dots) rises much faster than that of the bulk solution (black squares). For a 5 min exposure, the temperature change inside the nanoparticles is 42 °C compared to 19 °C for that of the bulk solution. Immediately after the exposure, the heating stops and the nanoparticle interior temperature quickly decreases. The solution continues to absorb heat from nanoparticles until its temperature equilibrates with the nanoparticles. The system gradually dissipates heat to the ambient environment and recovers to room temperature in 15 to 20 min after the exposure. In order to reduce the heat dissipated from the nanoparticles and examine the temperature change, we lowered the magnetic field induction power to the point that the solution temperature was almost constant over the exposure time. In this case, we still observed the temperature increase inside the dual-core nanoparticles, confirming that the temperature gradient exists between the nano and bulk environment (Figure 4.14 on page 109). A similar comparison experiment was also carried out in an ice water bath (Figure 4.15 on page 110).

The specific absorption rate (SAR) of the iron oxide nanoparticles, calculated from the measured nanoparticle and solution temperature changes, is about 500 W/g under our experimental conditions (see Methods section on page 93). This value is in close agreement with experimental results and theoretical calculations previously reported for iron oxide

nanocrystals under similar magnetic field conditions [2, 3].

4.7 Summary

We have developed a method of measuring the interior temperature of dual-core silica nanoparticles based on the luminescence intensity ratios in the spectra of $NaYF_4$:Yb^{3+}, Er^{3+} nanocrystals and have quantified the nanoenvironment temperature change induced by the superparamagnetic nanocrystals. A novel synthetic approach was developed to incorporate two types of nanocrystals with a one-to-one ratio in the same mesoporous silica nanoparticle. The UCNC nanothermometer detected the MSN temperature changes initiated by the superparamagnetic nanocrystals. The nanoparticle interior temperatures were studied under variable OMF exposure times and induction powers and also with different magnetic nanocrystal sizes. The temperature increase is proportional to the magnetic field induction power and initially increases linearly with the exposure time. During the OMF exposure, a temperature gradient between the nanoparticles and the bulk solution was observed, and it increased over the exposure period. To our knowledge, this is the first study of ratiometric optical measurement of the nanoenvironment temperature with temporal resolution. This unique nanothermometer technique opens a path for experimental quantification of both the temperature in nanoenvironments and heat transfer on the nanoscale, and it provides a novel method for small-scale temperature characterization in biomedical hyperthermia applications.

4.8 Methods

4.8.1 Material

Cetyltrimethylammonium bromide (CTAB) (95%, Aldrich), tetraethyl orthosilicate (TEOS) (98%, Aldrich), hexane (98.5%, Fisher), 1-octadecene (95.0% Aldrich), toluene (99.5%, Aldrich), methanol (99.9%, Firsher), oleic acid (90%, Aldrich), yttrium(III) chloride (99.99%, Aldrich), ytterbium(III) chloride hexahydrate (99.9%, Aldrich), erbium(III) chloride hexahydrate (99.9%, Aldrich), chloroform (99.8%, Fisher), ethanol (99.5%, Fisher), ammonium fluoride (98.0%, Aldrich), and iron oxide(II, III) magnetic nanoparticles (Aldrich) were used. All chemicals were reagent grade and used without further purification or modification.

4.8.2 Characterization

Transmission electron microscopy (TEM) was carried out on a JEM1200-EX (JEOL) instrument. High-resolution transmission electron microscopy (HRTEM), scanning transmission electron microscopy (STEM), and energy disperse X-ray (EDX) analysis were performed using a Titan S/TEM (FEI, 300 kV). Powder X-ray diffraction (XRD) spectra were collected using a Philips XPert Pro diffractometer equipped with Cu K-α radiation. A TechnicaLaser MLL-III-980-2w laser emitting 2 W at 980 nm was utilized as the exciting source. An Instrument SA HR 320 spectrograph/monochromator together with a PI-MAX intensified CCD camera from Princeton Instruments was used to record the luminescence spectra. The oscillation magnetic field was provided by a Magnetic Hyperthermia System manufactured by MSI Automation, Inc. The five-turn coil diameter was 50 mm, and the depth was about

50 mm. The oscillating frequency was 375 kHz and the full induction power was 5 kW. A 700 nm cut-on filter from Newport (10SWF-700-B) was employed to filter out the exciting light at the detector window.

4.8.3 Synthesis of UCNC

The upconversion nanocrystals were synthesized by a modified thermolysis method using lanthanide chlorides as the precursors [33, 34]. A 156 mg amount of YCl_3, 70 mg of $YbCl_3$, and 8 mg of $ErCl_3$ were mixed with 15 mL of 1-octadecene and 12 mL of oleic acid and heated to 120 °C for half an hour. In a separate container, 100 mg of NaOH and 119 mg of NH_4F were dissolved in 10 mL of methanol. After the lanthanide solution was cooled to 50 °C , the NH_4F methanol solution was added into the lanthanide solution and slowly heated to 80 °C to remove the methanol. The mixed solution was then purged with argon gas and reacted at 300 °C for an hour. After the solution was cooled to room temperature, an excess amount of ethanol was added to precipitate the UCNCs. The nanocrystals were washed several times with hexane and ethanol and then suspended in chloroform at a concentration of 20 mg/mL.

4.8.4 Synthesis of UCNC@MS

The synthesis of upconversion nanocrystal embedded core-shell mesoporous silica nanoparticles (UCNC@MS) started with changing the hydrophobicity of the nanocrystals with the help of CTAB [24, 29]. A 2 mL amount of UCNC chloroform solution was added into 20 mL of H_2O containing 400 mg of CTAB. The solution was sonicated thoroughly and slowly heated to 65 °C to evaporate the chloroform. A 1.5 mL portion of this UCNC aqueous solution

was added into 13.5 mL of H_2O and heated to 80 °C . After the temperature was stabilized, 110 μL of 2 M NaOH and 150 μL of TEOS were added. The reaction was maintained at 80 °C for 2 h before further centrifugation and washing with H_2O and methanol.

4.8.5 Synthesis of UCNC:MNC5@MS

The incorporation of two types of nanocrystals into the MSNPs was based on stepwise phase transfers of the nanocrystals. UCNCs and the 5 nm MNCs were both suspended in chloroform at a concentration of 20 mg/mL prior to this experiment. A 2 mL sample of UCNC chloroform solution was added into 20 mL of H_2O containing 400 mg of CTAB. The mixture was sonicated thoroughly and slowly heated to 65 °C to evaporate the chloroform. A 1.5 mL amount of this solution was mixed with 18.8 μL of MNC chloroform solution. Again, it was sonicated thoroughly and slowly heated to 65 °C to evaporate the chloroform. This aqueous solution was stirred overnight and added into 13.5 mL of H_2O. From there, the reaction followed the same procedure as that for the UCNC@MS. A magnet was used to make sure all collected particles contain Fe_3O_4 nanocrystals.

4.8.6 Synthesis of UCNC:MNC20@MS

A similar experiment was carried out to that for UCNC:MNC5@MS to make the 20 nm MNC embedded MSNPs. Instead of adding the 5 nm MNC chloroform solutions, 37.5 μL of a 20 nm MNC chloroform solution was used. All other procedures were the same.

4.8.7 Synthesis of MNC20@MS

Similar to the synthesis of UCNC@MS, 37.5 μL of a 20 nm MNC solution was added into 15 mL of H_2O with 30 mg of CTAB and sonicated thoroughly. The chloroform was evaporated. The solution was heated to 80 °C and 110 μL of 2 M NaOH was added followed by 150 μL of TEOS. The reaction was continued for 2 h before further washing.

4.8.8 Working Curve

Upconversion luminescence spectra were collected to generate the working curve between temperature and peak intensity ratios. All samples were dispersed in toluene at a concentration of about 10 mg/mL and placed on a stir heater plate. The hot plate was turned on to heat the solution slowly while stirring, and the temperature was monitored by a K-Type thermocouple immersed in the solution. The whole setup was placed in front of the monochromator and the CCD camera. A 980 nm infrared laser was used as the exciting source. After the temperature reached a recording point, the laser was turned on briefly and a spectrum of the sample was collected. A luminescence background baseline was also collected under the same conditions when the excitation laser was off.

The luminescence spectra were analyzed to calculate the intensity ratios between the 520 and 540 nm emission peaks. After subtracting the baseline, the spectra were fitted by a multipeak fitting program with the peak positions fixed. An example of a peak fitting result is shown in Figure 4.6b. The reason for the peak fitting calculation instead of direct integration of peak areas is that the 520 and the 540 nm peak overlap around 535 nm. To distinguish the contribution from the two peaks in this area, the peak fitting procedure is

necessary. The fitted peak areas were then summed up, and the area ratios between the two peaks were calculated. For each sample, the ratios were plotted against the inverse of absolute temperature and then fitted with a linear function. The working curve graphs and luminescence spectra for UCNC, UCNC@MS, UCNC:MNC5@MS, and UCNC:MNC20@MS are illustrated in Figure 4.7.

4.8.9 *In Situ* Luminescence Detection Setup

The exciting beam (cross section is about 8 mm × 4 mm) was focused with an 80 cm focal length plano-convex lens. The coil of the magnetic hyperthermia system was placed horizontally in front of the CCD detector. A polystyrene foam frame was placed inside the coil to secure the sample and to prevent direct heat conduction. The nanoparticle sample was contained in a 2 mL glass vial placed in the polystyrene foam in the center of the coil. The emitted light was collected with a 10 cm focal length convex lens placed between the CCD detector and the coil. A 6 cm plano-convex lens was in front of the monochromator slit to focus the light. The coil was tilted about 30 °C from the axis that connected the CCD detector and the collecting lens, due to the position limitations. A 700 nm cut-on filter was placed in front of the CCD detector window to filter out the excitation light (Figure 4.16 on page 110). For the pure UCNC luminescence detection, the detector slit size was 0.5 μm and spectrum integration time is 0.5 s. For all other nanoparticles, a slit size of 1 μm and an integration time of 1 s were used. The CCD camera gain was set as zero for all experiments.

The sample was placed inside the current coil of a magnetic hyperthermia system to characterize the induced heating effect. A background spectrum without the excitation laser

was used for data processing. The IR laser was on for 1 s to record the luminescence spectra of the nanoparticles at the initial state. The OMF was turned on for a defined exposure time, and the luminescence spectra of the sample under the OMF influence were collected at regular intervals, depending on the experiment. The same multipeak fitting program used in generating the working curves was then applied to calculate the peak area ratios for the spectra, and the ratios were then converted to temperatures according to the working curve. The experiment was repeated three to five times to generate the experimental deviations. The induction power of the magnetic field was tunable on the magnetic hyperthermia system for the induction power dependent study.

4.8.10 Systematic Error Propagation

For UCNC, the linear equation correlating the temperature and the luminescence intensity ratio is: $Ln\frac{I_{520}}{I_{540}} = \frac{A - \Delta E}{kT}$, where $A = 2.00061 \pm 0.02834, B = 1009.02004 \pm 9.72607$.

For the intensity ratio part, the peak area calculations have a coefficient of determination (R^2) that is at least 0.99. Thus, the systematic error of the intensity ratio calculation is:

$$\because \delta(\frac{I_{520}}{I_{540}}) = 0.01(\frac{I_{520}}{I_{540}})$$

$$\therefore \delta(Ln\frac{I_{520}}{I_{540}}) = \sqrt{(\frac{\partial Ln\frac{I_{520}}{I_{540}}}{\partial\frac{I_{520}}{I_{540}}})^2 \times \delta(\frac{I_{520}}{I_{540}})^2} = \frac{\delta(\frac{I_{520}}{I_{540}})}{\frac{I_{520}}{I_{540}}} = 0.01$$

$$T = \frac{B}{A - Ln\frac{I_{520}}{I_{540}}}$$

$$\delta T = \sqrt{(\frac{\delta T}{\delta Ln\frac{I_{520}}{I_{540}}})^2 \delta(Ln\frac{I_{520}}{I_{540}})^2 + (\frac{\delta T}{\delta A})^2(\delta A)^2 + (\frac{\delta T}{\delta B})^2(\delta B)^2}$$

$$= \sqrt{(\frac{B}{(A - Ln\frac{I_{520}}{I_{540}})^2})^2 \delta(Ln\frac{I_{520}}{I_{540}})^2 + (\frac{B}{(A - Ln\frac{I_{520}}{I_{540}})^2})^2(\delta A)^2 + (\frac{1}{A - Ln\frac{I_{520}}{I_{540}}})^2(\delta B)^2}$$

$$= \sqrt{\frac{1}{A - Ln\frac{I_{520}}{I_{540}}}(\frac{B^2\delta(Ln\frac{I_{520}}{I_{540}})^2 + B^2(\delta A)^2}{(A - Ln\frac{I_{520}}{I_{540}})^2} + (\frac{\delta B}{B})^2 B^2)}$$

$$= \frac{B}{A - Ln\frac{I_{520}}{I_{540}}} \sqrt{\frac{\delta(Ln\frac{I_{520}}{I_{540}})^2 + (\delta A)^2}{(A - Ln\frac{I_{520}}{I_{540}})^2} + (\frac{\delta B}{B})^2}$$

$$\frac{\delta T}{T} = \sqrt{\frac{\delta(Ln\frac{I_{520}}{I_{540}})^2 + (\delta A)^2}{(A - Ln\frac{I_{520}}{I_{540}})^2} + (\frac{\delta B}{B})^2}$$

At 25 °C, $\frac{\delta T}{T} = 0.013$, the systematic error is about 1.3 %.

4.8.11 Detection sensitivity calculation

For UCNC:

$$Ln\frac{I_{520}}{I_{540}} = 1.87 - \frac{948}{T}$$

$$S = \frac{d(\frac{I_{520}}{I_{540}})}{dT} = \frac{I_{520}}{I_{540}} \times \frac{948}{T^2}$$

$$\because T = 298.15K, \frac{I_{520}}{I_{540}} = 0.270$$

$$\therefore S = 28.8 \times 10^{-4}/K$$

Similarly, the detection sensitivity for UCNC@MS under room temperature is 43.2 $\times$ 10^{-4}/K; UCNC:MNC5@MS: 28.7 $\times$ 10^{-4}/K; UCNC:MNC20@MS: 32.1 $\times$ 10^{-4}/K.

4.8.12 Specific absorption rate (SAR) calculation

In Figure 4.13 on page 108, during a 5 min OMF exposure, the bulk solution was heated by about 20 K and the nanoparticles were heated by 42 K. The particle concentration was 10 mg/ml. The field oscillating frequency was 375 kHz and the magnetic field strength was about 20 - 24 kA/m.

Heat absorbed by 1 ml toluene solution:

$$155.96\,J/(mol \cdot K) \times 1\,ml \times 0.87\,g/ml \times 20\,K/92.14\,g \cdot mol^{-1} = 29.45\,J$$

Hear absorbed by the silica nanoparticles (Ignore the heat capacity differences between silica and the nanocrystals, given their small volume fractions.):

$$0.703\,J/(g \cdot K) \times 10\,mg \times 42\,K = 0.2953\,J$$

Total heat absorbed:

$$29.452\,J + 0.2953\,J = 29.747\,J$$

Assuming the MNC radius is 10 nm, UCNC radius is 15 nm and the silica particle radius is 50 nm, and their densities are 5.17 g/cm^3, 4.21 g/cm^3 [38] and 2.05 g/cm^3, respectively.

Iron oxide weight percentage of the 10 mg assembled nanoparticles is: $5.17 \times 4\pi/3 \times 103/(5.17 \times 4\pi/3 \times 103 + 4.21 \times 4\pi/3 \times 153 + 2.05 \times 4\pi/3 \times (503 - 103 - 153)) = 1.94\%$

The specific absorption rate regarding to the iron oxide nanocrystal weight is:

$$29.747\,J/300\,s/(10\,mg \times 1.94\%) = 511\,W/g \approx 500\,W/g$$

4.8.13 Heating Center Distance Estimation

The heating center MNCs are encapsulated in MSNs. Assuming that the MNCs are located in the center of the silica nanoparticles and that all the silica nanoparticles are perfectly separated without any interconnection, the average distance between the MNCs would depend on the concentration of nanoparticles in the solution (10 mg/ml in this study). Average nanoparticle weight for UCNC:MNC20@MS:

$5.17\,g/cm^3 \times 4\pi/3 \times 103\,nm^3 + 4.21\,g/cm^3 \times 4\pi/3 \times 153\,nm^3 + 2.05\,g/cm^3 \times 4\pi/3 \times (503 - 103 - 153)\,nm^3) = 1.117 \times 10^{-15}\,g$

In 1 ml of particle solution, the number of dual-core nanoparticles is:

$$10\,mg/(1.117 \times 10^{-15}\,g) = 8.953 \times 10^{12}$$

Average volume occupied by a single nanoparticle is:

$$1\,ml/(8.953 \times 10^{12}) = 0.1172\,\mu m^3$$

Assuming the nanoparticles are in cubic structures next to another cubic with a nanoparticle inside it, then the average distance between particle centers is the length of these cubic edge:

$$(0.1172\,\mu m^3)^{1/3} = 0.489\,\mu m$$

Thus, the estimated average distance between heating centers are about 489 nm. However, there is a small portion of particles that have two MNCs embedded. The average distance between these heating centers would be about 10-20 nm. On the other hand, some nanoparticles may be interconnected with other nanoparticles, in which case, the heating MNCs would be separated by the two silica shells and the gap between silica surfaces, probably around 100 nm.

4.9 Figures and Tables

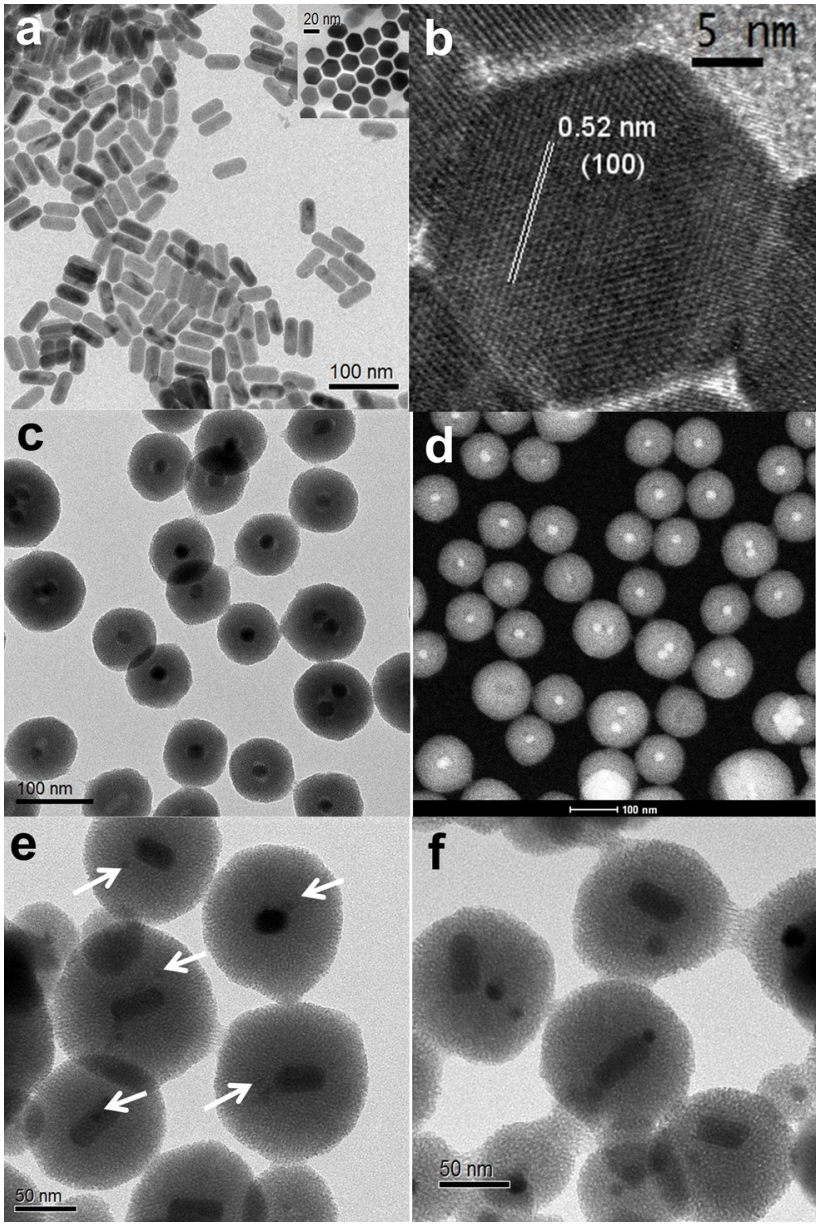

Figure 4.1 TEM, HRTEM, and STEM images of nanoparticles. (a) TEM image of UCNCs. The inset shows the hexagonal side of the nanocrystals. (b) HRTEM of UCNCs, confirming the hexagonal lattice structure. (c, d) TEM and STEM image of control group UCNC@MS. (e) TEM images of dual-core nanoparticles UCNC:MNC5@MS (arrows point to the MNCs). (f) TEM images of dual-core silica nanoparticles UCNC:MNC20@MS, with both the UCNCs and the 20 nm MNCs. Scale bars, 100 nm (a, c, d), 50 nm (e, f), 20 nm (a inset), 5 nm (b).

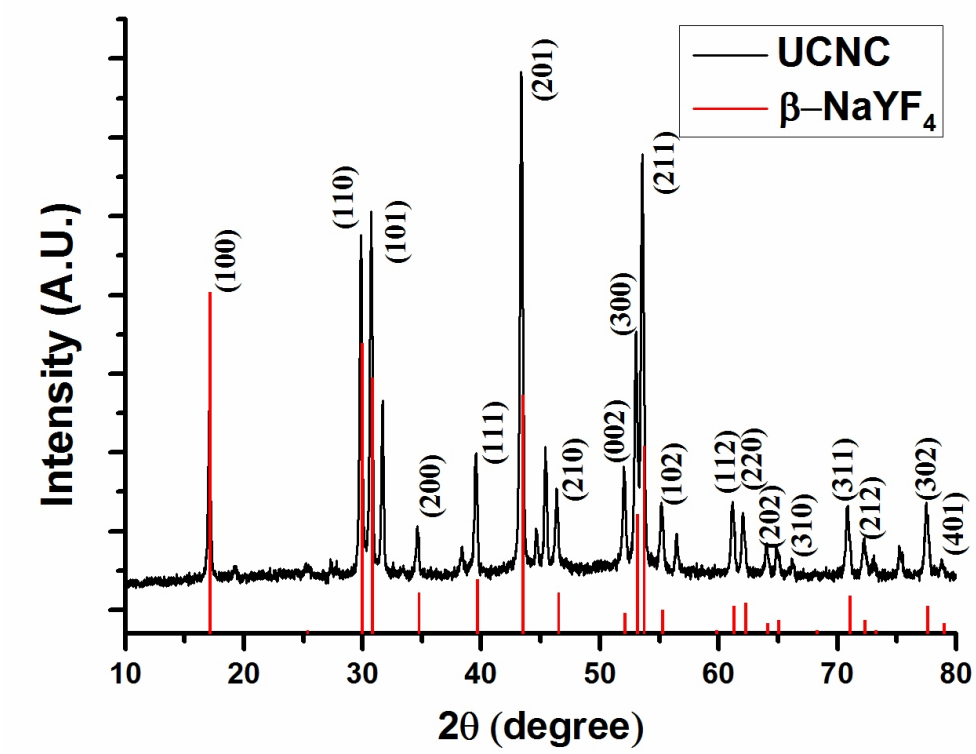

Figure 4.2 XRD pattern of the synthesized up-conversion nanocrystals (black curve) matches with that of the standard hexagonal $NaYF_4$ crystals (the red lines, JCPDs: 28-1192), confirming the lattice structure of the nanocrystals. The extra peaks belong to a small amount of YF_3 mixed in the matrix.

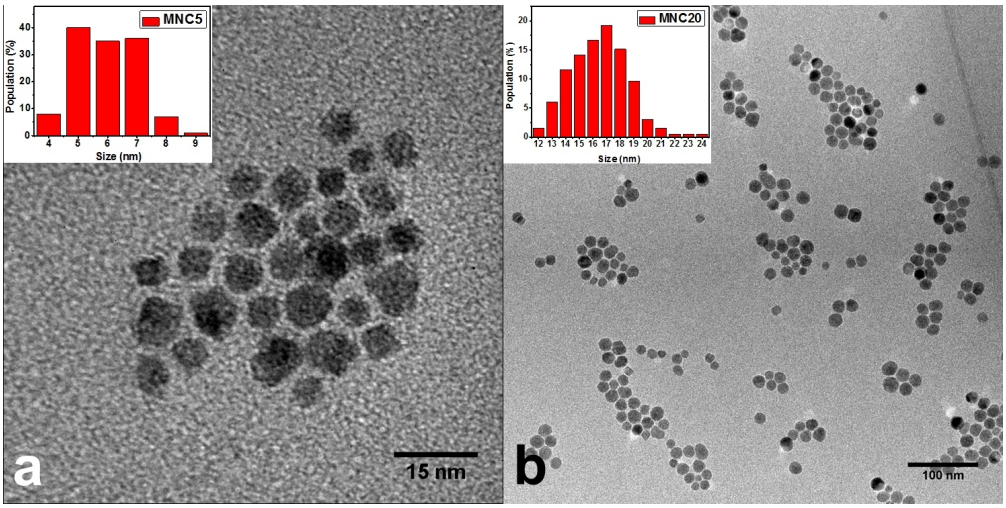

Figure 4.3 TEM images and size distribution analysis of MNCs. (a) Small MNCs denoted as MNC5 . (b) Large MNCs denoted as MNC20.

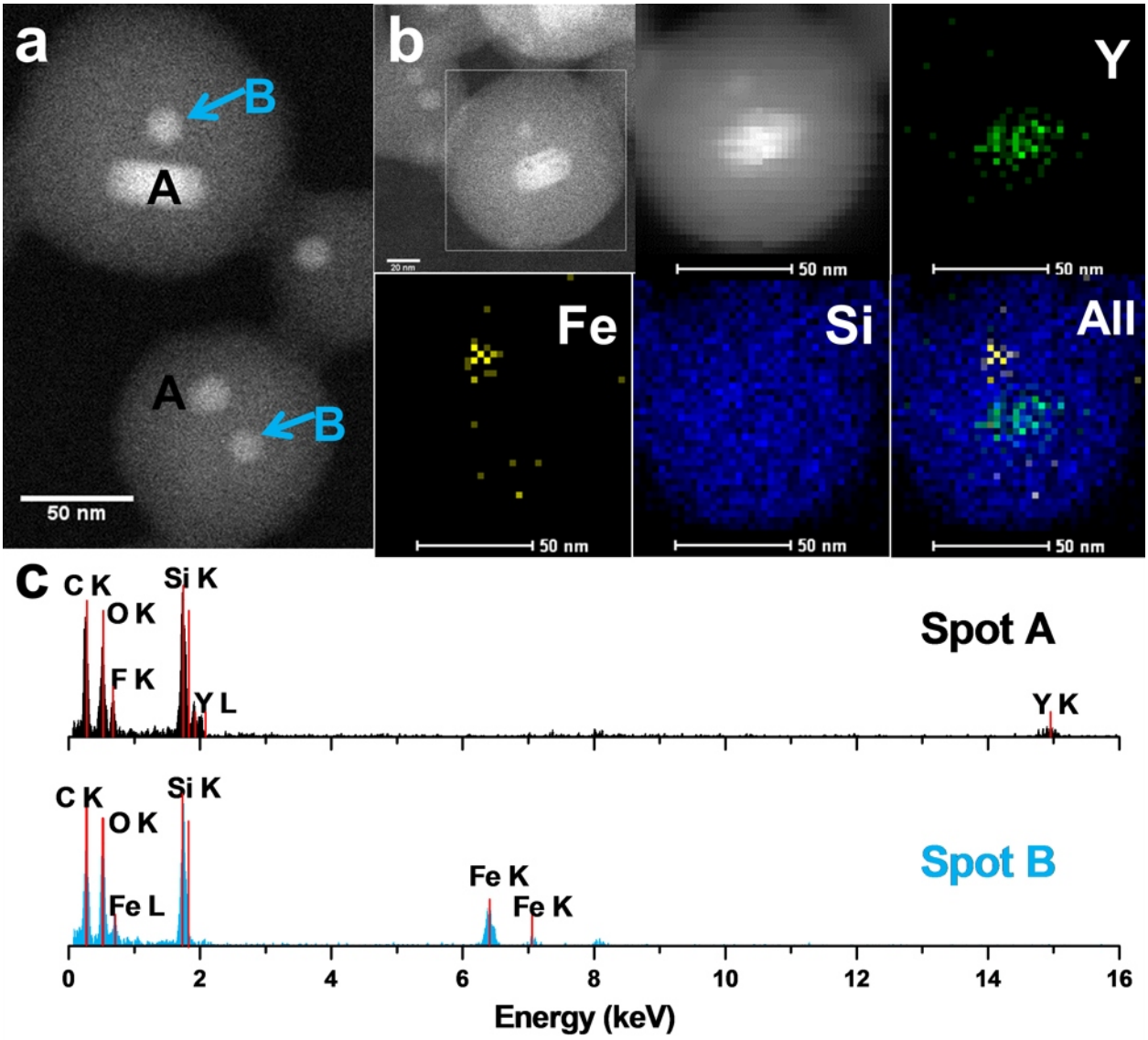

Figure 4.4 STEM image and elemental analysis of UCNC:MNC20@MS. (a) STEM image, scale bar: 50 nm. The spots A and B have different EDX spectra as shown in (c). (b) EDX element mappings of Y, Fe, and Si in the same nanoparticle and their merged picture. The first STEM image circles the detected particle (scale bar: 20 nm), and the second STEM image was obtained with an element mapping process (scale bar: 50 nm). (c) EDX spectra of spots A and B in (a), verifying that the two different types of nanocrystals are both embedded in the same MSNs.

Table 4.1 Statistical analysis result of the nanocrystal ratios between UCNCs and MNCs in the two samples and the average distance between the two types of nanocrystals. Analyses are based on about 150 UCNC:MNC5@MS nanoparticles and 230 UCNC:MNC20@MS nanoparticles.

Sample	Average distance between UCNC and MNC	Nanocrystal ratio (UCNC:MNC)			
		1:1	1:2	1:3 or more	MNC only
UCNC:MNC5@MS	8.0 ± 1.5 nm	67.77 %	10.74 %	9.09 %	12.40 %
UCNC:MNC20@MS	9 ± 2 nm	65.03 %	12.57 %	1.09 %	21.31 %

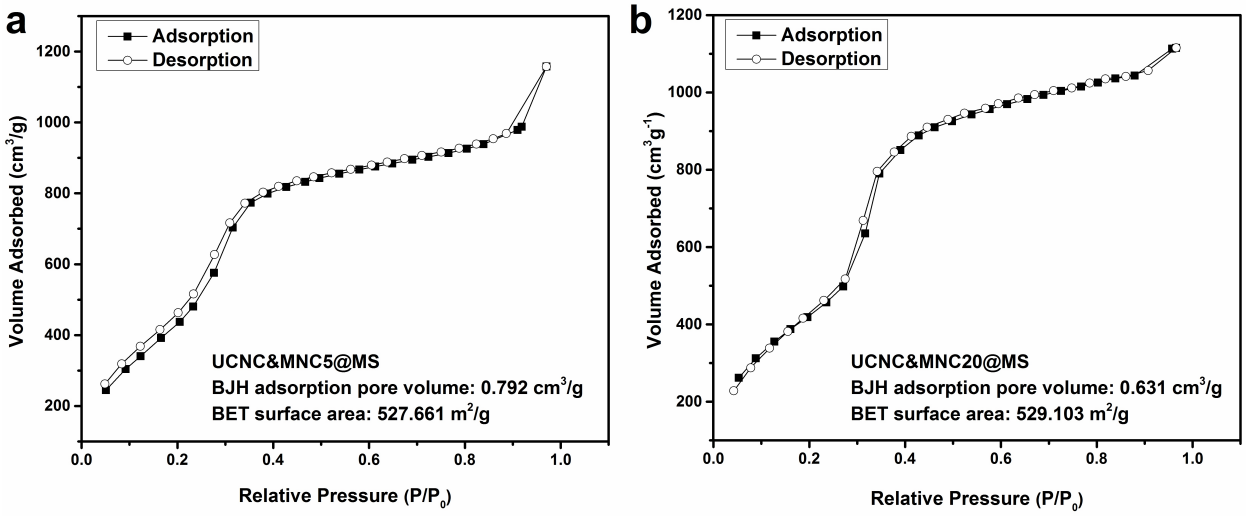

Figure 4.5 N_2 adsorption-desorption isotherms of the dual-core nanoparticles.

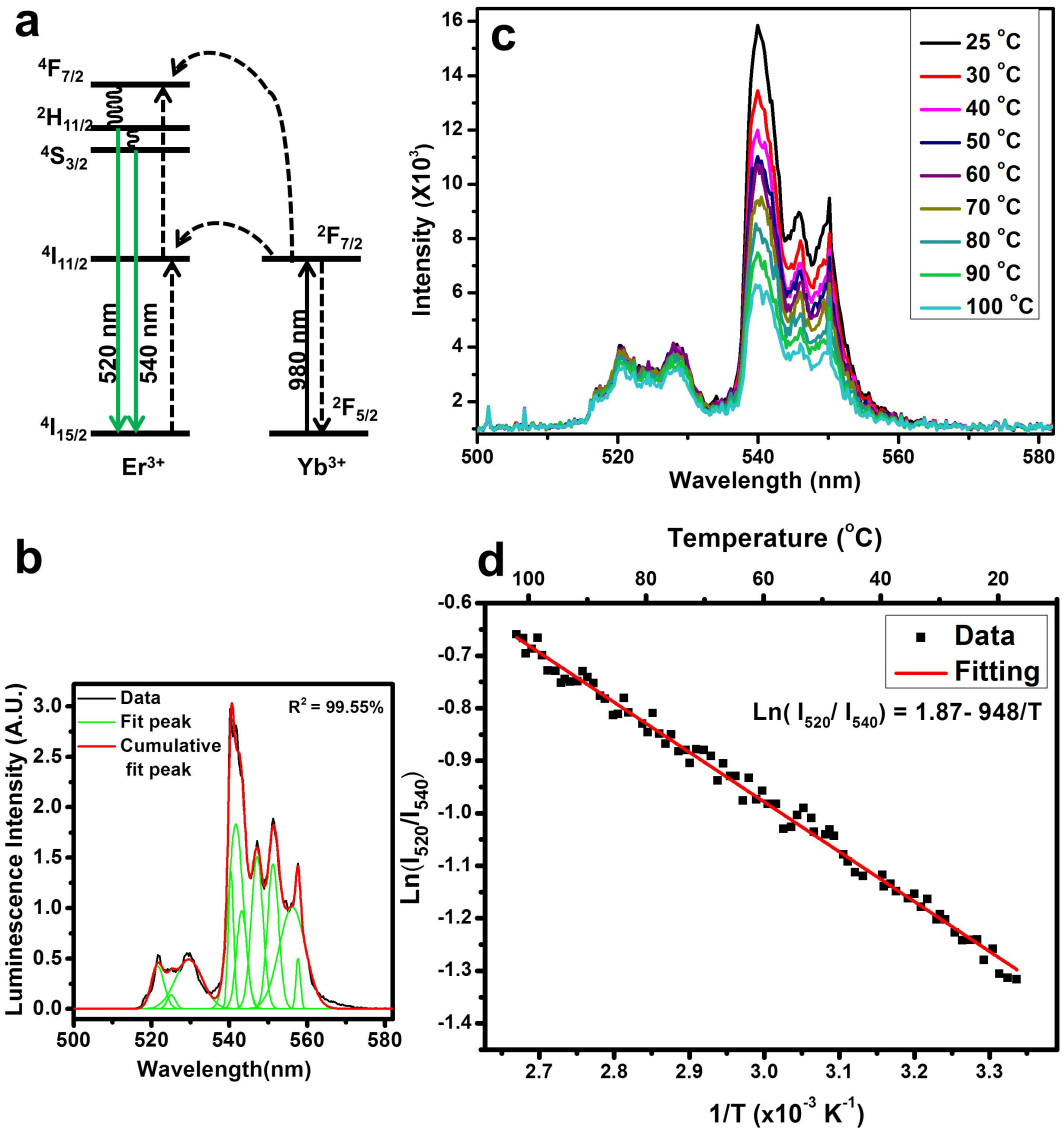

Figure 4.6 Upconversion luminescence mechanism and the temperature conversion working curve. (a) Illustration of the upconversion mechanism. The Yb^{3+} ions absorb the 980 nm photons and transfer the energy to the Er^{3+} ions. After two sequential energy transfers, the excited Er^{3+} ions relax to the thermally coupled states $^2H_{11/2}$ and $^4S_{3/2}$ (via nonradiative decays) and transit back to the ground state, corresponding to the green emissions centered at 520 and 540 nm.(b) Illustration of peak fitting process in calculating the emission band intensities. The black curve is the collected spectrum, the green curves are the fitting peaks, and the red curve is the sum of all fitting peaks. The coefficient of determination for this fitting is 99.55 %. (c) Emission spectra of UCNCs collected at different temperatures. (d) Linear working curve correlating the emission intensity ratios and the inverse temperatures for UCNC. As the temperature increases, the $^2H_{11/2}$ level gains more population, while the $^4S_{3/2}$ level loses population, resulting in the increase in emission intensity ratio.

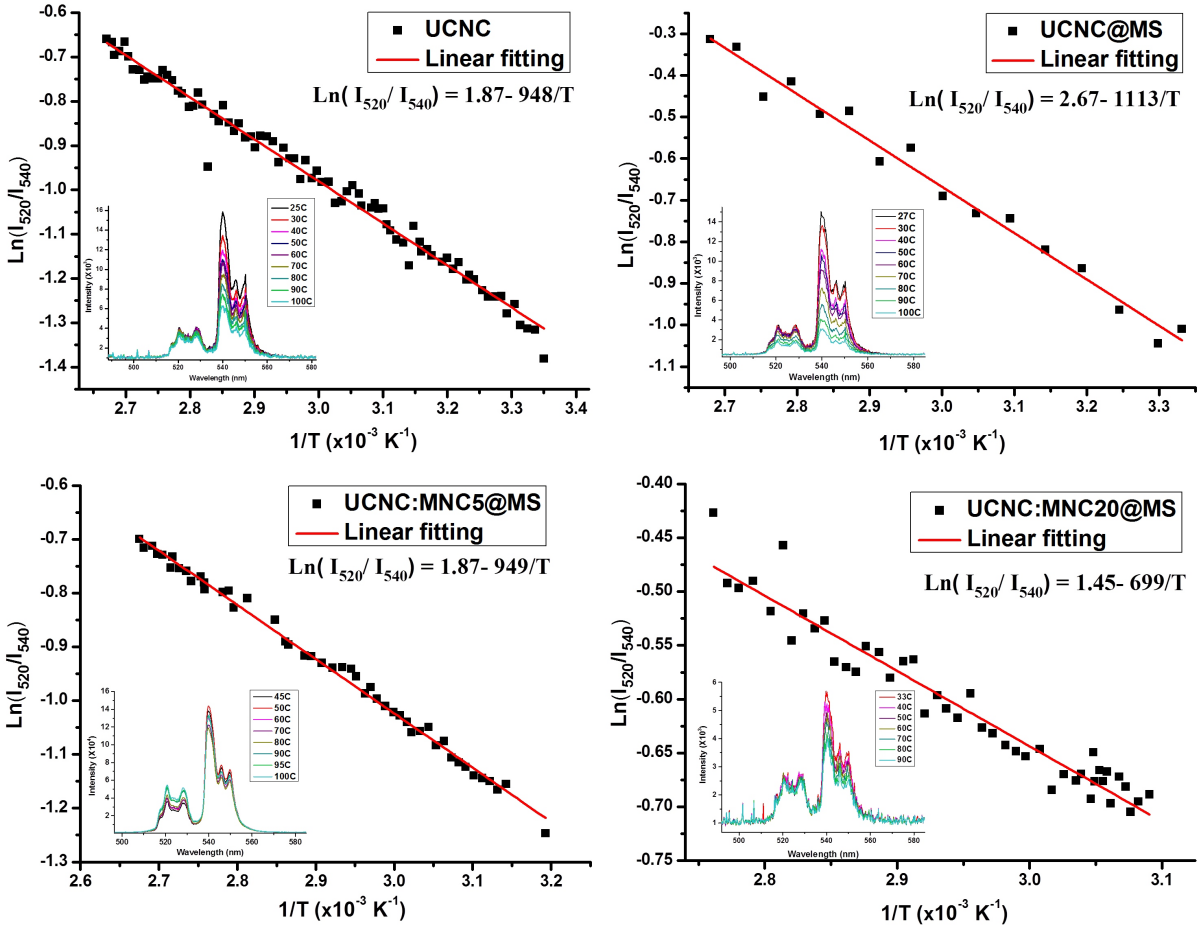

Figure 4.7 Intensity ratios between peak 520 and 540 nm are plotted versus the inverse of the temperature to generate linear working curves for sample UCNC (top left), UCNC@MS (top right), UCNC:MNC5@MS (bottom left) and UCNC:MNC20@MS (bottom right). Inset shows the luminescence spectra at different temperatures.

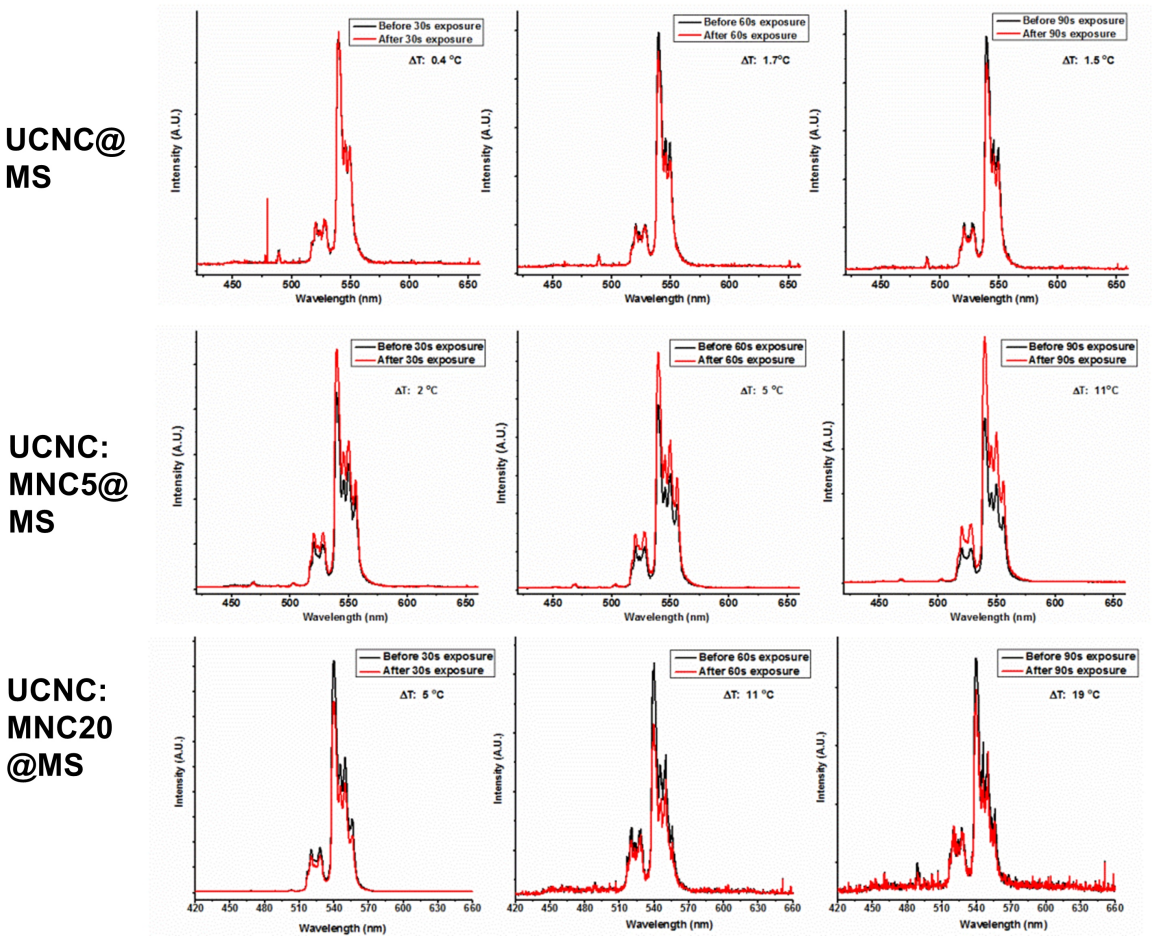

Figure 4.8 Luminescence spectra of samples before and after the OMF exposures. The three samples are UCNC@MS, UCNC:MNC5@MS, and UCNC:MNC20@MS. The exposure time is 30 s for the first column, 60 s for the second column and 90 s for the last column.

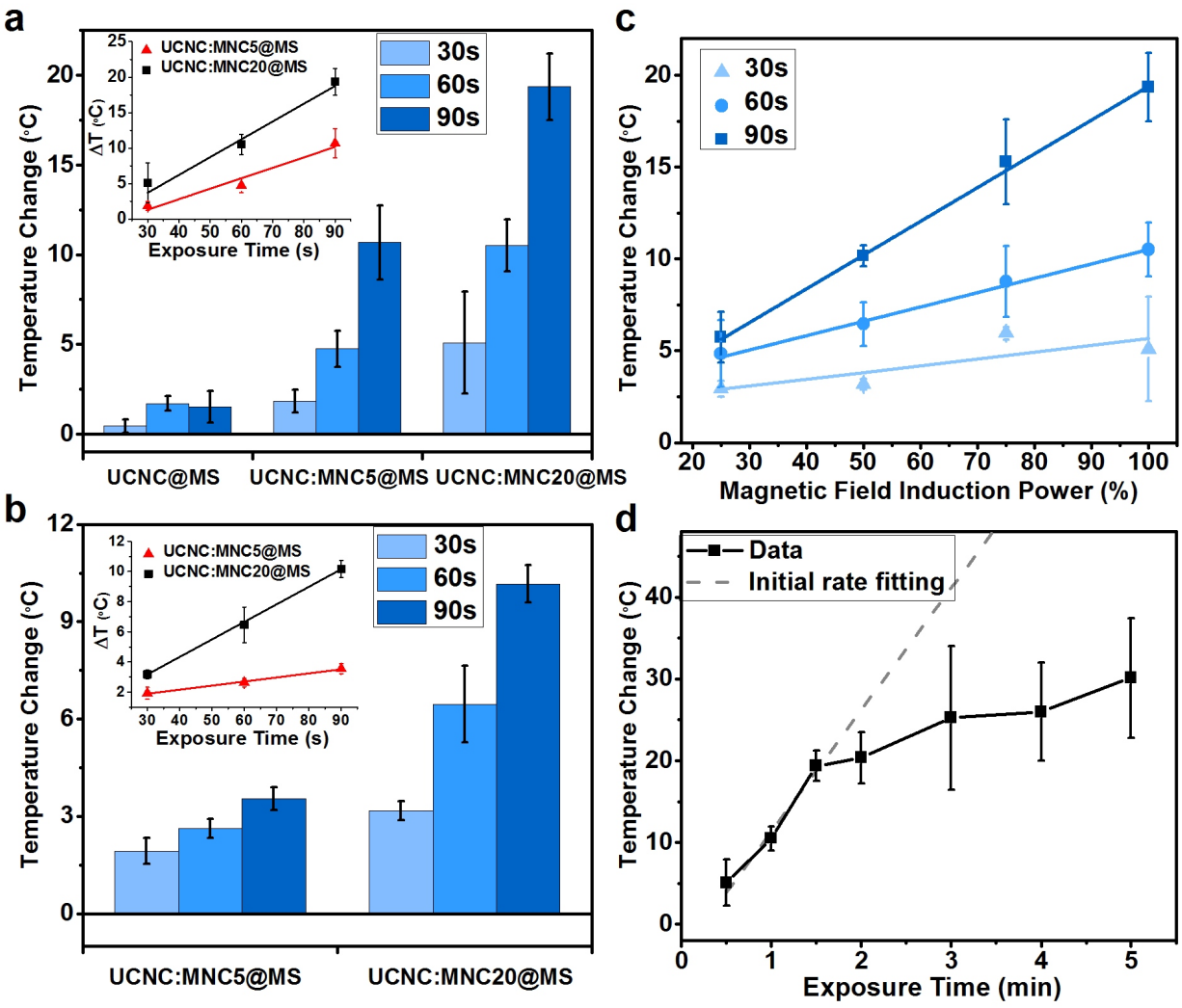

Figure 4.9 Nanoparticle temperature change under various experimental conditions. (a) Nanothermometer-detected temperature changes of UCNC@MS, UCNC:MNC5@MS and UCNC:MNC20@MS with a 30, 60, and 90 s OMF exposure. The UCNC:MNC20@MS experiences more heating than the UCNC:MNC5@MS. The control sample UCNC@MS shows neither a significant temperature increase nor an exposure time dependency. The inset shows the temperature change in response to the exposure time for UCNC:MNC5@MS (red triangles) and UCNC:MNC20@MS (black squares) and their linear fittings. A proportional increase is observed as the exposure time increases. (b) Parallel study to (a), when the magnetic field induction power is reduced to half. (c) UCNC:MNC20@MS temperature change under variable OMF induction power. The 30 s (light blue triangles), 60 s (blue dots), and 90 s (dark blue squares) indicate the exposure time. A linear dependency is present because the magnetic field induction power is proportional to the heat dissipation power of the nanocrystals. (d) UCNC:MNC20@MS heating effect as a function of OMF exposure time. The temperature increase is linearly related to the exposure time initially (gray dash line) and eventually saturates as the length approaches 5 min, as a result of the greater temperature gradient with the environment and the faster heat dissipation rate. Error bars are experimental standard deviations. See Methods section on page 93 for error propagation analysis.

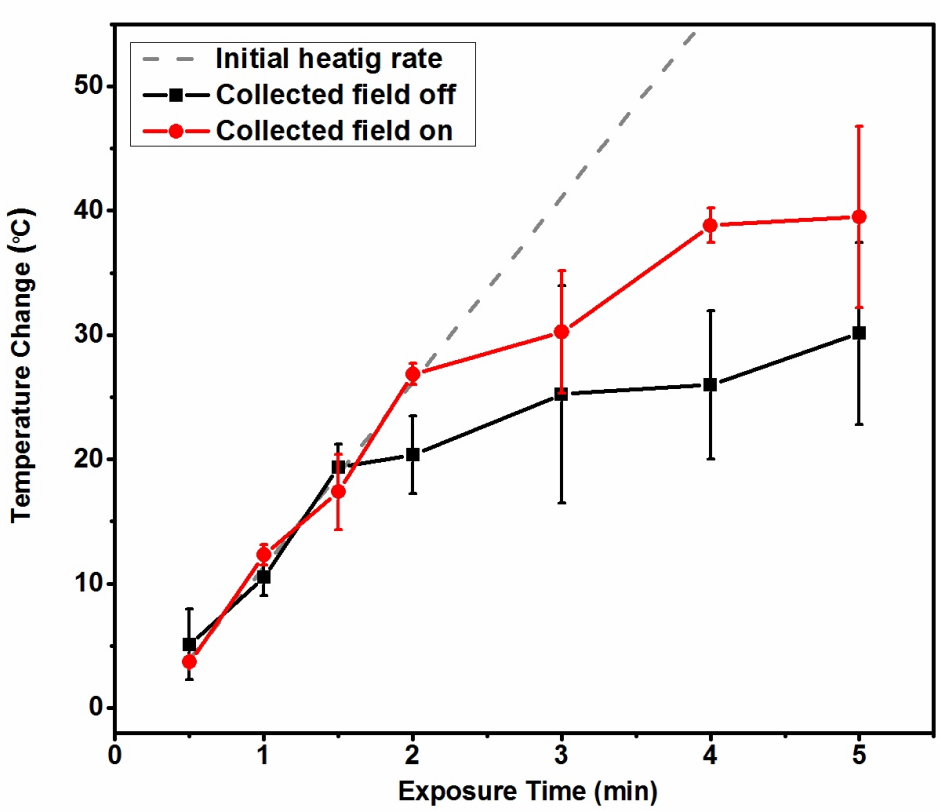

Figure 4.10 Nanoparticle heating effect as a function of oscillating magnetic field exposure time. The temperature increase is linearly related to the exposure time initially (grey dash line) and eventually saturates as the length approaches 5 min. The nanoparticle temperatures collected immediately after the field is off (black squares) are smaller than those of the points that are collected while the field is on (red dots), and the distinct difference grows as the exposure time lengthens, as a result of the faster heat dissipation rate.

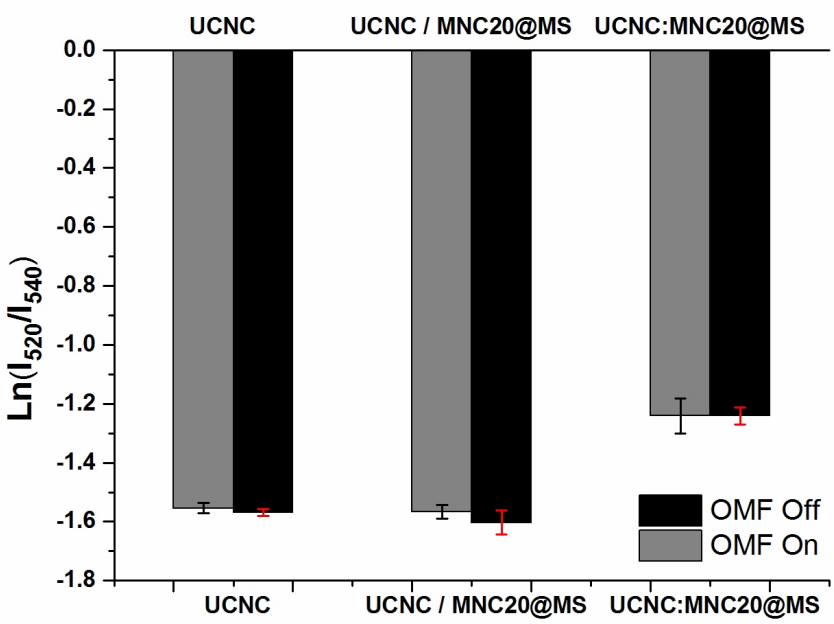

Figure 4.11 Experiment results confirm that the UCNC emission intensity ratios are not influenced by the OMF when no heating effect is placed, since the oscillating frequency (∼375 kHz) is several orders slower than the electron transitions. UCNC are nanocrystals without any silica coating. UCNC/ MNC20@MS have 20 nm magnetic nanocrystals embedded in MSNs and the MSNs are mixed with UCNC in the solution. UCNC:MNC20@MS are the dual-core MSNs that have both the UCNC and MNC embedded for nano temperature detection. OMF off: 10 spectra were collected every two minute for every sample. The laser was turned on for 1 s every time. The averages of emission intensity ratios were calculated together with the errors. OMF on: similar to the field off group, and the OMF was turned on briefly during the spectrum collection.

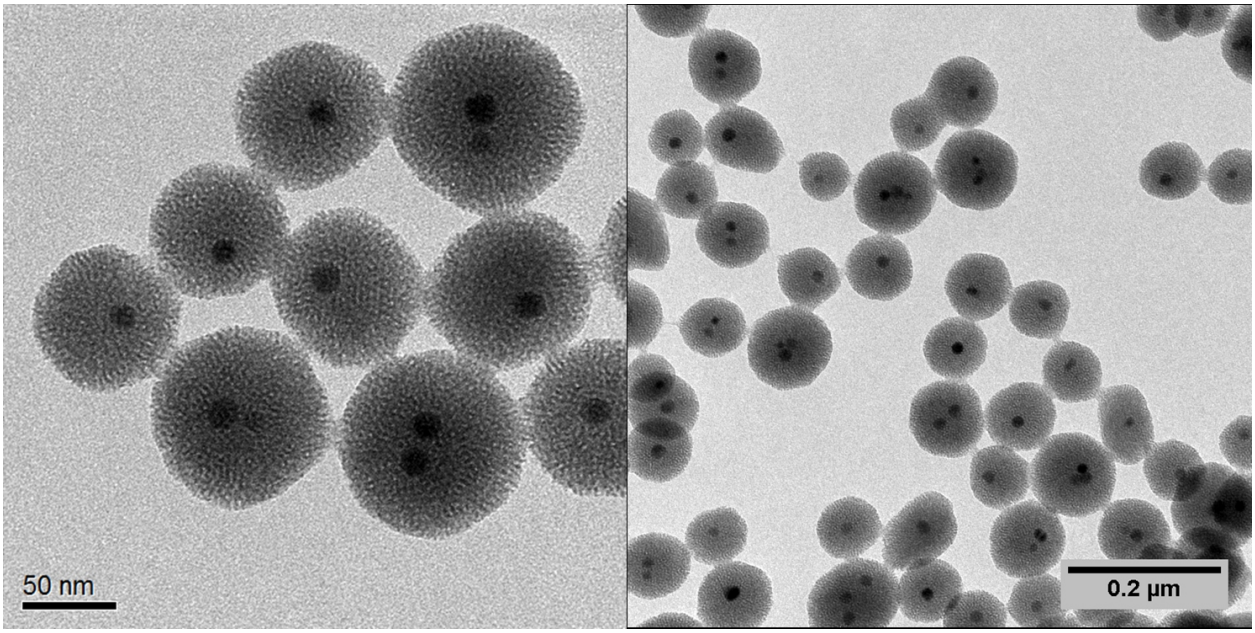

Figure 4.12 TEM images of MNC20@MS at different magnifications.

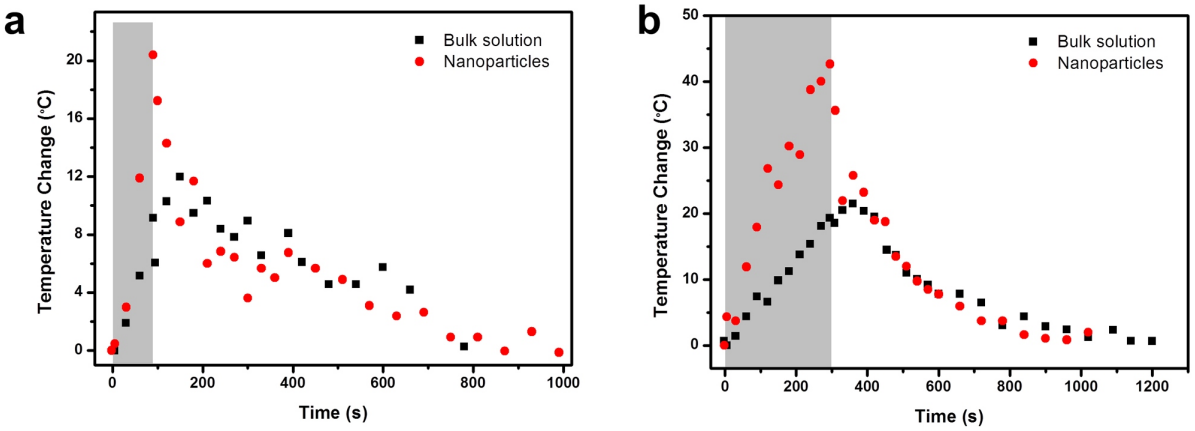

Figure 4.13 *In situ* nanoparticle temperature detection during and after exposure to the oscillating magnetic field. (a) Nanoparticle (red dots) and bulk solution (black squares) temperature changes during and after a 90 s OMF exposure. (b) Nanoparticle and bulk solution temperature changes during and after a 5 min OMF exposure. During the OMF exposure (gray area), the nanoparticle inside has a much higher heating rate than the bulk solution and the temperature gradient grows with time. At the end of the exposure, the nanoparticle temperature is about twice that of the solution. After the exposure, the nanoparticle temperature quickly decreases while the bulk solution slightly increased to equilibrate with the nanoparticles. Then the system gradually dissipates heat and recovers its initial state.

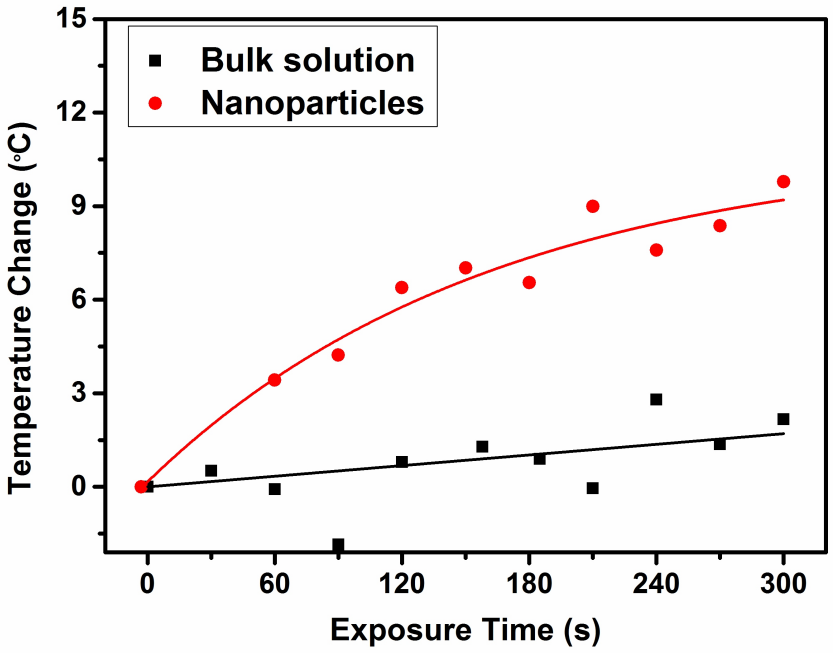

Figure 4.14 UCNC:MNC20@MS nanoparticle interior temperature compared with that of the solution during the exposure to the oscillating magnetic field. The solution temperature increases by about one degree over time while the nanoparticle interior was nine times larger, confirming the temperature gradient exists. The induction power of the field in this experiment was reduced to 25% of the maximum.

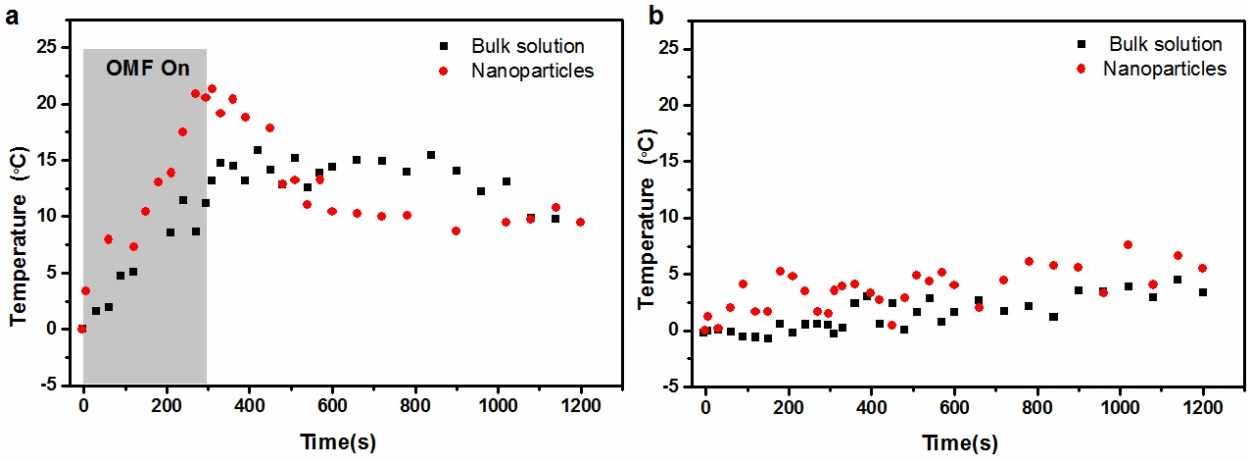

Figure 4.15 Temperatures of the nanoparticles and the bulk solution when placed in an ice bath. (a) Five minute OMF exposure. We observed much smaller temperature increases for both the nano and bulk environment, compared to when the system was in ambient air. The nanoparticles temperature still grew more than the bulk solutions, confirming the local heating effect. (b) Control group with no OMF applied. For both the nanoparticles and the solution, the temperature remained stable initially and slowly warmed up in the later stage. Thus, the heating effect in a origins from the nanoheaters in the MSNs. Due to the limitation of the experimental setup, the ice bath is rather small to sustain under the heating from the nanoheaters, that the solution temperature was raised too.

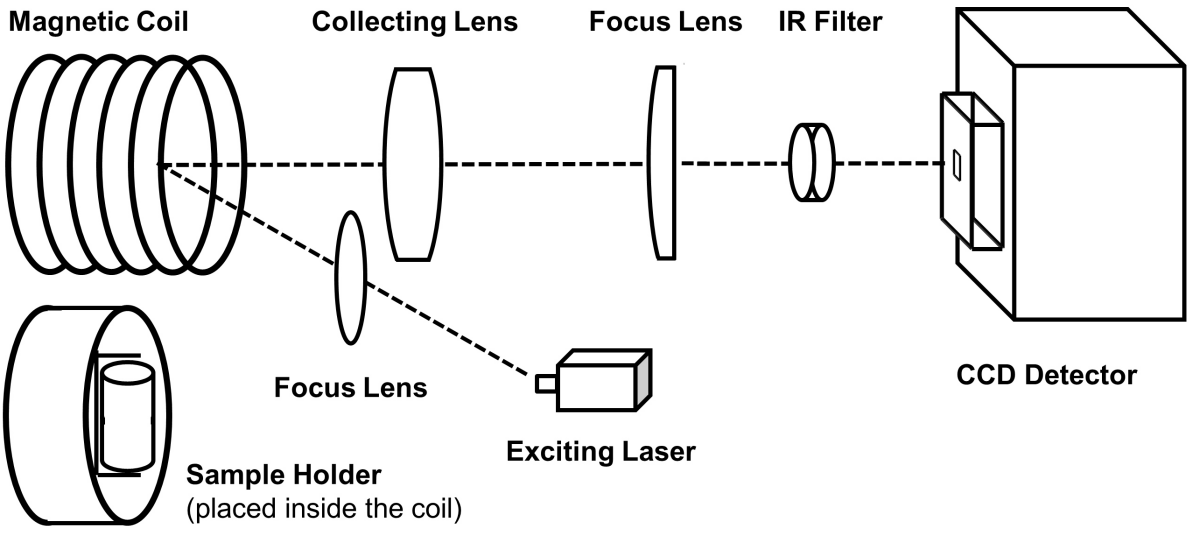

Figure 4.16 Illustration of the experimental setup for luminescence detection.

4.10 References

[1] R. E. Rosensweig. "Heating magnetic fluid with alternating magnetic field." *J. Magn. Magn. Mater.*, **252**(1-3):370–374, 2002.

[2] R. Hergt, S. Dutz, R. Mueller, and M. Zeisberger. "Magnetic particle hyperthermia: nanoparticle magnetism and materials development for cancer therapy." *J. Phys.-Condes. Matter*, **18**(38):S2919–S2934, 2006.

[3] M. L. Etheridge and J. C. Bischof. "Optimizing Magnetic Nanoparticle Based Thermal Therapies Within the Physical Limits of Heating." *Ann. Biomed. Eng.*, **41**(1):78–88, 2013.

[4] J. Kim, H. S. Kim, N. Lee, T. Kim, H. Kim, T. Yu, I. C. Song, W. K. Moon, and T. Hyeon. "Multifunctional Uniform Nanoparticles Composed of a Magnetite Nanocrystal Core and a Mesoporous Silica Shell for Magnetic Resonance and Fluorescence Imaging and for Drug Delivery." *Angew. Chem.-Int. Edit.*, **47**(44):8438–8441, 2008.

[5] A.-H. Lu, E. L. Salabas, and F. Schueth. "Magnetic nanoparticles: Synthesis, protection, functionalization, and application." *Angew. Chem.-Int. Edit.*, **46**(8):1222–1244, 2007.

[6] R. Hao, R. Xing, Z. Xu, Y. Hou, S. Gao, and S. Sun. "Synthesis, Functionalization, and Biomedical Applications of Multifunctional Magnetic Nanoparticles." *Adv. Mater.*, **22**(25):2729–2742, 2010.

[7] O. Veiseh, J. W. Gunn, and M. Zhang. "Design and fabrication of magnetic nanoparticles for targeted drug delivery and imaging." *Adv. Drug Deliv. Rev.*, **62**(3):284–304, 2010.

[8] R. T. Gordon, J. R. Hines, and D. Gordon. "Intracellular hyperthermia. A biophysical approach to cancer treatment via intracellular temperature and biophysical alterations." *Med. Hypotheses*, **5**(1):83–102, 1979.

[9] Y. Rabin. "Is intracellular hyperthermia superior to extracellular hyperthermia in the thermal sense?" *Int. J. Hyperthermia*, **18**(3):194–202, 2002.

[10] P. Keblinski, D. G. Cahill, A. Bodapati, C. R. Sullivan, and T. A. Taton. "Limits of localized heating by electromagnetically excited nanoparticles." *J. Appl. Phys.*, **100**(5):054305, 2006.

[11] S. A. Stanley, J. E. Gagner, S. Damanpour, M. Yoshida, J. S. Dordick, and J. M. Friedman. "Radio-Wave Heating of Iron Oxide Nanoparticles Can Regulate Plasma

Glucose in Mice." *Science*, **336**(6081):604–608, 2012.

[12] A. Riedinger, P. Guardia, A. Curcio, M. A. Garcia, R. Cingolani, L. Manna, and T. Pellegrino. "Subnanometer Local Temperature Probing and Remotely Controlled Drug Release Based on Azo-Functionalized Iron Oxide Nanoparticles." *Nano Lett.*, **13**(6): 2399–2406, 2013.

[13] K. Hamad-Schifferli, J. J. Schwartz, A. T. Santos, S. G. Zhang, and J. M. Jacobson. "Remote electronic control of DNA hybridization through inductive coupling to an attached metal nanocrystal antenna." *Nature*, **415**(6868):152–155, 2002.

[14] L. Polo-Corrales and C. Rinaldi. "Monitoring iron oxide nanoparticle surface temperature in an alternating magnetic field using thermoresponsive fluorescent polymers." *J. Appl. Phys.*, **111**(7):07B334, 2012.

[15] S. Freddi, L. Sironi, R. D'Antuono, D. Morone, A. Dona, E. Cabrini, L. D'Alfonso, M. Collini, P. Pallavicini, G. Baldi, et al. "A Molecular Thermometer for Nanoparticles for Optical Hyperthermia." *Nano Lett.*, **13**(5):2004–2010, 2013.

[16] H. Huang, S. Delikanli, H. Zeng, D. M. Ferkey, and A. Pralle. "Remote control of ion channels and neurons through magnetic-field heating of nanoparticles." *Nat. Nanotechnol.*, **5**(8):602–606, 2010.

[17] F. Ye, C. Wu, Y. Jin, Y.-H. Chan, X. Zhang, and D. T. Chiu. "Ratiometric Temperature Sensing with Semiconducting Polymer Dots." *J. Am. Chem. Soc.*, **133**(21):8146–8149, 2011.

[18] F. Vetrone, R. Naccache, A. Zamarron, A. Juarranz de la Fuente, F. Sanz-Rodriguez, L. Martinez Maestro, E. Martin Rodriguez, D. Jaque, J. Garcia Sole, and J. A. Capobianco. "Temperature Sensing Using Fluorescent Nanothermometers." *ACS Nano*, **4** (6):3254–3258, 2010.

[19] D. K. Chatterjee, M. K. Gnanasammandhan, and Y. Zhang. "Small Upconverting Fluorescent Nanoparticles for Biomedical Applications." *Small*, **6**(24):2781–2795, 2010.

[20] G. Wang, Q. Peng, and Y. Li. "Lanthanide-Doped Nanocrystals: Synthesis, Optical-Magnetic Properties, and Applications." *Accounts Chem. Res.*, **44**(5):322–332, 2011.

[21] S. A. Wade, S. F. Collins, and G. W. Baxter. "Fluorescence intensity ratio technique for optical fiber point temperature sensing." *J. Appl. Phys.*, **94**(8):4743–4756, 2003.

[22] H. Berthou and C. Jorgensen. "Optical-Fiber Temperature Sensor Based on

Upconversion-Excited Fluorescence." *Opt. Lett.*, **15**(19):1100–1102, 1990.

[23] N. Rakov and G. S. Maciel. "Three-photon upconversion and optical thermometry characterization of Er^{3+}:Yb^{3+} co-doped yttrium silicate powders." *Sens. Actuator B-Chem.*, **164**(1):96–100, 2012.

[24] M. Liong, J. Lu, M. Kovochich, T. Xia, S. G. Ruehm, A. E. Nel, F. Tamanoi, and J. I. Zink. "Multifunctional Inorganic Nanoparticles for Imaging, Targeting, and Drug Delivery." *ACS Nano*, **2**(5):889–896, 2008.

[25] Q. He, Z. Zhang, F. Gao, Y. Li, and J. Shi. "*In vivo* Biodistribution and Urinary Excretion of Mesoporous Silica Nanoparticles: Effects of Particle Size and PEGylation." *Small*, **7**(2):271–280, 2011.

[26] J. Dong, M. Xue, and J. I. Zink. "Functioning of nanovalves on polymer coated mesoporous silica Nanoparticles." *Nanoscale*, **5**(21):10300–10306, 2013.

[27] Y. Deng, Y. Cai, Z. Sun, J. Liu, C. Liu, J. Wei, W. Li, C. Liu, Y. Wang, and D. Zhao. "Multifunctional Mesoporous Composite Microspheres with Well-Designed Nanostructure: A Highly Integrated Catalyst System." *J. Am. Chem. Soc.*, **132**(24):8466–8473, 2010.

[28] R. M. Rioux, H. Song, J. D. Hoefelmeyer, P. Yang, and G. A. Somorjai. "High-surface-area catalyst design: Synthesis, characterization, and reaction studies of platinum nanoparticles in mesoporous SBA-15 silica." *J. Phys. Chem. B*, **109**(6):2192–2202, 2005.

[29] C. R. Thomas, D. P. Ferris, J.-H. Lee, E. Choi, M. H. Cho, E. S. Kim, J. F. Stoddart, J.-S. Shin, J. Cheon, and J. I. Zink. "Noninvasive Remote-Controlled Release of Drug Molecules *in Vitro* Using Magnetic Actuation of Mechanized Nanoparticles." *J. Am. Chem. Soc.*, **132**(31):10623–10625, 2010.

[30] Y.-S. Lin, S.-H. Wu, Y. Hung, Y.-H. Chou, C. Chang, M.-L. Lin, C.-P. Tsai, and C.-Y. Mou. "Multifunctional Composite Nanoparticles: Magnetic, Luminescent, and Mesoporous." *Chem. Mater.*, **18**(22):5170–5172, 2006.

[31] D. K. Yi, S. T. Selvan, S. S. Lee, G. C. Papaefthymiou, D. Kundaliya, and J. Y. Ying. "Silica-coated nanocomposites of magnetic nanoparticles and quantum dots." *J. Am. Chem. Soc.*, **127**(14):4990–4991, 2005.

[32] N. Insin, J. B. Tracy, H. Lee, J. P. Zimmer, R. M. Westervelt, and M. G. Bawendi. "Incorporation of iron oxide nanoplarticles and quantum dots into silica microspheres."

ACS Nano, **2**(2):197–202, 2008.

[33] C. Liu, H. Wang, X. Li, and D. Chen. "Monodisperse, size-tunable and highly efficient β-$NaYF_4$:Yb,Er(Tm) up-conversion luminescent nanospheres: controllable synthesis and their surface modifications." *J. Mater. Chem.*, **19**(21):3546–3553, 2009.

[34] Z. Li, Y. Zhang, and S. Jiang. "Multicolor Core/Shell-Structured Upconversion Fluorescent Nanoparticles." *Adv. Mater.*, **20**(24):4765–4769, 2008.

[35] W. T. Carnall, G. L. Goodman, K. Rajnak, and R. S. Rana. "A systematic analysis of the spectra of the lanthanides doped into single crystal LaF3." *J. Chem. Phys.*, **90**(7): 3443–3457, 1989.

[36] A. G. Skirtach, C. Dejugnat, D. Braun, A. S. Susha, A. L. Rogach, W. J. Parak, H. Mohwald, and G. B. Sukhorukov. "The role of metal nanoparticles in remote release of encapsulated materials." *Nano Lett.*, **5**(7):1371–1377, 2005.

[37] M. F. Bedard, D. Braun, G. B. Sukhorukov, and A. G. Skirtach. "Toward self-assembly of nanoparticles on polymeric microshells: Near-IR release and permeability." *ACS Nano*, **2**(9):1807–1816, 2008.

[38] L. Cheng, K. Yang, S. Zhang, M. Shao, S. Lee, and Z. Liu. "Highly-sensitive multiplexed *in vivo* imaging using pegylated upconversion nanoparticles." *Nano Res.*, **3**(10):722–732, 2010.

CHAPTER 5

Light or Heat?

- The Inefficiency of Photon Upconversion for Stimulating Drug Release by Functionalized Mesoporous Silica Nanoparticles

5.1 Abstract

To avoid the direct use of high-energy-photons, lanthanide doped nanocrystals have been studied to upconvert near infrared light into the visible or UV range for biomedical applications such as imaging, sensing and therapeutics. Despite the intensive effort, little attention has been paid to measuring and analyzing the substantial IR heating accompanying the limited photon generation. It is crucial to understand how much heat and light are produced in the upconversion process, and how each component contributes to the reaction mechanism. In this study, we quantify the nanoparticle interior temperature change induced by the IR irradiation, and focus on the photoisomerization reaction of azobenzenes in nanoimpellers as an example. The nanoimpeller function is evaluated under light and heat separately, and is compared with that of the upconversion nanocrystal embedded nanoimpellers. The re-

sults of an ice water bath experiment verify that the IR light optical heating is the primary element in triggering the cargo release. Our investigation prompts that the photothermal effect should be carefully evaluated in upconversion nanocrystal promoted photochemical reactions.

5.2 Introduction

Near-Infrared photon upconversion accomplished by lanthanide doped nanocrystals ($NaYF_4$: Yb^{3+}, Ln^{3+}) have been extensively studied for biological applications, including imaging, optical sensing, photodynamic therapy and drug delivery [1, 2, 3, 4, 5, 6]. The usage of the generated photons is fundamentally different in imaging as compared to the other applications. For imaging purposes, the high-energy-photons are directly collected by detectors and the technique benefits from the high photostability, low auto fluorescence, sharp contrast and deep tissue penetration for *in vivo* applications [1, 7, 8]. In contrast, in a different category of applications, the photons are re-absorbed by a photosensitive moiety to promote a photochemical reaction. In photodynamic therapies, this reaction involves the excitation of photosensitizers (such as zinc phthalocyanine, hypericin and Chlorin e6) to triplet excited states and subsequent energy transfer to generate singlet oxygen [9, 10, 11, 12, 13]. Other photoreactions include the photocleavage of o-nitrobenzyl ester or ether, (where the breaking of C-O bonds results in the release of molecules such as fluorescein, siRNA, D-luciferin and folic acid, [14, 15, 16, 17]) and in the collapse of polymer backbones [18]. Ring-open and ring-closing reactions of dithienylethene isomers can be triggered by the upconverted light too [19, 20]. In a more complicated system, the photoisomerization

of azobenzene was claimed to be stimulated by the upconversion process and released the contained cargo molecules from mesoporous silica nanoparticles (MSNs) [3]. Despite the variations between specific aims, all the photochemical reactions require sufficient photon generation by upconversion nanocrystals as well as efficient photon absorption by the reactive molecules.

A standard consideration in photochemistry is to determine whether a reaction is initiated via a photothermal or a photochemical pathway. This differentiation also applies to the photochemical process promoted by upconversion emission. However, most of the recent researches in the field did not evaluate the optical heating effect. Part of the reason is, although the heating effect could be studied relatively easily on the macroscopic scale, it is not so on a nano scale. The readily measured macro-environment temperature may not represent that of the nano-environment, as the internal generated heating could introduce thermal gradient between nanoparticles and bulk surroundings [5, 21]. In an effort to quantify the optical heating effect, we carry out both theoretical calculations and optical measurement. We employ two lanthanide upconversion nanocrystals that have different doping elements: one studies the nanocrystal temperatures as a luminescence nanothermometer (Er^{3+} doping) and the other generates blue and UV emissions to promote the photochemistry (Tm^{3+} doping). Thus the thermal and optical contribution of IR irradiations are distinguished. The reaction that we are focusing on in this chapter is the azobenzene conformational change for controlled drug delivery, because of our long-standing interest [22, 23, 24, 25, 26]. In this material, the azobenzenes are condensed in mesoporous silica nanoparticles, stretching out in the confined pores and blocking the cargo movement. Upon UV illumination, they

undergo reversible *trans-cis* photoisomerizations, which act as a large amplitude wagging motion forcing the cargo out of pores and achieving stimulus-controlled release [23, 25, 26]. Similar idea has been extended to upconversion nanocrystal stimulated drug delivery systems [3]. The fundamental question that needs to be answered when upconversion generates the higher energy photons that could stimulate the motion is: does the upconvert light or the heat that activates the nanoimpellers?

5.3 Theoretical Analysis

For lanthanide nanocrystal ($NaYF_4$:Yb^{3+}, Er^{3+} or Tm^{3+}) based photochemistry, the reaction involves the upconversion emission process and the re-absorption of high-energy photons by photolabile moieties, thus the efficiency is decided by both components.

5.3.1 Upconversion Photon Generation Efficiency

In regarding to the upconversion emission stage, lanthanide nanocrystals have intrinsic small extinction coefficients and low quantum yields. At 973 nm, the Yb molar extinction coefficient is 2.1 $cm^{-1}M^{-1}$ [27]. Assuming an irradiation power density of 4 W/cm^2 and the common doping composition (Yb = 18 mol.%, Ln = 2 mol.%), the number of IR photons being absorbed by a 25 nm upconversion nanocrystal is about 4400 /s, on the order of 1 hundred-thousandths (10^{-5}) of the total photons irradiated on the volume (see Methods section). Moreover, the absolute quantum yield of two-photon upconversion process was reported as 0.10 $\pm$ 0.05 % for a 30 nm $NaYF_4$:Yb^{3+}, Er^{3+} nanocrystal under 980 nm irradiation with a power density of 150 W/cm^2 [28]. For a UV or blue light activated photo-

chemical reaction, a three-photon upconversion process is required. We assume that under the 150 W/cm^2 illumination, the three-photon process has the same quantum yield as that of the two-photon process, which is unlikely but provides a conservative estimation for an upper limit. Under the commonly used power density for biological applications (1-10 W/cm^2) [3, 6, 9, 16, 20], the quantum yield upper limit is on the order of 10^{-8}, due to its nonlinear dependency on irradiation power densities. Even with a three- fold enhancement by an undoped $NaYF_4$ coating [28], the number of high-energy-photon generated by one nanocrystal is on the order 10^{-3} photons/s (see Methods section). In imaging applications, this low efficiency of photo generation is compensated by the use of a large number of nanocrystals (which is on the order of $10^{10}/\mu$g, see Methods section), such that a visible signal can be detected. In triggering the photochemical reactions, however, the small number of photons generated is outnumbered by large amount of photosensitive molecules and thus might not be able to induce the wagging motion of azobenzenes.

5.3.2 Photon Re-absorption Efficiency

Because the emitted photon wavelength is larger than the nanoparticle dimensions, the probability of an emitted photon being re-absorbed in the assemble is decided by the assemble dimension (d) in comparison with the mean free path of photons in the absorbing media (l). For the nanoimpeller particle system, the azobenzene co-condensed silica scaffold is the absorbing material. Using a simple model for calculation, l is related to the inverse of the product of the volume density of azobenzene molecules (n) and its absorption cross section (σ) following the equation $l = (\sigma n)^{-1}$. The former can be derived from the azobenzene

weight percentage measured by thermogravimetric analysis (TGA), and is usually on the order of 10 wt.%. The later can be calculated from the extinction coefficient, which is reported as 88 - 536 cm^{-1} M^{-1} in the range of 385 - 450 nm [30]. The calculated value of l is 66 μm (see Methods section), which is much smaller than the macroscopic dimension d (0.2 - 0.5 cm), and thus the transmission ($T = e^{-d/l}$) is almost 0. Hence, almost all of the emitted photons could be re-absorbed by azobenzenes, which would result in decreased emission of upconversion signals when the nanocrystals are embedded in the azobenzene matrix, as observed in previous studies [3]. However, the analysis also showed that in every silica nanoparticle, there are about 10^4 azobenzene molecules, and the blue photon emission rate from a single upconversion crystal is about 1×10^{-3}/s. It is debatable whether the limited upconversion photons could effectively stimulate the photoisomerization reaction of multiple azobenzenes in the pores.

On the other hand, the small quantum yield in the upconversion process, is accompanied with substantial optical heating generation inside the particles as the majority of the photons absorbed by Yb^{3+} ions are converted into non-radiative decays. Depending on the irradiation power density, for every emitted blue photon, there are at least another 10^6 IR photons being absorbed (see Methods section). Moreover, in the context of biological applications, the water media surrounding the upconversion nanocrystals will also be heated by the IR irradiation. The absorption coefficient of water at 980 nm is 0.482 cm^{-1}, almost 4 orders of magnitude greater than at 403 nm ($5.59 \times 10^{-4} cm^{-1}$)[31, 32]. For an 1 cm long pathway, 35 % of the 980 nm photons will be absorbed by water, while only 0.056 % of the 403 nm photons will be absorbed. Therefore, the heat generation and its contribution to the reaction

mechanism needs to be carefully quantified and evaluated, as we carry out the experimental examination.

5.4 Nanoparticle Optical Heating Measurement

The collective heating effect of upconversion nanocrystals in the nanoenvironment is measured based on the temperature dependent emission spectra of $NaYF_4$: Yb^{3+}, Er^{3+} (ErNCs) [5, 33, 34]. The nanocrystal has great similarity to most of the upconversion nanocrystals used for photochemical reactions and provides the convenience of absolute temperature sensing. The hexagonal phase nanocrystals were synthesized by a modified thermolysis procedure (doping ratio: Y : Yb : Er = 0.08 :0.18 :0.02) and transferred into water solutions with the help of surfactants (Figure 5.1a) [5, 35]. Following a templated sol-gel reaction, the homogeneous nanocrystals were embedded into the mesoporous silica framework forming the core-shell structures (ErNC@MSNs, Figure 5.1b, c) [5, 24]. Under the 980 nm excitation, the Yb^{3+} ions absorb the photons and sequentially transfer the energy to Er^{3+}, which subsequently emit from two thermally coupled excited states:$^2H_{11/2}$ and $^4S_{3/2}$. The relative populations of these two excited states follow the Boltzmann distribution [5, 33, 34]. Thus, the corresponding emission intensity ratios are correlated to the absolute temperature, following the equation:

$$Ln\frac{I_{520}}{I_{540}} = \frac{A - \Delta E}{kT}$$

I_{520} and I_{540} stand for the luminescence peak intensity at 520 nm and 540 nm respectively; A is a constant; ΔE is the energy gap between the two excited states; k is the Boltzmann constant and T is the absolute temperature. To generate the linear working curve, the lumi-

nescence spectra of the ErNC@MSNs under various temperatures were collected (Figure 5.1d, the inset), and the intensity ratios between peak 520 and 540 nm were plotted versus the inverse of temperature (Figure 5.1d). To measure the nanoparticle interior temperature, the particles were submerged in $\sim$ 3 - 4 mL of water in the cuvette with a weight ratio of 1 mg/g between the particles and the water. The emission spectra of ErNC@MSNs were collected continuously during the IR irradiation. As shown in Figure 5.1e inset, the visible emission intensity ratio between the 520 nm and 540 nm peak decreases. The nanoparticle temperature initially increases dramatically and gradually equilibrates with the bulk water temperature around 45 °C (Figure 5.1e). An overall of 25 °C temperature rise inside the nanoparticles is achieved within 15 min of 980 nm irradiation with a power density of 4 W/cm^2. The absolute value of temperature increase could be variable in different experimental setups, but the substantial optical heating by IR illumination is inevitable as shown by experimental results as well as the theoretically calculations.

5.5 Contribution of Optical Heating for Nanoimpeller Functioning

Because the IR heating is significant, experiments were conducted to distinguish the light and the heat contributions of IR irradiations, by examining the cargo release performance of azobenzene co-condensed MSNs with and without $NaYF_4$:Yb^{3+}, Tm^{3+} (TmNC) encapsulated. The former particles are denoted as TmNC@IP-MSNs (Figure 5.2c) and are susceptible to both the optical and thermal influence of IR irradiations. The latter are nanoimpellers which do not absorb the 980 nm photons (Figure 5.2b). In comparison with the ErNCs used in the temperature detection, the TmNCs have similar morphology and

crystal structures (Figure 5.2a), and Yb^{3+} serve as the 980 nm photon absorbing element in both cases. Thus, the optical heating measured by ErNCs is applicable to TmNCs.

The TmNCs were synthesized by a similar thermolysis procedure and the Tm doping was chosen to accommodate the azobenzene absorption band. To form nanoimpellers, 4-hydroxyazobenzene was co-condensed with silica precursors through an isocyanate linker molecule [23, 25]. TmNCs were introduced in the co-condensation reaction to synthesis the core-shell TmNC@IP-MSNs. TGA and Fourier transform infrared spectroscopy (FTIR) were performed to confirm the azobenzene modifications (Figure 5.6 on page 144 and Figure 5.7 on page 145).

5.5.1 Upconversion Nanocrystal Embedded Nanoimpellers

The functioning of upconversion nanocrystal-embedded nanoimpellers is verified under UV and IR irradiation. The particles were loaded with a cargo of fluorescent propidium iodide, washed thoroughly, placed in the corner of a cuvette and immersed in water, with a weight ratio of 1 mg/g between particles and water. The supernatant fluorescence intensity was recorded continuously to monitor the concentration of propidium iodide that is impelled from the MSNs. Before applying the stimulating light, the different intensity is negligible and stable, indicating that propidium iodide is trapped in the azobenzene-modified pores. Upon laser irradiation of the particles at 403 nm, the fluorescence intensity increases gradually, showing that the light triggers the azobenzene photoisomerization, forcing the propidium iodide molecules out of the nanopores and increasing its concentration in solution (Figure 5.3a). To calibrate the absolute release amount, a UV-vis absorption spectrum of the

supernatant solution was collected at the end and the release amount was calculated using Beer's law. In the second experiment, the 980 nm laser was turned on and off alternatively as the stimulating source, and was able to manipulate the cargo release correspondingly (Figure 5.3b). The TmNC@IP-MSNs particles seemed to respond similarly to the 980 nm and to the 403 nm irradiation. Release amounts are normalized to the 403 nm activated system.

5.5.2 Nanoimpeller Functioning Under Different Stimulations

For the nanoimpeller particles without the upconversion nanocrystals, three activation methods - the 403 nm irradiation, the direct solution heating and the 980 nm irradiation - were applied to examine their release functioning. The UV light initiates the cargo release due to the direct activation of azobenzene photoisomerizations (Figure 5.4a). Since the continuous IR irradiation raises the particle internal temperature to about 45 °C, bulk heating was performed to examine its influence on nanoimpellers. Surprisingly, similar cargo release feature is observed after the solution temperature reaches 45 °C (Figure 5.4b). The underlying mechanism, however, does not involve the isomerization reaction since the heating energy is much lower than the activation barrier for double bond rotations. The elevated temperature raises both the vibrational energy of azobenzenes and the kinetic energy of cargos, and reduces the nanoparticles viscosity. The azobenzenes render as a less rigid steric barrier to the propidium iodides. Driven by the concentration gradient, cargoes diffuse out of the particles, presenting a "release" profile.

We further verify our hypothesis by an IR activation experiment with nanoimpellers.

Since heating was able to trigger the cargo "release" and the IR irradiation increased the particle temperature substantially, whether the IR light optical heating could disturb the nanoimpeller function would distinguish the contribution from heat to light. The IR laser on-and-off experiment was repeated with the pure nanoimpellers. Interestingly, similar results were obtained as that of the TmNC embedded particles (Figure 5.4c). Because the upconversion nanocrystals were not introduced and the incident laser power density was too small to promote the two-photon cross-section of azobenzene moieties, the observed release is not driven by the 980 nm photons, but by the optical heating.

5.5.3 Ice Water Bath Cargo Release

In order to eliminate the substantial direct IR optical heating and to focus on its photon contribution, an ice water bath experiment was performed where the release was carried out by placing the cuvette in a 2 L ice water bath, keeping the other parameters the same. Unlike the results in the ambient air environment, both the pure nanoimpellers (Figure 5.5a) and the nanocrystal encapsulated nanoimpellers (Figure 5.5b) only response to the 403 nm laser activation, not to the 980 nm light. In the cold environment, the optical heating effect of 980 nm laser was effectively suppressed. The upconversion nanocrystals in the TmNC@IP-MSNs were not able to generated sufficient high-energy-photons to initiate the photoisomerization of azobenzenes, showing a unchanged release profile as that of the particles without upconversion nanocrystals.

The experimental results agree with the numerical calculations. Even if all the upconverted photons were be absorbed by the azobenzene molecules, the photon number is too

small to excite enough azobenzene molecules to function as impellers. If we take the isomerization reaction quantum yield into account, which is ranging from 0.1 to 0.5 at different wavelength, an even less efficient process results. At the same time, substantial heat is generated due to the large radiationless deactivation of Y and high water absorption. The IR irradiation triggers cargo release from the azobenzene modified silica particles via the photothermal pathway, not the photochemistry. Thus, the photochemistry application of upconversion process requires detailed evaluation of the accompanied thermal effect to fully understand the reaction mechanisms.

We, however, do not intend to withhold the idea of using upconversion nanocrystals for photochemical applications in biomedicine. We investigated one example among the numerous reactions, and given the results, we want to raise the attention in the field. Besides the system we have employed here, recent works on enhancing the upconversion quantum yield with structural and morphology optimizations has lightened the path [36, 37]. The sublattice crystal structure change effectively minimized the energy transfer from the excited states to defects and enabled a much higher Yb^{3+} doping amount. Also, efforts on using Förster resonance energy transfer (FRET) could also improve the energy transfer efficiency by eliminating restrictions of Er^{3+} ion emission efficiency [13, 38, 39, 40]. Different from the emission and re-absorption process, in FRET, the energy is transferred between two dipoles though the space without any photons involved. With all the extensive efforts in the field, the method will have a broader and stronger impact in the future.

5.6 Summary

In summary, an optical nanothermometer ($NaYF_4$:Yb^{3+}, Er^{3+}) embedded MSN system is designed to investigate the optical heating contribution in a light-activated nano delivery system. The nanoparticle internal temperature shows a 25 °C increase within 15 min of 980 nm laser irradiation. The pure nanoimpeller particles response to both the direct heating and the IR irradiation, exhibiting a similar "cargo release" feature in fluorescence intensity spectra as when they are under the UV illumination. Although the IR light is able to trigger the release from the upconversion nanocrystal embedded nanoimpellers, the effect is not repeated in an ice water bath environment. Both numerical calculations and experimental results indicate that the upconversion nanocrystals could not generate sufficient photons to initiate the azobenzene photoisomerization. The results suggest that the IR optical heating, rather than the upconversion, is responsible for the cargo release in nanoimpellers. Future work in using lanthanide upconversion for photochemical applications should carefully evaluate the photothermal effect and its contribution to the nanostructure performances.

5.7 Methods

5.7.1 Material

Yttrium(III) chloride (99.99 %, Aldrich), ytterbium(III) chloride hexahydrate (99.9 %, Aldrich), erbium(III) chloride hexahydrate (99.9 %, Aldrich), thulium chloride hexahydrate (99.99 %, Aldrich), oleic acid (90%, Sigma-Aldrich), 1-octadecene (95.0 % Aldrich), ammonium fluoride (98.0 %, Sigma-Aldrich), sodium hydroxide (97.0 %, Fisher), 4-phenylazophenol

(98 %, Sigma-Aldrich), 3-(triethoxysilyl)propyl isocyanate (95 % Aldrich), cetyltrimethylammonium bromide (CTAB) (95 %, Sigma-Aldrich), tetraethyl orthosilicate (TEOS) (98 %, Aldrich), hexane (98.5 %, Fisher), toluene (99.5 %, Sigma-Aldrich), methanol (99.9 %, Firsher), chloroform (99.8 %, Fisher) and ethanol (99.5 %, Fisher) were used. All chemicals are reagent grade and used without further purification or modification.

5.7.2 Characterization

Transmission electron microscopy (TEM) was carried out on a JEM1200-EX (JEOL) and a T12 Quick CryoEM and CryoET (FEI) instrument. Scanning transmission electron microscopy (STEM) and high resolution transmission electron microscopy (HRTEM), were performed using a Titan S/TEM (FEI, 300kV) instrument. An Instrument SA HR 320 spectrograph/monochromator together with a PI-MAX intensified CCD camera from Princeton Instruments was used to record the luminescence spectra. A TechnicaLaser MLL-III-980-2w laser emitting 2 W at 980 nm was utilized as the exciting source. A 700 nm cut-on filter from Newport (10SWF-700-B) was employed to filter out the exciting light at the detector window. UV-vis absorption spectra were collected by a Cary 5000 UV-vis-NIR spectrophotometer.

5.7.3 Synthesis of ErNC and TmNC

The upconversion nanocrystals were synthesized by a thermolysis method using lanthanide chlorides as the precursors [5, 35]. YCl_3 (156 mg), $YbCl_3{\cdot}6H_2O$ (70 mg) and $ErCl_3{\cdot}6H_2O$ (8 mg) were mixed with 15 mL 1-octadecene and 12 mL oleic acid for the synthesis of ErNCs. The mixture was heated to 120 °C for half an hour to evaporate the

water. In a separate container, 100 mg NaOH and 149 mg NH_4F were dissolved in 10 mL of methanol. After the lanthanide solution was cooled down to 50 °C, the NH_4F methanol solution was added into the lanthanide solution and slowly heated to 80 °C to remove the methanol. The mixed solution was purged with argon gas and reacted at 300 °C for an hour. After the solution was cooled to room temperature, an excess amount of ethanol was added to precipitate the nanocrystals. They were washed several times with hexane and ethanol and suspended in chloroform at a concentration of 20 mg/mL. In the synthesis of TmNCs, 8 mg of thulium chloride was used instead of the erbium chloride.

5.7.4 Synthesis of ErNC@MSN

The synthesis of ErNC@MSN follows a two-step reaction, starting with coating the hydrophobic nanocrystals with surfactant CTAB. 2 mL of ErNCs or TmNCs chloroform solution was added into 20 mL of H_2O containing 400 mg of CTAB. The solution was sonicated thoroughly and slowly heated to 65 °C to evaporate the chloroform. In a separate reaction flask, 13.5 mL of H_2O was heated to 80 °C. After the temperature stabilized, 1.5 mL of ErNC aqueous solution, 110 μL of 2 M NaOH and 150 μL of TEOS were added. The reaction was continued at 80 °C for 2 h before centrifuge and washing with H_2O and methanol. Surfactant extraction was carried out by suspending the as prepared particles into 20 mL of methanol, adding 0.767 mL of concentrate hydrochloride acid. The reaction was maintained at 60 °C overnight to remove the CTAB molecules.

5.7.5 Synthesis of Nanoimpeller Particles and TmNC@IP-MSN

Nanoimpeller particles were synthesized following our previous published co-condensation procedure [23, 25]. To synthesize the azobenzene linker, 0.565 mmol of 4-hydroxyazobenzene was reacted with 141 μL 3-(triethoxysilyl)propyl isocyanate in 5 mL of anhydrous acetone under nitrogen gas for 4 h at room temperature. In a different container, 0.5 g CTAB was dissolved in 240 mL of water with 1.75 mL NaOH solution (2 mol/L), followed by heating to 80 °C. The azobenzene linker solution was added into this water solution dropwise, together with 2.4 mL of TEOS. The solution was maintained at 80 °C for 2 h before washing. Similar surfactant extraction procedure as that of the ErNC@MSN was carried out. Core-shell nanoimpeller particles (TmNC@IP-MSNs) were synthesized by the co-condensation process with nanocrystals. The azobenzene linker solution was prepared by the same procedure as that of the nanoimpellers. 13.5 mL of H_2O with 1.5 mL of TmNC aqueous solution and 110 μL of 2 M NaOH was heated to 80 °C. To this solution, 320 μL of the as-prepared azobenzene linker solution was added, followed by 150 μL of TEOS. The reaction was conducted at 80 °C for 2 h, before washing and surfactant extraction.

5.7.6 Working Curve Generation and Nanoparticle Internal Temperature Measurement

The ErNC@MSN particles were submersed in water in a cuvette at a concentration of 1 mg/mL. As the solution was heated slowly by a hot stir plate, the 980 nm laser was tuned on for 10 s to collect the emission spectra of ErNC@MSN at various temperatures. After subtracting the background from the emission spectra, the 520 nm and 540 nm emission

peak intensities were calculated. The natural log of the intensity ratios was plotted against the inverse of temperatures to generate the working curve.

To monitor the nanoparticle interior temperature change induced by the continuous IR light irradiation, the same particle concentration and cuvette setup were used. The 980 nm laser was irradiated on particles serving also as the excitation light for nanothermometers. The luminescence spectra of nanocrystal embedded silica nanoparticles were collected continuously and the peak intensity ratios between 520 and 540 nm were calculated. The corresponding nanoparticle interior temperatures were derived according to the correlation working curve. The spectral frame time was 10 s and the CCD detector gain was set at zero.

5.7.7 Nanoparticle Cargo Loading and Release

The fluorescence dye propidium iodide was dissolved in water at a concentration of 1 mM. The particles were suspended in the dye solution at a concentration of 10 mg/mL, stirred for 24 h and washed with pure water to remove surface absorbed dyes. For the release study, 2 - 4 mg of the dried particles were weighted and carefully placed at the corner of the cuvette. Pure water was then added slowly to submerge the particles. A small stir bar was placed in the cuvette corner opposite to the particles, and was stirring the solution during the experiment without perturbing the particles. A 448 nm probe beam was shone on the water supernatant and the fluorescence intensity of this solution was monitored by the CCD detector continuously as an indication of the cargo amount. The excitation beam (either 403 nm or 980 nm) was turn on after collecting a baseline and irradiated the particle pile in the corner. At the end of the experiment, the supernatant solution absorption spectrum

was scanned, and the absolute cargo amount in the solution was calculated according to the Beers law. The fluorescence intensity of the supernatant solution was converted to the relative release amount. In the direct-heating-induced release study, instead of using an excitation beam, a hot stir plate was used to heat the solution and kept its temperature at 45 °C.

5.7.8 Release Study in an Ice Water Bath

In order to eliminate the optical heating and to examine the influence of different excitation sources in triggering azobenzene photoisomerizations, the release studies were carried out by placing the cuvette in a 2 L ice water bath. The other experimental parameters were the same as that of the ambient environment release experiment. The cuvette was positioned at the edge of the water bath glass container, so that the distance of the optical path between the glass container and the cuvette exterior was minimum.

5.8 Theoretical Calculation

5.8.1 Photon Count in Direct 403 nm Excitation

Assumption: laser power: 20 mW; beam size: 2 mm in diameter; single silica particle size: 50 nm in diameter; all samples are tightly packed with particles.

Laser power density: $20/(\pi \times 1^2) = 0.64$ W/cm^2

Single photon energy: $E_{403} = hc/\lambda = 1.98645 \times 10^{-25}/(403 \times 10^{-9}) = 4.93 \times 10^{-19}$ J

Photon flux: $F_{403} = 0.64/(4.93 \times 10^{-19}) = 1.3 \times 10^{18}$ s^{-1}·cm^{-2}

Single particle irradiated area: $S_{silica} = \pi r^2 = \pi(25 \times 10^{-7})^2 = 2.0 \times 10^{-11}$ cm^2

Number of 403 nm photons irradiated on a single silica particle per second:

$$F_{403}S_{silica} = 1.3 \times 10^{18} \times 2 \times 10^{-11} = 2.6 \times 10^7/\text{s}$$

5.8.2 Photon Count in 980 nm Upconversion Process

Assumption: laser power: 2 W; beam size: 0.5 cm^2; single upconversion nanocrystal size: 25 nm in diameter

Laser power density: $2/0.5 = 4$ W/cm^2

Single photon energy: $E_{980} = hc/\lambda = 1.98645 \times 10^{-25}/(980 \times 10^{-9}) = 2.03 \times 10^{-19}$ J

Photon flux: $F_{980} = 4/(2.03 \times 10^{-19}) = 2.0 \times 10^{19}$ s^{-1}·cm^{-2}

Single nanocrystal irradiated area:

$$S_{nanocrystal} = \pi r^2 = \pi(12.5 \times 10^{-7})^2 = 4.9 \times 10^{-12} \text{ cm}^2$$

Number of 980 nm photons irradiated on a single upconversion nanocrystal per second:

$$F_{980}S_{nanocrystal} = 2.0 \times 10^{19} \times 4.9 \times 10^{-12} = 9.8 \times 10^7/\text{s}$$

In order to calculate how many photons are absorbed by the nanocrystals, it is necessary to estimate the molarity of the absorbing element. The molar concentration of absorbing element Yb is calculated according to the doping composition: Y: Yb: Tm= 0.8 : 0.18: 0.02. The apparent molar weight of $NaYF_4$:Yb^{3+}, Tm^{3+} is :

$$m = 22.990 + 18.998 \times 4 + 88.906 \times 0.8 + 173.04 \times 0.18 + 168.94 \times 0.02 = 204.63 \text{ g/mol}$$

The bulk $NaYF_4$ density was reported as 4.21 g/cm^3 [41]. We assume the density holds

constant for the doped nanocrystals, given the small amount of doping elements in the matrix. We discuss the absorption efficiency of two scenarios: either the upconversion nanocrystals, or the nanocrystals encapsulated mesoporous silica particles.

5.8.2.1 Pure Upconversion Nanocrystals

The molar amount of Yb in one 25 nm nanocrystal is:

$$n_{Yb} = \frac{V_{nanocrystal} \cdot \rho \cdot Yb \cdot wt.\%}{M_{Yb}} = (4\pi/3 \times 12.5^3 \times 4.21 \times \frac{173.04 \times 0.18}{204.63})/173.04$$

Thus, the molarity of Yb is:

$$\begin{aligned} c_{Yb-nanocrystal} &= \frac{n_{Yb}}{V_{nanocrystal}} \\ &= \frac{4\pi/3 \times 12.5^3 \times 4.21 \times \frac{173.04 \times 0.18}{204.63}}{173.04} / (4\pi/3 \times 12.5^3) \\ &= \frac{4.21 \times 0.18}{204.63} = 3.7\, mol/L \end{aligned}$$

Single nanocrystal absorption length: 25 nm = 2.5 $\times 10^{-6}$ cm

At 973 nm, the molar extinction coefficient of Yb is reported as 2.10 $cm^{-1} \cdot M^{-1}$ [27]. The transmittance is : $T_{nanocrystal} = 10^{-\varepsilon cl} = 10^{-2.10 \times 3.7 \times 2.5 \times 10^{-6}} = 10^{-1.94 \times 10^{-5}}$

The percentage of absorbed IR photons is: $1 - \frac{I}{I_0} = 1 - T = 4.5 \times 10^{-5}$

The number of absorbed photon is:

$$N_{nanocrystal} = 9.8 \times 10^7 \times 4.5 \times 10^{-5} = 4.4 \times 10^3 \text{ /s}$$

5.8.2.2 Upconversion Nanocrystal Embedded Mesoporous Silica Particles

The above calculation has been based on pure upconversion nanocrystals. When they are embedded in the mesoporous silica matrix, the Yb^{3+} concentration will be diluted by

the silica media. The silica naonparticle radius is 25 nm.

Thus, the Yb molarity in this condition will be:

$$\begin{aligned} c_{Yb-silica} &= \frac{n_{Yb}}{V_{silicaparticle}} \\ &= \frac{4\pi/3 \times 12.5^3 \times 4.21 \times \dfrac{173.04 \times 0.18}{204.63}}{173.04} / (4\pi/3 \times 25^3) \\ &= \frac{4.21 \times 0.18}{204.63 \times 8} = 0.46\, mol/L \end{aligned}$$

The absorption efficiency in this case would be:

$$1 - \frac{I}{I_0} = 1 - 10^{-2.10 \times 0.46 \times 2.5 \times 10^{-6}} = 5.6 \times 10^{-6}$$

The number of absorbed photon is:

$$N_{silica} = 9.7 \times 10^7 \times 5.6 \times 10^{-6} = 5.4 \times 10^2 \ /\text{s}$$

5.8.2.3 Upconversion Quantum Yield

The absolute quantum yield for a 30 nm $NaYF_4$:Yb^{3+}, Er^{3+} system under the 980 nm irradiation with a laser power density of 150 W/cm^2 for a two-photon upconversion process was reported as 0.10 ± 0.05 % [28]. To calculate the upper limite, we assume the three-photon upconversion of $NaYF_4$:Yb^{3+}, Tm^{3+} has the same quantum yield as that of the two-photon process under the 150 W/cm^2 980 nm irradiation. Three-photon upconversions should be less efficient, thus the value we are calculating is the upper limit for Tm^{3+} doped systems. Given that the reported system used similar doping ratios as our nanocrystals and that the quantum yield of the non-linear upconversion process highly depends on the irradiation power density, it is reasonable to estimate that for a three-photon process under a lower irradiation power, the quantum yield of $NaYF_4$:Yb^{3+}, Tm^{3+} is:

$$0.10\ \% \times (\frac{4}{150})^3 = 2 \times 10^{-8}$$

The same research pointed out that by coating the nanocrystal surface with an undoped $NaYF_4$ shell, the quantum yield was enhanced by 3 fold [28]. Other researches have also reported similar improvement, but did not specify quantitatively. As we are trying to calculate the upper limit, assuming the coated nanocrystals $NaYF_4$:Yb^{3+},Tm^{3+}@$NaYF_4$ have a 100 fold increase compared to $NaYF_4$:Yb^{3+},Tm^{3+}, the quantum yield would be:

$$QY = 0.10\ \% \times (\frac{4}{150})^3 \times 100 = 2 \times 10^{-6}$$

Thus, for every emitted photon, there are at least another 5×10^5 IR photons being absorbed.

5.8.2.4 Number of Generated High-Energy-Photons

In the upconversion nanocrystal sample, number of blue photons emitted by a single nanocrystal per second is:

$$N_{e-nanocrystal} = N_{nanocrystal} \cdot QY = 4.4 \times 10^3 \times 2 \times 10^{-6} = 8.8 \times 10^{-3}\ /\text{s}$$

In the nanocrystal embedded particles, number of blue photons emitted per second by a single silica particle with one upconversion nanocrystal embedded is:

$$N_{e-silica} = N_{silica} \cdot QY = 5.4 \times 10^2 \times 2 \times 10^{-6} = 1.1 \times 10^{-3}\ /\text{s}$$

5.8.3 Emitted Photon Re-absorption Efficiency

All the emitted blue photons have the chance to be absorbed by azobenzene molecules either in the same silica particle or in a different particle in the sample pile. Since photon wavelength is larger than the nanoparticle dimensions, the probability of an emitted photon

being re-absorbed in the assemble is decided by the assemble dimension (d) in compare with the mean free path of photons in the absorbing media (l).

The mean free path of the photons equals to:

$$l = (\sigma n)^{-1}$$

where σ is the cross section of azobenzene and n is the molecule volume density.

The extinction coefficient of azobenzene is reported as 88 - 536 cm^{-1} M^{-1} in the range of 385 - 450 nm [30], corresponding to the cross section of 1.5×10^{-5} - 8.9×10^{-5} nm^2.

The TGA result showed that the azobenzene weight percentage is about 9 % in the embedded system. The mesoporous silica density was reported as 0.835 g/cm^3 [42]. Assuming the particle density is not influenced by the azobenzene part, thus in a 50 nm silica particle, the total weight of azobenzene molecules is:

$$m_{azo} = 4\pi/3 \times 25^3 \times 0.835 \times 9\% = 4.9 \times 10^{-18} \text{ g}$$

Divided by the azobenzene molecular weight (283.33 g/mol), the molecule amount in a single silica particles is:

$$n_{azo} = 4.9 \times 10^{-18}/(283.33/(6.02 \times 10^{23})) = 1.0 \times 10^4$$

Divided by the single silica matrix volume (the azobenzene occupied volume), the molecule density in the particle is:

$$n = 1.0 \times 10^4/(4\pi/3 \times 25^3 - 4\pi/3 \times 12.5^3) = 0.17 \text{ /nm}^3$$

Use the upper limit of cross section for maximum re-absorption:

$$l = (\sigma n)^{-1} = 1/(8.9 \times 10^{-5} \times 0.17) = 66 \ \mu\text{m}$$

Since l is much smaller than the particle assemble macroscopic dimension d (0.2 - 0.5 cm),

the transmission is: $T = e^{-d/l} \approx 0$. Almost all of the emitted photons could be re-absorbed by azobenzenes.

5.8.4 Photon Count for Imaging Applications

Assuming the upconversion nanocrystal embedded particles are applied for biological imaging, the total number of silica particles in a 1 μg of sample is :

$$N = 1/(4\pi/3 \times 12.5^3 \times 4.21 + 4\pi/3 \times (25^3 - 12.5^3) \times 0.835) = 1.2 \times 10^{10}$$

Total converted photons from the 1 μg sample is :

$$N_{e-silica} \cdot N = 1.1 \times 10^{-3} \times 1.2 \times 10^{1}0 = 1.3 \times 10^{7}/\text{s}$$

Thus, the number of emitted photons is much higher than the detection threshold for imaging.

5.9 Figures

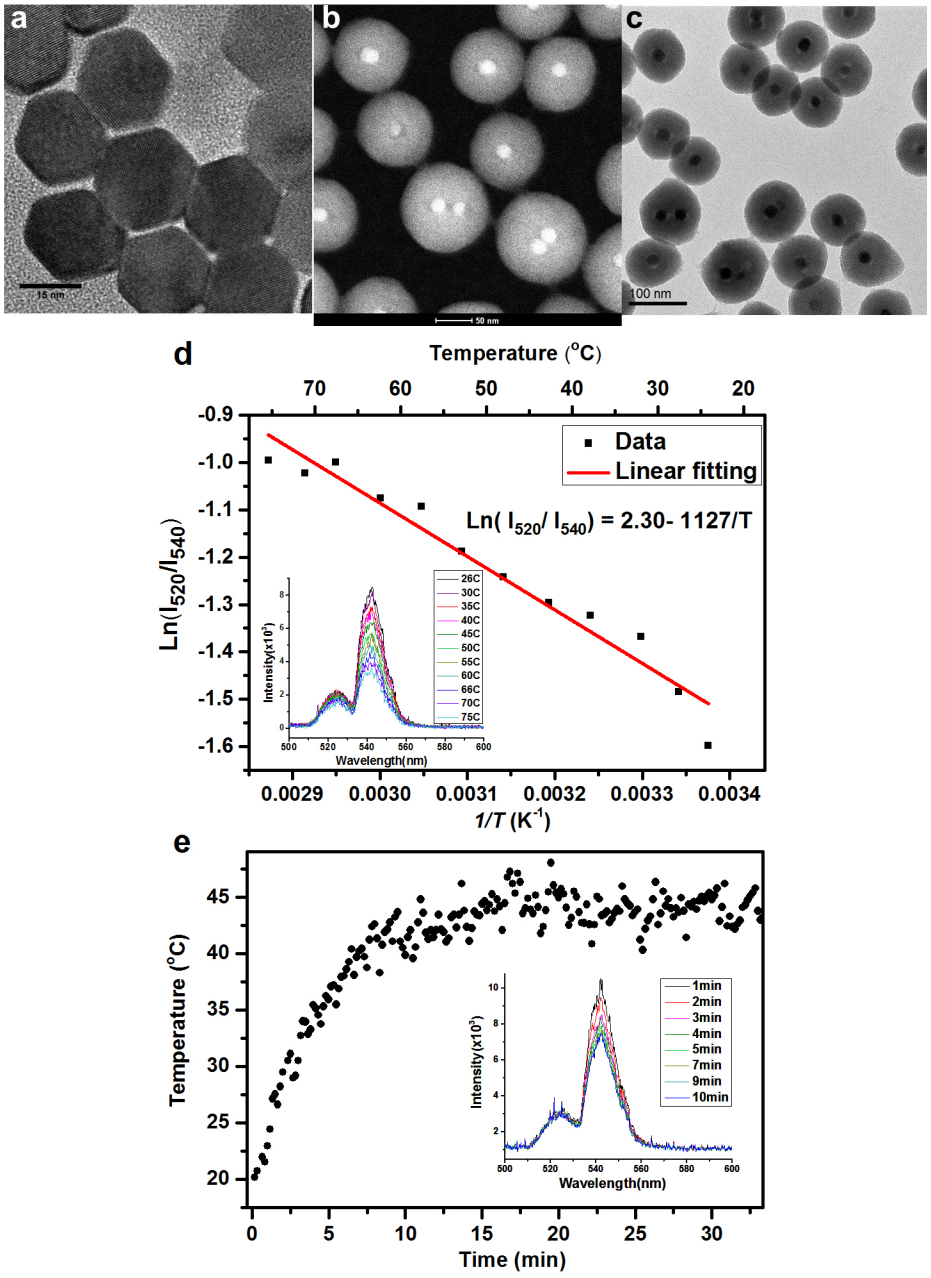

Figure 5.1 $NaYF_4$:Yb^{3+}, Er^{3+} nanocrystal transmission electron microscopy (TEM) images and IR irradiation heating measurement of nanoparticle interiors. (a), High resolution TEM image of the ErNCs, with a size distribution of 23.1 ± 0.1 nm. (b-c) STEM and TEM images of ErNC@MSNs. The average particle size is 109 nm. (d) Luminescence intensity ratio and temperature correlation working function of ErNC@MSNs. Inset is the emission spectra under different temperatures. (e) ErNC@MSNs interior temperature under the 980 nm irradiation. Inset is the luminescence spectra collected at the beginning of irradiation. Scale bar: 15 nm (a), 50 nm (b), 100 nm (c).

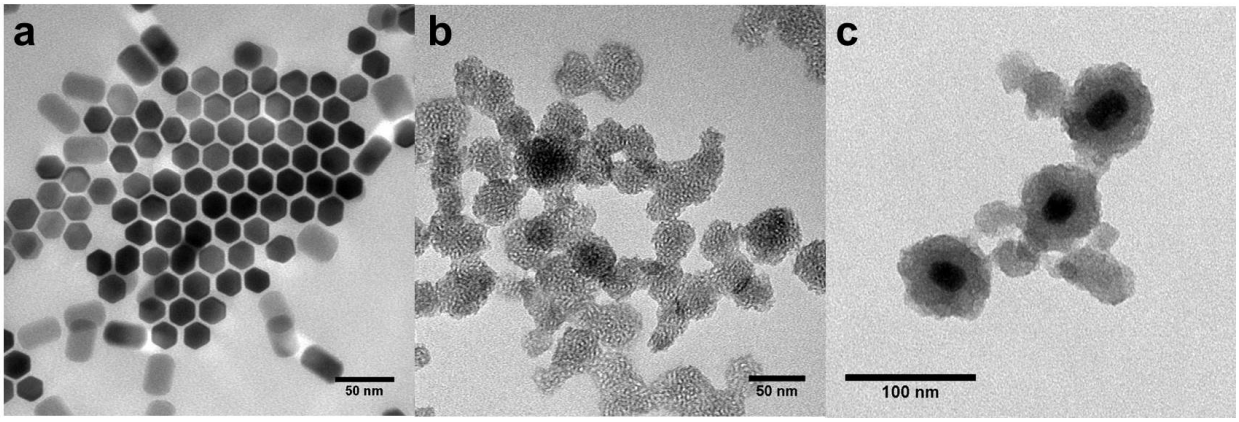

Figure 5.2 TEM images of nanocrystals and azobenzene particles. (a), Tm^{3+} doped upconversion nanocrystals with an average size of 23.4 nm(hexagonal side) × 35.8 nm (rod side). (b), nanoimpeller particles. (c), upconversion nanocrystal embedded nanoimpeller particles TmNC@IP-MSNs. Scale bar: 50 nm (a, b), 100 nm(c).

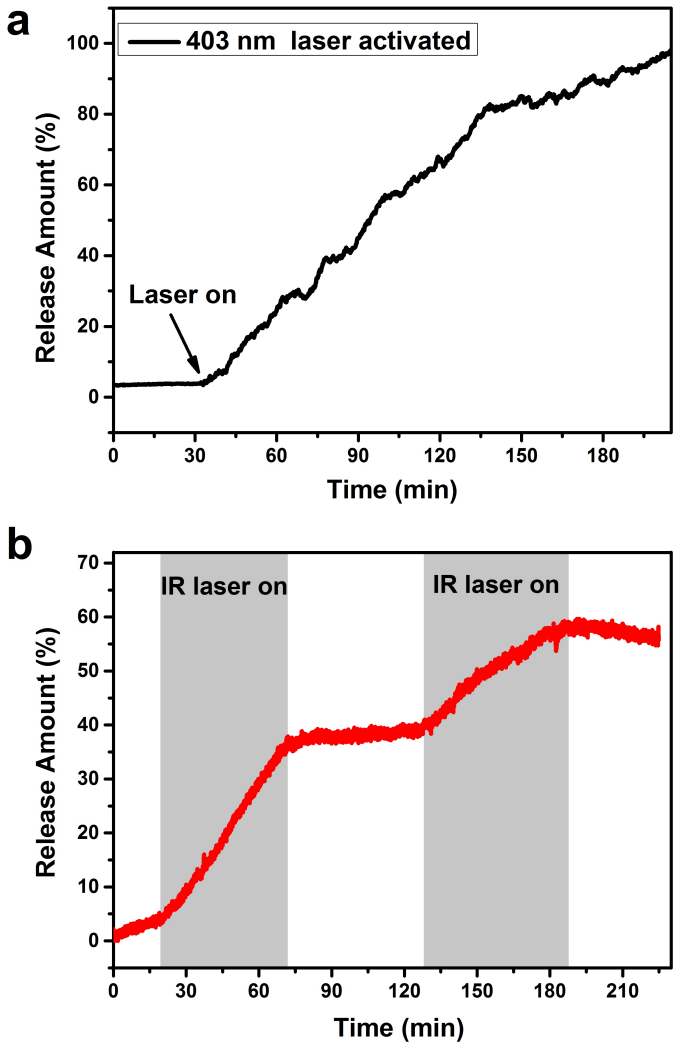

Figure 5.3 Controlled release profiles of TmNC@IP-MSNs, under (a) 403 nm light irradiation, (b) 980 nm laser periodic irradiation. The gray areas indicate the time when the IR laser was on. A light dependent cargo release pattern was observed for both irradiation sources.

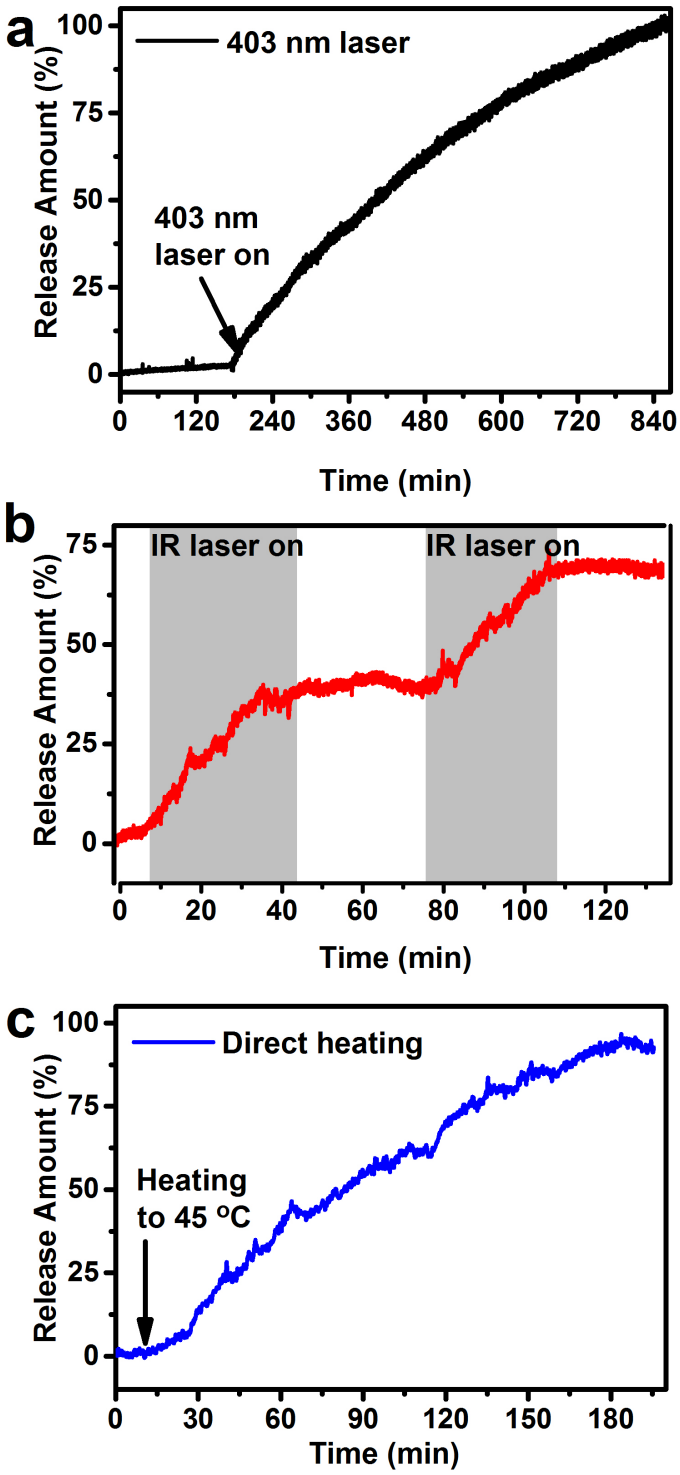

Figure 5.4 Release profiles of nanoimpeller particles under different stimulations: (a) 403 nm activation, (b) 980 nm laser activation, (c) solution heating to 45 °C. In (b), the 980 nm laser was turned on (gray background) and off alternatively. All release amounts are normalized with the 403 nm activated system.

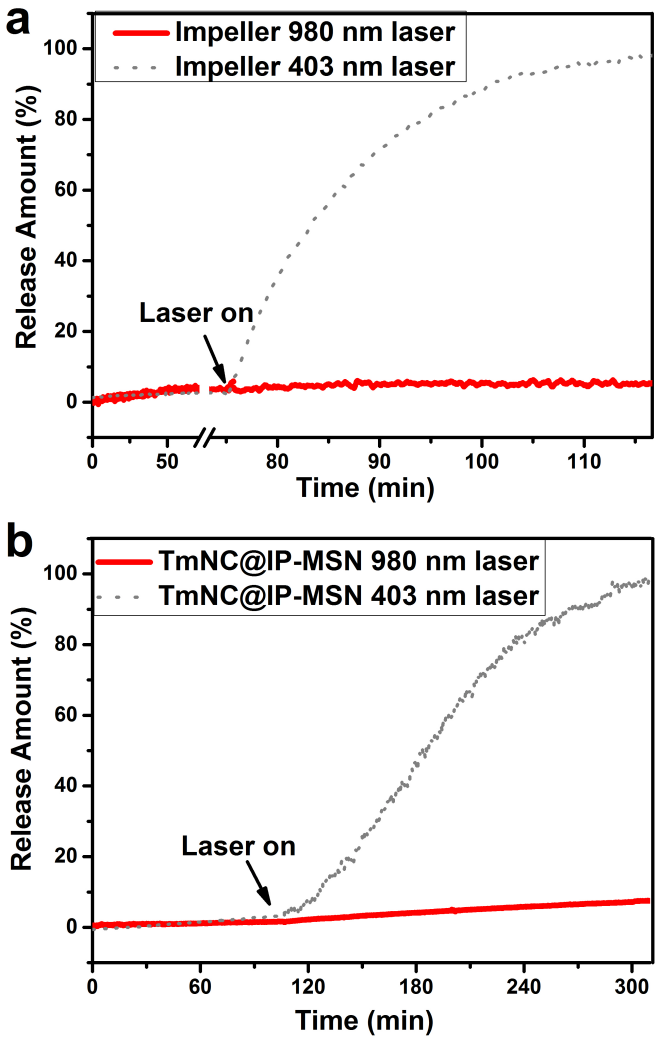

Figure 5.5 Release profiles of (a) nanoimpellers and (b) $NaYF_4$:Yb^{3+}, Tm^{3+} encapsulated nanoimpellers in an ice water bath experiment. Grey dot curves: 403 nm laser illumination. Red curves: 980 nm irradiation. Arrows point at the time when either the 403 nm laser or the 980 nm laser was switched on.

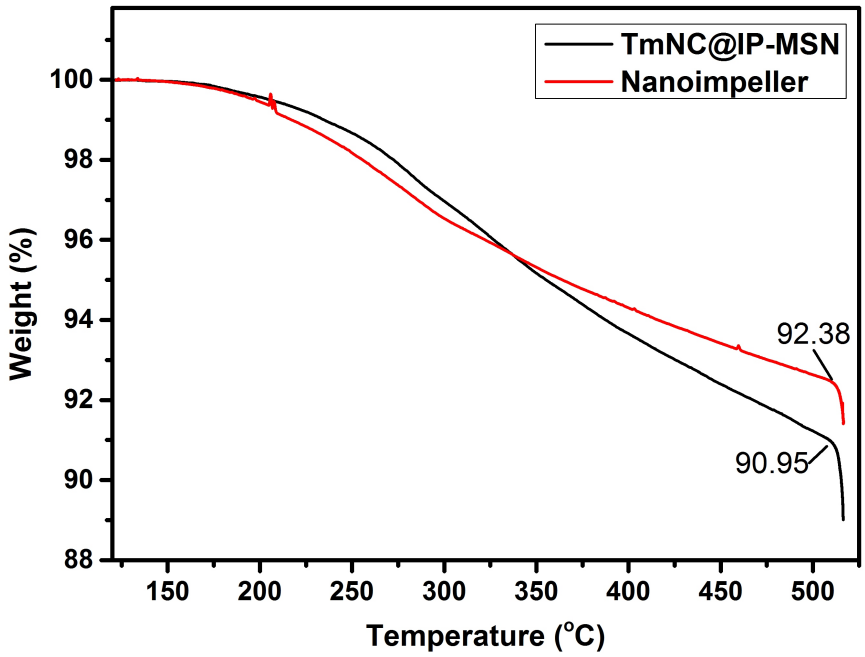

Figure 5.6 Thermogravimetric analysis (TGA) results for pure nanoimpeller particles (red curve) and upconversion nanocrystal embedded impeller particles (black curve). The weight loss from 120 °C to 520 °C corresponds to the weight of azobenzene molecules. The azobenzene weight percentages of the two samples are 7.62 % and 9.05 % respectively, confirming that a substantial amount of azobenzene is condensed in the silica matrix.

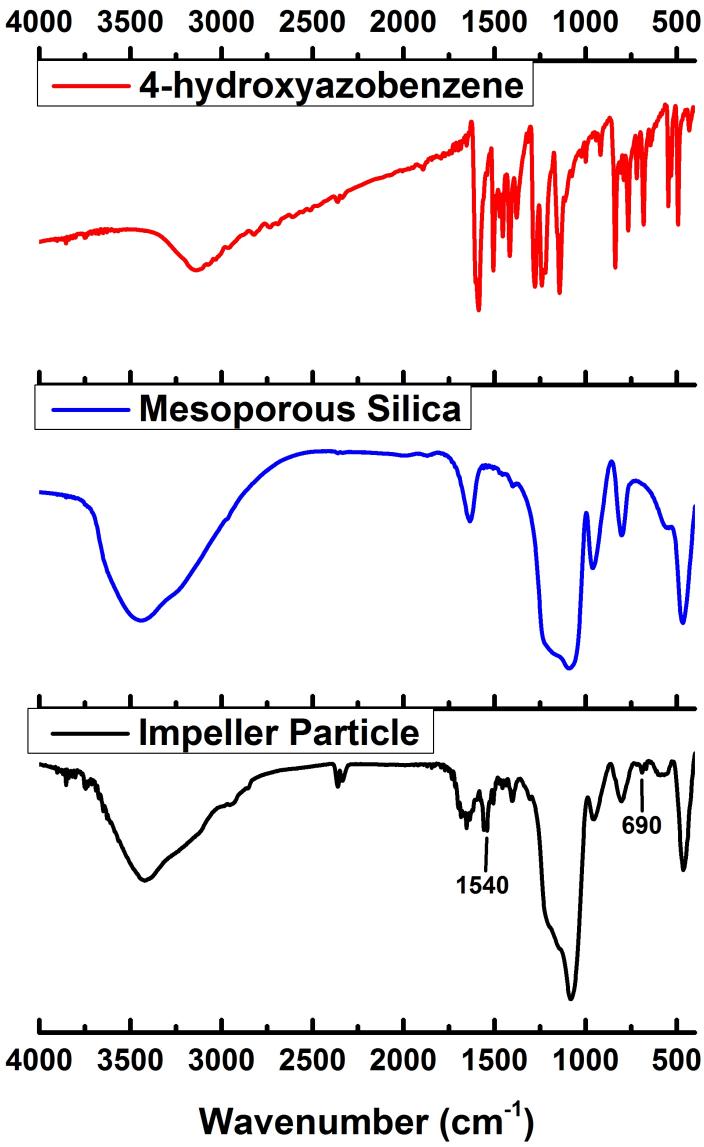

Figure 5.7 FTIR absorption spectra. Top: pure 4-hydroxyazobenzene compound used for synthesis; middle: mesoporous silica particles; bottom: azobenzene co-condensed nanoimpeller particles. The vibration at around 1540 cm^{-1} is related to the amine N-H bend of azobenzene linker part and the 690 cm^{-1} band corresponds to the aromatic C-H bend of azobenzenes. Both vibration modes confirm the attachment of azobenzene molecules.

5.10 References

[1] J. Zhou, Y. Sun, X. Du, L. Xiong, H. Hu, and F. Li. "Dual-modality *in vivo* imaging using rare-earth nanocrystals with near-infrared to near-infrared (NIR-to-NIR) up-

conversion luminescence and magnetic resonance properties." *Biomaterials*, **31**(12): 3287–3295, 2010.

[2] Y. Dai, H. Xiao, J. Liu, Q. Yuan, P. Ma, D. Yang, C. Li, Z. Cheng, Z. Hou, P. Yang, et al. "*In vivo* Multimodality Imaging and Cancer Therapy by Near-Infrared Light-Triggered *trans* -Platinum Pro-Drug-Conjugated Upconverison Nanoparticles." *J. Am. Chem. Soc.*, **135**(50):18920–18929, 2013.

[3] J. Liu, W. Bu, L. Pan, and J. Shi. "NIR-Triggered Anticancer Drug Delivery by Upconverting Nanoparticles with Integrated Azobenzene-Modified Mesoporous Silica." *Angew. Chem. Int. Ed.*, **52**(16):4375–4379, 2013.

[4] Y. Min, J. Li, F. Liu, E. K. L. Yeow, and B. Xing. "Near-Infrared Light-Mediated Photoactivation of a Platinum Antitumor Prodrug and Simultaneous Cellular Apoptosis Imaging by Upconversion-Luminescent Nanoparticles." *Angew. Chem. Int. Ed.*, **53**(4): 1012–1016, 2014.

[5] J. Dong and J. I. Zink. "Taking the Temperature of the Interiors of Magnetically Heated Nanoparticles." *ACS Nano*, **8**(5):5199–5207, 2014.

[6] J. V. Garcia, J. Yang, D. Shen, C. Yao, X. Li, R. Wang, G. D. Stucky, D. Zhao, P. C. Ford, and F. Zhang. "NIR-Triggered Release of Caged Nitric Oxide using Upconverting Nanostructured Materials." *Small*, **8**(24):3800–3805, 2012.

[7] D. Chatterjee, A. Rufaihah, and Y. Zhang. "Upconversion fluorescence imaging of cells and small animals using lanthanide doped nanocrystals." *Biomaterials*, **29**(7):937–943, 2008.

[8] C. T. Xu, N. Svensson, J. Axelsson, P. Svenmarker, G. Somesfalean, G. Chen, H. Liang, H. Liu, Z. Zhang, and S. Andersson-Engels. "Autofluorescence insensitive imaging using upconverting nanocrystals in scattering media." *Appl. Phys. Lett.*, **93**(17):171103, 2008.

[9] N. M. Idris, M. K. Gnanasammandhan, J. Zhang, P. C. Ho, R. Mahendran, and Y. Zhang. "*In vivo* photodynamic therapy using upconversion nanoparticles as remote-controlled nanotransducers." *Nat. Med.*, **18**(10):1580–1585, 2012.

[10] H. S. Qian, H. C. Guo, P. C.-L. Ho, R. Mahendran, and Y. Zhang. "Mesoporous-Silica-Coated Up-Conversion Fluorescent Nanoparticles for Photodynamic Therapy." *Small*, **5**(20):2285–2290, 2009.

[11] M. E. Lim, Y.-l. Lee, Y. Zhang, and J. J. H. Chu. "Photodynamic inactivation of viruses using upconversion nanoparticles." *Biomaterials*, **33**(6):1912–1920, 2012.

[12] X. Yang, Q. Xiao, C. Niu, N. Jin, J. Ouyang, X. Xiao, and D. He. "Multifunctional core-shell upconversion nanoparticles for targeted tumor cells induced by near-infrared light." *J. Mater. Chem. B*, **1**(21):2757–2763, 2013.

[13] C. Wang, H. Tao, L. Cheng, and Z. Liu. "Near-infrared light induced *in vivo* photodynamic therapy of cancer based on upconversion nanoparticles." *Biomaterials*, **32** 6145–6154, 2011.

[14] Y. Yang, F. Liu, X. Liu, and B. Xing. "NIR light controlled photorelease of siRNA and its targeted intracellular delivery based on upconversion nanoparticles." *Nanoscale*, **5** (1):231–238, 2013.

[15] Y. Yang, Q. Shao, R. Deng, C. Wang, X. Teng, K. Cheng, Z. Cheng, L. Huang, Z. Liu, X. Liu, et al. "*In Vitro* and *in Vivo* Uncaging and Bioluminescence Imaging by Using Photocaged Upconversion Nanoparticles." *Angew. Chem. Int. Ed.*, **51**(13):3125–3129, 2012.

[16] J. Shen, G. Chen, T. Y. Ohulchanskyy, S. J. Kesseli, S. Buchholz, Z. Li, P. N. Prasad, and G. Han. "Tunable Near Infrared to Ultraviolet Upconversion Luminescence Enhancement in (α-$NaYF_4$:Yb,Tm)/CaF_2 Core/Shell Nanoparticles for *In situ* Real-time Recorded Biocompatible Photoactivation." *Small*, **9**(19):3213–3217, 2013.

[17] Y.-H. Chien, Y.-L. Chou, S.-W. Wang, S.-T. Hung, M.-C. Liau, Y.-J. Chao, C.-H. Su, and C.-S. Yeh. "Near-Infrared Light Photocontrolled Targeting, Bioimaging, and Chemotherapy with Caged Upconversion Nanoparticles *in Vitro* and *in Vivo*." *ACS Nano*, **7**(10):8516–8528, 2013.

[18] B. Yan, J.-C. Boyer, D. Habault, N. R. Branda, and Y. Zhao. "Near Infrared Light Triggered Release of Biomacromolecules from Hydrogels Loaded with Upconversion Nanoparticles." *J. Am. Chem. Soc.*, **134**(40):16558–16561, 2012.

[19] C.-J. Carling, J.-C. Boyer, and N. R. Branda. "Remote-Control Photoswitching Using NIR Light." *J. Am. Chem. Soc.*, **131**(31):10838–10839, 2009.

[20] J.-C. Boyer and F. C. J. M. van Veggel. "Absolute quantum yield measurements of colloidal $NaYF_4$: Er^{3+}, Yb^{3+} upconverting nanoparticles." *Nanoscale*, **2**(8):1417–1419, 2010.

[21] L. Polo-Corrales and C. Rinaldi. "Monitoring iron oxide nanoparticle surface temperature in an alternating magnetic field using thermoresponsive fluorescent polymers." *J. Appl. Phys.*, **111**(7):07B334, 2012.

[22] J. Dong, M. Xue, and J. I. Zink. "Functioning of nanovalves on polymer coated mesoporous silica Nanoparticles." *Nanoscale*, **5**(21):10300–10306, 2013.

[23] Y. A. Lau, B. L. Henderson, J. Lu, D. P. Ferris, F. Tamanoi, and J. I. Zink. "Continuous spectroscopic measurements of photo-stimulated release of molecules by nanomachines in a single living cell." *Nanoscale*, **4**(11):3482–3489, 2012.

[24] M. Liong, J. Lu, M. Kovochich, T. Xia, S. G. Ruehm, A. E. Nel, F. Tamanoi, and J. I. Zink. "Multifunctional Inorganic Nanoparticles for Imaging, Targeting, and Drug Delivery." *ACS Nano*, **2**(5):889–896, 2008.

[25] J. Lu, E. Choi, F. Tamanoi, and J. I. Zink. "Light-Activated Nanoimpeller-Controlled Drug Release in Cancer Cells." *Small*, **4**(4):421–426, 2008.

[26] P. Sierocki, H. Maas, P. Dragut, G. Richardt, F. Vögtle, L. De Cola, F. A. M. Brouwer, and J. I. Zink. "Photoisomerization of Azobenzene Derivatives in Nanostructured Silica." *J. Phys. Chem. B*, **110**(48):24390–24398, 2006.

[27] D. C. Stewart and D. Kato. "Analysis of Rare Earth Mixtures by Recording Spectrophotometer." *Anal. Chem.*, **30**(2):164–172, 1958.

[28] J.-C. Boyer, C.-J. Carling, B. D. Gates, and N. R. Branda. "Two-Way Photoswitching Using One Type of Near-Infrared Light, Upconverting Nanoparticles, and Changing Only the Light Intensity." *J. Am. Chem. Soc.*, **132**(44):15766–15772, 2010.

[29] N. Liu, Z. Chen, D. R. Dunphy, Y.-B. Jiang, R. A. Assink and B. C. Brinker. "Photoresponsive Nanocomposite Formed by Self-Assembly of an Azobenzene-Modified Silane." *Angew. Chem. Int. Ed.*, **42**(15):1731–1734, 2003.

[30] G. Zimmerman, L.-Y. Chow, and U.-J. Paik. "The Photochemical Isomerization of Azobenzene[1]." *J. Am. Chem. Soc.*, **80**(14):3528–3531, 1958.

[31] R. M. Pope and E. S. Fry. "Absorption spectrum (380–700 nm) of pure water. II. Integrating cavity measurements." *Appl. Opt.*, **36**(33):8710–8723, 1997.

[32] L. Kou, D. Labrie, and P. Chylek. "Refractive indices of water and ice in the 0.65- to 2.5 μm spectral range." *Appl. Opt.*, **32**(19):3531–3540, 1993.

[33] F. Vetrone, R. Naccache, A. Zamarroń, A. Juarranz de la Fuente, F. Sanz-Rodriǵuez, L. Martinez Maestro, E. Martiń Rodriguez, D. Jaque, J. Garciá Sole; and J. A. Capobianco. "Temperature Sensing Using Fluorescent Nanothermometers." *ACS Nano*, **4**(6):3254–3258, 2010.

[34] S. A. Wade, S. F. Collins, and G. W. Baxter. "Fluorescence intensity ratio technique for optical fiber point temperature sensing." *J. Appl. Phys.*, **94**(8):4743, 2003.

[35] C. Liu, H. Wang, X. Li, and D. Chen. "Monodisperse, size-tunable and highly efficient β-$NaYF_4$:Yb,Er(Tm) up-conversion luminescent nanospheres: controllable synthesis and their surface modifications." *J. Mater. Chem.*, **19**(21):3546-3553, 2009.

[36] J. Wang, R. Deng, M. A. MacDonald, B. Chen, J. Yuan, F. Wang, D. Chi, T. S. Andy Hor, P. Zhang, G. Liu, et al. "Enhancing multiphoton upconversion through energy clustering at sublattice level." *Nat. Mater.*, **13**(2):157–162, 2013.

[37] D. J. Gargas, E. M. Chan, A. D. Ostrowski, S. Aloni, M. V. P. Altoe, E. S. Barnard, B. Sanii, J. J. Urban, D. J. Milliron, B. E. Cohen, et al. "Engineering bright sub-10-nm upconverting nanocrystals for single-molecule imaging." *Nat. Nanotechnol.*, **9**(4): 300–305, 2014.

[38] S. Jiang and Y. Zhang. "Upconversion Nanoparticle-Based FRET System for Study of siRNA in Live Cells." *Langmuir*, **26**(9):6689–6694, 2010.

[39] Y. Wang, K. Liu, X. Liu, K. Dohnalova, T. Gregorkiewicz, X. Kong, M. C. G. Aalders, W. J. Buma, and H. Zhang. "Critical Shell Thickness of Core/Shell Upconversion Luminescence Nanoplatform for FRET Application." *J. Phys. Chem. Lett.*, **2**(17): 2083–2088, 2011.

[40] Y. Ding, H. Zhu, X. Zhang, J.-J. Zhu, and C. Burda. "Rhodamine B derivative-functionalized upconversion nanoparticles for FRET-based Fe^{3+}-sensing." *Chem. Commun.*, **49**(71):7797–7799, 2013.

[41] L. Cheng, K. Yang, S. Zhang, M. Shao, S. Lee, and Z. Liu. "Highly-sensitive multiplexed *in vivo* imaging using pegylated upconversion nanoparticles." *Nano Res.*, **3**(10):722–732, 2010.

[42] K. J. Edler, P. A. Reynolds, J. W. White, and D. Cookson. "Diffuse wall structure and narrow mesopores in highly crystalline MCM-41 materials studied by X-ray diffraction." *J. Chem. Soc. Faraday Trans.*, **93**(1):199–202, 1997.

CHAPTER 6

Simultaneous Spectral Detection of Nanoparticle Interior Temperature and the Corresponding Cargo Release of Functional Mesoporous Silica Nanoparticles

6.1 Abstract

The evaluation of the on-command release of nanocarriers has been limited to measuring the cargo amount in the surrounding medium, despite of their various compositions and properties. This indirect examination merely monitors the overall macroscopic result of a series of nanoscale chemical and physical reactions, providing little information of the nature and mechanism of the process. In an effort to address this issue, we synthesized a nanothermometer-embedded thermally responsive release system, and recorded the temperature-dependent luminescence emission of nanothermometers together with the cargo molecule fluorescence intensity change. Our spectral method simultaneously detects the nanoparticle interior temperatures and the resulting macroscopic cargo release, and opens a path to examine the nanoscale events to study the nature of these reactions.

6.2 Introduction

The field of controlled therapeutic delivery performed by nano vehicles has been intensively pursued over the past few decades [1, 2, 3, 4, 5, 6] . In the early investigations, drug molecules were sustainedly released into the circulation system from the storing matrix, which undergoes slow degradations or allows diffusion of small molecules [7, 8, 9, 10]. To advance the control of the delivery, nanocarriers that experience structural transformations upon condition change have been applied to manipulate the cargo loading and releasing behavior. Various compositions and chemical features have been employed, including soft materials such as liposomes, dendrimers and polymers, as well as the hard materials like silica, iron oxide and gold nanoparticles [1, 2, 4, 11]. The stimulations for conformational change can be internal or external, including pH variations, light irradiations, temperature change, redox reactions and biomolecule recognitions [12, 13, 14, 15, 16, 17, 18]. Despite the numerous functional mechanisms for different vehicles, the general strategy to introduce the on-demand release has been to induce the material morphology change for soft carriers and the surface chemical structure change for hard carriers [5, 19, 20, 21, 22].

Many efforts have focused on creating new release systems based on different nanostructures, yet the evaluation methods of their performances are still quite limited. Often times, the cargo concentration increase in the release media is used as the sole characterization approach, which merely monitors the overall result of a series of physical and chemical reactions on the nanoscale, and does not provide details of the events themselves. In addition, more and more nanocarriers are employing several structural components to fulfill the task, but a simple release amount characterization is far from enough to prove the point. Our

discussion in the last chapter presents a good example: the infrared laser irradiation triggered cargo release from azobenzene modified MSNs was caused by photon induced heating, not by the direct photochemical isomerization. Similar cargo concentration increases in the media were observed, but different reaction mechanisms were involved. Therefore, the direct monitoring of events on the small scale is in need to obtain information for precisely controlling and optimizing release, especially for the therapeutic delivery in complicated biological environments.

In an effort to simultaneously detect the physical property change and its stimulated on-command release from nano vehicles, we synthesized a temperature-responsive nanocarrier incorporating a temperature detection probe in the particle. Mesoporous silica nanoparticles, one of the most widely applied delivery platform for nanomedicines, are condensed with azobenzene moieties as the functional component to trap cargo molecules and to release them upon heating. The particles also contain a lanthanide doped fluoride nanocrystal ($NaYF_4$: Yb^{3+}, Er^{3+}) that gives out temperature dependent luminescence emissions. A small organic dye molecule - cascade blue - was loaded into the mesoporous structure, and its release was monitored by the fluorescence intensity change of water media. Both of these emission signals were collected in the same spectrum and were mathematically resolved to extract the information of nanoparticle temperatures and release performances. Upon the optical heating, we have successfully observed the particle interior temperature change together with its triggered cargo release. Our analysis presents a novel strategy for simultaneous detection of nanoscale events and their corresponding macroscopic result.

6.3 Results and discussion

The idea of monitoring both the physical condition change and the consequent cargo release of functionalized MSNs is pursued by embedding a temperature probing nanocrystal into the azobenzene condensed silica matrix. The bulky azobenzene molecules stretch out of the pores and block the free movement of cargoes inside the pores. As we have shown in the last chapter, both heat and UV light could initiate the controlled cargo release, although via different routes: the UV light excites the photoisomerization reaction of both isomers and prompts the large amplitude wagging motion of azobenzenes forcing the cargoes out of pores. The heat increases the kinetic energy of cargo and the fluidity of particles. Thus, the azobenzene molecules do not present a sufficient physical barrier to stop the cargo from diffusing out, resulting in a temperature-sensitive controlled release platform.

The temperature detection method used in this system is based on the same principle as we have discussed in the last two chapters. The upconversion emission spectra of lanthanide fluoride ($NaYF_4$:Yb^{3+}, Er^{3+}) nanocrystals are temperature dependent: the natural log of intensity ratios between the luminescence peak 520 nm and 540 nm is linearly related to the inverse of temperatures, following the Boltzmann distribution. The working curve was plotted by placing the particles in solutions of different temperatures, collecting the emission spectra, calculating the peak intensity ratios and linearly fitting to the inverse of temperatures. The resulted correlation between the intensity ratio and the absolute temperature serves as the probe for unknown temperature measurement (Figure 6.1 on page 165). Continuous IR irradiation is used to excite the lanthanide nanocrystals and monitor the temperature change. Besides, the IR illumination also generate optical heatings that promote

the cargo release in nanoimpeller systems as we have shown in the last chapter.

The other part of the simultaneous monitoring - the cargo release - is carried out by the continuous recording of supernatant solution fluorescence intensities. Fluorescent molecules - cascade blue in this case - are loaded into the azobenzene modified core-shell nanoparticles, thoroughly washed to remove surface absorbed dyes and dried before use. In the detection experiment, the particles were placed in a corner of a cuvette. Water was carefully added into the cuvette without disturbing the particles and stirred to prompt the homogeneity, with a particle/water weight ratio of 1:1000 (1 mg/ml). A 403 nm probe laser beam irradiated the supernatant solution. Since all the fluorescent dye molecules come from the loaded particles, the fluorescent intensity in supernatant represents its cascade blue concentration and thus, the cargo release amount.

We want to monitor both of these spectral signals simultaneously to derive the correlation between the nanoscale physical property change and the macroscopic release behavior. However, the lanthanide emissions often overlap with that of the dye molecules. In order to obtain the accurate peak intensity ratios of lanthanides to calculate the temperature, the collected luminescence spectra need to be analyzed. The bright side of this challenge is that the lanthanide emissions are characterized by sharp and narrow peaks, in contrast with the broad bands of fluorescent organic dyes. Taking advantage of their distinguishable peak shapes, we designed a simple algorithm to resolve the two components in the collected emission spectra (Equation 6.1). The contribution of cascade blue in the overlapped range is calculated by normalizing a standard cascade blue solution emission to the same intensity as that of the collected spectrum in the non-overlapped part. Thus, by subtracting the

dye molecule emission, the lanthanide emission is retrieved and could be further analyzed to extract the temperature information. The fluorescence intensity of cascade blues in the non-overlapped range represents the cargo release amount in the supernatant solution. The standard cascade blue emission in water solution was collected under the same irradiation condition as that of the sample group. The following equation expresses this mathematical process to obtain the lanthanide luminescence spectra.

$$I'(j) = I(j) - k \cdot C(j),\ where\, k = \frac{\int_{464}^{487} I(j)dj}{\int_{464}^{487} C(j)dj} \tag{6.1}$$

$I(j)$ stands for the raw intensity value of the collected spectrum at a certain wavelength j; $C(j)$ is the intensity value of the standard cascade blue solution at the wavelength j; $I'(j)$ is the lanthanide nanocrystal emission at the wavelength j, and k is the scale factor to normalize the cascade blue standard emissions. For both of the raw spectra and the standard cascade blue spectra, the intensity was integrated from 464 nm to 487 nm to calculate their relative ratio k. In this range, cascade blue emission is the only component in the spectrum. k represents the scale factor of cascade blue emission in the collected spectrum compared to that of the standard solution. In the overlapped part, the contribution of cascade blue emission is derived by normalizing the standard solution emission intensity ($C(j)$) with the factor k. After subtracting the cascade blue band in the overlapped range, we could resolve the lanthanide emission intensity ($I'(j)$) at a certain wavelength j in the collected spectrum. Figure 6.2 on page 166 illustrates this processing method. Part **a** shows the original raw spectrum; part **b** is the calculated cascade blue contribution in the raw spectrum (The inset is the cascade blue standard solution emission); part **c** is the resolved upconversion emission;

part **d** is the overlay of the three spectra. The same baseline was subtracted from all of the spectra before this processing.

Both of the simultaneously recorded signals are plotted as a function of time in Figure 6.3 on page 167. The black squares are the cargo release amount indicated by the cascade blue emissions in the supernatant. The blue empty circles are the temperatures of nanoparticle interiors, extracted from the resolved lanthanide upconversion emissions. The release amount was recorded continuously over the whole experiment and the temperature was only tracked after turning on the 980 nm laser, which also initiated the cargo release from nanoimpeller particles. At the beginning of IR irradiation, there is a small dent in the black trace showing the cascade blue fluorescence intensity "drop" in the supernatant, which is due to the quenched fluorescence of organic dyes at higher temperature. Gradually, this effect is overcome by the increase of cargo molecules in the solution as the IR illumination generates heat and stimulates the cargo diffusion out of the pores. In contrast, the particle temperature rises immediately upon the start of 980 nm irradiation. The initial fast increase has slowly leveled off after 25 min. The cargo amount trace indicates that the release happened about 5 min after the IR irradiation started and was at approximately 33 - 34 °C. The delayed response could be contributed to three elements. One is that the fluorescence of cascade blue is quenched at high temperature, thus the observed concentration is lower than the actual value. On the other hand, the diffusion of cascade blue out of the nanopores needs sufficient energy to overcome the physical barrier of azobenzenes. Until the kinetic energy of dyes rises and the rigidity of particles reduces to allow the dyes to pass through, a significant cargo concentration increase in the solution would not occur. Moreover, the diffusion of dyes from

the particle pile into the solution might also contribute to the delay, although the solution was gently stirred to facilitate the diffusion in the liquid phase.

In an effort to evaluate the accuracy of temperature measurement in this dual-model detection system, a control experiment was carried out where the core-shell particles were not loaded. In this case, the lanthanide emission signal is the only component in the spectra, so that we could compare their temperature changes upon IR irradiation with those that we calculated from the overlapped spectra by mathematical methods. The same particles without dye molecules were placed in the corner of the cuvette, and the nanoparticle temperatures were recorded under the same irradiation conditions. As illustrated in the inset of Figure 6.3, the temperatures collected in the cargo loaded particles (blue empty squares) match that of the unloaded bare particles (red empty circles), which validates the accuracy of this dual-model detection strategy and its mathematical processing.

As an extension of the temperature detection study, we want to experimentally examine the heating mechanism of IR irradiation in order to deepen the understanding. We have mentioned and briefly analyzed in last chapter that the thermal contribution of IR illuminations could result both the high absorption coefficients of water in the range and the low quantum yields of lanthanide upconversion nanocrystals. For water, about 35 % of the 980 nm photons are absorbed in a 1 cm long optical pathway, while only 0.056 % of the 403 nm photons is absorbed. For the nanocrystals, we calculated that for a two-photon upconversion process, the quantum yield upper limit is on the order of 10^{-8} when the excitation source power density is between 1-10 W/cm^2. Thus, both factors could contribute to the IR irradiation induced heating effect.

To examine how much each component contributes and more specifically, to investigate whether the lanthanide heating is the primary factor, we synthesized particles without azobenzene modifications, because the component does not generate heat but only absorb heat and is not relevant in studying the heating mechanism. Thus, the $NaYF_4$:Yb^{3+}, Er^{3+} nanocrystal embedded core-shell mesoporous silica nanoparticles (UCNC@MSN) are employed. Two temperature curves were recorded in parallel experiments either with nanoparticles in solution or without. The water solution temperature rise without nanoparticles immersed were recorded by a K-Type thermocouple. Shown in Figure 6.4a on page 168 are the nanoparticle interior temperatures as a function of IR irradiation time (red circles) and the water temperatures under the same irradiation condition (black squares). The former detects the particle temperature change as a result of non-radiative decay of IR photon absorptions by lanthanide elements as well as the heat conduction with the water media. The later only senses the optical heating of water due to its high absorption cross section in the spectral range. Initially, the particle interiors feel more heat compared to the water environment, which is magnified in the inset graph. Interestingly, the effect was only observed for the first five minutes after turning on the 980 nm laser beam. The two curves gradually converge with each other afterwards. Thus, in the absence of lanthanide nanocrystals, the water solution was susceptible to IR illuminations and experienced a substantial optical heating that is comparable to the case when lanthanide nanocrystals were present. Although the nanoparticles sensed a few degrees of higher temperatures initially, the primary contribution of the heating effect in this condition is the water absorption of IR photons and the consequent energy conversion from photons to heat.

Another interesting observation in the graph is that the $NaYF_4$:Yb^{3+}, Er^{3+} nanocrystal temperature sensing suffers more uncertainty at higher temperature compared to that at lower temperature. Our hypothesis is that the fluorescence emission fluctuates more at an elevated temperature, as the thermal-quenching effect takes a more active role. Also, as our error propagation has shown in Chapter 4, the systematic error is proportional to the absolute temperature value. Thus, the increase of both T and $\frac{I_{520}}{I_{540}}$ would result in bigger temperature fluctuations.

In an effort to reduce the IR optical heating effect and to analyze the temperature differences between the nanoparticles and the bulk solutions detailedly, we performed a temperature comparison experiment in an ice water bath. A 2 cm $\times$ 1 cm cuvette with the UCNC@MSN particles in water was placed in a glass container with about 2 L of ice water. The temperature information was extracted from both the luminescence emissions of lanthanide nanocrystals and a thermocouple immersed in water. The cuvette was next to the edge of the glass water container to minimize the laser power reduction by the ice water absorption. The results are shown in Figure 6.4b on page 168, where the red circles are the particle temperatures and the black squares are the bulk solution temperatures. The gray dashed line shows the exponential fitting of nanoparticle temperatures. Interestingly, after the bulk water temperature came to an equilibrium as the heat absorption from the IR laser and the heat dissipation to the ice water bath balanced, approximately 3 min after the irradiation was on, the nanoparticle interior temperatures kept on increasing for another 7 min. The nanoparticles were able to maintain a temperature difference of about 2 °C higher than that of the solution environment.

The uncertainty of nanothermometers is greater in the ice water bath condition due to the weaker emission signals collected by the spectrometer. In a control to quantify the experimental errors in these experiments, we turned on the laser beam briefly to repeatedly record the nanoparticle temperature deviations. As shown in the inset graph of Figure 6.4b, about 10 data points were gathered over a 15 min time window. Because that the laser beam was not able to raise the bulk solution temperature significantly, the nanoparticle temperature should not experience major changes between different points. Yet, the interior temperatures fluctuated between $\pm$ 2 °C, which represents the experimental error in this ice water bath condition.

6.4 Summary

In summary, we have incorporated the nanothermometer into the temperature responsive release system based on mesoporous silica nanoparticles with azobenzene modifications. The embedded lanthanide nanocrystal $NaYF_4$:Yb^{3+}, Er^{3+} generates temperature sensitive luminescence emissions and the particles are loaded with fluorescent cargoes as an indication of the release behavior. Upon the 980 nm irradiation, the photons are absorbed by both the water environment and the lanthanide elements, which raise the particle interior temperatures significantly and initiate the dye molecule release. Emissions of both of the lanthanide nanocrystals and the cargo molecules were continuously recorded in the same luminescence spectrum. By using a simple algorithm to resolve the two signals, we monitored the nanoscale temperature increase with the macroscopic cargo release performance simultaneously. We believe the new detection strategy will benefit the evaluation of nanocarriers

for controlled release, as well as the correlation of reaction natures on the micro scale with their macroscopic results.

6.5 Methods

6.5.1 Material

Yttrium(III) chloride (99.99 %, Aldrich), ytterbium(III) chloride hexahydrate (99.9 %, Aldrich), erbium(III) chloride hexahydrate (99.9 %, Aldrich), oleic acid (90 %, Sigma-Aldrich), 1-octadecene (95.0 % Aldrich), ammonium fluoride (98.0 %, Sigma-Aldrich), sodium hydroxide (97.0 %, Fisher), 4-phenylazophenol (98 %, Sigma-Aldrich), 3-(triethoxysilyl)propyl isocyanate (95 % Aldrich), cetyltrimethylammonium bromide (CTAB) (95 %, Sigma-Aldrich), tetraethyl orthosilicate (TEOS) (98 %, Aldrich), hexane (98.5 %, Fisher), toluene (99.5 %, Sigma-Aldrich), methanol (99.9 %, Firsher), chloroform (99.8 %, Fisher) and ethanol (99.5 %, Fisher) were used. All chemicals are reagent grade and used without further purification or modification.

6.5.2 Characterization

A TechnicaLaser MLL-III-980-2w laser emitting 2 W at 980 nm was utilized as the exciting source. An Instrument SA HR 320 spectrograph/monochromator together with a PI-MAX intensified CCD camera from Princeton Instruments was used to record the luminescence spectra. A 700 nm cut-on filter from Newport (10SWF-700-B) was employed to filter out the exciting light at the detector window. A Coherent CUBE 403-100C emitting at 403 nm (20 mW) was used as the irradiation source for the supernatant solution lumines-

cence detection. The laser beam was reflected from optical glass twice, losing about 90 % of intensity each time, thus the estimated effective irradiation power was 0.20 mW. A 435 nm cut-off filter was placed after the sample to filter out the 403 nm light.

6.5.3 Synthesis

Lanthanide nanocrystals ($NaYF_4$:Yb^{3+}, Er^{3+}, molar ratio: Y: Yb: Er = 0.8:0.18:0.02), nanocrystal embedded mesoporous silica nanoparticles (UCNC@MS), and nanocrystal embedded nanoimpeller particles were synthesized with similar experimental methods as discussed in Chapter 4 and Chapter 5.

6.5.4 Spectroscopic Experiments

6.5.4.1 Working Curve Collection

The upconversion nanocrystal ($NaYF_4$:Yb^{3+}, Er^{3+}) embedded nanoimpeller particles were immersed in water with a weight ratio of 1:1000 (5 mg of particle in 5 ml of water) in a 2 cm $\times$ 1 cm rectangle cuvette. The cuvette was heated slowly and the water solution temperature was measured by a K-Type thermocouple. The sample was placed on the same horizontal level as the CCD detector in front of it. The nanoparticle luminescence spectra were collected at different temperatures using a 980 nm infrared laser as the exciting source. For each spectrum, the peak intensities were integrated to calculate the intensity ratios between the peaks at 520 nm and 540 nm. The natural log of these intensity ratios were plotted against the inverse of absolute temperatures and linearly fitted to generate the working curve. The CCD detector had a gain of zero and the slit opening was set at 1 μm.

The exposure time was 10 s. The same baseline was subtracted from all collected spectra to remove the background.

6.5.4.2 Simultaneous Recording and Spectra Processing

In order to study both the nanoparticle temperature and the cargo release performances, two excitation sources were applied for these two signals. The $NaYF_4$:Yb^{3+}, Er^{3+} nanocrystal embedded particles were placed in the corner of the cuvette and immersed in water using the same method as we have discussed before. About 3 - 4 mg of particles were used and its weight ratio with water was 1:1000. The 980 nm laser (beam size about 0.5 cm^2) was shone on the particles to excite the nanothermometer. The beam orientation was along to the long axis of the cuvette. On the other hand, the 435 nm laser beam was directs onto the supernatant part of the cuvette to monitor the solution cargo fluorescence. Thus, in the collected spectra, both signals were present.

A background baseline was collected when all the excitation sources were turned off. All collected spectra had the baseline curve subtracted before processing. In order to normalize the cascade blue emission and distinguish its contribution in the overlap range in the spectra, a standard cascade blue emission spectrum was collected under the same experimental conditions. In the non-overlapped range, from 464 nm to 487 nm, the collected spectrum intensity was integrated and compared to that of the standard cascade blue spectrum. The ratio between them was termed k in Equation 6.1. The standard emission spectrum was then normalized by this factor k and subtracted from the collected spectrum to generate the resolved lanthanide emission spectrum.

6.5.4.3 Heating Mechanism

The room temperature optical heating mechanism was investigated by two parallel studies. In one experiment, the lanthanide core-shell mesoporous silica nanoparticles were placed in the cuvette as in the previous experiments, and their emission spectra were collected continuously after turning on the 980 nm laser beam. In another experiment, same amount of water was added into the cuvette without any nanoparticles. The solution was also irradiated under the IR beam and the water temperature was recorded by a K-Type thermocouple throughout the process.

The ice water bath examination was carried out similarly, only that the nanoparticle temperature and the bulk solution temperature were studied in the same experiment. The cuvette was placed close to the edge in a round glass bath container with a diameter of about 25 cm and a volume of about 2 L. The container was full of ice water. The nanoparticle temperature was monitored by the emission of lanthanide nanocrystals and the bulk solution temperature was characterized by a K-Type thermocouple.

6.6 Figures

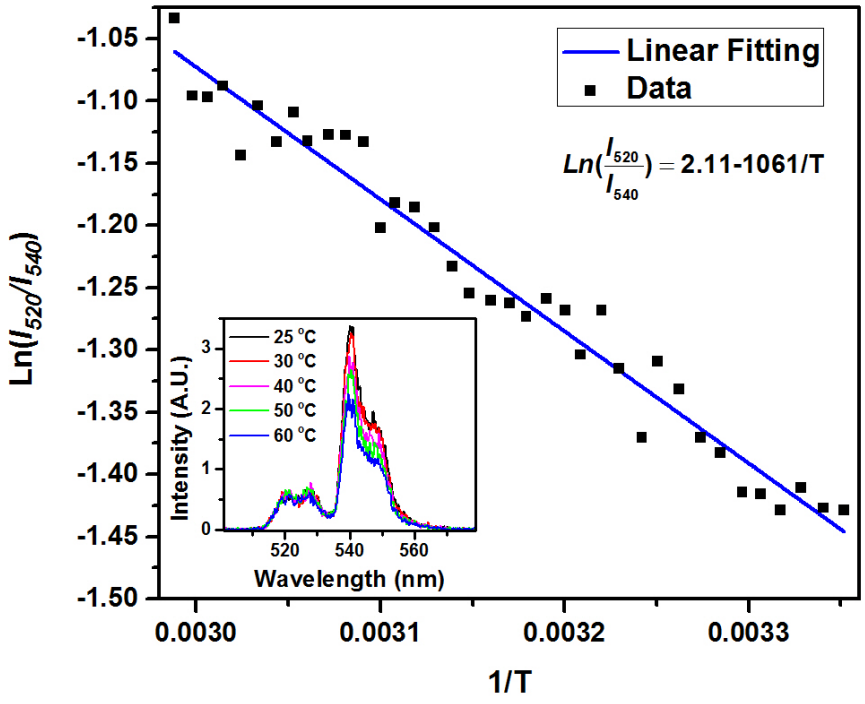

Figure 6.1 Working curve for $NaYF_4$:Yb^{3+}, Er^{3+} nanocrystal embedded nanoimpeller particles. The inset shows the representative emission spectra collected at various temperatures.

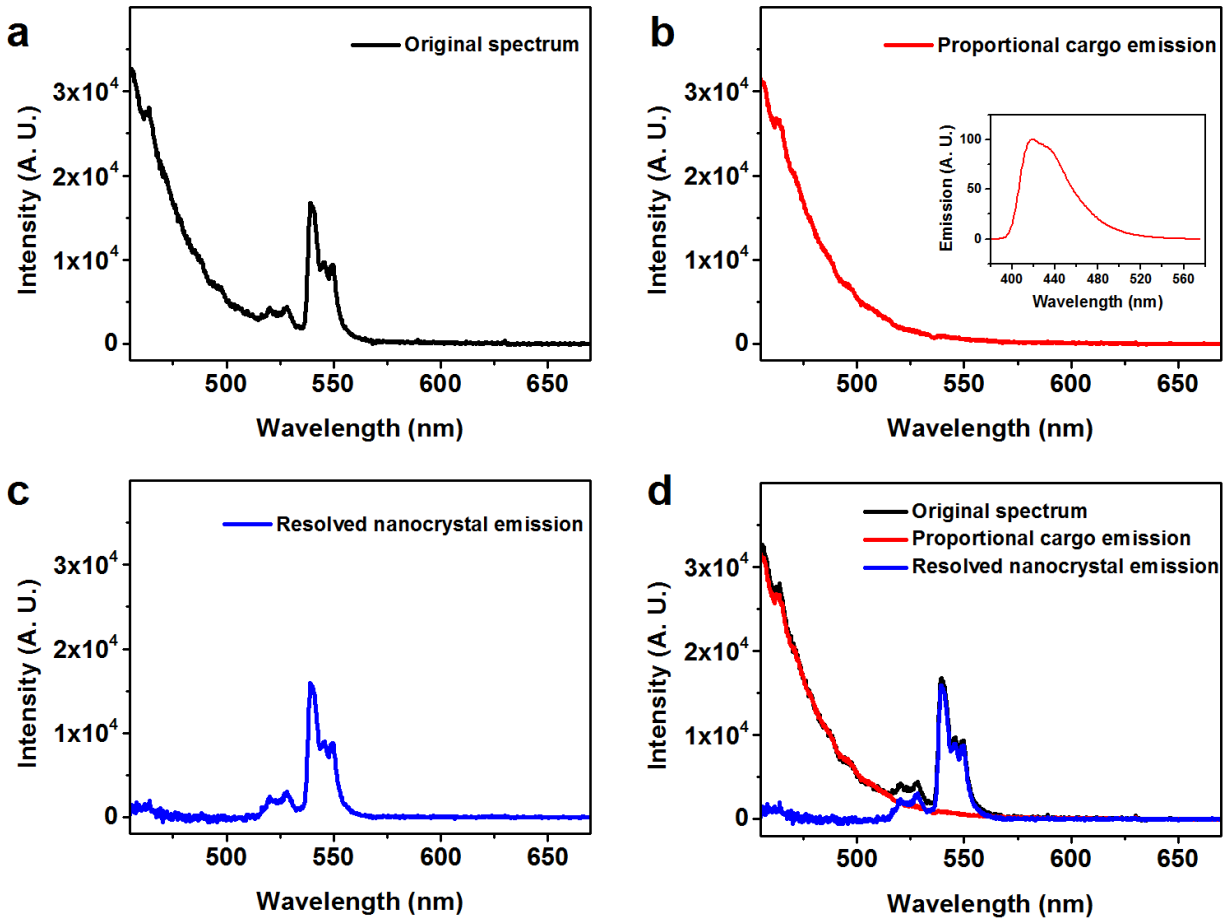

Figure 6.2 Dual-model detection spectral processing. (a) The original emission spectrum. (b) Calculated cascade blue contribution in the original spectrum. The inset is the cascade blue standard solution emission spectrum. (c) Resolved upconversion emission in the collected spectrum. (d) Overlay of all three spectra. The same baseline was subtracted from all emission spectra before this processing.

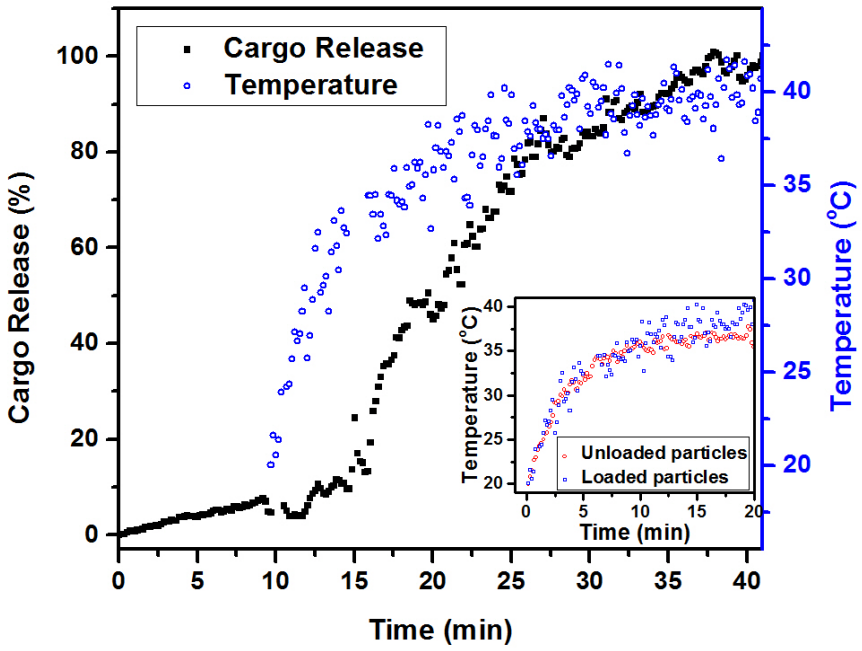

Figure 6.3 Simultaneous detection of nanoparticle temperature change and the corresponding cargo release. The amount of cargo release as a function of time are shown as the black squares and the nanoparticle temperatures detected by the lanthanide nanocrystals are the blue empty circles. The inset is the temperature measured in this dual-model detection method (blue empty squares) in comparison with that of it in the single detection model (red empty circles).

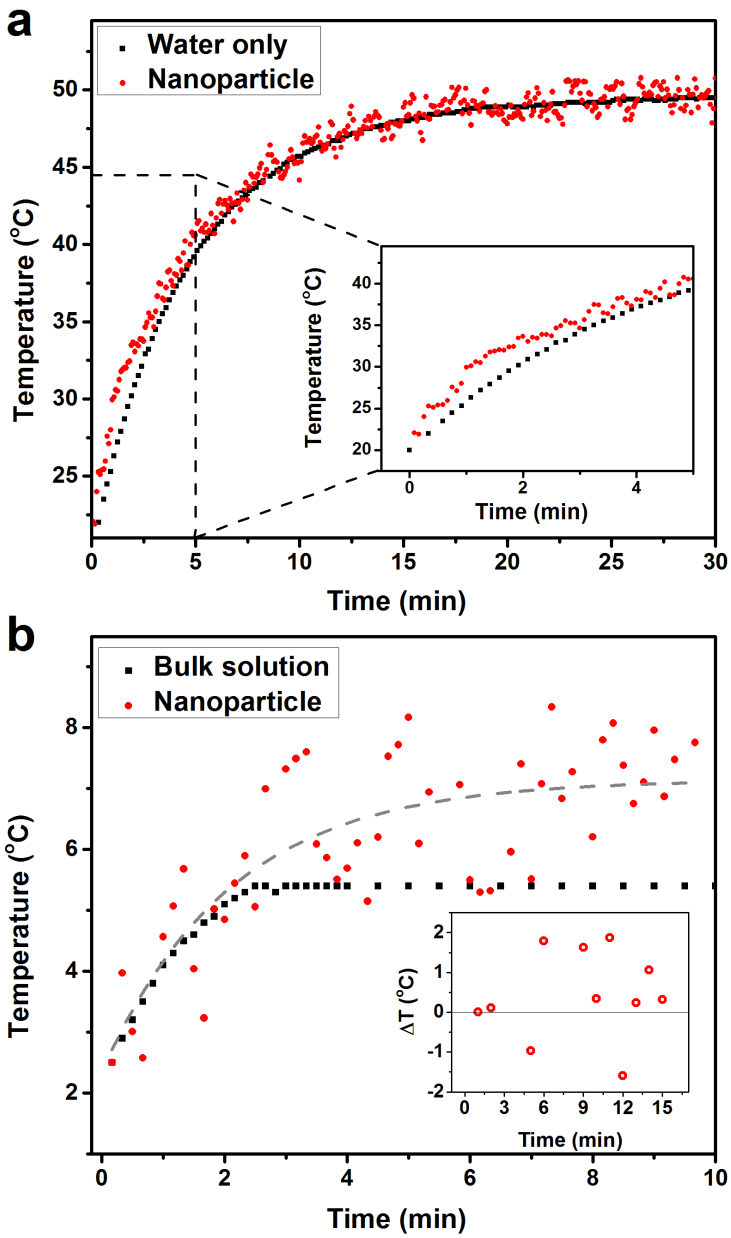

Figure 6.4 IR irradiation optical heating mechanism analysis. (a) UCNC@MSN particle interior temperature increases (red dots) in comparison with the water (black squares) optical heating behavior. The detected temperatures were plotted as a function of 980 nm illumination time. The inset is the magnification of first five minutes. (b) Nanoparticle (UCNC@MSN) interior temperature compared to that of the bulk solution under the IR illumination in the ice water bath. The grey dashed line shows the exponential fitting of nanoparticle temperatures. The inset is the experimental error analysis. The 980 nm laser was on briefly 10 times to quantify the experimental errors of the fluorescence temperature detection in this condition.

6.7 References

[1] Z. Li, J. C. Barnes, A. Bosoy, J. F. Stoddart, and J. I. Zink. "Mesoporous silica nanoparticles in biomedical applications." *Chem. Soc. Rev.*, **41**(7):2590–2605, 2012.

[2] A. K. Gupta and M. Gupta. "Synthesis and surface engineering of iron oxide nanoparticles for biomedical applications." *Biomaterials*, **26**(18):3995–4021, 2005.

[3] J. Huwyler, D. Wu, and W. M. Pardridge. "Brain drug delivery of small molecules using immunoliposomes." *PNAS*, **93**(24):14164–14169, 1996.

[4] D. Needham, G. Anyarambhatla, G. Kong, and M. W. Dewhirst. "A New Temperature-sensitive Liposome for Use with Mild Hyperthermia: Characterization and Testing in a Human Tumor Xenograft Model." *Cancer Res.*, **60**(5):1197–1201, 2000.

[5] B. Jeong, Y. H. Bae, D. S. Lee, and S. W. Kim. "Biodegradable block copolymers as injectable drug-delivery systems." *Nature*, **388**(6645):860–862, 1997.

[6] Y. Sun, B. T. Mayers, and Y. Xia. "Template-Engaged Replacement Reaction: A One-Step Approach to the Large-Scale Synthesis of Metal Nanostructures with Hollow Interiors." *Nano Lett.*, **2**(5):481–485, 2002.

[7] S. A. Agnihotri, N. N. Mallikarjuna, and T. M. Aminabhavi. "Recent advances on chitosan-based micro- and nanoparticles in drug delivery." *J. Control. Release*, **100** (1):5–28, 2004.

[8] M. Liu, K. Kono, and J. M. J. Fréchet. "Water-soluble dendritic unimolecular micelles:: Their potential as drug delivery agents." *J. Control. Release*, **65**(1–2):121–131, 2000.

[9] H. S. Yoo and T. G. Park. "Biodegradable polymeric micelles composed of doxorubicin conjugated PLGA–PEG block copolymer." *J. Control. Release*, **70**(1–2):63–70, 2001.

[10] N. Bhattarai, H. R. Ramay, J. Gunn, F. A. Matsen, and M. Zhang. "PEG-grafted chitosan as an injectable thermosensitive hydrogel for sustained protein release." *J. Control. Release*, **103**(3):609–624, 2005.

[11] T. Niidome, M. Yamagata, Y. Okamoto, Y. Akiyama, H. Takahashi, T. Kawano, Y. Katayama, and Y. Niidome. "PEG-modified gold nanorods with a stealth character for *in vivo* applications." *J. Control. Release*, **114**(3):343–347, 2006.

[12] K. Patel, S. Angelos, W. R. Dichtel, A. Coskun, Y.-W. Yang, J. I. Zink, and J. F. Stoddart. "Enzyme-Responsive Snap-Top Covered Silica Nanocontainers." *J. Am.*

Chem. Soc., **130**(8):2382–2383, 2008.

[13] J. Lu, E. Choi, F. Tamanoi, and J. I. Zink. "Light-Activated Nanoimpeller-Controlled Drug Release in Cancer Cells." *Small*, **4**(4):421–426, 2008.

[14] D. P. Ferris, Y.-L. Zhao, N. M. Khashab, H. A. Khatib, J. F. Stoddart, and J. I. Zink. "Light-Operated Mechanized Nanoparticles." *J. Am. Chem. Soc.*, **131**(5):1686–1688, 2009.

[15] B. Jeong, S. W. Kim, and Y. H. Bae. "Thermosensitive sol–gel reversible hydrogels." *Adv. Drug Deliver Rev.*, **54**(1):37–51, 2002.

[16] R. Liu, X. Zhao, T. Wu, and P. Feng. "Tunable Redox-Responsive Hybrid Nanogated Ensembles." *J. Am. Chem. Soc.*, **130**(44):14418–14419, 2008.

[17] Y. Ma, W.-F. Dong, M. A. Hempenius, H. Möhwald, and G. Julius Vancso. "Redox-controlled molecular permeability of composite-wall microcapsules." *Nat. Mater.*, **5**(9): 724–729, 2006.

[18] J.-M. Pernaut and J. R. Reynolds. "Use of Conducting Electroactive Polymers for Drug Delivery and Sensing of Bioactive Molecules. A Redox Chemistry Approach." *J. Phys. Chem. B*, **104**(17):4080–4090, 2000.

[19] K. E. Uhrich, S. M. Cannizzaro, R. S. Langer, and K. M. Shakesheff. "Polymeric Systems for Controlled Drug Release." *Chem. Rev.*, **99**(11):3181–3198, 1999.

[20] M. A. C. Stuart, W. T. S. Huck, J. Genzer, M. Müller, C. Ober, M. Stamm, G. B. Sukhorukov, I. Szleifer, V. V. Tsukruk, M. Urban, et al. "Emerging applications of stimuli-responsive polymer materials." *Nat. Mater.*, **9**(2):101–113, 2010.

[21] J. Dong, M. Xue, and J. I. Zink. "Functioning of nanovalves on polymer coated mesoporous silica Nanoparticles." *Nanoscale*, **5**(21):10300–10306, 2013.

[22] Z. Luo, K. Cai, Y. Hu, L. Zhao, P. Liu, L. Duan, and W. Yang. "Mesoporous Silica Nanoparticles End-Capped with Collagen: Redox-Responsive Nanoreservoirs for Targeted Drug Delivery." *Angew. Chem. Int. Ed.*, **50**(3):640–643, 2011.

Part IV

Biomedical Application of Nanoparticles

CHAPTER 7

Biomedical Studies Involving Mesoporous Silica Nanoparticles and other Nanomaterials

The performances of mesoporous silica nanoparticles for biomedical applications are evaluated with our collaborators: Dr. Ruibin Li, Dr. Zhaoxia Ji, Dr. Bingbing Sun, Dr. Yang Zhao and Dr. Huan Meng from the Center for Environmental Implications of Nanotechnology (CEIN) at UCLA; Dr. James B. Finlay and Dr. Carlotta A. Galckin from City of Hope; and several ongoing projects with a few other groups. With each project focusing on different aspects, we were able to collect a rather comprehensive understanding of the material functioning in different biomedical contexts. Three projects are explained in detail in this chapter.

7.1 Mesoporous Silica Nanoparticles for TGF-β Inhibitor Delivery to Target the Stroma in a Human Pancreatic Cancer Model in Mice

7.1.1 Introduction

The success of chemotherapy in curing pancreatic ductal adenocarcinoma is greatly sabotaged by the dense stroma that surround the vessels and prevent the transportation of therapeutics from vasculature to cancer cells[1, 2]. Although the cancer cells are relatively sensitive to drugs such as gemcitabine (GEM), paclitaxel, and 5-FU, the chemotherapy treatment usually has poor efficacy and serious side effects as a result of the blocked drug delivery. In an effort to overcome the drug resistance caused by the stromal barrier, methods have been proposed to alternate or eliminate the stromal compartment[3]. The transforming growth factor beta (TGF-β) plays an essential role in the pericyte coverage of endothelial cells by initiating the signaling pathway[3], which could be intervened by a receptor kinase inhibitor[4]. Successful delivering of the TGF-β signaling pathway inhibitor would enhance the therapeutic delivery efficacy to tumor sites and improve the clinical treatment of pancreatic cancers.

7.1.2 TGF-β Inhibitor Delivery by MSNs

A co-polymer coated mesoporous silica nanoparticle platform is designed to carry the molecular inhibitor for TGF-β signaling pathway, LY364947. The inhibitor molecule (structure showing in Figure 7.1a on page 178) is trapped inside the polymer-MSN matrix by

hydrogen bonding and hydrophobic force. The co-polymer is composed of polyethylene imine-polyethylene glycol (PEI-PEG), where the abundant amine groups form hydrogen bondings with the TGF-β inhibitors. Moreover, it provides the necessary surface modification to stablize the 50 nm MSNs and to prolong the particle circulation time as well as to improve their biodistribution[5]. The PEI component is electrostatically absorbed onto the negatively modified silica surface, with a molecular weight of 1.8 kDa, to take the advantage of its minimal cytotoxicity [6]. The PEG component is covalently bonded to the PEI part via a N-hydroxysulfosuccinimide ester bond. Similar experimental procedures were carried out to synthesize the particles and to perform the co-polymer coatings as that in Chapter 3.

To determine the MSNs incorporation capacity of LY364947, 500 μg of co-polymer coated particles was incubated with different amount of inhibitors (50 to 400 μg) at 25 °C for 24 h. The particles were washed after loading, and the UV-vis absorption peak of LY364947 at 269 nm was used to characterize the loading amount. Maximized at about 74 wt.%, the high loading capacity is resulted from the abundant hydrogen bondings between LY364947 and the amine groups on particle surfaces. The loading of TGF-β inhibitors increases the hydrodynamic size of PEI-PEG MSNs by 13 nm (from 120 to 143 nm), and decreases their surface ζ-potential from +45 mV to +30 mV in water (Figure 7.1b). Figure 7.1c demonstrates that the inhibitor loaded particles could suspend stably in water, saline (plus 2% serum) and cell culture medium for 72 h. LY364947 could be released from the MSNs in a time-dependent manner upon lowering the solution pH to 5.5 (Figure 7.1d). Approximately, 40 wt.% of the inhibitor was released within the first 24 h. This release property is beneficial since the stroma is slightly more acidic due to the increased lactic acid production as a result

of glycolysis (Warburg effect) [7].

7.1.3 *In vitro* and *in vivo* Performances of Inhibitor Incorporated MSNs

The biological activity of TGF-β inhibitor delivered by MSNs was first examined in cultured human vascular smooth muscle cells (phenotypically similar to pericyte [8, 9]) and human microvascular endothelial cells. We used a Matrigel assay to compare the performances of nanocarriers to free inhibitor delivery [8]. Figure 7.2 on page 179, in which endothelial cells and pericytes are stained with CellTracker Green and CellTracker Red, respectively, demonstrate that the percent of pericyte/endothelial cell colocalization was significantly decreased by TGF-β inhibitor delivery through the nanocarrier in comparison to the free inhibitors (at 1 μM). Representative fluorescent images of the cellular co-migration are shown on the right of the figure. Moreover, the signaling pathway of TGF-β is indicated by the level of Smad2 phosphorylation [10], which is illustrated by a green color in fluorescence images due to the FITC conjugation (Figure 7.2b). TGF-β inhibitor loaded MSNs demonstrated efficient and sustained inhibition of Smad2 phosphorylation for up to 24 h in pericytes, in contrast with the free inhibitor (suppressing pSmad2 for 6 h). Quantitative assessment of the green fluorescence intensity by ImageJ software confirmed a statistically significant and sustained inhibition of Smad2 phosphorylation by inhibitor loaded MSNs (Figure 7.2c).

In order to evaluate TGF-β delivery efficiency to tumor sites in animals, we established BxPC3 xenografts in nude mice. These xenografts are known to produce a dense infiltrating stroma, which surrounds nests of cancer cells and also covers tumor blood vessel fenestrations [11]. The presence of a dense stroma in our animal model after 25 days was verified

by Massons trichrome staining, which showed heavy collagen deposition in the BxPC3 tumor site (Figure 7.3a on page 180). The MSN nanocarriers were freshly prepared at 50% inhibitor/particle ratio before the animal experiment. The particles were injected intravenously at an inhibitor dose of 1 mg/kg (delivered by 2 mg/kg MSN) in nude mice expressing tumors ranging from 0.8 to 1.0 cm in diameter. Tail vein injections of saline or the free inhibitor (at the same dose) were used as controls. To investigate the impact of the inhibitor on the colocalization of pericyte and endothelial cells, dual-color immunohistochemistry was used to detect endothelial cell (FITC-conjugated antibody, recognizing CD31) and pericyte (Alexa Fluor 594-conjugated antibody, recognizing NG2) fluorescence (Figure 7.3) [12]. The results demonstrated that the IV-injected TGF-β inhibitor loaded MSNs could disrupt the composite (yellow) fluorescence staining that are the merge of endothelial cell (green) and pericyte (red) fluorescence. No separation of the green and red fluorescence distribution was observed in saline-treated animals, and the free inhibitor injection resulted in a slight but nonsignificant reduction of the composite fluorescence staining pattern (Figure 7.3b). We could observe the presence of the MSN nanocarrier in the tumor vasculature by electron microscopy, which presented as monodispersed, porous nanoparticles in small tumor blood vessels (Figure 7.4). Drug release at this site was likely promoted by the anoxic conditions and drop in the pH at the tumor site and in the stroma [7].

7.1.4 Summary

The *in vitro* and *in vivo* experimental results provide proof-of-concept evidences that the incorporation of LY364947 into MSNs could be used to target the PDAC stromal barrier and

potentially useful for promoting vascular access to the tumor. The delivery of chemotherapeutics - such as the gemcitabine - could be carried out by MSNs or other nanocarriers. Experiments following the interruption of stroma formation by the TGF-β inhibitor loaded MSNs have been performed, and the success delivery of gemcitabine by another carrier have been demonstrated [13].

For experimental procedure details regarding the biological studies, please refer to Reference 13.

7.1.5 Figures

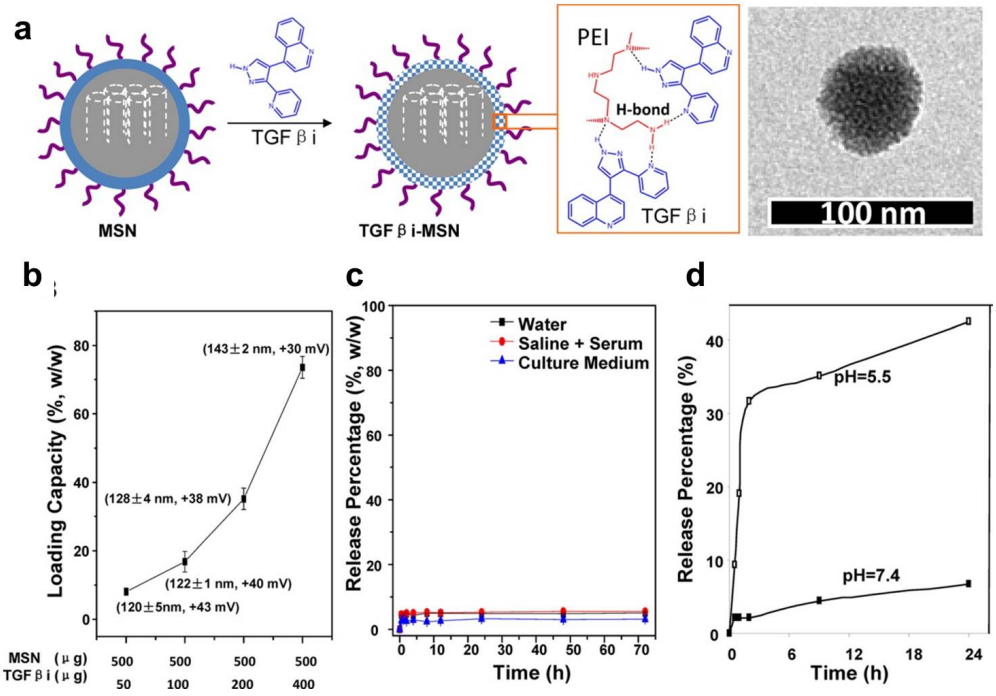

Figure 7.1 Characterization of TGF-β inhibitor -LY364947- loaded PEI-PEG-coated MSNs. (a) Scheme showing the co-polymer coated MSNs and the incorporation of TGF-β inhibitor (TGFβi) via the hydrogen bond, and the TEM image of the MSN particle. (b) Evaluation of the loading capacity for LY364947 by the particles. 500 μg of co-polymer coated particles was incubated with different amount of inhibitors (50 to 400 μg). UV-vis absorption peak of LY364947 at 269 nm was used to characterize the loading amount. Particle size and ζ-potential in solution were measured by a ZetaSizer Nano and are indicated in brackets. The size and ζ-potential prior to dug attachment were 118 $\pm$ 3 nm and + 45 mV. (c) Stability of LY364947 attachment in different solutions. The LY364947 release was studied in deionized water, saline with 2 % serum, and DMEM supplemented with 10 % FCS at different time points at 37 °C. (d) LY364947 release was studied in pH 5.5 aqueous solution for 24 h and compared with the release profile in PBS (pH 7.4).

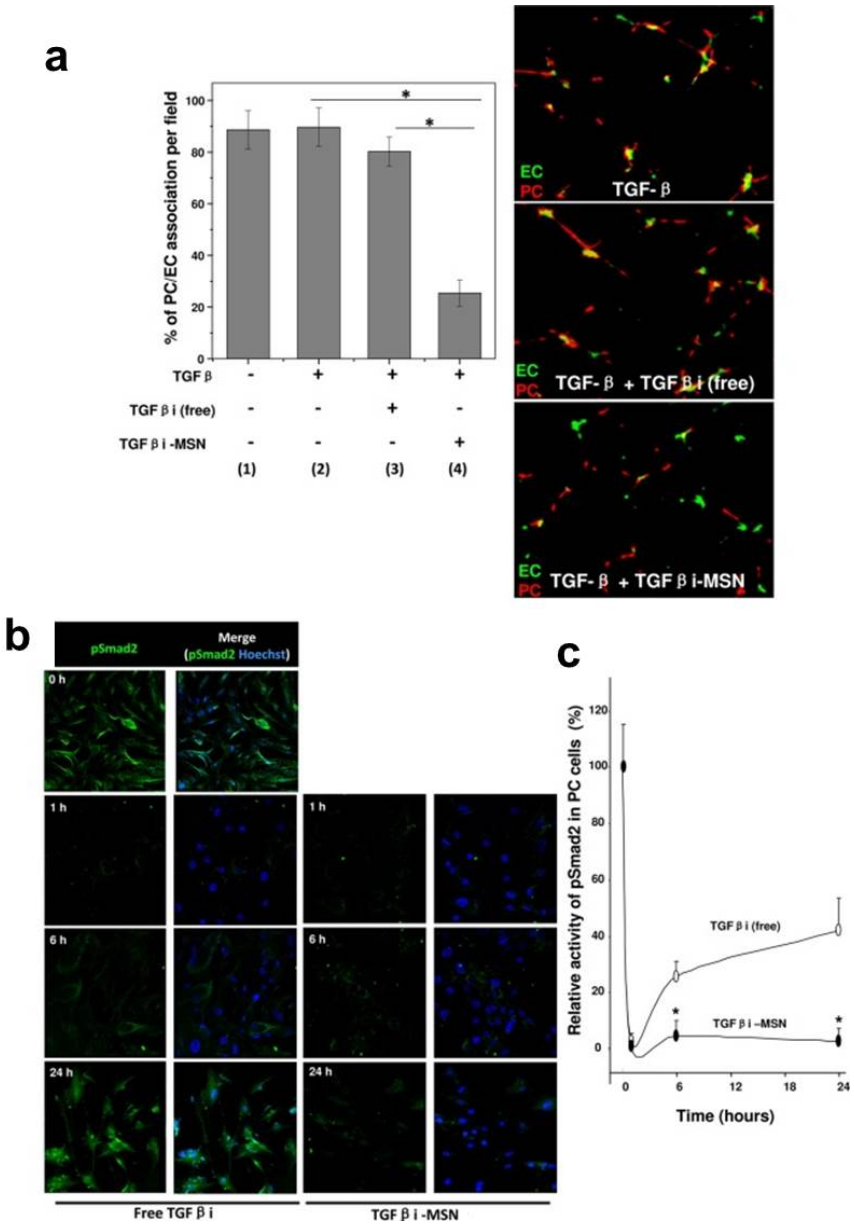

Figure 7.2 *In vitro* dissociation of pericyte (PC) binding to endothelial cell (EC) by TGF-β inhibitor loaded MSNs. (a) HDME (104 cells/mL) and HSM cells (5 $\times$ 103 cells/mL) were stained with green and red fluorescent markers, respectively. ECs were treated with 2 ng/mL of TGF-β for 3 h, and PCs were treated with free inhibitor or inhibitor loaded-MSNs (TGFβi-MSN) at inhibitor dose of 1 μM for 3 h. Subsequently, both cell types were cocultured in Matrigel-coated plates for 16 h at 37 °C. PC/EC adhesions were quantitatively determined in five fields using fluorescence microscopy (Zeiss, Germany); $^*p < 0.05$. (b) Use of fluorescence microscopy to determine the level of Smad2 phosphorylation. PCs were treated with 2 ng/mL TGFβ for 3 h. Subsequently, the cells were treated with TGF-βi-MSN at an inhibitor dose of 1 μM for 124 h. For comparison, free LY364947 was used to treat cells at the same dose. These cells were stained with primary anti-pSmad2 antibody that was detected by a FITC-conjugated secondary antibody. The nucleus was stained by Hoechst 33342. (c) Signal intensity of the green channel, reflecting activated Smad2 (pSmad2), was calculated, using Image J software (version 1.37c, NIH); $^*p < 0.05$.

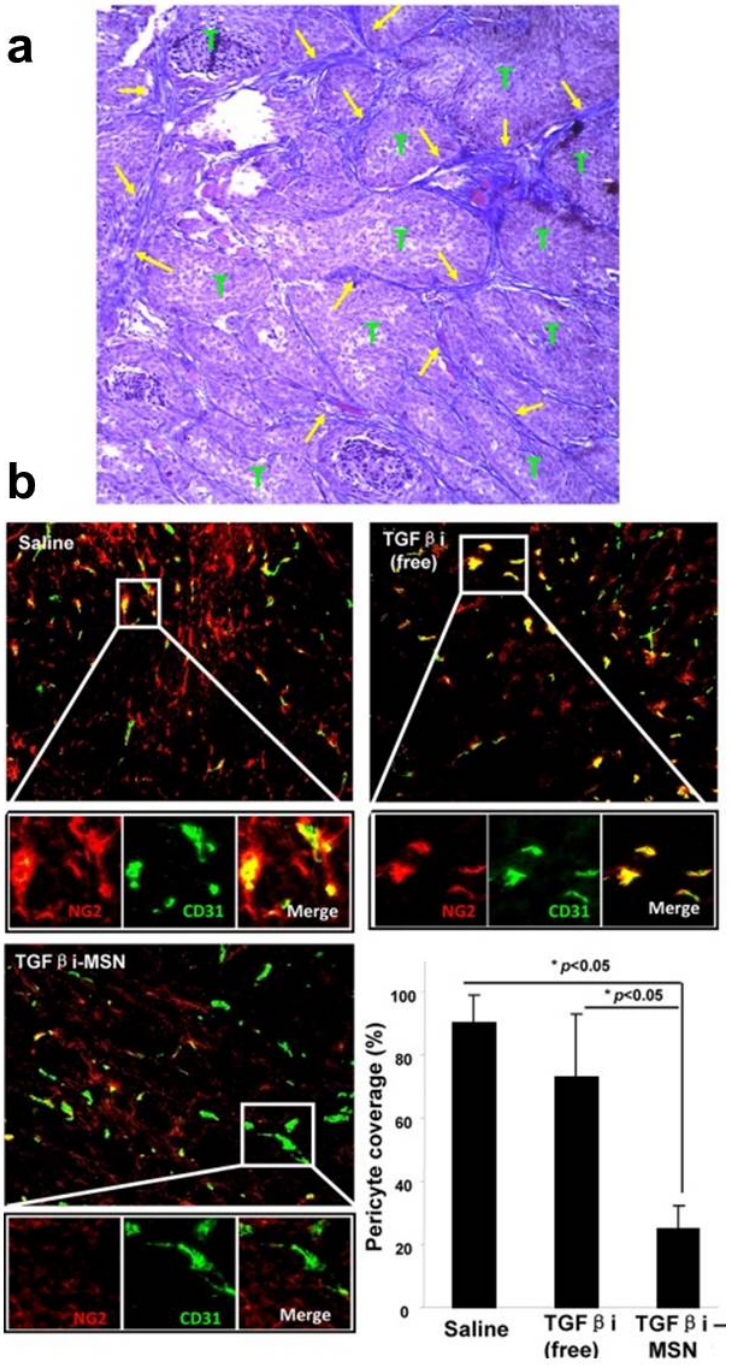

Figure 7.3 *In vivo* TGF-β inhibitor delivery by MSNs to BxPC3 xenograft sections showing the disrupted PC interactions with EC. (a) Staining with Massons trichrome to show prominent interstitial collagen deposition (in blue). "T" indicates tumor cells. Arrows point to the stroma. (b) Two groups of tumor-bearing animals received IV-injected TGFβi-MSN at an inhibitor dose of 1 mg/kg (MSN dose of 2 mg/kg). Saline and IV injection of the same dose of free inhibitor were controls. Tumor tissues (0.81 cm diameter) were collected 12 h post-injection and OCT embedded for frozen section and dual-color immunohistochemistry staining. The EC marker (CD31) was green (FITC), and the PC marker (NG2) was red (Alexa Fluor 594). Magnification shows the extent of PC/EC colocalization in each group. PC coverage of EC was quantified in three random fields in each group; $^*p < 0.05$.

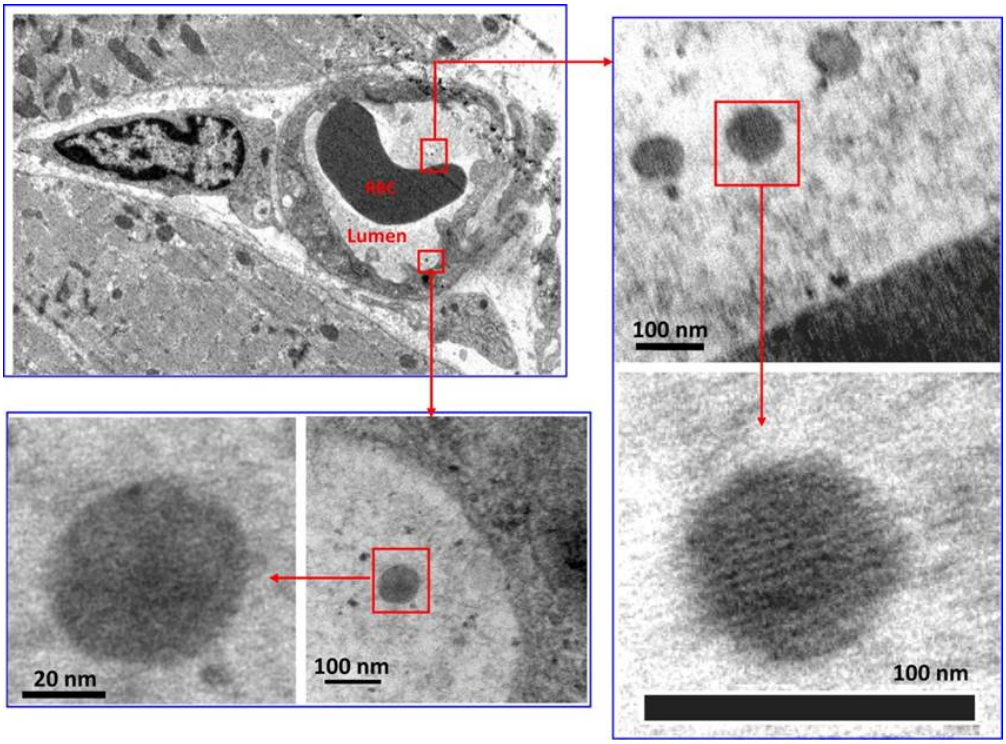

Figure 7.4 TEM ultrastructural analysis to elucidate the presence of TGF-β inhibitor loaded MSNs in BxPC3 xenografts. Electron microscopy to determine the ultrastructure of the tumor 2 h after administration of TGFi-MSN. RBC denotes red blood cell. The porous structure of the nanocarrier can be seen inside the tumor blood vasculature.

7.2 Biosafety of Upconversion Nanocrystals for Biological Imaging

7.2.1 Introduction

Lanthanide-doped fluoride nanocrystals ($NaYF_4$:Yb^{3+}, Ln^{3+}) have gained lots of attentions as novel fluorescence probes for biological imaging [14, 15, 16, 17, 18]. Different from the widely applied organic molecular biomarkers, these nanocrystals emit at a lower wavelength than the excitation light source. The long wavelength incident photons are converted to the high energy emitted photons by an excited state energy transfer mechanism. Compared to the downshifting of energy, the upconversion emission in imaging applications benefits from the high photostability, low auto fluorescence, sharp contrast and deep tissue penetration for *in vitro* and *in vivo* studies [14, 16, 17].

The use of lanthanides nanoparticles in biological environments, however, is limited by their toxicities to various types of tissues [19]. The mechanism of pathological changes caused by lanthanide nanoparticles is not fully understood, yet necessary in order to reduce these effect with an appropriate method. The whole project involves three parts of work: the mechanism of lanthanide toxicity is thoroughly examined; in light of that, a treatment strategy has been proposed and evaluated; the strategy is applied to upconversion nanocrystals for *in vitro* and *in vivo* imaging. We will briefly explain the first two parts and discuss primarily the third component in this section.

7.2.2 Upconversion Nanocrystal Structural Transformation in Biological Environment

Both lanthanide oxide nanoparticles and lanthanide fluoride upconversion nanocrystals ($NaYF_4$:Yb^{3+}, Er^{3+}, doping molar ratio: Y : Yb : Er = 0.8 : 0.18 : 0.02) have been examined for their structural transformation in biological systems. The former work has been published recently [19], and the later is still under investigation, which will be our focus in this section. The lanthanide compounds have higher solubilities in acidic solutions and the dissolved lanthanide ions tend to have high binding affinity with phosphate groups [20, 21]. Considering the low pH in lysosomes and the high concentration of phosphates in cell membranes, we hypothesize that the lanthanide particles undergo structural changes in this environment.

By using phagolysosomal simulated fluid (PSF) to mimic the lysosome fluid, the influence of the lysosome environment on lanthanide nanoparticles was examined. As shown in the TEM images in Figure 7.5 on page 186 (lower left image), the $NaYF_4$:Yb^{3+}, Er^{3+} nanocrystals lost their original particle morphology and became amorphous after suspending in PSF solution for 24 h, at a concentration of 100 μg/mL. Whereas in the aqueous solution, $NaYF_4$:Yb^{3+}, Er^{3+} nanocrystal structure was maintained after the treatment (upper left image). Thus, the lanthanide nanoparticle does undergo conformational change from homogeneous particles to amorphous structures in the phosphate abundant solution, probably due to the dissolving of the ions and the re-binding with the phosphate groups. The structural transformation has also resulted in a luminescence property change. As illustrated on the right side of Figure 7.5, the nanoparticle upconversion emission (black curve)

was quenched dramatically after the treatment with PSF (red curve), indicating the lattice structure disorganization in the transformation process and hence the low efficiency of energy transfers between Yb^{3+} ions and Er^{3+} ions.

This luminescence quenching effect as a result of the morphology change is also observed in cellular experiments. THP-1 cells (a human monocytic cell line), in which the nuclei were stained by Hoechst 33342 and the lysosomes were stained by Alexa Fluor 594, were incubated with the upconversion nanocrystals and imaged by confocal spectroscopy to illustrate the particle uptake and their emissions (Figure 7.6 on page 187). Immediately after the incubation, the nanoparticles were internalized by cells and localized in the lysosomes. The upconversion emissions and the lysosome stains luminescence overlapped. 20 h post the incubation, the red emission from lanthanides were quenched significantly with barely any signals observed in the cells, let alone the colocalization with either lysosomes or nuclei.

Based on the analysis that the high binding affinity of phosphate group with the lanthanide is the major factor in inducing the morphology change, we propose to cover the nanoparticle surfaces with coating agents that have higher binding affinities to prevent the competitive binding from molecules in biological environment. A few candidates were chosen including polyvinylpyrrolidinone (PVP), a common polymer coating for nanoparticles, and molecules containing phosphate groups like N-(phosphonomethyl)iminodiacetic acid (PMIDA) and ethylenediamine tetra(methylene phosphonic acid) (EDTMP). Whether these molecules are capable of protecting the lanthanide nanostructures from being transformed by the cellular environment was examined by suspending the coated particles in PSF solution. TEM images and luminescence spectra were collected afterwards and compared

to those of it before the treatment. As shown in Figure 7.7 on page 188, only the particles coated with the EDTMP that contains four phosphate groups were able to preserve them particle morphology and their luminescence property. The other two coating agents were not effective enough to insulate the nanocrystals.

In vitro and *in vivo* examinations were performed to evaluate the protection of nanocrystal by the EDTMP coating. Confocal images with THP-1 cells and primary alvedar macrophages proved that the EDTMP coating could preserve the nanoparticle luminescence property in cellular environment (Figure 7.8 on page 189). The nanoparticle emission quenching by biomolecules was confirmed in animal studies, as the PSF treated $NaYF_4$:Yb^{3+}, Er^{3+} nanoparticle gave out quite weak emission signals from mice, in contrast with the untreated particles (Figure 7.9 on page 190). Upon the EDTMP coating, this effect was no longer observable. The nanocrystals from the subcutaneous injection presented a bright green emission and served as an ideal imaging probes even after the PSF treatment.

7.2.3 Summary

The structural transformation of lanthanide upconversion nanoparticles in biological environment has been thoroughly examined by the morphology analysis and their luminescence spectra. The mechanism involves the competitive binding of phosphate groups in biomolecules with the original surfaces. A coating agent containing abundant amount of phosphate groups is thus introduced to protect the nanocrystal from degradation. The coating has effectively protected the particles from conformational change in *in vitro* and *in vivo* studies.

7.2.4 Figures

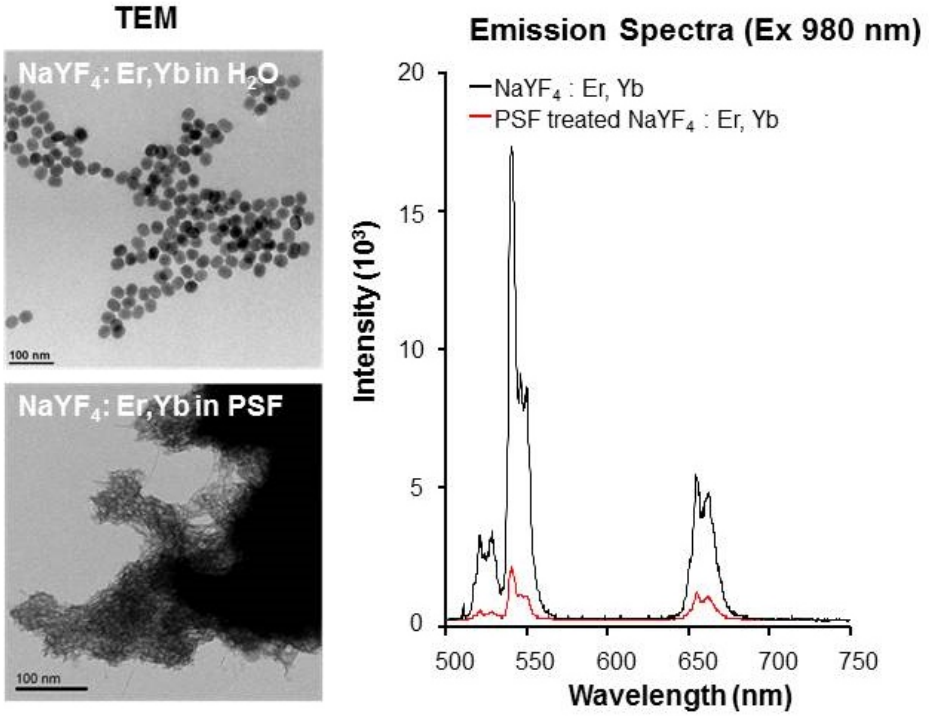

Figure 7.5 Transformation and fluorescence quenching of $NaYF_4$:Yb^{3+}, Er^{3+} in PSF. $NaYF_4$:Yb^{3+}, Er^{3+} nanoparticles were dispersed in PSF at 100 g/mL for 24 h. Then, the particle suspensions were centrifuged at 100, 000 rpm/min for 1 h to collect transformed particles. After washing with DI H2O for three times, the pellets were resuspended in DI H_2O. PSF-treated and untreated $NaYF_4$:Yb^{3+}, Er^{3+} suspensions at 50 μg/mL and 2 mg/mL were used to determine the morphology change by TEM and emission spectrum at 980 nm excitation wavelength, respectively.

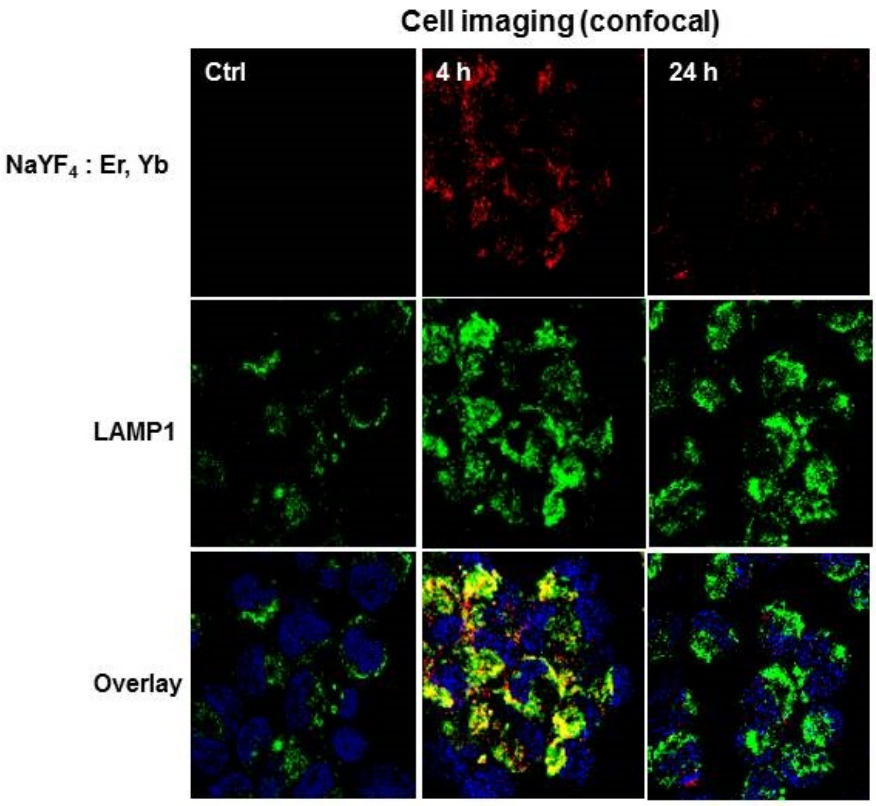

Figure 7.6 Imaging of upconversion nanocrystals in THP-1 cells by confocal microscope. After treated with 25 μg/mL nanocrystals for 4 h, THP-1 cells were cultured in nanocrystal-free media for additional 0 or 20 h. The cell samples were collected, fixed and stained with with Hoechst 33342 or Alexa Fluor 594 labeled anti-LAMP 1 to visualize nuclei or lysosomes.

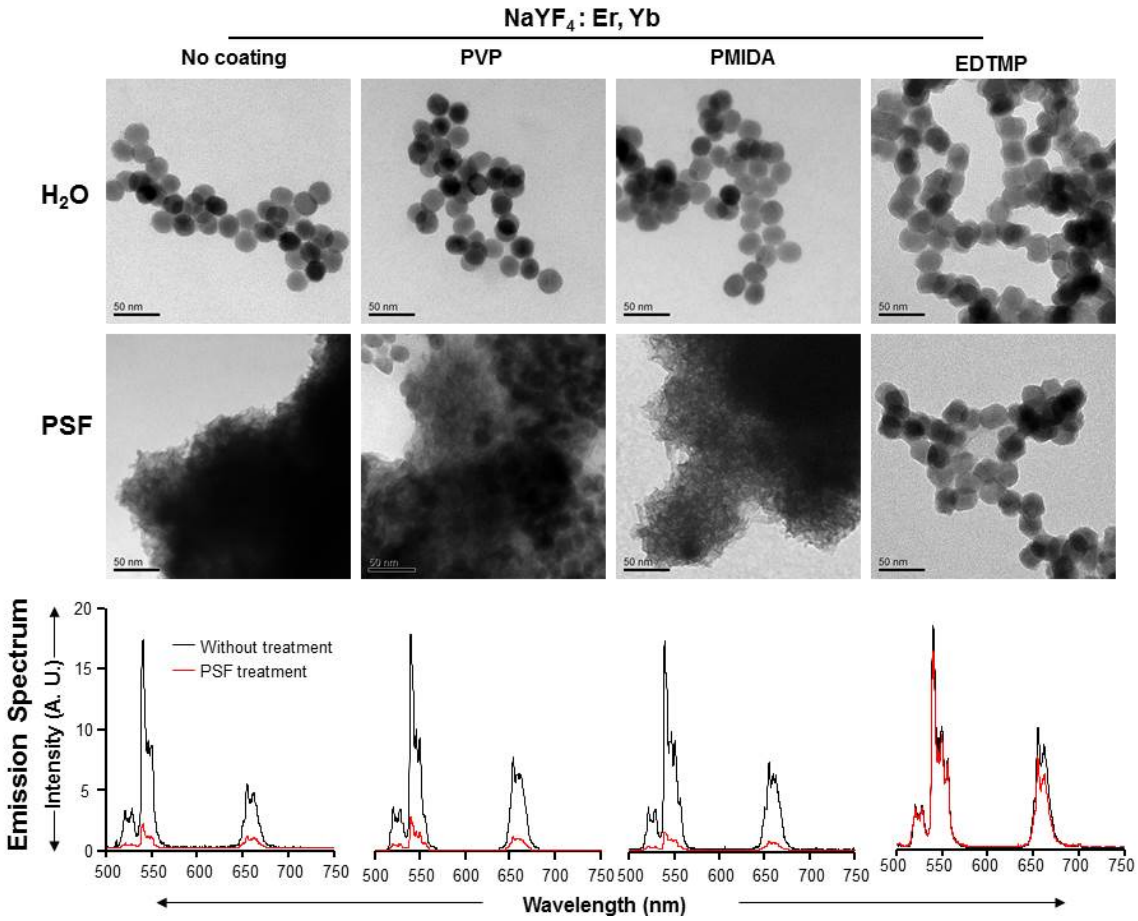

Figure 7.7 Comparison of morphology change and fluorescence emission of uncoated and coated upconversion nanocrystals after PSF treatment. Upconversion nanocrystals (200 μg/mL) were reacted with 400 μg/mL PVP, PMIDA, or EDTMP in DI H_2O for 48 h. Then the coated particles were collected by centrifugation and washed for three times. Upconversion nanocrystals in water solution at 50 μg/mL and 2 mg/mL were used for TEM observation and emission spectra detection, respectively.

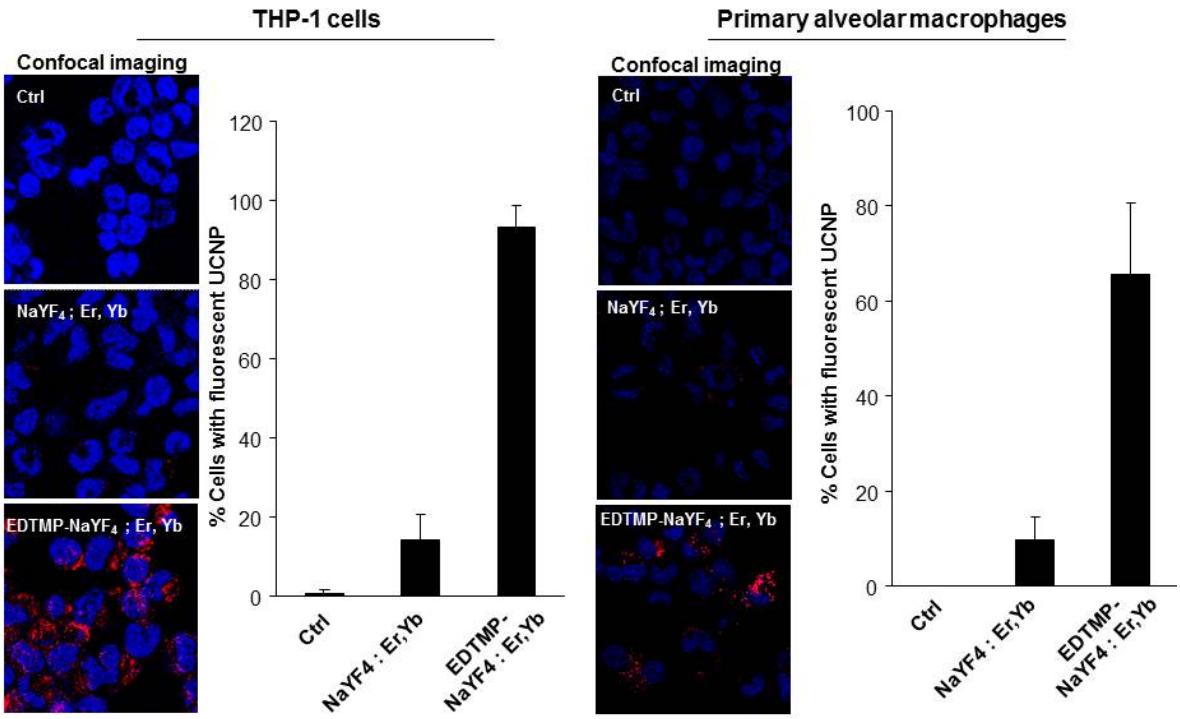

Figure 7.8 Imaging uncoated and EDTMP coated $NaYF_4$:Yb^{3+}, Er^{3+} nanoparticles in THP-1 cells and primay alveolar macrophages. THP-1 cells were treated with 25 μg/mL nanocrystals for 4 h, followed by 20 h incubation in nanocrystal-free media before confocal imaging. Primary alveolar macrophages were extracted from the BALF of mice exposed to 2 mg/kg for 40 h.

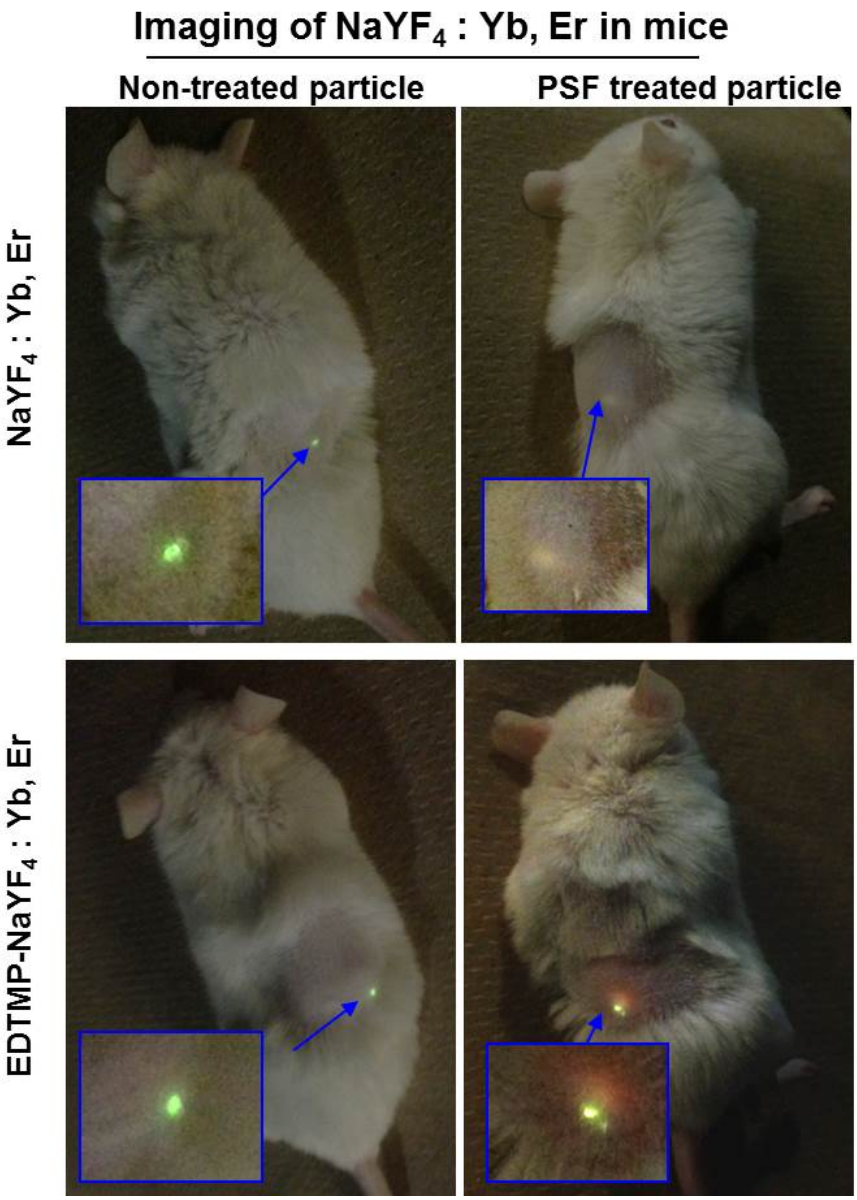

Figure 7.9 Balb/c mice were subcutaneously injected with 0.1 mg (50 μL of 2 mg/mL) untreated or PSF treated $NaYF_4$:Yb^{3+}, Er^{3+} and EDTMP-$NaYF_4$:Yb^{3+}, Er^{3+} particles. Then the animals were anesthetized and positioned under a 980 nm laser beam to excite the crystals for imaging.

7.3 Aluminum Oxyhydroxide Nanoparticles Surface Hydroxyl Group Characterization and Its Impact on the Cellular Uptake Performances

7.3.1 Background

The research in this section the chemical component for a multidisciplinary project, involving engineering an effective immune adjuvant by designed control of shape and crystallinity of aluminum oxyhydroxide (AlOOH) nanoparticles [22]. The project utilizes a group of AlOOH nanoparticles with different shapes, crystallinities and hydroxyl content, to investigate the influence of particle structures on their adjuvant activities at an *in vivo* level. The adjuvant activities are characterized by the NLRP3 inflammasome and the IL-1β production, which is putatively one of the major mechanisms. The particles are thoroughly examined in regarding to their physical and chemical properties. TEM images revealed their variable shapes, including plates, polyhedra and rods of variable aspect ratios. γ - AlOOH nanocrystals evolve into nanorods under acidic conditions, and into nanoplates and nanohedra under basic conditions (Figure 7.10 on page 196). XRD analysis showed that the crystallinity of rod particles could be finely tuned from $\sim$ 6% to 100 % by extending the hydrothermal reaction time from 2 h to 16 h at 200 °C (Figure 7.11a on page 196). Sample Rod 1, 2, 3, 4, and 5 were prepared by reacting for 2 h, 3 h, 4 h, 6 h and 24 h, respectively.

7.3.2 Surface Hydroxyl Group Characterization by Thermogravimetric Analysis

To characterize the content of hydroxyl groups on the particle surface, thermogravimetric analysis (TGA) was performed by heating the samples from 20 to 1000 °C. The results demonstrated significant weight loss over the temperature range (Figure 7.11b). For Rod 1, 2, 3, 4, and 5, this value is 30.4, 23.2, 19.0, 17.7, and 16.5 wt. %, respectively. All samples showed higher weight loss than the theoretical estimation ($\sim$ 15 wt.%) that was expected for the transformation of AlOOH to Al_2O_3. This suggests that these particles, from inception, carry a relatively high water content and hydroxyl display on their surfaces. The derivative thermogravimetric curve (DTG in Figure 7.11b) illustrates the emergence of two weight loss stages over the heating range. The first stage, leading to a weight loss of 0.5 - 2.9 wt.% at around 100 °C, is assigned as the desorption of water from the particle surface. The second stage, showing a weight loss of 13.6 - 24.8 wt.% at 395 - 485 °C, resulted from the removal of interstitial water and hydroxyl groups on the AlOOH nanorods [23]. Generally speaking, particles of lower crystallinity tend to have higher weight loss in the second stage, and the dehydroxylation occurs at a relatively lower temperature. Since the dehydroxylation process starts with the protons reacting with hydroxyl ions to form water, followed by their desorption from the internal surface, it is possible that the diffusion occurs much easier in the lower-crystallinity particles (therefore requiring a lower dehydroxylation temperature). Above 500 °C, there is a weight loss of $\sim$ 2 wt.% for all particles, which is from the hydroxyl content of the converted product (Al_2O_3). Consistent with the XRD results, all nanoplates and nanopolyhedra showed relatively low weight loss by TGA analysis (16.0 - 19.0 wt.% for

the plates and 16.1 wt.% for the polyhedra), because of the high crystallinity. In contrast, aluminum salts displayed a multistage TGA profile with the total weight loss up to 37 wt.%, which could be contributed to the dehydroxylation and/or decomposition of various active components in the product (Figure 7.12b on page 197), suggesting that aluminum salts is composed of different materials.

7.3.3 Quantification of Particle Intracellular Uptake by Flow Cytometry

We assessed the cellular uptake of the AlOOH nanorods by transmission electron microscopy (TEM) and flow cytometry. The TEM images showed that all AlOOH nanorods were taken up into membrane-lined vesicles in THP-1 cells (Figure 7.13a on page 198). Because the TEM analysis is not quantitative, we performed a flow cytometry study using FITC-labeled rod particles. The reaction of attaching the fluorescent probes was carried out by first reacting the surface hydroxyl groups on AlOOH particles with the aminopropyltriethoxysilane (APTES) to decorate them with functional amine groups, followed by the amine - isothiocyanate reaction with the FITC molecules. As we have mentioned in the last part, the hydroxyl group density on the different rod particles are different, minimum amount of functional amine groups was applied to all samples, so that samples with same concentrations would have similar fluorescence intensities regardless of their hydroxyl group variations. Thus, the quantification of cellular uptakes by flow cytometry is reliable.

We found that Rod 1 and 2 were taken up in significantly higher quantities than Rod 3 - 5 (Figure 7.13b). This could be explained by the larger agglomeration of Rod 1 and 2 as shown by the TEM images. To confirm that the cellular uptake is important for inflammasome

activation, the actin polymerization inhibitor, cytochalasin D (Cyto D) (Sigma, St. Louis, MO), was used to show that the interference in rod uptake is accompanied by reduced IL-1β production (Figure 7.13c).

7.3.4 Method

TGA analysis was performed by heating the samples from 20 to 1000 °C at a rate of 10 °C/min under air with a Perkin-Elmer Diamond Thermogravimmetric/Differential Thermal Analyzer.

AlOOH nanorods were labeled with the fluorescein isothiocyanate (FITC) by resuspending 7 mg of nanoparticles in 1.5 mL of dimethylformamide (DMF). To this we added 2.5 μL of 4% aminopropyltriethoxysilane. The nanoparticle-APTES mixed solution was allowed to react under nitrogen gas at room temperature for 24 h. The particles were washed with DMF and resuspended in 0.5 mL of DMF. The FITC-DMF solution was prepared by dissolving 2 mg of FITC in 1 mL of DMF. 88 μL of FITC-DMF solution was added into the nanoparticle-DMF mixture and reacted overnight. The FITC-labeled nanoparticles were washed with purified water several times and suspended in water at 20 mg/mL for future use. THP-1 cells in 2 mL of tissue culture medium were plated at the density of 4 $\times$ 105 per well in a 12-well plate in the presence of 1 μg/mL of phorbol, 12-myristate, 13-acetate (PMA) for 16 h. The medium was replenished, and the differentiated THP-1 cells were treated with AlOOH nanoparticles (500 μg/mL) in the presence of LPS (10 ng/mL) for 6 h. Cells were washed and resuspended in PBS for flow cytometry analysis. The cells were analyzed using FACScan flow cytometer (Becton Dickinson), and the data were analyzed using

FlowJo (Ashland, OR).

7.3.5 Summary

A group of aluminum oxyhydroxide nanomaterials with different shapes, crystallinities and hydroxyl content have been thoroughly characterized by chemical methods in order to investigate their adjuvant immune effects. Thermogravimetric analysis has been used to evaluate the particle surface hydroxyl group amounts. Fluorescent modifications based on the hydroxyl groups are carefully carried out to provide the particle quantification basis in flow cytometry. The result deepens the understanding of AlOOH physicochemical properties, which play a key role in the ability of AlOOH nanorods to activate the NLRP3 inflammasome, leading to IL-1β production in dendritic cells and boosting OVA-specific immune responses in mice [22]. Overall, not only are these adjuvants superior to aluminum salts in terms of relative strength, but we also demonstrate that it is possible to boost the *in vivo* immune responses by coinjection with antigen or dendritic cell adoptive transfer. The engineered design of aluminum-based adjuvants in combination with structure-activity analysis of the events around NLRP3 inflammasome activation could be used as a platform to enhance aluminum-based vaccines.

7.3.6 Figures

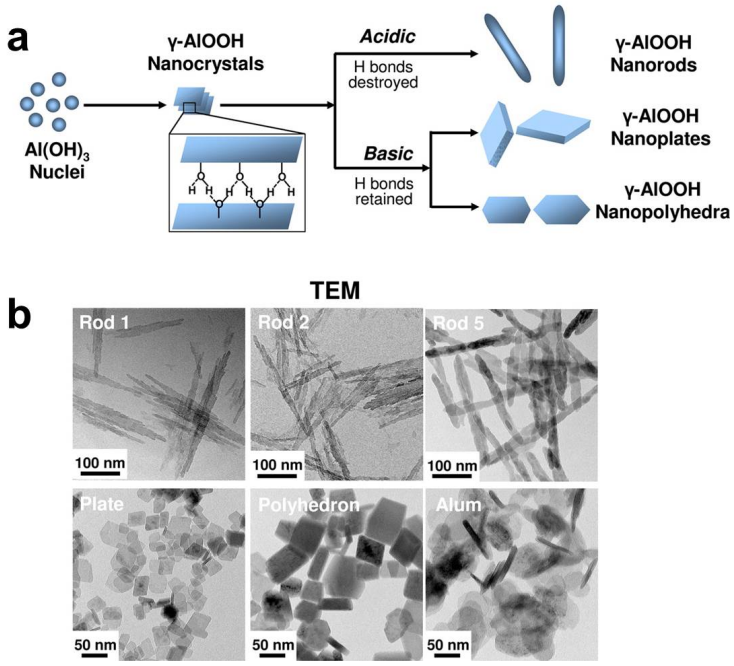

Figure 7.10 Schematic representation of the synthetic chemistry and TEM analyses of AlOOH nanoparticles. (a) Schematic representation of the synthetic chemistry and mechanisms of AlOOH nanoparticle formation under acidic and basic conditions. (b) Representative TEM images of AlOOH nanorods obtained after a synthesis period of 2 h (Rod 1), 3 h (Rod 2), and 24 h (Rod 5). AlOOH nanoplates were synthesized using a reaction time of 24 h, while nanopolyhedra were generated after a reaction time of 72 h. All synthesis was conducted at 200 °C. The TEM image of commercial Alum, used as control material, is also shown. The images were taken with a JEOL 1200 EX TEM with an accelerating voltage of 80 kV.

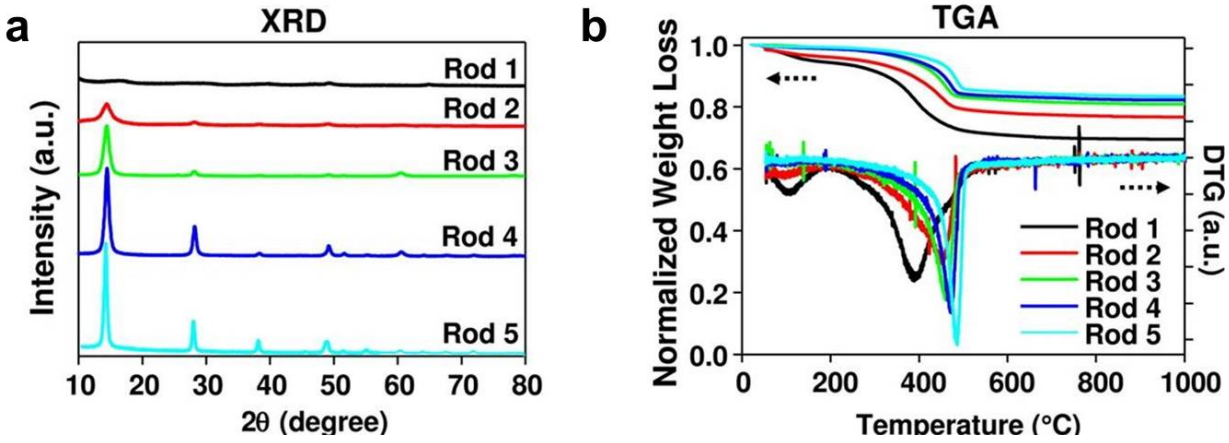

Figure 7.11 XRD and TGA analysis of AlOOH nanorods. (a) XRD patterns of the nanorods. (b) TGA and DTG analyses of the nanorods.

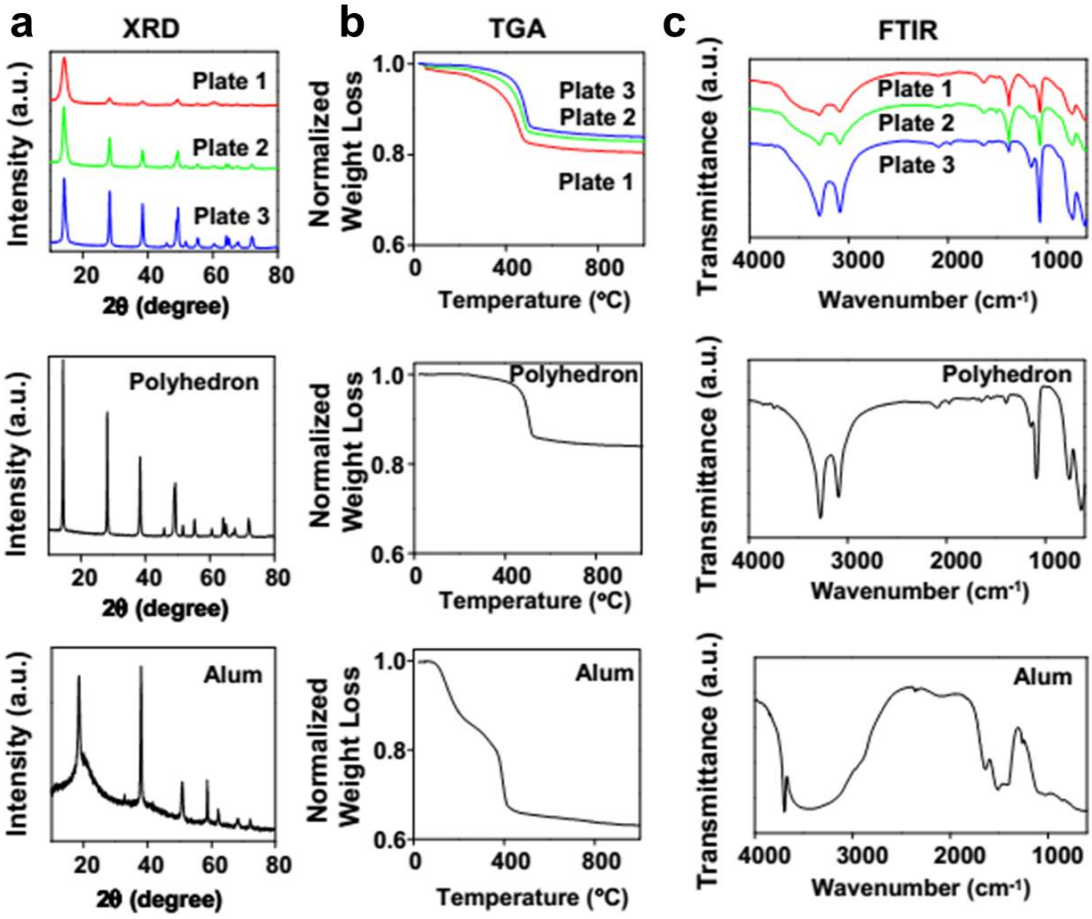

Figure 7.12 XRD and TGA analysis of AlOOH nanorods. (a) XRD patterns, (b) TGA analysis, and (c) FTIR spectra of AlOOH nanoplates, AlOOH nanopolyhedra and aluminum salts (labeled as Alum).

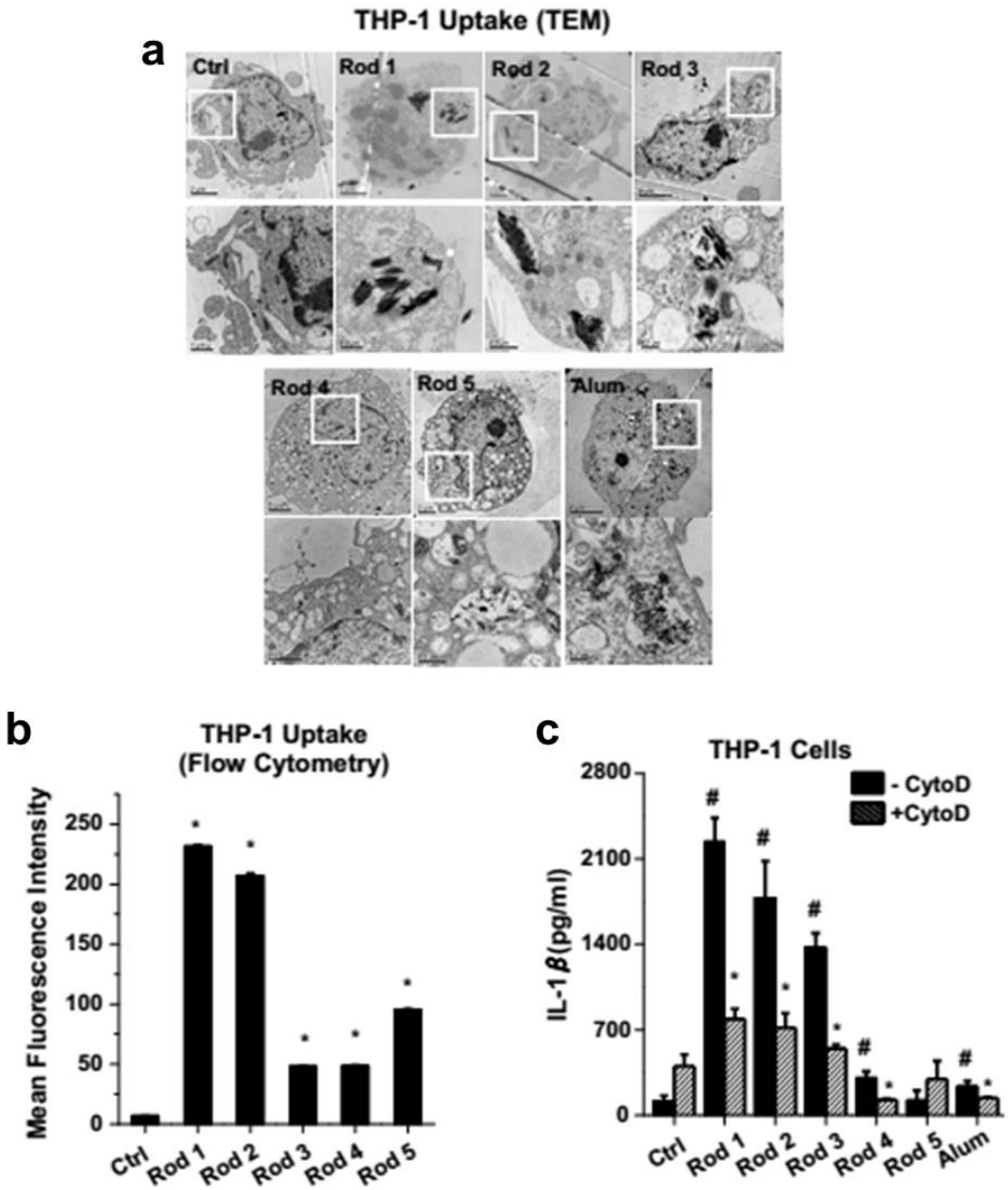

Figure 7.13 (a) Cellular uptake of nanorods was determined by TEM analysis of THP-1 cells exposed to AlOOH nanorods for 24 h. The images were taken with a JEOL 1200EX electron microscope at 80 kV. (b) Flow cytometry analysis of AlOOH nanorod associated with THP-1 cells. FITClabeled AlOOH nanorods were exposed to THP-1 cells for 6 h, then the cells were collected for flow cytometry analysis. $^{*}p < 0.05$ compared to control. (c) THP-1 cells were pre-treated with 5 μM of cytochalasin D (Cyto D) for 30 min and then the cells were exposed to AlOOH nanorods for an additional 6 h. IL-1β content in the supernatant was quantified by ELISA. $^{*}p < 0.05$ compared to THP-1 cells without CytoD treatment; $^{\#}p < 0.05$ compared to control.

7.4 References

[1] S. Morikawa, P. Baluk, T. Kaidoh, A. Haskell, R. K. Jain, and D. M. McDonald. "Abnormalities in Pericytes on Blood Vessels and Endothelial Sprouts in Tumors." *Am. J. Pathol.*, **160**(3):985–1000, 2002.

[2] A. Armulik, A. Abramsson, and C. Betsholtz. "Endothelial/Pericyte Interactions." *Circ. Res.*, **97**(6):512–523, 2005.

[3] S. Goel, D. G. Duda, L. Xu, L. L. Munn, Y. Boucher, D. Fukumura, and R. K. Jain. "Normalization of the Vasculature for Treatment of Cancer and Other Diseases." *Physiol. Rev.*, **91**(3):1071–1121, 2011.

[4] E. A. Winkler, R. D. Bell, and B. V. Zlokovic. "Central nervous system pericytes in health and disease." *Nat. Neurosci.*, **14**(11):1398–1405, 2011.

[5] H. Meng, M. Xue, T. Xia, Z. Ji, D. Y. Tarn, J. I. Zink, and A. E. Nel. "Use of Size and a Copolymer Design Feature To Improve the Biodistribution and the Enhanced Permeability and Retention Effect of Doxorubicin-Loaded Mesoporous Silica Nanoparticles in a Murine Xenograft Tumor Model." *ACS Nano*, **5**(5):4131–4144, 2011.

[6] T. Xia, M. Kovochich, M. Liong, H. Meng, S. Kabehie, S. George, J. I. Zink, and A. E. Nel. "Polyethyleneimine Coating Enhances the Cellular Uptake of Mesoporous Silica Nanoparticles and Allows Safe Delivery of siRNA and DNA Constructs." *ACS Nano*, **3**(10):3273–3286, 2009.

[7] V. Estrella, T. Chen, M. Lloyd, J. Wojtkowiak, H. H. Cornnell, A. Ibrahim-Hashim, K. Bailey, Y. Balagurunathan, J. M. Rothberg, B. F. Sloane, et al. "Acidity Generated by the Tumor Microenvironment Drives Local Invasion." *Cancer Res.*, **73**(5):1524–1535, 2013.

[8] N. Song, Y. Huang, H. Shi, S. Yuan, Y. Ding, X. Song, Y. Fu, and Y. Luo. "Overexpression of Platelet-Derived Growth Factor-BB Increases Tumor Pericyte Content via Stromal-Derived Factor-1/CXCR4 Axis." *Cancer Res.*, **69**(15):6057–6064, 2009.

[9] G. Bergers. "The role of pericytes in blood-vessel formation and maintenance." *Neuro-Oncol.*, **7**(4):452–464, 2005.

[10] X. Varelas, P. Samavarchi-Tehrani, M. Narimatsu, A. Weiss, K. Cockburn, B. G. Larsen, J. Rossant, and J. L. Wrana. "The Crumbs Complex Couples Cell Density Sensing to Hippo-Dependent Control of the TGF--SMAD Pathway." *Dev. Cell*, **19**(6):831–844,

2010.

[11] P. Farace, F. Merigo, S. Fiorini, E. Nicolato, S. Tambalo, A. Daducci, A. Degrassi, A. Sbarbati, D. Rubello, and P. Marzola. "DCE-MRI using small-molecular and albumin-binding contrast agents in experimental carcinomas with different stromal content." *Eur. J. Radiol.*, **78**(1):52–59, 2011.

[12] H. Cabral, Y. Matsumoto, K. Mizuno, Q. Chen, M. Murakami, M. Kimura, Y. Terada, M. R. Kano, K. Miyazono, M. Uesaka, et al. "Accumulation of sub-100 nm polymeric micelles in poorly permeable tumours depends on size." *Nat. Nano.*, **6**(12):815–823, 2011.

[13] H. Meng, Y. Zhao, J. Dong, M. Xue, Y.-S. Lin, Z. Ji, W. X. Mai, H. Zhang, C. H. Chang, C. J. Brinker, et al. "Two-Wave Nanotherapy To Target the Stroma and Optimize Gemcitabine Delivery To a Human Pancreatic Cancer Model in Mice." *ACS Nano*, **7**(11):10048–10065, 2013.

[14] D. Chatterjee, A. Rufaihah, and Y. Zhang. "Upconversion fluorescence imaging of cells and small animals using lanthanide doped nanocrystals." *Biomaterials*, **29**(7):937–943, 2008.

[15] Z. Li, Y. Zhang, and S. Jiang. "Multicolor Core/Shell-Structured Upconversion Fluorescent Nanoparticles." *Adv. Mater.*, **20**(24):4765–4769, 2008.

[16] J. Zhou, Y. Sun, X. Du, L. Xiong, H. Hu, and F. Li. "Dual-modality *in vivo* imaging using rare-earth nanocrystals with near-infrared to near-infrared (NIR-to-NIR) upconversion luminescence and magnetic resonance properties." *Biomaterials*, **31**(12):3287–3295, 2010.

[17] C. T. Xu, N. Svensson, J. Axelsson, P. Svenmarker, G. Somesfalean, G. Chen, H. Liang, H. Liu, Z. Zhang, and S. Andersson-Engels. "Autofluorescence insensitive imaging using upconverting nanocrystals in scattering media." *Appl. Phys. Lett.*, **93**(17):171103, 2008.

[18] G. Wang, Q. Peng, and Y. Li. "Lanthanide-Doped Nanocrystals: Synthesis, Optical-Magnetic Properties, and Applications." *Accounts Chem. Res.*, **44**(5):322–332, 2011.

[19] R. Li, Z. Ji, C. H. Chang, D. R. Dunphy, X. Cai, H. Meng, H. Zhang, B. Sun, X. Wang, J. Dong, et al. "Surface Interactions with Compartmentalized Cellular Phosphates Explain Rare Earth Oxide Nanoparticle Hazard and Provide Opportunities for Safer Design." *ACS Nano*, **8**(2):1771–1783, 2014.

[20] F. H. Firsching and S. N. Brune. "Solubility products of the trivalent rare-earth phos-

phates." *J. Chem. Eng. Data*, **36**(1):93–95, 1991.

[21] E. Austreng, T. Storebakken, M. S. Thomassen, S. Refstie, and Y. Thomassen. "Evaluation of selected trivalent metal oxides as inert markers used to estimate apparent digestibility in salmonids." *Aquaculture*, **188**(1-2):65–78, 2000.

[22] B. Sun, Z. Ji, Y.-P. Liao, M. Wang, X. Wang, J. Dong, C. H. Chang, R. Li, H. Zhang, A. E. Nel, et al. "Engineering an Effective Immune Adjuvant by Designed Control of Shape and Crystallinity of Aluminum Oxyhydroxide Nanoparticles." *ACS Nano*, **7**(12):10834–10849, 2013.

[23] S. Shen, W. K. Ng, L. S. O. Chia, Y. Dong, and R. B. H. Tan. "Morphology Controllable Synthesis of Nanostructured Boehmite and -Alumina by Facile Dry Gel Conversion." *Cryst. Growth Des.*, **12**(10):4987–4994, 2012.

Part V

Conclusion and Future Direction

CHAPTER 8

Conclusion and Future Directions

8.1 Conclusion

The research described in this dissertation focuses on the physical properties and the chemical functionalizations of mesoporous silica nanoparticles for their biomedical applications in drug delivery and imaging. More specifically, the three components: the particle functionalizations involved with nanomachines, the thermal properties of silica nanoparticles and their biomedical applications have been thoroughly studied and investigated.

Several chemical approaches have been employed to study and optimize the on-demand drug deliver performance of mesoporous silica nanoparticles. A series of acid-responsive nanovalves based on the variable binding affinity between phenylamine groups and α -cyclodextrin has been employed to trap and release the cargoes. In an effort to explore the imaging capacity of MSNs, these nanovalve modified particles were loaded with gadolinium complexes to enhance the MR imaging contrast. Although the initial investigation did not observe an on-command release event of Gd-DTPA in the time resolved fluorescence spectroscopy, a different strategy has succeeded in bonding the complex onto the α-cyclodextrin caps. Another gadolinium complex, Gd-DOTA, has been attached onto the

PEI-PEG copolymer coated particles, which was verified by the EPR absorption spectrum and the shortened proton T_1 relaxation time in NMR measurement. Moreover, two polymer-nanomachine combined systems have been developed for the purpose of integrating siRNA delivery capacity and enhancing their biodistribution. The acid nanovalves in the presence of polymer surface coatings were still able to trap and release the cargo molecules accordingly with the environmental pH change, presenting a multifunctional platform that exhibits properties of all components.

The thermal property of mesoporous silica nanoparticles was examined using the temperature dependent luminescence spectra of $NaYF_4$:Yb^{3+}, Er^{3+} nanocrystals. The lanthanide-doped fluoride nanocrystal has two emission bands that originate from two thermally coupled excited states and thus their intensity ratios serve as a nano probe for temperature detection. The idea has been applied to study the magnetic heating efficiency of superparamagnetic nanocrystals in a high frequency oscillating magnetic field, by embedding both types of nanocrystals into the same mesoporous silica particle. The heating depended on the exposure time to the oscillating magnetic field and the field induction power. We were able to measure the nanoparticle interior temperature and quantify the temperature gradient between this nano-environment and the bulk surroundings. Moreover, the temperature detection strategy has been employed to solve a mystery about whether the IR irradiation triggered cargo release of nanoimpellers was a photochemical or a photothermal reaction. Azobenzene modified silica particles were embedded with the upconversion lanthanide nanocrystals.The temperature measurement showed substantial optical heating, and the release performance under either light or heat stimulation revealed that the upconversion process could not generate

sufficient high energy photons to initiate the photoisomerization of azobenzenes. Thus, in a photon responsive release system, the irradiation thermal contribution should be precisely evaluated. In a step forward, we used these lanthanide nanocrystal embedded particles to simultaneously monitor the interior temperature change and the corresponding dye molecule release. By recording the two signals in one emission spectrum, we have opened a new path to examine the nanoscale event together with its macroscopic result.

For biological applications, the silica particles have delivered inhibitors to pancreatic tissues and interrupted the stroma formation to reduce their drug resistance. In another project, the lanthanide nanocrystals have successfully served as a bright luminescence probe in *in vitro* and *in vivo* imaging.

8.2 Future Directions

The future direction of this work should focus on deepening the physical property investigation in order to facilitate the design and construction of the on-demand cargo delivery systems. The thermal study of nanoparticles could certainly benefit the manipulation of temperature-responsive release carriers. Other physical properties, such as the rigidity of the silica matrix and the cargo packing patterns inside the pores would all be crucial components in guiding the development of silica based drug delivery vehicles.